

UNIVERSIDADE DE SÃO PAULO
INSTITUTO DE QUÍMICA DE SÃO PAULO
PROGRAMA DE POS-GRADUAÇÃO EM QUÍMICA

Matheus Schiavon Kronka

"New insights into modified carbon-based catalysts shaped as gas diffusion electrodes for efficient H₂O₂ production under wastewater treatment processes: a material engineering approach"

São Carlos

2023

MATHEUS SCHIAVON KRONKA

"New insights into modified carbon-based catalysts shaped as gas diffusion electrodes for efficient H₂O₂ production under wastewater treatment processes: a material engineering approach"

Thesis presented to the Institute of Chemistry of São Carlos, University of São Paulo (USP) as part of the requirements for the degree of Doctor of Science.

Concentration area: Analytical and Inorganic Chemistry

Supervisor: Prof. Dr. Marcos Roberto de Vasconcelos Lanza

São Carlos

2023

Autorizo a reprodução e divulgação total ou parcial deste trabalho, por qualquer meio convencional ou eletrônico para fins de estudo e pesquisa, desde que citada a fonte.

Assinatura: *Matheus S. Kronka*
Data: 30/06/2023

Ficha Catalográfica elaborada pela Seção de Referência e Atendimento ao Usuário do SBI/IQSC

Kronka, Matheus Schiavon

New insights into modified carbon-based catalysts shaped as gas diffusion electrodes for efficient H₂O₂ production under wastewater treatment processes: a material engineering approach / Matheus Schiavon Kronka. — São Carlos, 2023.

114 f.

Tese (Doutorado em Química Analítica e Inorgânica) — Instituto de Química de São Carlos / Universidade de São Paulo, 2023.

Orientador: Prof. Dr. Marcos Roberto de Vasconcelos Lanza

1. Peróxido de hidrogênio. 2. Modificação de materiais carbonáceos. 3. Eletrodo de difusão gasosa. 4. Processos oxidativos avançados eletroquímicos. 5. Efluente real. I. Título.



ACKNOWLEDGMENTS

- To my parents Marisa de Fátima Schiavon and José Maria Viana Kronka and to my brother Luis Henrique Schiavon Vargas for the family core of love, care, and emotional support in following my dream in the research area.
- To Prof. Dr. Marcos R. V. Lanza for the opportunity to conduct my PhD under the support, incentive, supervision and teachings of a recognized researcher at a renowned Institute of Chemistry of São Carlos from the University of São Paulo.
- To Prof. Dr. Ignasi Sirés Sadornil, from the University of Barcelona, for accepting me as one of his exchange students and for all the support and teachings that helped me to improve my critical thinking and scientific skills.
- To researchers Drs. Guilherme Vilalba Fortunato, Alexsandro Jhones dos Santos and Paulo Jorge Marques Cordeiro Junior for their friendship, support and contribution to my professional and scientific development.
- To the members and ex-members of the *Grupo de Processos Eletroquímicos e Ambientais* (GPEA), at the University of São Paulo, who helped me over the years in the execution of this thesis with discussions and partnerships.
- To all the friends who always supported me and contributed to my personal and critical development.
- To the friends and members of the *Laboratori d'Electroquímica dels Materials i del Medi Ambient* (LEMMA), from the University of Barcelona, that during my exchange in Spain provide me great theoretical discussions and a very good working atmosphere.
- To my friends, colleagues, teachers, workers from the cleaning services, university restaurant, transport, and USP office, who have been motivated me to pursue my dream and not give up on it.
- To the GPEA chemical technicians, José Augusto Fragale Baio and Benedito Manoel dos Santos, for the assistance and lessons on equipment analysis and solution preparation.
- To São Paulo Research Foundation (FAPESP) for the financial support with scholarships awarded in the country and abroad, grants: 2017/23464-3 and 2021/10973-21.

-
- This study was financed in part by the National Council for Scientific and Technological Development – CNPq, grant #134370/2017-1.
 - To Coordenação de Aperfeiçoamento de Pessoal de Nível Superior – Brasil (CAPES) – Finance Code 001.

EPHIGRAPH

"Nothing in life is to be feared; it is only to be understood."

(Marie Curie)

ABSTRACT

The design of highly efficient catalysts to produce hydrogen peroxide (H_2O_2) through oxygen reduction reaction (ORR) is crucial to make electro-Fenton (EF) and photoelectro-Fenton (PEF) processes feasible for real wastewater treatment. The aim of this thesis was to develop and optimize low metal catalysts supported on Printex L6 carbon (PL6C) to achieve high selectivity for the production of H_2O_2 ($S_{\text{H}_2\text{O}_2}$). The feasibility of a novel design of gas diffusion electrodes (GDE) operating at flow-by reactor for treating real effluents contaminated with pesticides was also aimed studied in this thesis. In Chapter I, a catalyst containing a <1 wt.% Pd loading modifying PL6C matrix ($\text{Pd}_{1\%}/\text{PL6C}$) was developed, which achieved high $S_{\text{H}_2\text{O}_2}$ ($\sim 90\%$) and an overpotential gain at the onset reaction of 320 mV compared to the matrix unmodified. This effect was explained thanks to the low metal content and the large interparticle spacing of Pd nanoparticles that avoided the readsorption mechanism of H_2O_2 . The $\text{Pd}_{1\%}/\text{PL6C}$ was efficiently applied for the removal of 0.5 mmol L^{-1} of methylparaben in 8 minutes by the PEF process at $j = 33.3 \text{ mA cm}^{-2}$. However, it was noted that the functional groups of the carbon matrix had an effect on the partial positive charge of the metal nanoparticles. Then, an alternative support based on ZrO_2 dispersed in PL6C was developed in Chapter II through microwave assisted hydrothermal synthesis (MAH). The material consisting of 5.1wt.% ZrO_2 was obtained in the optimum condition of the MAH synthesis, exhibiting 88.8% of $S_{\text{H}_2\text{O}_2}$. Apart from being stable in acidic media, the $\text{ZrO}_2/\text{PL6C}$ support material exhibited a 140 mV gain on the overpotential of ORR onset. Thus, the use of $\text{ZrO}_2/\text{PL6C}$ as a hybrid substrate suitable for noble metal nanoparticles was evaluated in Chapter III as a catalyst for H_2O_2 production. Instead of Pd, Au nanoparticles were used in order to study the interaction between the noble metal nanoparticle and the hybrid support. The electrochemical results revealed that the $\text{Au}_{\text{ZrO}_2}/\text{PL6C}$ showed excellent catalytic performance by showing a $S_{\text{H}_2\text{O}_2}=97\%$ with an early reaction onset of 350 mV compared to bare PL6C. For H_2O_2 production assays, the $\text{Au}_{\text{ZrO}_2}/\text{PL6C}$ -modified GDE produced 600 mg L^{-1} compared to 374 mg L^{-1} for the $\text{Au}/\text{PL6C}$ catalyst at $j = 50 \text{ mA cm}^{-2}$, confirming its higher catalytic effectiveness. The Au_{ZrO_2} GDE was also effectively applied in a continuous flow-by reactor for the complete removal of 10 mg L^{-1} of Carbaryl contained in the real effluent after 6 minutes using the PEF process. Although the presence of H_2O_2 scavenger species on real wastewater, the high performance of the catalyst provided sufficient H_2O_2 concentration to achieve homogeneous $\bullet\text{OH}$ for the complete removal of the pollutant. Therefore, it is expected that the contributions present in this thesis can contribute to further advances in the development of materials and systems for producing high-efficiency H_2O_2 that enables wastewater treatment by using electrochemical technology.

Keywords: Hydrogen peroxide. Oxygen reduction reaction. Modification of carbon-based materials. Gas diffusion electrode. Electrochemical advanced oxidation process. Flow-by reactor. Real wastewater.

RESUMO

O desenvolvimento de catalisadores altamente eficientes para produção de H_2O_2 através da reação de redução do oxigênio (RRO) é crucial para viabilizar os processos electro-Fenton (EF) e fotoelectro-Fenton (FEF) para o tratamento de efluentes reais. O objetivo desta tese foi desenvolver e otimizar catalisadores com baixo teor de metais suportados em carbono Printex L6 (PL6C) para alcançar uma elevada seletividade na produção de H_2O_2 ($S_{\text{H}_2\text{O}_2}$). Além disso, esta tese também teve como objetivo avaliar a viabilidade da implementação de um novo modelo de eletrodo de difusão gasosa (EDG) aplicado em um reator de fluxo para o tratamento de efluentes reais contaminados. No Capítulo I foi desenvolvido um catalisador contendo um carregamento de $<1\%$ Pd sobre a matriz PL6C ($\text{Pd}_{1\%}/\text{PL6C}$), que alcançou alta $S_{\text{H}_2\text{O}_2}$ ($\sim 90\%$) e um ganho de 320 mV no início da reação em comparação com a matriz não modificada. Esse efeito foi devido ao baixo teor de metal e pelo grande espaçamento entre as nanopartículas de Pd, que evitaram o mecanismo de readsorção de H_2O_2 , impedindo sua redução indesejada a H_2O . O $\text{Pd}_{1\%}/\text{PL6C}$ foi eficientemente aplicado para a remoção de $0,5 \text{ mmol L}^{-1}$ de metilparabeno em 8 minutos pelo processo FEF a $j = 33,3 \text{ mA cm}^{-2}$ em escala laboratorial. No entanto, constatou-se que os grupos funcionais da matriz de carbono causaram um efeito de carga positiva parcial das NPs metálicas. Então, um suporte alternativo baseado em ZrO_2 disperso em PL6C foi desenvolvido no Capítulo II por meio de síntese hidrotérmica assistida por micro-ondas (MAH). O material composto por $5,1\%$ de ZrO_2 (m/m) foi obtido na condição ótima da síntese MAH, exibindo 89% de $S_{\text{H}_2\text{O}_2}$. Além de ser estável em meio ácido, o material de suporte $\text{ZrO}_2/\text{PL6C}$ apresentou um ganho de 140 mV no sobrepotencial do início da ORR. Assim, o uso de $\text{ZrO}_2/\text{PL6C}$ como um substrato híbrido adequado para nanopartículas de metais nobres foi avaliado no Capítulo III. Em vez de Pd, foram usadas NPs de Au para facilitar o estudo da interação entre a nanopartículas e o suporte híbrido. O $\text{Au}_{\text{ZrO}_2}/\text{PL6C}$ apresentou um excelente desempenho catalítico exibindo $S_{\text{H}_2\text{O}_2}=97\%$ com um ganho no início de reação de 350 mV em comparação com o PL6C puro. Nos ensaios de produção de H_2O_2 , o EDG de $\text{Au}_{\text{ZrO}_2}/\text{PL6C}$ alcançou 600 mg L^{-1} em comparação a 374 mg L^{-1} pelo $\text{Au}/\text{PL6C}$ em $j=50 \text{ mA cm}^{-2}$. O EDG de $\text{Au}_{\text{ZrO}_2}/\text{PL6C}$ foi empregado com eficácia em reator de fluxo para a completa remoção de 10 mg L^{-1} de Carbaryl contido em efluente real após 6 minutos usando o processo FEF. Embora efluentes reais contenham espécies sequestradoras de H_2O_2 , o alto desempenho deste catalisador forneceu concentração suficiente de H_2O_2 para obter $\bullet\text{OH}$ homogêneo durante o processo FEF para a remoção completa do poluente. Portanto, espera-se que as contribuições apresentadas nesta tese possam contribuir para avanços futuros no desenvolvimento de materiais para a produção de H_2O_2 com alta eficiência que permita a viabilidade do tratamento de águas residuais utilizando tecnologia eletroquímica.

Palavras-chave: Peróxido de hidrogênio. Reação de redução de oxigênio. Modificação de materiais carbonáceos. Eletrodo de difusão gasosa. Processos oxidativos avançados eletroquímicos. Reator de fluxo. Efluente real.

LIST OF ABBREVIATIONS

- Au NPs** – Gold nanoparticles
- CE** – Current Efficiency
- CV** – Cyclic Voltammetry
- E_{1/2}** – half-wave potential
- EAOP** – Electrochemical Advanced Oxidation Process
- EC** – Energy consumption
- ECSA** - Electrochemically Active Surface Area
- EDX** - Energy Dispersive X-ray Spectroscopy
- GC-MS** – Gas Chromatography tandem Mass Spectrometry
- GDE** – Gas Diffusion Electrode
- HPLC** – High Performance Liquid Chromatography
- IC** – Ionic Chromatography
- LC/MS-MS** - High Performance Liquid Chromatography tandem Mass Spectrometry
- LSV** – Linear Sweep Voltammetry
- MAH** – Microwave Assisted Hydrothermal Synthesis
- MW** – Microwave
- ORR** – Oxygen reduction reaction
- Pd NPs** – Palladium nanoparticles
- PL6C** – Printex L6 Carbon
- RRDE** – Rotating Ring and Disc Electrode
- SAED** – Selected Area Electron Diffraction
- SEM** – Scanning Electron Microscopy
- S_{H2O2}** – Selectivity of H₂O₂
- TEM** – Transmission electron microscopy
- TGA** – Thermogravimetric analysis
- XDR** – X-ray diffraction
- XPS** - X-ray Photoelectron Spectroscopy

LIST OF FIGURES

Chapter I - Low Pd loadings onto Printex L6: synthesis, characterization and performance towards H₂O₂ generation for electrochemical water treatment technologies.

Figure 1. Representative (a and c) virtual high-angle angular dark field (images reconstructed from electron diffraction patterns), (b and d) bright-field STEM, and (e) HR-TEM images of Pd_{1%}/PCL6. (f) Size distribution histograms and interparticle distance (ipd) for Pd_{1%}/PCL6.....**34**

Figure 2. Physico-chemical characterization of PCL6 and Pd_{1%}/PCL6 catalysts. (a) Thermogravimetric responses. (b) XRD patterns. (c) Survey XPS spectra for PCL6 and Pd_{1%}/PCL6. (d) Narrow scan XPS spectrum for Pd 3d regions of Pd_{1%}/PCL6 catalysts.....**35**

Figure 3. (a, b) Cyclic voltammograms obtained in N₂ and O₂-sat 0.1 mol L⁻¹ K₂SO₄ at pH 2.5 for GC electrodes modified with PCL6 and Pd_{1%}/PCL6 (scan rate: 50 mV s⁻¹; scans started at 1.0 VAg/AgCl). (c) Linear sweep voltammetry in an RRDE configuration scanning the potential at 5 mV s⁻¹ and 900 rpm in O₂-sat 0.1 mol L⁻¹ K₂SO₄ at pH 2.5 (scans started at -0.9 or -0.2 VAg/AgCl). (d) S_{H₂O₂} during the ORR at varying potentials (obtained from the corresponding RRDE data). (e, f) Linear sweep RDE results scanning the potential at 5 mV s⁻¹ recorded in O₂-sat 0.1 mol L⁻¹ K₂SO₄ at pH 2.5 solution at various rotation rates. Insets: corresponding K-L plots.....**35**

Figure 4. Influence of different cathodes on (a) accumulated H₂O₂ concentration vs time (b) current efficiency and (c) energy consumed per kg H₂O₂ using 150 mL of 50 mM Na₂SO₄ solution at pH 2.5 and 25 °C, using (●) PW03, (■) PCL6/PW03 and (▼) Pd_{1%}/PCL6/PW03/gas diffusion.....**36**

Figure 5. Effect of different H₂O₂ based EAOPs (▲)AO-H₂O₂, (▼)AO-H₂O₂/UV, (■) EF and (●) PEF on the treatment of 0.50 mM of MetP solutions at pH 2.5 and j ¹/₄ 33.3 mA cm⁻². (a) and (b) MetP degradation over time; (c) and (d) Pseudo-first order kinetics; (e) TOC removal over time; (f) mineralization efficiency over time. (■) only UVC light.....**37**

Figure 6. Reaction sequence for MetP mineralization by the PEF process using a Pd_{1%}/PCL6/PW03 gas diffusion cathode and a BDD anode.....**38**

Figure S1. Thermogravimetric response for Pd_{20%}/PCL6 catalyst.....**43**

Figure S2. Narrow-scan XPS spectra in Cl 2p region for PCL6 and Pd_{1%}/PCL6 catalysts.....**44**

Figure S3. Cyclic voltammograms for (a) PCL6 and (c) Pd_{1%}/PCL6 obtained in N₂-sat 0.1 mol L⁻¹ K₂SO₄ at pH 2.5 at scan rates from 10 to 400 mV s⁻¹ in a range of 0.1 V potential window centered at the OCP. (b and d) ΔI/2 vs. v plots for modified GC electrodes.....**45**

Figure S4. Fig. S4. (a) Linear sweep RRDE results scanning the potential at 5 mV s⁻¹ and 900 rpm in O₂-sat 0.1 mol L⁻¹ K₂SO₄ at pH 2.5 for GC electrodes modified with PCL6 and Pd_{1%}/PCL6 catalysts before and after the stability test (scans started at -0.2 VAg/AgCl). (b) Cyclic voltammograms before and after the stability test obtained in N₂-sat 0.1 mol L⁻¹ K₂SO₄ at pH 2.5 for GC electrodes modified with PCL6 and Pd_{1%}/PCL6

catalysts at a scan rate of 50 mV s^{-1} ; scans started at 1 VAg/AgCl). (c) Electrocatalytic performance comparison (in terms of kinetic current densities to H_2O_2 production as a function of the applied potential) of different metallic nanoparticles-based synthesized catalysts: Pd-Hg (Verdaguer-casadevall et al., 2014), Pt-Hg (Siahrostami et al., 2013), Ag-Hg (Siahrostami et al., 2013), hydrothermally produced Pd/Graphene nanoribbon (S1) (Fortunato et al., 2018), hydrothermally produced Pd/Vulcan carbon (S1) (Fortunato et al., 2018), $\text{Pd}_{1\%}/\text{PCL6}$ before and after the stability test [this study].....47

Chapter II - Sustainable microwave-assisted hydrothermal synthesis of carbon-supported ZrO_2 nanoparticles for H_2O_2 electrogeneration.

Figure 1. (a) An illustrative scheme of the microwave-assisted hydrothermal synthesis. SEM images of (b) 5, (c) 10 and (d) 15 wt% of $\text{ZrO}_2/\text{PL6C}$; (e) thermogravimetric analysis of the $\text{ZrO}_2/\text{PL6C}$ catalyst produced from the application of different initial Zr precursor concentrations; (f) XRD pattern for $\text{ZrO}_2/\text{PL6C}$ catalyst produced from the initial Zr precursor concentration of 15 wt%.....54

Figure 2. (a) Cyclic voltammograms obtained from the application of N_2 -saturated $0.1 \text{ mol L}^{-1} \text{ K}_2\text{SO}_4$, with $\text{pH} = 2.5$ (H_2SO_4 adjusted), at scan rate of 50 mV s^{-1} and potential window ranging from 1 to -0.8 VAg/AgCl . (b) Linear sweep voltammetry in RRDE curves for the disk electrode obtained in O_2 -saturated $0.1 \text{ mol L}^{-1} \text{ K}_2\text{SO}_4$, with $\text{pH} = 2.5$ (H_2SO_4 adjusted), at scan rate of 5 mV^{-1} and potential window ranging from 0.4 to -0.8 V at 900 rpm. (c) The values of the currents obtained for the Pt ring electrode during the potential scan on the disk electrode. The ring potential was kept at 1.0 VAg/AgCl . (d) Correlation between improvement in catalytic performance (in terms of $E_{1/2}$), selectivity for H_2O_2 ($S_{\text{H}_2\text{O}_2}$), and wt.% of ZrO_2 on PL6C.....55

Figure 3. SEM images in SE mode for the $\text{ZrO}_2/\text{PL6C}$ catalyst produced under different MAH synthesis in (a) 10, (b) 40 and (c) 120 min. (d) Dark-field STEM image and particle size distribution (inset) for the $\text{ZrO}_2/\text{PL6C}$ sample produced in 40 min. (e) ZrO_2 wt.% on carbon vs. MAH time plot. Data obtained by XRF quantification.....56

Figure 4. (a) Cyclic voltammograms obtained in N_2 -saturated $0.1 \text{ mol L}^{-1} \text{ K}_2\text{SO}_4$, $\text{pH} = 2.5$ (H_2SO_4 adjusted), at scan rate of 50 mV s^{-1} and potential window ranging from 1 to -0.8 VAg/AgCl . (b) Linear sweep voltammetry in RRDE curves for the disk electrode obtained in O_2 -saturated $0.1 \text{ mol L}^{-1} \text{ K}_2\text{SO}_4$, $\text{pH} = 2.5$ (H_2SO_4 adjusted), at scan rate of 5 mV^{-1} and potential window ranging from 0.4 to -0.8 V at 900 rpm; (c) The values of the currents obtained for the Pt ring electrode during the potential scan on the disk electrode. The ring potential was kept at 1.0 VAg/AgCl . (d) Correlation between improvement in the catalytic performance (in terms of $E_{1/2}$), selectivity toward H_2O_2 ($S_{\text{H}_2\text{O}_2}$), and synthesis time.....56

Figure 5. SEM images in (a–c) BSE and SE (inset) mode, (d–f) TEM images, and (g–h) XRD pattern for the $\text{ZrO}_2/\text{PL6C}$ catalyst produced at different MAH temperatures.....58

Figure 6. (a) Cyclic voltammograms obtained using N_2 -saturated $0.1 \text{ mol L}^{-1} \text{ K}_2\text{SO}_4$, $\text{pH} = 2.5$ (H_2SO_4 adjusted), at scan rate of 50 mV s^{-1} and potential window ranging from 1 to

-0.8 V_{Ag/AgCl}. **(b)** Linear sweep voltammetry in RRDE curves for the disk electrode obtained in O₂-saturated 0.1 mol L⁻¹ K₂SO₄, pH = 2.5 (H₂SO₄ adjusted) at scan rate of 5 mV⁻¹ and potential window ranging from 0.4 to -0.8 V at 900 rpm; **(c)** The values of the currents obtained for the Pt ring electrode during the potential scan on the disk electrode. The ring potential was kept at 1.0 V_{Ag/AgCl}. **(d)** Correlation between the improvement in catalytic performance (in terms of E_{1/2}), selectivity toward H₂O₂ (S_{H₂O₂}), and the temperature applied in the MAH synthesis process.....59

Figure 7. (a,b) HR-TEM images, (c) selected area electron diffraction pattern, and (d) XPS survey spectrum for the optimized ZrO₂/PL6C catalyst. Inset: Narrow XPS spectrum for the Zr 3d region.....60

Figure S1. Bright-field STEM and TEM images for 10 wt.% Zr and 15 wt.% Zr on PL6C.....65

Figure S2. SEM images of (b) 5, (c) 10 and (d) 15wt.% of ZrO₂/PL6C from backscatter electrons (BSE) mode.....66

Figure S3. SEM images with magnification of 1000 x (inset: magnification of 10.000 x) in BSE mode and EDS spectra for (a,b) control PL6C (0 wt.% Zr) and (c,d) 15 wt.% Zr/PL6C.....66

Figure S4. Cyclic voltammograms obtained from the application of N₂-saturated 0.1 mol L⁻¹ K₂SO₄ (pH = 2.5), at several scan rates for (a) bare PL6C, and (b) 10 wt.% Zr on PL6C. ΔI/2 vs. scan rate plots for (c) bare PL6C and (d) 10 wt.% Zr on PL6C.....67

Figure S5. SEM images of (b) 5, (c) 10 and (d) 15wt.% of ZrO₂/PL6C from backscatter electrons (BSE) mode.....68

Figure S6. Results obtained from the electrochemical synthesis using microwave in the absence of the metallic precursor. **(a)** Cyclic voltammograms obtained from the application of N₂-saturated 0.1 mol L⁻¹ K₂SO₄, pH=2.5 (H₂SO₄ adjusted), with scan rate of 50 mV s⁻¹, potential window ranging from 1 to -0.8 V_{Ag/AgCl}. **(b)** Linear sweep voltammetry in RRDE curves for the disk electrode obtained from the application of O₂-saturated 0.1 mol L⁻¹ K₂SO₄, pH=2.5 (H₂SO₄ adjusted), with scan rate of 5 mV⁻¹ and potential window ranging from 0.4 to -0.8 V at 900 rpm; **(c)** The values of the currents obtained for the Pt ring electrode during the potential scan on the disk electrode. The ring potential was kept at 1.0 V_{Ag/AgCl}.....68

Figure S7. EDX spectra for ZrO₂/PL6C catalysts produced at (a) 120, (b) 140, and (c) 160 °C of MAH synthesis temperature.....69

Figure S8. (a) Linear sweep voltammetry curves before and after long-term stability test obtained from the application of O₂-saturated 0.1 mol L⁻¹ K₂SO₄, pH=2.5 (H₂SO₄ adjusted), at scan rate of 5 mV⁻¹ and potential window ranging from 0.4 to -0.8 V at 900 rpm; (b) ring current (polarized at 1.0 V) for detection of H₂O₂ during the voltametric test on the RRDE disk; (c) Selectivity toward H₂O₂ (S_{H₂O₂}) production under several different potentials.....71

Figure S9. Structural scheme of gas diffusion electrode (GDE) used in H₂O₂ electrogeneration assays.....72

Figure S10. Analysis of H₂O₂ production for a period of 90 minutes using bench-scale electrochemical cell with 0.1 mol L⁻¹ K₂SO₄ (pH 2.5), platinized titanium counter

electrode, Ag/AgCl reference electrode, and (a) PL6C and (b) 5 wt% ZrO₂/PL6C GDEs used as working electrodes; (c) comparison of the maximum production of H₂O₂ after 90 min.....73

Chapter III – Using Au NPs anchored on ZrO₂_ carbon black toward more efficient H₂O₂ electrogeneration in flow-by reactor for carbaryl removal in real wastewater.

Figure 1. FE-SEM, HR-TEM, and SAED images for the (a,b,c) Au/PL6C and FE-SEM, dark-field STEM, HR-TEM, and SAED images for (d,e,f,g) Au-ZrO₂/PL6C catalysts, respectively. (h) Survey XPS spectra for Au/PL6C and Au-ZrO₂/PL6C catalysts. (i) High resolution XPS spectrum in Zr 3d region for Au-ZrO₂/PL6C. (j) High resolution XPS spectra recorded in the Au 4f region for Au/PL6C and Au-ZrO₂/PL6C catalysts.....81

Figure 2. Electrochemical analysis of the GC disk (RRDE system) modified with PL6C, ZrO₂/PL6C, Au/PL6C and Au-ZrO₂/PL6C catalysts. (a) Cyclic voltammograms obtained at 50 mV s⁻¹, with the application of 150 mL using N₂ bubbling to deaerate 0.1 mol L⁻¹ K₂SO₄ solution (at pH 2.5). Linear sweep voltammetry curves of the (b) disk and (c) Pt ring electrodes obtained in a RRDE configuration at scan rate of 5 mV s⁻¹ and rotation of 900 rpm, using O₂-saturated solution of 0.1 mol L⁻¹ K₂SO₄ at pH 2.5 (the abscissa of Fig. 2C refers to the applied potential at the disk electrode). (d) Selectivity toward H₂O₂ production as a function of applied potential. (e) Capacity of H₂O₂ accumulation during electrolysis at 50 mA cm⁻² for 120 min in 0.1 mol L⁻¹ K₂SO₄ (pH = 2.5) based on the application of GDE modified with PL6C, ZrO₂/PL6C, Au/PL6C and Au-ZrO₂/PL6C and using BDD as anode. (f) Current efficiency (CE) and energy consumption (EC) values obtained from H₂O₂ electrogeneration tests performed for the PL6C, ZrO₂/PL6C, Au/PL6C and Au-ZrO₂/PL6C catalysts..... 82

Figure 3. (a) Analysis of the decay of 10 mg L⁻¹ CBR based on the application of different electrochemical treatment processes. Pseudo-first order kinetics evaluated in acid medium composed of 0.1 mol L⁻¹ K₂SO₄ (pH = 2.5), at current density (*j*) of 50 mA cm⁻² for the following processes: (b) UVC, AO, AO/H₂O₂ and H₂O₂/UVC and (c) EF and PEF. (d) Profile of the percentage of mineralization in relation to energy consumption in kWh kg_{TOC}⁻¹ obtained in 60 min of treatment based on the application of EAOPs with initial TOC of ~ 6.0 mg L⁻¹..... 84

Figure 4. (a) Analysis of the effect of initial CBR concentration using 5, 10 and 20 mg L⁻¹ CBR concentrations, and (b) influence of applied current density (*j*) = 25, 50 and 100 mA cm⁻² on the pollutant removal profile over time based on the application of 0.1 mol L⁻¹ K₂SO₄ (pH 2.5) as electrolyte solution at *j* = 50 mA cm⁻².....85

Figure 5. Proposed route of carbaryl mineralization via hydroxyl radicals based on the application of PEF process in acid medium.....86

Figure 6. Concentration of (a) small-chain carboxylic acids and (b) nitrogen species of NH₄⁺, NO₃⁻ and NO₂⁻ identified during 120 min of 10 mg L⁻¹ CBR degradation under the PEF process, based on the application of 150 mL of 0.1 mol L⁻¹ K₂SO₄ (pH 2.5) as electrolyte and temperature of 25 °C.....87

Figure 7. (a) Stability tests related to H₂O₂ production in real wastewater effluent conducted with the aid of a flow reactor at applied current density (*j*) of 50 mA cm⁻² using Au-ZrO₂/PL6C cathode and BDD anode. (b) Analysis of CBR removal and (c) TOC mineralization in flow electrochemical reactor based on the application of the PEF process at *j* = 50 mA cm⁻² and O₂ flow at 100 mL min⁻¹ in both synthetic and real effluents.

(d) Final values of nitrogenous and chlorinated species detected in real wastewater effluent after 60 min of PEF treatment.....	87
Figure S1. TEM and HR-TEM images for the (a,b) Au/PL6C and TEM, HR-TEM and dark-field STEM images for the (c-f) Au-ZrO ₂ /PL6C catalysts. The arrows indicate the presence of ZrO ₂ NPs.....	92
Figure S2. Scanning electron microscopic (SEM) image of the Au-ZrO ₂ /PL6C catalyst; energy dispersive X-ray spectroscopy (EDX) of carbon, oxygen, zirconium, and gold elements present in the catalyst sample; overlay of the elements on the PL6C support...	93
Figure S3. Scanning electron microscopic (SEM) image of the Au-ZrO ₂ /PL6C catalyst produced by using one-step synthesis procedure; energy dispersive X-ray spectroscopy (EDX) of carbon, oxygen, zirconium, and gold elements present in the catalyst sample; overlay of the elements on the PL6C support.....	94
Figure S4. FEG-SEM images in (first column) SE and (second column) BSE mode obtained for Au-ZrO ₂ /PL6C catalyst produced by using one- and two-steps synthesis procedure.....	95
Figure S5. Thermogravimetric analysis of the PL6C, ZrO ₂ /PL6C, Au/PL6C and Au-ZrO ₂ /PL6C catalysts.....	95
Figure S6. (a) Cyclic voltammograms before and after the accelerated stress test, obtained in O ₂ -saturated 0.1 mol L ⁻¹ K ₂ SO ₄ at pH 2.5 for GC electrodes modified with Au-ZrO ₂ /PCL6 at a scan rate of 50 mV s ⁻¹ ; (b) RRDE profile of Au-ZrO ₂ /PL6C linear sweep voltammetry using the scan rate of 5 mV s ⁻¹ and 900 rpm in O ₂ -sat 0.1 mol L ⁻¹ K ₂ SO ₄ at pH 2.5 before and after the stability test.....	96
Figure S7. Current efficiency values obtained for the PL6C, ZrO ₂ /PL6C, Au/PL6C and Au-ZrO ₂ /PL6C catalysts relative to the time of electrolysis based on the application of 0.1 mol L ⁻¹ K ₂ SO ₄ (at pH 2.5) as electrolyte solution, current density of 50 mA cm ⁻² , and temperature of 25 °C.....	96
Figure S8. FEG-SEM images obtained in SE mode for GDE modified with Au-ZrO ₂ /PL6C catalyst produced by using one-step after consecutive tests of H ₂ O ₂ electrogeneration in flow-by reactor.....	98

LIST OF TABLES**Chapter I - Low Pd loadings onto Printex L6: synthesis, characterization and performance towards H₂O₂ generation for electrochemical water treatment technologies.****Table S1.** Compositional and morphologic characteristics of Pd_{1%}/PCL6 catalyst obtained from TGA, XPS, and TEM.....43**Table S2.** Surface composition of Pd_{1%}/PCL6 catalyst determined by XPS narrow-scans. Peaks, positions, relative sensitivity factors (R.S.F.), and atomic and weight percentages of the elements.....44**Table S3.** Deconvolution results in the Pd 3d region for Pd_{1%}/PCL6 catalyst. Values obtained from the narrow-scan XPS spectrum in inset of Figures 1F.....44**Table S4.** Estimated *ECSA* values by the capacitance for catalyst samples.....46**Table S5.** Aromatic intermediates detected by GC-MS during the degradation of 0.50 mM MetP solution by PEF process.....48**Chapter II - Sustainable microwave-assisted hydrothermal synthesis of carbon-supported ZrO₂ nanoparticles for H₂O₂ electrogeneration.****Table S1.** Estimated *ECSA* values by capacitance for the catalysts investigated.....67**Table S2.** Comparing the catalyst composition, synthesis approach, and electrocatalytic performance for ORR in terms of onset potential (E_{onset} vs. RHE) and selectivity to H₂O₂ production (in %) for reported metal oxide-based electrocatalysts.....70**Table S3.** Values obtained related to energy consumption (EC) and pseudo-zero order kinetics (k_{app}) for ZrO₂/PL6C and PL6C under different electrolysis potential.....74**Chapter III – Using Au NPs anchored on ZrO₂_carbon black toward more efficient H₂O₂ electrogeneration in flow-by reactor for carbaryl removal in real wastewater.****Table S1.** Particle size, EDS, TG metal (unburned mass), and TG and EDS mass and atomic percentages recorded for the metal/PL6C samples.....97**Table S2.** Total degradation time, TOC mineralization (%), energy consumption (kWh kg⁻¹), and apparent kinetic constant for the concentration decay (min⁻¹) with corresponding R-squared values, determined over 60 min of treatment of 150 mL CBR solution under the application of the PEF process using 0.1 mol L⁻¹ K₂SO₄ (at pH 2.5) as electrolyte solution and temperature of 25°C.....98**Table S3.** Intermediates compounds detected by GC-MS during the degradation of 10 mg L⁻¹ CBR solution under the PEF treatment process.....99**Table S4.** Summary of recent work that applied electrochemical processes for degradation of carbaryl present in aqueous solutions.....100

TABLE OF CONTENTS

INTRODUCTION..... 17

Chapter I - Low Pd loadings onto Printex L6: synthesis, characterization and performance towards H₂O₂ generation for electrochemical water treatment technologies.....29

CHAPTER II - Sustainable microwave-assisted hydrothermal synthesis of carbon-supported ZrO₂ nanoparticles for H₂O₂ electrogeneration..... 50

CHAPTER III - Using Au NPs anchored on ZrO₂_carbon black toward more efficient H₂O₂ electrogeneration in flow-by reactor for carbaryl removal in real wastewater.....76

CONCLUSION.....104

SCIENTIFIC PRODUCTION.....106

REFERENCES.....108

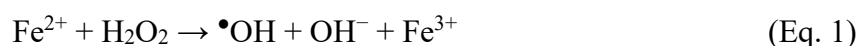
INTRODUCTION

1. Motivation

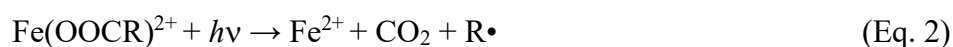
The arrival of the Industrial Revolution triggered a huge increase in environmental pollution, whereas the huge increase in the global population is leading to alarming levels of pollutants in water bodies. This is a consequence of the growing number of new products designed to ensure the food supply, human health and social well-being. Due to their chemical composition designed to be stable under severe conditions, synthetic compound especially from the antibiotics, hormones, dyes, and pesticides classes are classified as persistent organic pollutants (POP). Also triggered by the high chemical stability of the contaminants, the conventional treatment model has not shown adequate efficiency for the complete removal of POP from industrial, hospital, and urban wastewater. Consequently, part of the wastewater that returns to its cycle as drinking water, still contaminated, potentially causing harmful effects to living beings over the years. These effects are mostly related to the carcinogenic and endocrine disrupting action that synthetic organic compounds can cause to human even at low concentrations. Further barriers in removing POP are due to the conventional treatment that using oxidizing chlorinated species can also produce organochlorines considered to have a high carcinogenic potential, while biological treatment plants have been reported to produce super-resistant bacteria. Thus, the development of a novel and highly efficient technology for wastewater treatment has become extremely crucial (1–5).

2. Electrochemical advanced oxidative process (EAOP)

The advanced oxidative processes (AOP) have been developed over recent decades as an alternative technique for wastewater treatment. AOP are based on the production of highly oxidizing radical species, such as the hydroxyl radical ($\bullet\text{OH}$), that has a higher reduction potential ($E^0 = 2.80 \text{ V vs SHE}$) compared to oxidizers commonly used, as ClO^- ($E^0 = 1.48 \text{ V vs SHE}$). The advantage of using AOP for wastewater treatment can be attributed to the high potential of $\bullet\text{OH}$ to mineralize organic matter, producing CO_2 , H_2O and inorganic ions. Besides, if not fully mineralized, the degradation by-products produced by AOPs become more oxygenated and thus may be easier to be biodegraded in nature (6–8). According to the literature, the most popular method for obtaining $\bullet\text{OH}$ is using the Fenton reaction that involves the activation of H_2O_2 by Fe^{2+} species as shown in Eq. 1.



However, the ferric ions (Fe^{3+}) produced by the Fenton reaction can lead to complexation with short-chain carboxylic acids, named $\text{Fe}(\text{OOCR})^{2+}$, that makes iron species unavailable on the homogeneous solution. Numerous authors have investigated the use of UV radiation or sunlight radiation in photo-Fenton and solar photo-Fenton processes as very efficient approach for the photodegradation of $\text{Fe}(\text{OOCR})^{2+}$ capable of regenerating Fe^{2+} species (Eq. 2). In addition, the regeneration of Fe^{2+} species can also proceed chemically by reacting back with H_2O_2 from Eq. 3 and 4 (9,10)



The low concentration of solubilized iron allowed of 0.3 mg L^{-1} for drinking water up to 15 mg L^{-1} present in wastewater discharges, as well as the slow kinetics of chemical and photochemical regeneration of Fe^{2+} species features iron as a limiting reagent for the Fenton reaction. So, the coupling of AOPs with electrochemical technology, the so-called electrochemical advanced oxidative processes (EAOP), has brought significant progress to these processes. One of them was the electrochemical regeneration of Fe^{2+} by direct electron transfer at the electrode surface as seen in Eq. 5. The coupling of the Fenton reactions to electrochemical regeneration of Fe^{2+} species is named as electro-Fenton process (EF) (9–12)



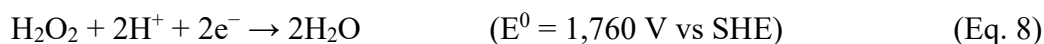
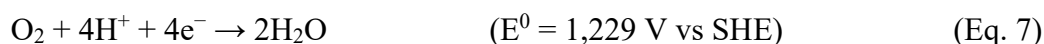
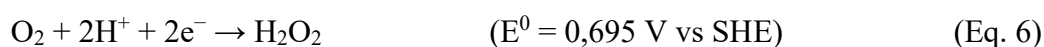
Several authors have reported efficient removal of organic compounds using EF and photo-electroFenton (PEF) processes at low concentrations of Fe^{2+} due to the fast kinetics of electrochemical regeneration of Fe^{2+} species (7–10,13,14). On the other hands, one of the most important challenges to increase the efficiency of EAOP draws attention to the mode of production and use of the most common chemical precursor of $\bullet\text{OH}$, the hydrogen peroxide (H_2O_2). A significant improvement in electrochemical technology

applied in advanced oxidation processes, apart from Fe^{2+} regeneration, is the versatility of decentralized H_2O_2 production (15–18).

The large-scale industrial production of H_2O_2 occurs by the autooxidation process of anthraquinones. This approach consists of using high-pressure reactors with H_2 and O_2 gases to catalyze the hydrogenation and oxidation of anthraquinones in an organic solvent, leading to the production of H_2O_2 . However, such this batch synthesis mode requires the purification and distillation steps to transport concentrated H_2O_2 (highly explosive), so this method is considered impractical for environmental applications. Additionally, as the required concentrations of H_2O_2 for wastewater treatment using the EF and PEF process reach a maximum of 2% (w/w), decentralized or *in situ* approaches to produce H_2O_2 are strongly recommended (16). One method that has been widely studied to produce decentralized H_2O_2 for wastewater treatment involves electrochemical reduction of molecular O_2 through the oxygen reduction reaction (ORR). This advantageous method is recognized as environmentally friendly given the high availability of O_2 in atmospheric air and due to the use of electrons as a green reagent.

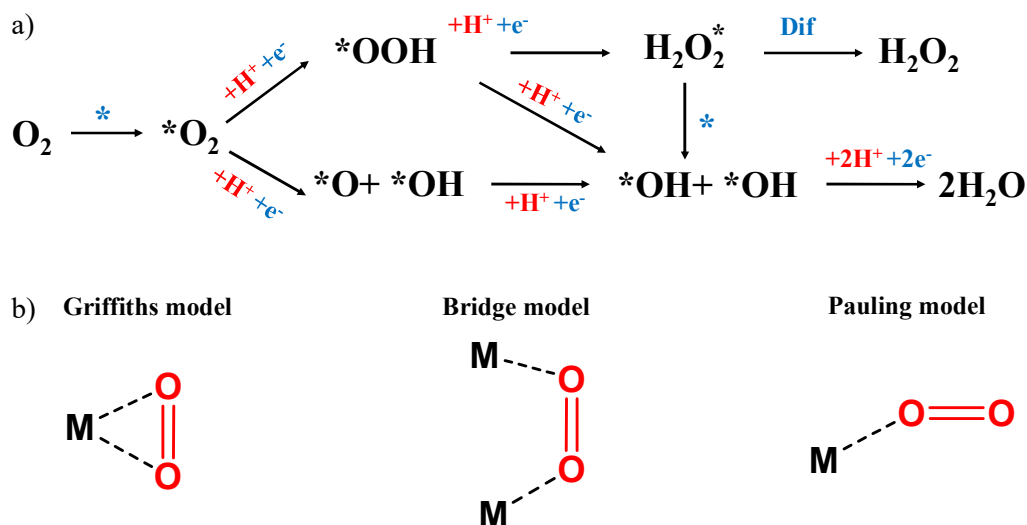
3. Oxygen reduction reaction (ORR)

The ORR is a selective electrochemical reaction that involves the cathodic reduction of molecular oxygen by different reaction pathways producing H_2O_2 via 2 electrons (Eq. 6) or H_2O via 4 electrons (Eq. 7). The production of H_2O_2 is expected to occur via the 2-electron pathway, but if the product remains adsorbed on the catalyst surface, a further $2e^-$ reduction can consume the H_2O_2 to produce H_2O (Eq. 8).



Since the reaction pathway resides in the energy adsorption between the ORR intermediates and the electrode surface, Figure 1 supports a better understanding of the possible ORR pathways and how each product can be obtained. Several authors justify their choices of electrode materials of desired selectivity towards H_2O_2 based on the mechanisms presented in Figure 1 (16,19–23).

Figure 1. a) Schematic diagram of the oxygen reduction reaction including the formation of the reaction intermediate; b) The models of Griffiths, Bridge and Pauling for the adsorption of O₂ on the surface (M) of the electrochemical catalyst.



Source: Adapted from Katsounaros et. al. (21) and Yeager et. al (20).

In Figure 1a, the * denotes that the chemical species is adsorbed onto an active site of the catalytic material. The initial step of the reaction is therefore considered crucial in determining the selectivity of the material. According to the literature, O₂ can interact with the active site of the catalyst using one or two of its oxygen atoms depending on the interaction strength among the O₂ and the surface to produce *O₂ (Eq. 9).



Yeager in 1984 and 1986 showed distinct models for the adsorption of O₂ on catalytic carbonic, metal, and metallic complex surfaces (19,20). The summarize models for O₂ adsorption on the surface of catalysts (M) is presented on Figure 1b. All three models can occur for metal catalysts, but only the Bridge (24) and Pauling (25) models are feasible for carbon-based catalysts, according to Gartes and Weiss et. al (26). The models of O₂ adsorption onto the (M) indicate that both the Griffith and Bridge models has a double oxygen interaction with the catalyst, whereas in the Pauling model only a single oxygen atom is involved. Considering that each model is dependent on the interaction energy between O₂ and the catalyst, a strong interaction causes O₂ adsorption to tend to follow the Griffith (27) or Bridge models, resulting in the pathway of O-O bond breaking to produce the intermediates O* and OH* (Eq. 10).



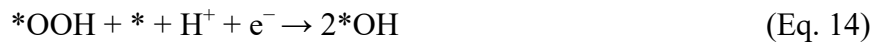
This step will lead to the reaction pathway to produce *OH that follows the 4-electron transfer reaching the production of H₂O as the major product (Eq. 11 and 12).



On the other hand, a not strong interaction energy between the oxygen and the catalyst surface or a steric hindrance (e.g., due to the presence of a competing adsorptive species) can result in O₂ adsorption following the Pauling model involving a single oxygen atom. In this pathway, the intermediate produced is the *OOH. As described in the literature, the *OOH specie must interact weakly with the electrode surface for ORR to produce H₂O₂* as displayed on Eq. 13 (16,21).



Once the reduction of O₂ leads to the production of H₂O₂*, the energy interaction between the specie and the electrochemical surface should decrease, allowing for the release of H₂O₂ into the solution. If both the *OOH and the H₂O₂* species remain strongly adsorbed on the surface, further dissociation can occur, resulting in the formation of *OH, as shown in Eq. 14 and Eq. 15, and the production of H₂O, as showed in Eq. 12.



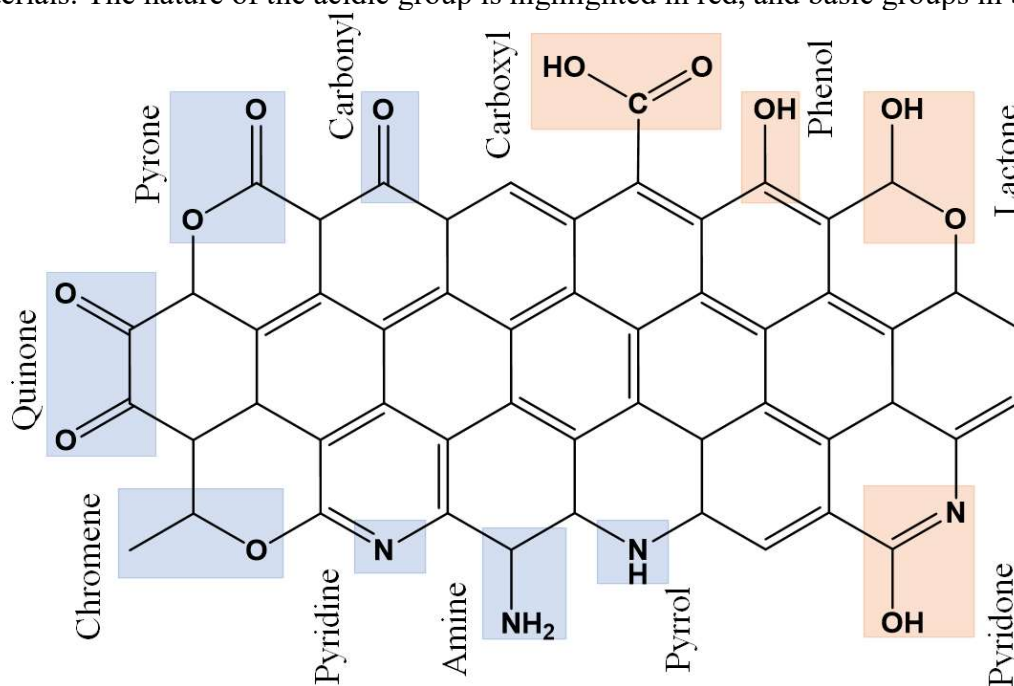
Thus, cathodic catalyst that presents properties to promote the reduction of O₂ via 2e⁻ pathway is extremely relevant for the development of electrochemical technologies for the decentralized production of H₂O₂.

4. Selective catalysts for H₂O₂ production

Catalysts based on Au, Ag, or Hg are thought to interact weakly with oxygen. This weak interaction renders these surfaces incapable of breaking the O=O bond, thereby tending to reduce O₂ to H₂O₂ formation via a 2e⁻ pathway (15,28,29). Unfortunately, the

ecological damage caused by mercury derivatives and the high cost and scarcity of precious metals make large-scale application of such catalysts impractical. On the other hand, several studies have shown that amorphous carbon-based materials have high selectivity for H_2O_2 production. This occurs due to the small particle size, large surface area, surface edges and the presence of functional groups that activate the ORR for H_2O_2 production (30–33). The oxygen and nitrogen functional groups found in carbonaceous materials are summarized according to their acidic or basic nature in Figure 2.

Figure 2. Principal oxygen and nitrogen functional groups found on the surface of carbon materials. The nature of the acidic group is highlighted in red, and basic groups in blue.



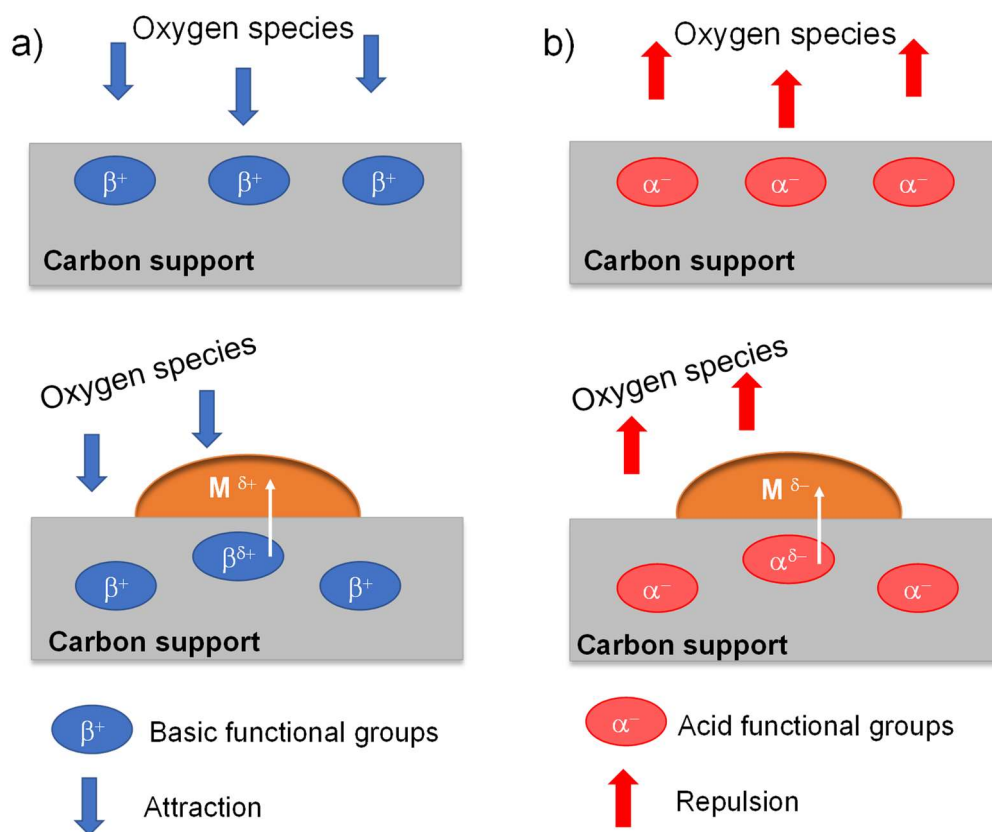
Source: adapted from Donoeva et al (34).

Yeager et al. reported that the functional group is recognized to be the main activator for the O_2 adsorption in carbonaceous materials (19). This is attributed due to the highly electronegativity of these functional groups, which induces charge redistribution from adjacent carbon atoms that act as an active site for O_2 adsorption towards selective H_2O_2 production. However, the amorphous nature of the material associated with its limited charge-transfer capacity leads to reduced electrochemical activity of the carbon-based catalysts for the ORR when compared to metal-based catalysts. This represents a significant drawback for their application to H_2O_2 electrogeneration, especially given the high levels of energy consumption reached using such catalysts in electrochemical reactors. On the other hand, amorphous carbon-based

materials demonstrate significant potential as supports for nanoparticles. The functional groups of carbon matrix also play an important function as support for metallic modifiers. They exhibit excellent stability in aqueous media, covering a wide pH range, and facilitate the easy recovery of the metal through complete combustion. (38,55,56). Given the mentioned properties, different strategies have been developed to reduce the overpotential of ORR in carbonaceous materials, including its modification using heteroatoms as -O, -N, -F, -S (35–38), using redox organic compounds (39–41), metal complexes (42–45), metal nanoparticles (46–48) and metal oxides (49–54).

Furthermore, Donoeva et al. previously reported that the predominance of basic functional groups onto the carbon surface resulted in the transfer of positive charge to the nanoparticles present on the surface of the material. Then, due to its high electronegativity, oxygenated species tend to show high affinity for positive active sites and repulsion for negative one, as illustrated in Figure 3 (34,38). In this way, the feature of carbon-based material functionalization for use as ORR catalyst and nanoparticle support should go towards materials with predominantly positive charges. The Printex L6 carbon (PL6C) has proved to be an excellent cathodic material for the electrochemical production of H_2O_2 due to its surface catalytic properties (17,31–33,57). Apart from its high surface area and small particle size, the high degree of functionalization of PL6C makes it highly selective for peroxide production and an excellent support material for metallic particles.

Figure 3. Representative scheme of the charges acting on the surface of carbonic catalysts according to the predominance of (a) basic and (b) acidic groups.



Source: adapted from Donoeva et al. (34)

Several approaches are found in the literature to design effective strategies using modifiers to improve the electrochemical activity and selectivity of carbon materials towards H_2O_2 production. An attractive approach was found by Fortunato et al. when evaluating the electrochemical matrix based on graphene nanoribbons (GNR) modified by Palladium nanoparticles. Fortunato and co-workers found that a very active noble metals (such as Pd) display high selectivity to obtain H_2O from the reduction of oxygen as a result of the phenomenon of H_2O_2 readsorption on the Pd surface, promoting a further reduction of H_2O_2 to H_2O . High selectivity for H_2O production was observed in materials with the catalytic surface containing high Pd loading and close interparticle distance, thereby favoring the H_2O_2 readsorption processes. On the other hand, the GNR matrix containing a low Pd content displayed larger interparticle distance which disfavors the readsorption of H_2O_2 on the metal. Thus, the material with low loading of Pd showed higher selectivity for H_2O_2 production in the electrochemical studies. The same strategy was used in Chapter I of this thesis entitled “*Low Pd loadings onto Printex L6: synthesis,*

characterization and performance towards H₂O₂ generation for electrochemical water treatment technologies” as an innovative way for high production of H₂O₂ by modifying the Printex L6 carbon matrix using low loading of Pd. Also in this chapter, the accumulation of H₂O₂ in an electrochemical lab-scale was evaluated to assess the degradation of methyl paraben using electro and photoelectron-Fenton processes.

As far as the studies containing modifiers are concerned, oxophilic materials such as oxides from transition metals, apart from providing a contribution to the electrochemical stability of the carbon support, have also been widely used to collect positive charge from the surface of carbon catalysts, facilitating the release of H₂O₂. Several authors have shown promising results from the modification of carbonaceous substrates with metallic oxides towards the increase of the electrochemical activity and selectivity for H₂O₂ production (49,51–53,58). Zirconium shows one of the most oxophilic tendencies among the transition elements, suffering electron loss from its 4d² and 5s² orbitals to form ZrO₂ and reaching its maximum oxidation state as Zr⁴⁺. Moreover, the low cost and non-toxic composition contribute to make ZrO₂ a suitable model catalyst for the modification of carbonic substrates (49,58,59).

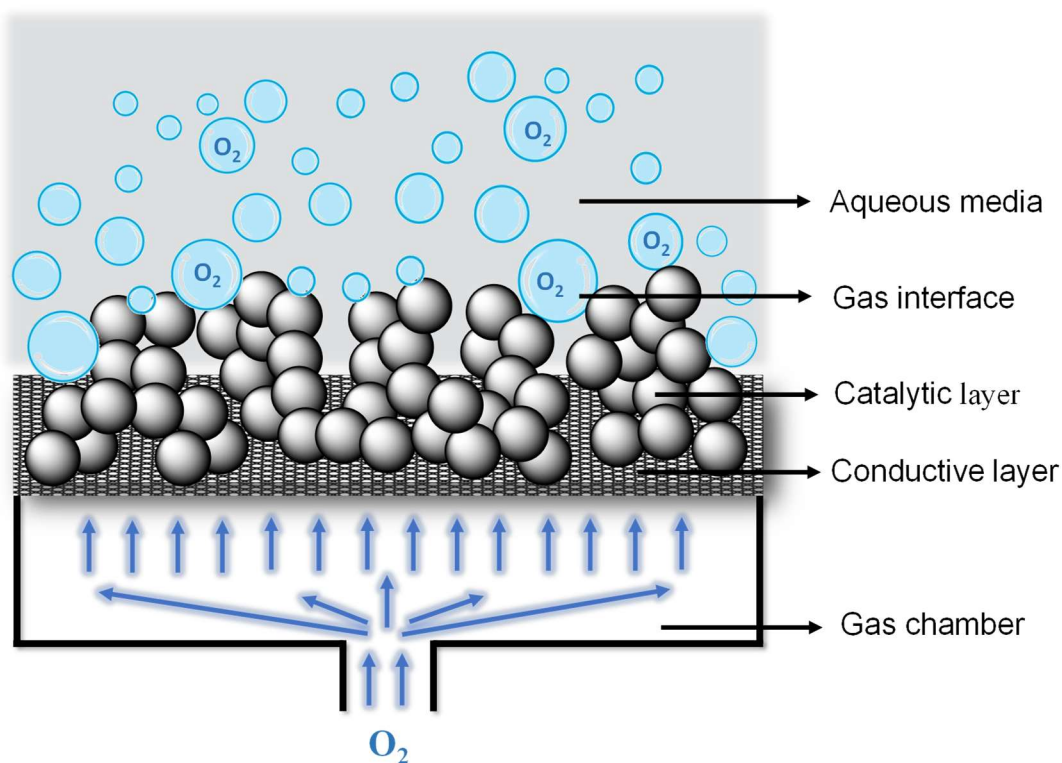
Although the synthesis of metal oxides supported on carbon-based substrates can occur by different methodologies, the most common is by thermal decomposition route. The thermal decomposition method of polymeric precursors has proven to be highly efficient to obtain metal oxides with crystalline phases well-defined by the burning temperature (49,51,60). However, the use of temperatures above 500 °C may compromise the structure of the carbon-based substrate and also affect its degree of functionalization, thus driving down the efficiency of the catalyst towards H₂O₂ production. Therefore, the development of new approaches to synthesize metal oxides in the presence of carbonaceous materials has been strongly encouraged. The microwave-assisted hydrothermal method (MAH) has emerged as an alternative for attaining modified carbon composites due to the low synthesis temperature required and the rapid nucleation of oxides on the surface of the material. In Chapter II of this Thesis entitled “*Sustainable microwave-assisted hydrothermal synthesis of carbon-supported ZrO₂ nanoparticles for H₂O₂ electrogeneration*”, we evaluated the different parameters of MAH synthesis to develop an optimal ZrO₂-based catalyst supported on PL6C with high efficiency for H₂O₂ production in acid medium. Thus, further theoretical background and advantages of MAH synthesis will be better described in Chapter II.

Going deeper into materials engineering, several studies have shown synergism between different classes of modifiers, such as organometallic compounds, bimetallic alloys, MOF, single atoms, etc., to promote enhanced catalysis of H_2O_2 production in carbonaceous materials (46,61–67). Organometallic modifiers have shown excellent results as carbonaceous support modifiers for ORR since they involve the catalytic contribution of the organic ligands in addition to isolate the metal center in the structure. Recently, Cordeiro Junior et al. demonstrated that the incorporation of 5% cobalt porphyrin into the carbonaceous matrix of the gas diffusion electrode (GDE) resulted in an increase of H_2O_2 production from 177 to 333 $mg\ L^{-1}$ over the unmodified GDE after a 90-minute electrolysis performed in a high conductivity acidic media (68). Thus, one can see that several material engineering approaches have been extensively explored aiming to enhance the catalysis of carbonaceous materials towards H_2O_2 production. From a different perspective, an interesting strategy to produce catalysts with improved properties for obtaining H_2O_2 is using noble metals supported under non-noble metal particles to modified carbon-based supports. This strategy makes use of metal oxides as a shield for the positive charge from the carbon surface in order to control the size and distribution of the noble metal nanoparticles while improve their catalytic efficiency for H_2O_2 production. Thus, Chapter III of this thesis entitled “*Using Au NPs anchored on ZrO_2 _carbon black toward more efficient H_2O_2 electrogeneration in flow-by reactor for carbaryl removal in real wastewater*” has focused on the development of a catalyst highly selective for H_2O_2 production based on Au nanoparticles supported on a ZrO_2 /PL6C hybrid material (developed in Chapter II), so called Au_ ZrO_2 /PL6C.

5. Gas diffusion electrodes (GDE)

Apart from being versatile for the anchoring of metal-based modifiers, the use of amorphous carbon-based materials offers significant advantages for H_2O_2 production due to the ability to shape porous 3D electrodes, the so-called gas diffusion electrodes (GDE). The GDE are pointed out as model electrodes for H_2O_2 production in light of its high efficiency in the directly reducing oxygen in aqueous media, despite the low solubility of O_2 . The reason behind this lies in the porous structure of the GDE that allows the constant renewal of gaseous reagents on the catalytic surface, thereby producing a triple interface (exhibited in Figure 4) that does not depend on the mass transport of O_2 such as it is found in conventional electrodes (17,18,69–71).

Figure 4. Schematic of the GDE triple interface by connecting the gas chamber with the aqueous environment.



Source: the author

Different authors have reported investigations using GDE for H_2O_2 electrogeneration achieving concentrations ranging from 100 - 1000 mg L^{-1} in both acidic and basic media at higher conductivity solution. Furthermore, the use of GDE in electrochemical systems (including lab and pre-pilot scale) for the successful removal of POP from simulated aqueous matrices has also been reported (17,18,52,68,72,73). However, the application of GDE in real wastewater faces challenges, such as reduced efficiency for H_2O_2 production in low conductivity matrix. Also, the presence of organic and inorganic impurities in real effluents can also affect the stability of the GDE, reducing its catalytic efficiency (69,73). Therefore, it is a major challenge to continuously optimize GDE designs to ensure their stability and catalysis in real wastewater matrix for H_2O_2 production. In fact, those new GDE arrangements that facilitate use of carbon-based materials modified with metal oxides or nanoparticles have been strongly encouraged for application in real wastewater treatment. The $\text{Au_ZrO}_2/\text{PL6C}$ catalyst was also incorporated into the surface of a new design of GDE supported on carbon cloth as a means of evaluating the influence of scale-up systems for H_2O_2 production. The modified GDE was also investigated coupled with an anode of boron doped diamond (BDD)

present in a pre-pilot plant for the treatment of a real sewage effluent contaminated with Carbaryl pesticide using electrochemical advanced oxidative processes.

The results presented in these 3 chapters of this thesis were obtained during 6 years of research funded by CNPq (grant #134370/2017-1) and FAPESP (grant FAPESP 2017/23464-3 and 2021/10973-2). In summary, the chapters focus on the major subject of using different strategies for developing high efficiency cathodic materials for H₂O₂ production. Then, innovative findings in the areas of sustainable inorganic synthesis, materials engineering towards the development of catalysts for H₂O₂ production and electrochemical catalysis in real systems applied to wastewater treatment have been addressed in this document.

Chapter I

Low Pd loadings onto Printex L6: Synthesis, characterization and performance towards H₂O₂ generation for electrochemical water treatment technologies

Author Contributions: Guilherme V. Fortunato: Investigation, Methodology, Supervision, Writing - original draft, Writing - review & editing. **Matheus S. Kronka**: Investigation, Methodology, Writing – original draft. Alexsandro J. dos Santos: Investigation, Methodology, Supervision, Writing - original draft, Writing - review & editing. Marc Ledendecker: Conceptualization, Supervision, Writing - review & editing. Marcos R.V. Lanza: Conceptualization, Supervision, Funding acquisition, Writing - review & editing.

The present study evaluated the catalytic performance of low loading of Pd nanoparticles disposed on a Printex L6 carbon matrix in order to facilitate the production of H₂O₂ in acidic medium. Previous studies suggested that low loading of this noble metal prevents the readsorption of H₂O₂ and thus inhibits the production of H₂O as a preferential product. The potentiality of using the cathode material for methylparaben removal was evaluated on a laboratory scale consisting of GDE of carbon cloth modified with Pd_{1%}/PL6C and anode of boron doped diamond (BDD) by using electro-Fenton (EF) and photoelectro-Fenton (PEF) processes.

This article/chapter was published in Chemosphere, v. 259, G. V. Fortunato, **M. S. Kronka**, A. J. dos Santos; M. Ledendecker; M. R. V. Lanza, Low Pd loadings onto Printex L6: Synthesis, characterization and performance towards H₂O₂ generation for electrochemical water treatment technologies, 127523, Copyright Elsevier (2020).



Contents lists available at ScienceDirect

Chemosphere

journal homepage: www.elsevier.com/locate/chemosphere

Low Pd loadings onto Printex L6: Synthesis, characterization and performance towards H₂O₂ generation for electrochemical water treatment technologies

Guilherme V. Fortunato^{a, **, 1}, Matheus S. Kronka^{a, 1}, Alexandro J. dos Santos^{a, *, 1}, Marc Ledendecker^b, Marcos R.V. Lanza^{a, ***}

^a Institute of Chemistry of São Carlos, University of São Paulo, Avenida Trabalhador São-Carlense 400, São Carlos, SP, 13566-590, Brazil

^b Department of Technical Chemistry, Technical University Darmstadt, Alarich-Weiss-Straße 8, 64287, Darmstadt, Germany

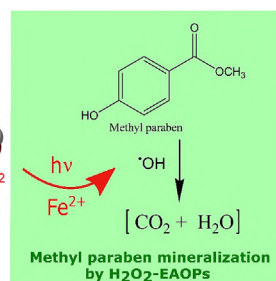
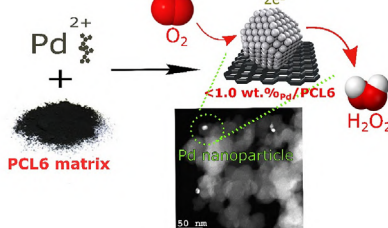


HIGHLIGHTS

- H₂O₂ generation using less than 1 wt % of Pd nanoparticles on Printex L6 carbon black.
- Treatment of 0.50 mM methyl paraben by EAOPs based H₂O₂ generation.
- 100% of pollutant removal by EF and PEF processes.
- Main by-products detected: 3 aromatic compounds and 1 short-chain carboxylic acid.

GRAPHICAL ABSTRACT

Production of H₂O₂ by gas-diffusion cathode



ARTICLE INFO

Article history:

Received 11 May 2020

Received in revised form

22 June 2020

Accepted 23 June 2020

Available online 6 July 2020

Handling Editor: E. Brillas

Keywords:

H₂O₂ electrogeneration

Palladium

Wastewater treatment

Electrochemical advanced oxidation processes

Methyl paraben

ABSTRACT

In order to enhance hydrogen peroxide (H₂O₂) electrogeneration, a catalyst based on less than 1 wt% of Pd nanoparticles dispersed onto commercially available Printex L6 carbon black (PCL6) is proposed and synthesized. The material was characterized by physico-chemical and electroanalytical methods, demonstrating high activity with a 320 mV lower onset potential compared to pristine PCL6 and high stability after 5000 potential cycles. Its performance places it among the most efficient bi- and mono-metallic electrocatalysts for H₂O₂ production. When testing the accumulation of H₂O₂, a 1.69-fold molar increase was observed for Pd_{1%}/PCL6 compared to PCL6. Different electrochemical advanced oxidation processes based on H₂O₂ generation have been performed to oxidize and remove pollutants as exemplarily shown on methyl paraben in Na₂SO₄ solution as model pollutant. A boron-doped diamond electrode was used as anode while Pd_{1%}/PCL6 was tested in a rotating ring disk electrode (RRDE) and gas diffusion setup. Pollutant degradation followed a pseudo-first-order reaction kinetic in the following order: anodic oxidation along with H₂O₂ generation (AO-H₂O₂) < AO-H₂O₂/UVC < electro-Fenton (EF) < photoelectro-Fenton (PEF). The best mineralization performance was found for PEF due to the photodecarboxylation of Fe (III) complexes with UVC light, while the process with lowest energy

* Corresponding author.

** Corresponding author.

*** Corresponding author.

E-mail addresses: g.fortunato@usp.br (G.V. Fortunato), alexandrojhones@usp.br (A.J. dos Santos), marcoslanza@usp.br (M.R.V. Lanza).

¹ These authors contributed equally to this work.

<https://doi.org/10.1016/j.chemosphere.2020.127523>
0045-6535/© 2020 Elsevier Ltd. All rights reserved.

consumption per order was EF with $0.488 \text{ kWh m}^{-3} \text{ order}^{-1}$. At the end of the work a route for pollutant mineralization was suggested.

© 2020 Elsevier Ltd. All rights reserved.

1. Introduction

Hydrogen peroxide (H_2O_2) plays a critical role in a wide range of industrial, commercial, and domestic applications, including wastewater treatment (Campos-Martin et al., 2006; Pesterfield, 2009; Edwards et al., 2015; Jiang et al., 2018). Technologies based on the *in-situ* electrochemical H_2O_2 production via the oxygen reduction reaction (ORR, Eq. (1)) represent an environmentally friendly way to generate H_2O_2 , overcoming its transportation and storage drawbacks (Carneiro et al., 2017).



Electrochemical advanced oxidation processes (EAOP) based on H_2O_2 such as anodic oxidation with H_2O_2 , (AO- H_2O_2), electro-Fenton (EF) and photoelectro-Fenton (PEF) allow the generation of reactive oxygen species such as hydroxyl radicals ($\cdot\text{OH}$) (Brillas, 2020; Moreira et al., 2017). This strong oxidizing agent ($E^\circ(\cdot\text{OH}/\text{H}_2\text{O}) = 2.80 \text{ V}_{\text{SHE}}$) is capable of non-selectively convert organic pollutants to less toxic products or even total mineralization to carbon dioxide, water and inorganic ions (dos Santos et al., 2018a). In the last decade, the H_2O_2 -EAOPs have been widely used in the treatment of dyes (Brillas and Martínez-Huitle, 2015; dos Santos et al., 2020, 2016; Nakamura et al., 2019; Paz et al., 2018), pesticides (Carneiro et al., 2018; Dominguez et al., 2018; Rosa Barbosa et al., 2018; Fdez-Sanromán et al., 2020), and pharmaceuticals (Dirany et al., 2012; Ganiyu et al., 2016; Zhang et al., 2019; Lima et al., 2020) in synthetic and real effluents (dos Santos et al., 2018a; Ganiyu et al., 2018; Ren et al., 2020). However, an obstacle being faced in the electrochemical production of H_2O_2 and its coupling to EAOPs is the development of efficient catalyst materials that selectively reduce O_2 to H_2O_2 (Fellinger et al., 2012; Siahrostami et al., 2013; Verdaguer-casadevall et al., 2014). Active and selective ORR (electro)catalysts to form H_2O_2 must have sufficiently strong interaction with O_2 so that the reaction can occur on the catalysts surface without breaking the intermolecular $\text{O}=\text{O}$ bond (Lobytseva et al., 2007; Fellinger et al., 2012; Siahrostami et al., 2013; Choi et al., 2014; Verdaguer-casadevall et al., 2014). An ideal catalyst should demonstrate high selectivity, activity and stability at low costs. Recent studies demonstrated that the metal loading in the carrier material affect the activity and selectivity toward ORR (Inaba et al., 2004; Schneider et al., 2008; Nesselberger et al., 2013; Fabbri et al., 2014; Taylor et al., 2016; Fortunato et al., 2018). At low metal loading, the selectivity for H_2O_2 increases and the $\text{O}-\text{O}$ bond breakage is suppressed. As an example, the group of Arenz (Nesselberger et al., 2013) evaluated the effect of Pt-particle proximity on the catalytic ORR activity. They noticed a decrease in ORR activity with increase of the inter particle distance (*ipd*). The diffusion-limited current decreased at lower cluster density (increasing *ipd*), suggesting a shift of the ORR mechanism from 4e^- to 2e^- . Fabbri and co-workers (Fabbri et al., 2014) supported different Pt loadings onto carbon and realized that the transition from dispersed Pt nanoparticles to extended surfaces strongly influences ORR selectivity. Highly dispersed nanoparticles promote significantly the production of H_2O_2 .

Effects on selectivity caused by varied catalyst loading and *ipd* were also suggested for Pd (Fortunato et al., 2018; Mittermeier

et al., 2017). Catalysts with different Pd loadings and different *ipd* onto different carbon supports have been synthesized and tested (Fortunato et al., 2018). Low Pd-catalyst loadings ($<2 \text{ wt}\%$) and high *ipd* ($>125 \text{ nm}$) achieve selectivities to H_2O_2 close to 100% at low overpotentials resulting in high mass activities. The strong interaction between carbonaceous materials and metal nanoparticles (catalyst-support interaction), which may be responsible for changes of metal cluster electronic properties, becomes a key contributor to achieve the observed catalytic performance as well as the long-term stability (Fortunato et al., 2018; Ma et al., 2013). Carbon materials such as graphene and carbon black have been reported to be selective towards H_2O_2 in alkaline (Assumpção et al., 2011; Wu et al., 2017; Han et al., 2019; Jiang et al., 2019; Kim et al., 2019; Cordeiro-Junior et al., 2020) and acidic (Fellinger et al., 2012; Zhang et al., 2018; Kim et al., 2019; Melchionna et al., 2019) medium, mainly due to their oxygenated and nitrogenated functional groups. However, in acidic conditions, the ORR typically takes place at high overpotentials (Cordeiro-Junior et al., 2020; Daems et al., 2014; Fellinger et al., 2012; Lu et al., 2019). Additionally, oxygenated and nitrogenated functional groups in carbon materials offer ample anchor sites to stabilize metal catalysts. (Antolini, 2012; Barros et al., 2015; Fortunato et al., 2016, 2018; Luo and Alonso-Vante, 2015; Ma et al., 2013).

In this work, a highly active, selective and stable catalyst toward the production of H_2O_2 is synthesized and evaluated using less than 1 wt% of Pd nanoparticles (NPs) well dispersed onto commercially available Printex L6 carbon black (PCL6), a carbonaceous material with oxygenated and nitrogenated functional groups (Assumpção et al., 2011). The Pd_{1%}/PCL6 catalyst was analyzed by physical characterization techniques and electroanalytical methods. Besides the significantly enhanced activity/selectivity/stability compared to commonly applied carbon black and Pd-based materials, the novelty of the here described study lies in the fact of the *in-situ* produced H_2O_2 in a gas diffusion electrode (GDE) setup was evaluated and used to catalyze the degradation of methyl paraben (MetP), chosen as exemplary organic pollutant. MetP is a well-known endocrine disruptor with potential harmful effects to environment and human life when incorrectly disposed (Dionisio et al., 2020; Gmurek et al., 2015; Steter et al., 2016). The performance of the catalyst in the electrogeneration of H_2O_2 was evaluated galvanostatically, following the pollutant concentration, its mineralization and formed by-products and a mineralization route was suggested. The energy consumption per order was determined as well.

2. Experimental section

2.1. Reagents

MetP with 99% purity was acquired from Supelco. The salts and precursor solutions employed were palladium chloride (PdCl_2), sulfuric acid (H_2SO_4), potassium sulfate (K_2SO_4), sodium sulfate (Na_2SO_4), ascorbic acid (AA) and dimethylformamide ($(\text{CH}_3)_2\text{NC}(\text{O})\text{H}$), all acquired from Vetec. Sodium sulfate (Na_2SO_4) and Iron (II) sulfate heptahydrate ($\text{FeSO}_4 \cdot 7\text{H}_2\text{O}$) were of analytical grade and supplied by Sigma-Aldrich. All solutions were prepared with ultrapure water obtained from a Milli-Q system with resistivity

>18 M Ω cm at 25 °C. All other chemicals used for analysis were of analytical grade or HPLC grade provided by Sigma-Aldrich.

2.2. Synthesis of Pd_{1%}/PCL6

Firstly, the Printex carbon (PCL6, from Evonik®) was thermally treated at 120 °C for 24 h. Pd_{1%}/PCL6 electrodes were synthesized by the hydrothermal procedure proposed in Fortunato et al., 2018. Briefly, 160 mg of PCL6 were dispersed with 3 mg of PdCl₂ in 20 mL of ultrapure water under ultra-sonication bath for 1 h. Afterwards, the mixture was heated up to its boiling point using a hot plate with magnetic stirring. Subsequently, 78 mg of AA (previously solubilized in 2 mL of water) were added. After 5 min, the heating was stopped and the mixture was kept stirring for 2 h. The formed nanocomposite was washed 15 times by centrifugation to remove the unreacted species present in the mixture, and finally dried in an oven at 60 °C overnight. In order to have a gas diffusion electrode (GDE) to perform EAOPs, a carbon cloth (PW03 - 33" wide, 80 yards long - average 15.6 pounds per roll, acquired from Plain Weave Fabric) with geometric area of 2.7 cm² was used as substrate to the deposition of the produced film of 200 μ g cm⁻² by dropping 206 mL of 2.5 mg mL⁻¹ catalyst solution and addition of 100 μ L of a Nafion 0.1% on isopropanol solution. Afterwards, it was dried under N₂-gas flow for 2 h in an open system.

2.3. Physico-chemical characterization methods

To perform transmission electron microscopy (TEM) and scanning-TEM (STEM) experiments, the catalyst dispersion was drop-casted onto a TEM grid constituted by a lacey carbon film on a copper grid (300-mesh acquired from Electron Microscopy Sciences). TEM and STEM analyses were conducted using a FEI TECNAI G² F20 HRTEM microscope at 200 kV. For the determination of Pd loading, a TGA-50 thermogravimetric analyzer (Shimadzu) was used; samples of 2–5 mg were placed under a synthetic air 5.0 FID gas flow (50 mL min⁻¹) at temperatures ranging between 25 and 900 °C, at a heating rate of 10 °C min⁻¹, using alumina crucibles. The X-ray photoelectron spectroscopy (XPS) analyses were performed using a Scienta Omicron ESCA + spectrometer.

The Al K α line (energy = 1486.6 eV) was used as excitation source operating at 20 kV and 25 W. The binding energies were calibrated using the C1s signal (284.6 eV) as reference. The Shirley method was used to subtract the inelastic noise from the narrow scan (High-resolution) spectra. The composition (at. % and mass conc. %) of the surface (<5 nm) was estimated by using the (relative) peak area proportions compensated by Scofield atomic sensitivity factors (accuracy of \pm 5%) (Scofield, 1976) from the narrow scan spectra. For the Pd 3d region spectrum, deconvolution, a Voigt type function with Gaussian and Lorentzian (in a proportion of 70:30) combinations was used. Structural characterization was carried out based on X-ray diffraction (XRD) measurements. The XRD measurements were performed with the aid of a Bruker X-ray diffractometer model D8 Advance, operating at 40 kV and 40 mA (1.6 kW), using Cu-K α radiation (λ = 1.540501 Å/8,047 keV). The scan rate applied was 0.02° s⁻¹ in 2θ , and silicon powder was employed as reference.

2.4. Treatment of MetP by EAOPs

Assays were performed in a bench scale electrochemical cell with an external jacket for thermostatic water recirculation at 25 °C (dos Santos et al., 2016). Pure oxygen (O₂) was coupled to the GDE to ensure the fed of O₂ gas at 500 mL min⁻¹ in order to electro-generate H₂O₂ from Eq. (1). A boron-doped diamond (BDD) thin film with a geometric area of 3.0 cm² was used as anode. The

interelectrode gap distance was kept around 1.0 cm. Before each experiment, both anode and cathode were activated by using a 50 mM NaSO₄ at pH 2.5 and j = 100 mA cm⁻² during 60 min (dos Santos et al., 2019).

Electrolysis at constant current density (j) at 33.3 mA cm⁻² was performed at an Instrutherm DC power supply FA-2030 coupled to Instrutemp ITMDB 100 A m and Instrutemp MDB-450 voltmeter. All experiments were carried out with 150 mL of 0.50 mM MetP solution with 50 mM Na₂SO₄ as support electrolyte. Before electrolysis, the solution pH was adjusted to 2.5 using a pH-meter ION pHB500 with a diluted H₂SO₄ solution. Acidic conditions are considered the best for Fenton's reactions, since it avoids the precipitation of iron. All the processes were performed under pH 2.5, in order to maintain the same operating conditions for comparison between the different EAOPs.

Different concentrations Fe²⁺ (0.1, 0.25 and 0.50 mM) were tested to perform EF and PEF treatment. In PEF, the solution was illuminated with a 5W UVC lamp (Pen-Ray model 11SC-2.12) that provided 19 W m⁻² of irradiance.

2.5. Analytical techniques

The H₂O₂ concentration was determined by the Molybdate method where the absorbance of the colored complex formed with H₂O₂ and (NH₄)₆Mo₇O₂₄ was measured at λ = 350 nm using a Shimadzu UV-1900 spectrophotometer (Lima et al., 2020). This value allowed the calculation of the percentage of current efficiency (CE) following the Faraday's law (Eq. (2)):

$$CE_{H_2O_2}(\%) = \frac{2 F C_{H_2O_2} V_s}{I t} \times 100 \quad (2)$$

where 2 corresponds to the number of electrons needed to the reduction of O₂ to form H₂O₂, F to the Faraday constant (96,487 C mol⁻¹), C_{H₂O₂} to the H₂O₂ concentration in mol L⁻¹, V_s to the volume of the solution in L, I to the applied current intensity in A, and t to the reaction time in s.

The concentration of MetP was determined on a high-performance liquid chromatography (HPLC) system equipped with a Phenomenex Luna C18 (250 × 4.6 mm, 5 μ m) column and a Supelcosil C18 (4 mm × 3.0 mm i.d.) pre-column at 35 °C and coupled to an SPD-20A UV detector selected at λ = 258 nm. The mobile phase consisted of an aqueous solution containing water-acetonitrile mixture (60/40, v/v) at a flow rate of 1.0 mL min⁻¹. The retention time for MetP was 6.3 min. The acid intermediates were analyzed by ion exchange chromatography. The ion exchange column used was Metrosep Organic Acids (250 mm/7.8 mm) from Metrohm, whereas a diluted H₂SO₄ solution (5 mmol L⁻¹) was employed as the solvent in 20 μ L sample injection and 20 min of running. Analyzes were performed on an 850 Professional IC ion chromatograph (Metrohm) using a conductivity detector. Total organic carbon (TOC) was obtained using a Shimadzu TOC-VCNP equipment and its removal is given by Eq. (3). All withdrawn samples before HPLC and TOC analyzes were filtered with 0.45 μ m filters (chromafil Xtra PET-45/25). The experiments were carried out in duplicate and figures related to degradation and mineralization show the error bar related to the 95% confidence interval.

$$TOC\ removal(\%) = \frac{TOC_0 - TOC_f}{TOC_0} \times 100 \quad (3)$$

The percentage of mineralization current efficiency (MCE) was calculated from Eq. (4):

$$MCE (\%) = \frac{nFV\Delta(TOC)_{exp}}{4.32 \times 10^7 m I t} \times 100 \quad (4)$$

where 4.32×10^7 is the conversion factor ($3600 \text{ s h}^{-1} \times 12,000 \text{ mg C mol}^{-1}$), m is the number of carbon atoms of MetP molecule ($m = 8$). The number of electrons (n) for the mineralization process was taken as 34 considering the theoretical mineralization for the MetP (Steter et al., 2016) (Eq. (5)):



In order to follow the evolution of by-products of MetP degradation by gas chromatography–mass spectrometry (GC-MS), the samples were extracted in CH_2Cl_2 using a flow of 1 mL of $N_2(g)$ to concentrate the organic compounds for analyses. This analysis was executed in a gas chromatograph GC-2010 Plus coupled to a mass spectrometer QP2020 (Shimadzu), equipped with an automatic sampler model AOC-6000. The column used was a non-polar capillary Rtx-5MS ($30 \text{ m} \times 0.25 \text{ mm} \times 0.25 \mu\text{m}$) (Shimadzu) and Helium (purity 99.999%) was the carrier gas applied at a flow rate of 1.0 mL min^{-1} . The initial temperature of the oven was $36 \text{ }^\circ\text{C}$ for 1 min, increased to $320 \text{ }^\circ\text{C}$ at $5 \text{ }^\circ\text{C min}^{-1}$, hold for 10 min, totaling 67.80 min of analysis. There was a solvent cut time of 3 min. The injection volume was $1 \mu\text{L}$ of the liquid sample. The injection temperature was $250 \text{ }^\circ\text{C}$ and splitless injection was used. The mass spectrometer, equipped with an electron impact source (EI), was operated in SCAN mode at 70 eV of electronic energy. The ion source and interface temperatures were 230 and $280 \text{ }^\circ\text{C}$, respectively.

3. Results and discussion

3.1. Physico-chemical characterization

Compared to metal-based materials, commercial PCL6 typically demonstrates relatively low activity toward ORR while the selectivity towards H_2O_2 both in alkaline (Assumpção et al., 2011; Barros et al., 2015) and acidic (Cordeiro-Junior et al., 2020) medium is rather high. Specifically at low pH values, the ORR takes place at high overpotentials emphasizing the need for better catalysts (Cordeiro-Junior et al., 2020; Lu et al., 2019). Its surface composition contains oxygen, sulfur, and nitrogen functional groups (Assumpção et al., 2011) that can assist to control the dispersion and the interaction with metallic species (metal-support interaction) (Antolini, 2012; Barros et al., 2015; Fortunato et al., 2016, 2018; Luo and Alonso-Vante, 2015; Ma et al., 2013). As aforementioned, Pd at low loadings ($<2 \text{ wt}\%$) and high *ipd* can achieve selectivities towards H_2O_2 close to 100% with low overpotentials (Fortunato et al., 2018). In this context, we combined these two effects (low metal loading and abundant carbon material with relatively high metal-support interaction) to produce an efficient catalyst toward H_2O_2 production via ORR. The challenge lies in distributing low amounts of Pd NPs homogeneously onto the carbon surface to obtain a *ipd* over 100 nm. The strategy proposed by Fortunato and co-authors (Fortunato et al., 2018) was used to tune the Pd loading so that high selectivities towards H_2O_2 can be achieved.

In Figs 1 and 2, the physico-chemical characterizations of the different catalysts are shown. For Pd_{1%}/PCL6, a low Pd amount ($\sim 0.6 \text{ wt}\%$) resulted in highly dispersed Pd nanoparticles in the size range of $\sim 5.5 \text{ nm}$ with octahedral and spherical shapes and edge-to-edge interparticle distances around 170 nm, as shown in Fig. 1a–f (c.f. Table S1). The HR-TEM image (Fig. 1e) reveals lattice fringes of 0.22 nm (on average) which is expected for (1 1 1) face-centered

cubic (fcc) planes of crystalline Pd (Fortunato et al., 2018; Saha et al., 2011; Venarusso et al., 2018; Vukmirovic et al., 2011). A metal loading of 0.9 wt% was obtained by thermogravimetric analysis (c.f. Fig. 2a). The diffractograms (Fig. 2b) evidence the presence of less than 1 wt% of Pd on PCL6 showing the patterns of fcc crystalline with peaks (1 1 1), (2 0 0), (2 2 0), (3 1 1), and less visible (2 2 2) for Pd (Boone and Maia, 2017; Kabir et al., 2016; Saha et al., 2011; Venarusso et al., 2018, 2016). The presence of a characteristic broad peak (0 0 2) at $2\theta = 25.9^\circ$, associated to the graphitic structure of the carbon support (Boone and Maia, 2019, 2017; Kabir et al., 2016), is also observed. To resolve the surface characteristics, XPS measurements were performed. The XPS survey spectra (Fig. 2c) shows only peaks in the C 1s and O 1s regions due to the low Pd amount.

The narrow-scan spectrum in the Pd 3d region (Fig. 2d) exhibits the expected spin-orbit splitting and binding energy of metallic Pd species (Pd⁰ 3d_{5/2} at $\sim 335.4 \text{ eV}$, Pd⁰ 3d_{3/2} at $\sim 341.0 \text{ eV}$, c.f. Table S3), and as well as the spin-orbit splitting for oxidized Pd species (Pd²⁺ 3d_{5/2} at $\sim 337.6 \text{ eV}$, Pd²⁺ 3d_{3/2} at $\sim 343.0 \text{ eV}$, c.f. Table S3). The XPS analysis was not able to detect a signal in the Cl 2p region (Fig. S2), although we do not rule out the presence of Cl adsorbed to the Pd surface since halides can adsorb strongly to Pd surfaces enhancing H_2O_2 production. (Damjanovic et al., 1967; Marković et al., 1999; Schmidt et al., 2001; Su et al., 2018; Yan et al., 2011). High-resolution XPS quantification reveals ca. 0.10 at% Pd ($=0.87 \text{ wt}\%$, c.f. Tables S1 and S2), which corresponds well to thermogravimetric analysis.

3.2. Electrochemical profile and ORR performance

Fig. 3 presents the CVs, RRDE, and RDE responses for PCL6 and Pd_{1%}/PCL6. The CV obtained in N_2 -saturated solution for the synthesized materials (Fig. 3a) reveals that in the absence of Pd, the characteristic quinone/hydroquinone peaks (at $\sim 0.2 \text{ V}$) from the carbon surface (Fortunato et al., 2018; Jukk et al., 2013) are observed. Under O_2 -saturated conditions, an additional peak at $\sim -0.2 \text{ V}_{Ag/AgCl}$ was observed corresponding to the reduction of molecular oxygen. When $\sim 1 \text{ wt}\%$ Pd is present (c.f. Fig. 3b), in N_2 -saturated solution, the characteristic polycrystalline Pd surface processes of hydrogen underpotential deposition (H_{UPD}) (-0.4 and $0 \text{ V}_{Ag/AgCl}$) are observed. Due the low metal loading (and presumable Cl-speciations on the surface), Pd oxidation in the potential region of 0.5 – $1.0 \text{ V}_{Ag/AgCl}$ is suppressed. Careful inspection of the corresponding oxide back reduction region (0.45 – $0.25 \text{ V}_{Ag/AgCl}$) reveals the expected oxide reduction peak at $\sim 0.34 \text{ V}_{Ag/AgCl}$. Under O_2 -saturated condition, with $\sim 1 \text{ wt}\%$ of Pd onto PCL6, the ORR peak appears at a potential $\sim 500 \text{ mV}$ more positive than the bare carbon matrix (c.f. Fig. 3a and b). For Pd_{1%}/PCL6, a lower potential limit of $-0.4 \text{ V}_{Ag/AgCl}$ was selected due the hydrogen production at lower potentials. Additionally, the electrochemically active surface area (ECSA) determined from the electrical double-layer capacitance revealed comparable surface areas for both catalysts. In the presence of Pd NPs, the ECSA decreases $\sim 10\%$ in comparison to pure PCL6 (78.4 vs. $86.5 \text{ m}^2 \text{ g}^{-1}_{catalyst}$, respectively—c.f. Table S4), which could be related to not fully covered glassy carbon areas.

Fig. 3c shows the linear sweep voltammetry in RRDE configuration. The samples were tested towards the production of H_2O_2 by scanning the potential from 0.1 to $1.0 \text{ V}_{Ag/AgCl}$ under O_2 saturation in $0.1 \text{ mol L}^{-1} \text{ K}_2\text{SO}_4$ at pH 2.5. For pure PCL6, the onset potential for ORR occurs at $\sim 0 \text{ V}_{Ag/AgCl}$. The disk current density achieves the diffusion-limited values at $\sim -0.7 \text{ V}_{Ag/AgCl}$. The ring current densities are comparably large in comparison to the disk current densities, evidencing large H_2O_2 production amounts. From RRDE results, the potential dependent selectivity towards H_2O_2 ($S_{H_2O_2}$) in the course of the ORR could be obtained, and the responses are

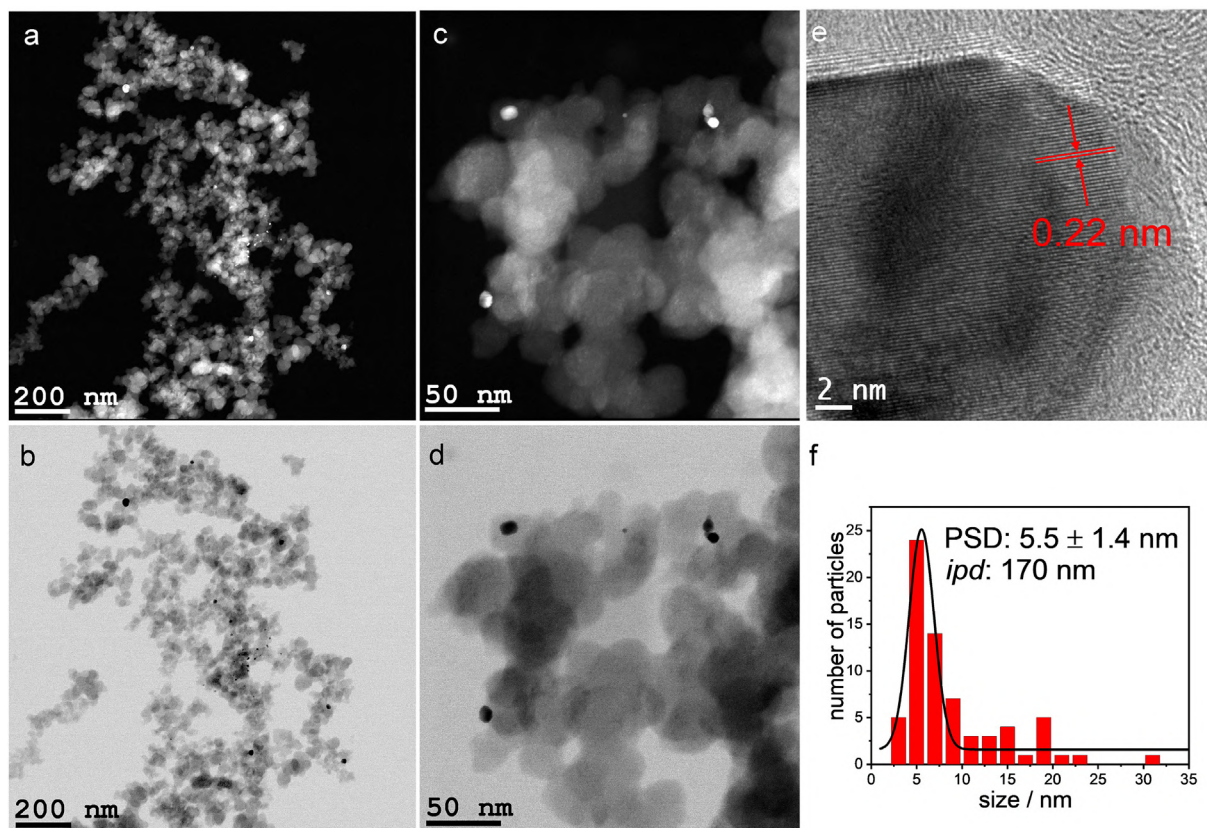


Fig. 1. Representative (a and c) virtual high-angle angular dark field (images reconstructed from electron diffraction patterns), (b and d) bright-field STEM, and (e) HR-TEM images of Pd_{1%}/PCL6. (f) Size distribution histograms and interparticle distance (*ipd*) for Pd_{1%}/PCL6.

shown in Fig. 3d. The $S_{H_2O_2}$ for PCL6 reaches ~84% over the measured potential range from -0.9 V to -0.15 V_{Ag/AgCl}, in line with previously reported results (Cordeiro-Junior et al., 2020). As stated before, Pd-loadings >2 wt% typically favor full reduction to H₂O. To test our hypothesis, PCL6 was modified with 20 wt% Pd (Pd_{20%}/PCL6) and tested towards the production of H₂O₂.

As expected, 20 wt% of Pd leads to a drop in selectivity to ~10% over the measured potential range from -0.2 to 0.3 V_{Ag/AgCl} (c.f. Fig. 3c and d). Additionally, one part of Pd_{20%}/PCL6 was physically combined with 9 parts of PCL6. Here, the 2% Pd-loading leads to a drastic increase in H₂O₂ selectivity of over 80% (c.f. Fig. 3c and d).

Additionally, a set of LSV curves recorded at different rotation rates are presented in Fig. 3e and f. Below -0.6 V_{Ag/AgCl} (Fig. 3e), the ORR is controlled by mass transport limitations for PCL6. For Pd_{1%}/PCL6, the mass transport region is not well defined due the hydrogen evolution with occurs concomitantly below -0.2 V_{Ag/AgCl}. From these curves, the electron transfer number (n_{K-L}) at different potentials was estimated (see details in Support Information). PCL6 and Pd_{1%}/PCL6 have average n_{K-L} values of 1.9 and 2.9, respectively, supporting the high selectivity for 2-electron-transfer ORR on both catalysts. In order to evaluate the electrochemical stability performance for the catalyst surfaces, changes in the activity and selectivity were monitored by RRDE before and after 5000 cycles between -0.2 and 0.5 V_{Ag/AgCl} at a scan rate of 0.5 V s⁻¹ and the results are presented in Fig. S4. In general, no drastic changes in electrocatalytic behavior, in terms of activity and selectivity, are observed for PCL6 and Pd_{1%}/PCL6. The CVs prior to and after stability tests (c.f. Fig. S4b) show small differences in the electrochemical behavior, suggesting high stability of the carbon structures. Fig. S5c compares the electrocatalytic performance of

Pd_{1%}/PCL6 with other noble metal-based state-of-the-art catalysts reported in literature in terms of kinetic current densities to H₂O₂ as a function of applied potential. Pd_{1%}/PCL6 shows high stability while maintaining high activity and selectivity relatively close to the most active Pd- and Pt-based catalysts. We point out that Pd_{1%}/PCL6 is easily synthesized, demonstrate high reproducibility and can be produced on a large scale by using commercially available carbon black materials as well as omitting any toxic metal which would be detrimental in wastewater treatment devices.

3.3. MetP treatment by H₂O₂-based EAOPs

3.3.1. Electrochemically generation and accumulation of H₂O₂

After establishing a greater picture on the potential dependent selectivities via RRDE, in real applications, higher current densities are sought after. By using a gas diffusion setup (GDE), the oxygen reduction is not limited by the solubility of oxygen in the liquid electrolyte and oxygen can be fed directly in gaseous form to the catalyst's surface. The GDE setup allows the application of practical relevant current densities. The GDE cathode was fabricated by deposition of Pd_{1%}/PCL6 onto a PW03 substrate. For comparison, PCL6/PW03 was studied. These experiments were accomplished with 150 mL in sulfate medium at pH 2.5, $j = 33.3$ mA cm⁻² and 25 °C. After 180 min of electrolysis, the maximum H₂O₂ concentrations varied between 1.33, 5.27 and 8.89 mM for PW03, PCL6/PW03 and Pd_{1%}/PCL6/PW03, respectively (Fig. 4a). For PCL6 on PW03, the generation of H₂O₂ was increased by a factor of 3.9 compared to the bare PW03 substrate. For Pd_{1%}/PCL6, the H₂O₂ generation was increased by a factor of 6.7 which is in line with RRDE results.

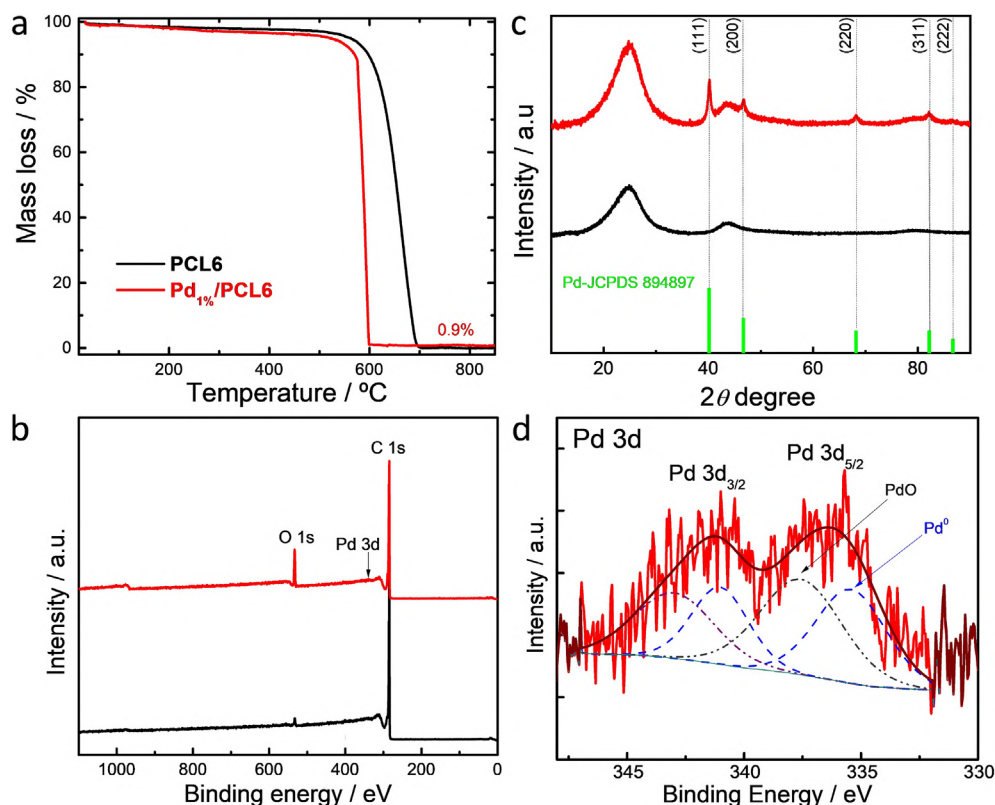


Fig. 2. Physico-chemical characterization of PCL6 and Pd_{1%}/PCL6 catalysts. (a) Thermogravimetric responses. (b) XRD patterns. (c) Survey XPS spectra for PCL6 and Pd_{1%}/PCL6. (d) Narrow scan XPS spectrum for Pd 3d regions of Pd_{1%}/PCL6 catalysts.

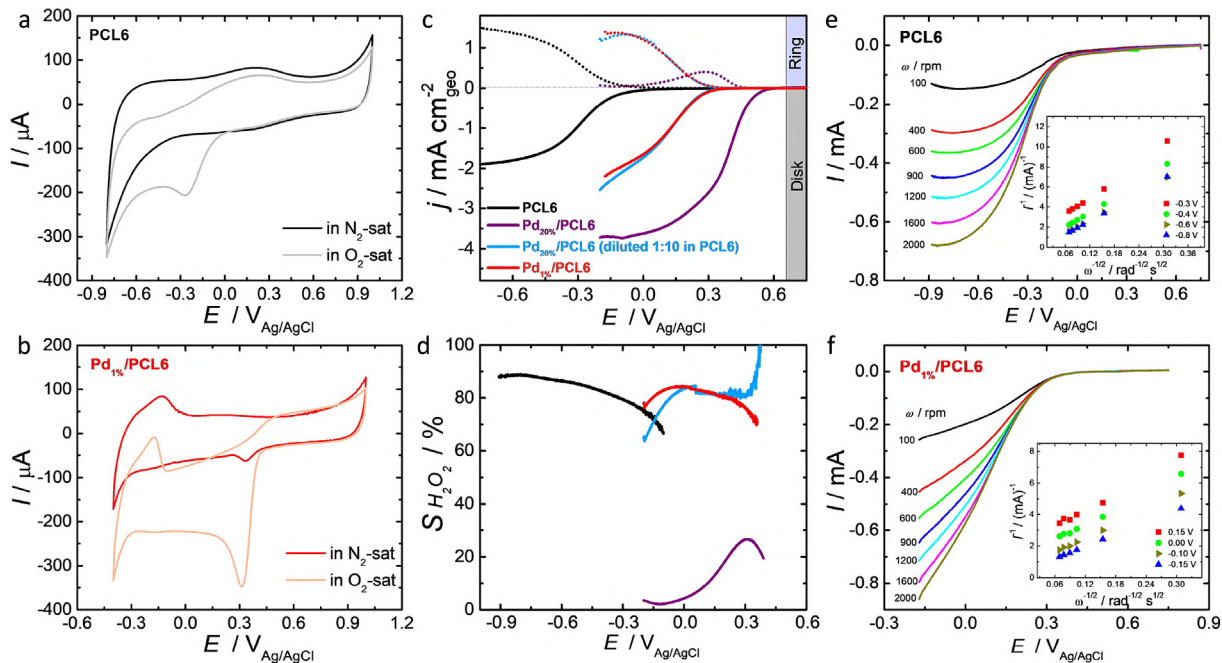


Fig. 3. (a, b) Cyclic voltammograms obtained in N₂ and O₂-sat 0.1 mol L⁻¹ K₂SO₄ at pH 2.5 for GC electrodes modified with PCL6 and Pd_{1%}/PCL6 (scan rate: 50 mV s⁻¹; scans started at 1.0 V_{Ag/AgCl}). (c) Linear sweep voltammetry in an RRDE configuration scanning the potential at 5 mV s⁻¹ and 900 rpm in O₂-sat 0.1 mol L⁻¹ K₂SO₄ at pH 2.5 (scans started at -0.9 or -0.2 V_{Ag/AgCl}). (d) S_{H₂O₂} during the ORR at varying potentials (obtained from the corresponding RRDE data). (e, f) Linear sweep RDE results scanning the potential at 5 mV s⁻¹ recorded in O₂-sat 0.1 mol L⁻¹ K₂SO₄ at pH 2.5 solution at various rotation rates. Insets: corresponding K-L plots.

Fig. 4b shows a decrease in current efficiency (CE) over time. This effect is most pronounced for Pd_{1%}/PCL6/PW03 with 36.9% and

23.9% CE after 20 and 180 min, respectively. For PCL6/PW03, the CE drops to 21.6% and 14.1%, respectively. H₂O₂ is not inert in solution

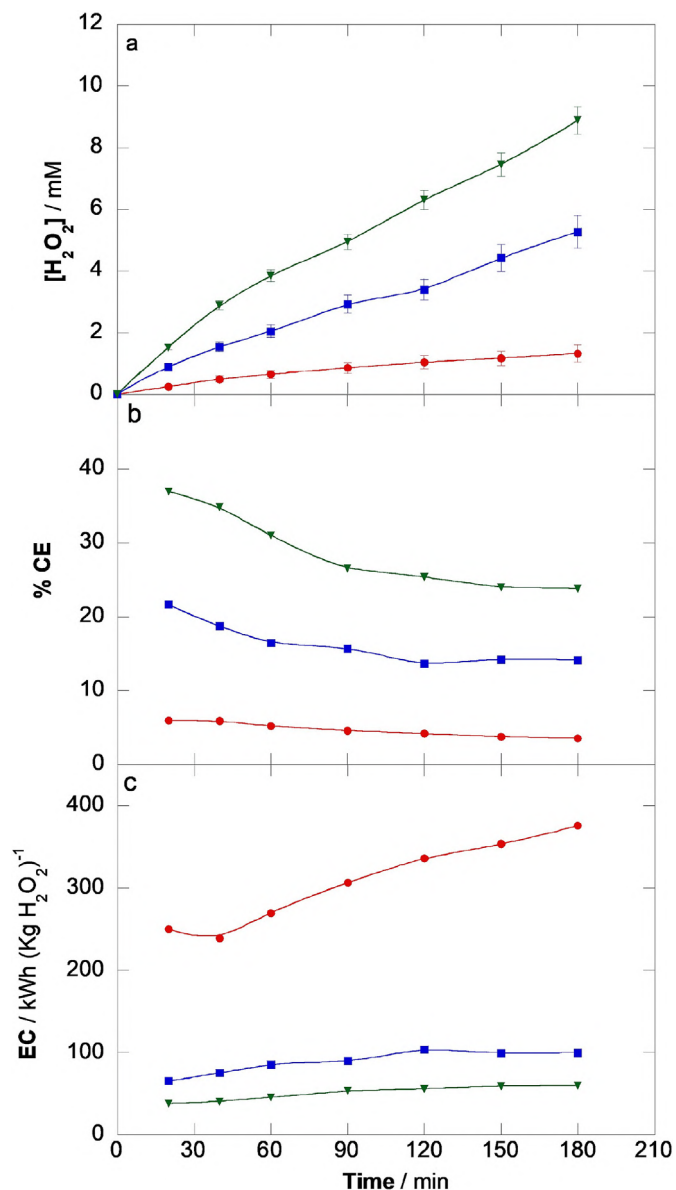
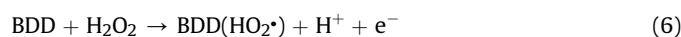


Fig. 4. Influence of different cathodes on (a) accumulated H_2O_2 concentration vs time (b) current efficiency and (c) energy consumed per kg H_2O_2 using 150 mL of 50 mM Na_2SO_4 solution at pH 2.5 and 25 °C, using (●) PW03, (■) PCL6/PW03 and (▼) Pd1%/PCL6/PW03/gas diffusion.

and might be oxidized to hydroperoxyl radicals (HO_2^\bullet) (Eq. (6)) at the surface of the BDD anode, decreasing the overall CE (dos Santos et al., 2018b). This behavior has already been observed with other materials such as Pt and dimensional stable anodes (DSA) (Alcaide et al., 2020; Fajardo et al., 2019). Pd1%/PCL6/PW03 possesses the lowest energy consumption (EC) per $\text{kg}_{\text{H}_2\text{O}_2}$ with 59.4 kWh $\text{kg}(\text{H}_2\text{O}_2)^{-1}$ (Fig. 4c), followed by PCL6/PW03 with 110.3 kWh $\text{kg}(\text{H}_2\text{O}_2)^{-1}$, and the bare PW03 substrate with 396.1 kWh $\text{kg}(\text{H}_2\text{O}_2)^{-1}$.

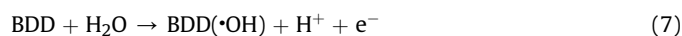


3.3.2. MetP degradation and energy consumption per order

Based on the promising results obtained with Pd1%/PCL6/PW03,

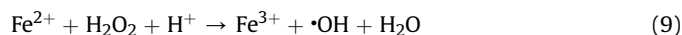
its performance towards the degradation of organic pollutants was tested on 0.50 mM MetP at pH 2.5, $j = 33.3 \text{ mA cm}^{-2}$ and 25 °C by AO- H_2O_2 , AO- $\text{H}_2\text{O}_2/\text{UVC}$, EF and PEF. After 180 min of treatment, AO- H_2O_2 leads to the lowest MetP degradation rate of 51.6% as shown in Fig. 5a. Conversely, AO- $\text{H}_2\text{O}_2/\text{UV}$ attains almost total degradation (95.8%) under similar operating conditions.

The kinetic rate constants (k_1) fit well a pseudo-first-order kinetic model (c.f. Fig. 5b), with values of $6.90 \times 10^{-5} \text{ s}^{-1}$ ($R^2 = 0.991$) and $2.28 \times 10^{-4} \text{ s}^{-1}$ ($R^2 = 0.989$) for AO- H_2O_2 and AO- $\text{H}_2\text{O}_2/\text{UVC}$ respectively. In the AO- H_2O_2 process, the greatest contribution to the MetP degradation is the physisorbed $\cdot\text{OH}$ formed at the BDD anode surface from water electrolysis (Eq. (7)) (dos Santos et al., 2019; Garcia-Segura et al., 2018). The electrogeneration of H_2O_2 does not show any significant effect on the degradation of MetP, since H_2O_2 itself is considered a relatively weak oxidant ($E^\circ(\text{H}_2\text{O}_2/\text{H}_2\text{O}) = 1.76 \text{ V}_{\text{SHE}}$) (dos Santos et al., 2018b), as well as HO_2^\bullet . For AO- $\text{H}_2\text{O}_2/\text{UVC}$, the k_{app} increased by a factor of 3.3 and that can be related to additional generation of $\cdot\text{OH}$ radicals formed from H_2O_2 photodecomposition by UVC irradiation (Eq. (8)) (Moreira et al., 2017; Xu et al., 2019). MetP alone is relatively stable against UVC light (Fig. 5a) and only 12.7% degrades after 180 min.



EF and PEF processes promote total degradation in less than 10 min (Fig. 5c). This rapid degradation is due to BDD($\cdot\text{OH}$) and the additional generation of high amounts of homogeneous $\cdot\text{OH}$ in the bulk by Fenton's reaction (Eq. (9)), that react rapidly with MetP. The necessary Fe^{2+} ion for Fenton's reaction can be regenerated by Eq. (10) and low catalyst concentrations can be used (Brillas, 2020; Garcia-Segura et al., 2014).

These processes should have an optimal ratio between H_2O_2 concentration generated and Fe^{2+} added. Therefore, various Fe^{2+} concentrations were tested (data not shown) in order to determine the ideal amount of this catalyst. We found that concentrations over 0.25 mM Fe^{2+} , excess of Fe^{2+} may scavenge $\cdot\text{OH}$ present in solution (Eq. (11)) (dos Santos et al., 2018c; Pérez et al., 2015). The obtained constant kinetics (k_1) were $5.52 \times 10^{-3} \text{ s}^{-1}$ ($R^2 = 0.997$) and $7.85 \times 10^{-3} \text{ s}^{-1}$ ($R^2 = 0.992$) for EF and PEF (c.f. Fig. 5d), respectively.



H_2O_2 -based EAOPs can be compared in terms of the amount and costs related to the electrical energy per order required to reduce the concentration of the contaminant by one order of magnitude in a unit volume as shown in Eq. (12) (Garcia-Segura et al., 2020; Montenegro-Ayo et al., 2019):

$$E_{\text{EO}} \left(\text{kWh m}^{-3} \text{ order}^{-1} \right) = \frac{6.39 \times 10^{-4} (P_{\text{cell}} + P_{\text{lamp}})}{V_s k_1} \quad (12)$$

where 6.39×10^{-4} is a conversion factor (1 h/3600 s/0.4343), P_{cell} is the power of the electrochemical cell and P_{lamp} is the power of the lamp both in W, V_s is the solution volume in L and k_1 is the pseudo-first order rate constant in s^{-1} . The values of E_{EO} were 0.488 and 1.27 kWh $\text{m}^{-3} \text{ order}^{-1}$ for EF and PEF, respectively. The E_{EO} for EF is by a factor of 2.6 lower compared to PEF, despite the fact that PEF

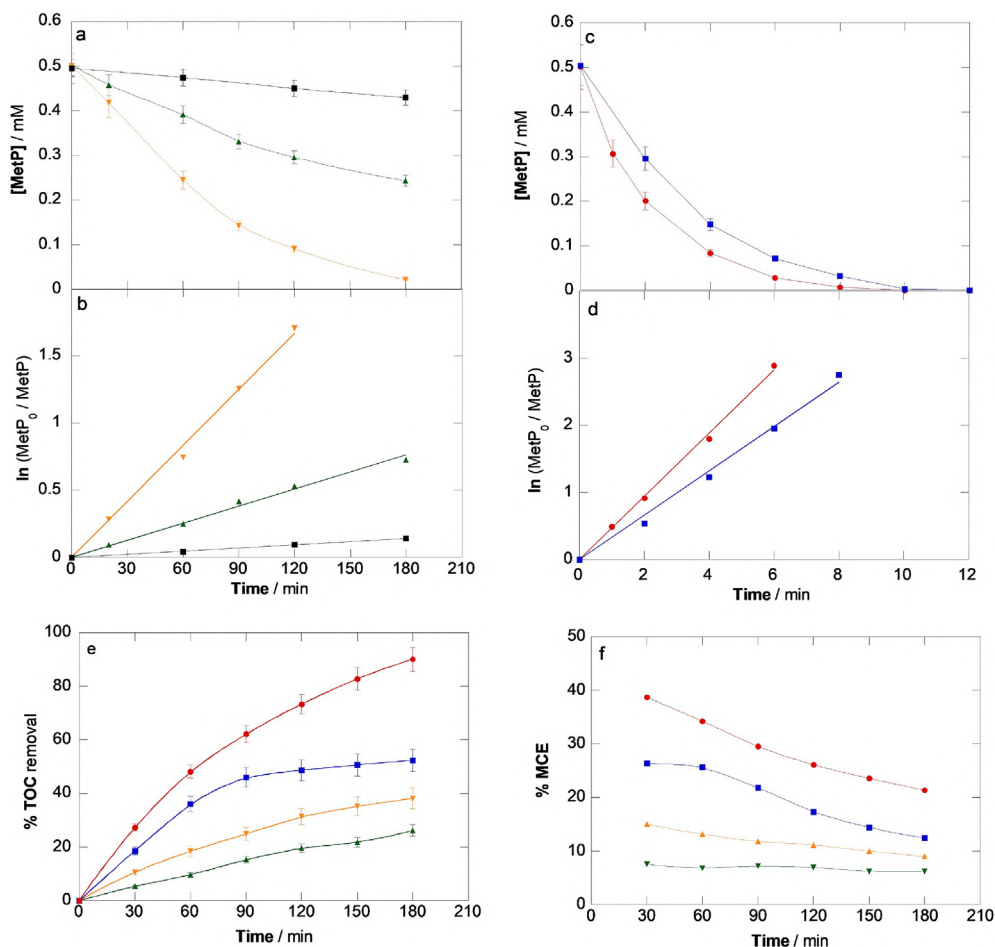


Fig. 5. Effect of different H₂O₂ based EAOPs (▲)AO-H₂O₂, (▼)AO-H₂O₂/UVC, (■) EF and (●) PEF on the treatment of 0.50 mM of MetP solutions at pH 2.5 and $j = 33.3 \text{ mA cm}^{-2}$. (a) and (b) MetP degradation over time; (c) and (d) Pseudo-first order kinetics; (e) TOC removal over time; (f) mineralization efficiency over time. (■) only UVC light.

has a 30% higher k_1 value compared to EF. From our results, the EF process seems the most economical viable process to degrade MetP in a real application.

3.4. MetP mineralization and by-products identification

As shown in Fig. 5e, the TOC removal was performed to evaluate the mineralization of 0.50 mM MetP (48 mg L⁻¹ TOC). AO-H₂O₂ and AO-H₂O₂/UVC reached poor mineralization of 26.1% and 38.4%, respectively. The rate of TOC decrease is usually lower than the degradation rate due to the formation of by-products. Therefore, a longer treatment time is necessary to achieve high mineralization. In the EF process, during the first 90 min, the mineralization had a sharp decrease attaining a value of 45.9%, remaining practically constant afterwards. This behavior may be because of the formation of Fe(III)-carboxylate complexes, formed during the degradation of MetP. These complexes are stable and highly resistant to the attack of •OH radicals (Antonin et al., 2015; Sopaj et al., 2016). For PEF, the process led to the best mineralization, with 90.1%. This can be explained by the photodecarboxylation of Fe(III)-carboxylate species (Fe(OOCR)²⁺) via Eq. (13), along with the additional Fe²⁺ regeneration and •OH production from the photolysis of FeOH²⁺ by Eq. (14) (Brillas, 2020; dos Santos et al., 2018b):

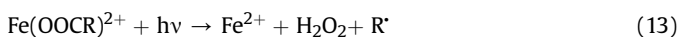


Fig. 5f reveals that the higher MCE values are related to the processes with higher oxidation capacity, following the order PEF > EF > AO-H₂O₂/UVC > AO-H₂O₂. During treatment, MCE remained constant for the AO-H₂O₂ and AO-H₂O₂/UVC processes as a consequence of their low mineralization power. However, MCE decreased for the others processes, in e.g. PEF to 38.7% and 21.5% at 30 and 180 min, respectively. This is probably due to the decrease of organic matter with formation of recalcitrant by-products, as reported by other authors (Alcaide et al., 2020; Antonin et al., 2015; dos Santos et al., 2020).

Fig. 6 shows a proposed mineralization route for MetP. Aromatic intermediates and carboxylic acids were identified by GC-MS and ion exclusion HPLC, respectively. Table S5 summarizes the characteristics of by-products such as retention time and main fragmentation (m/z). The proposed mineralization route considered only the contribution of the heterogeneous and homogeneous •OH formed on the surface of the BDD and Fenton's reactions, respectively. The degradation was initiated by the successive hydroxylation of **1** (MetP) that could yield the intermediates **2** (2,6-dihydroxy-methyl ester) and **3** (2,5-hydroxy-methylparaben). The attacks on the benzylic carbon atom of MetP bonded to the carbonyl group yielded **4** hydroquinone (Gmurek et al., 2015). The oxidation of hydroquinone causes the cleavage of the aromatic ring producing short-chain linear carboxylic acids. Intermediate **5**

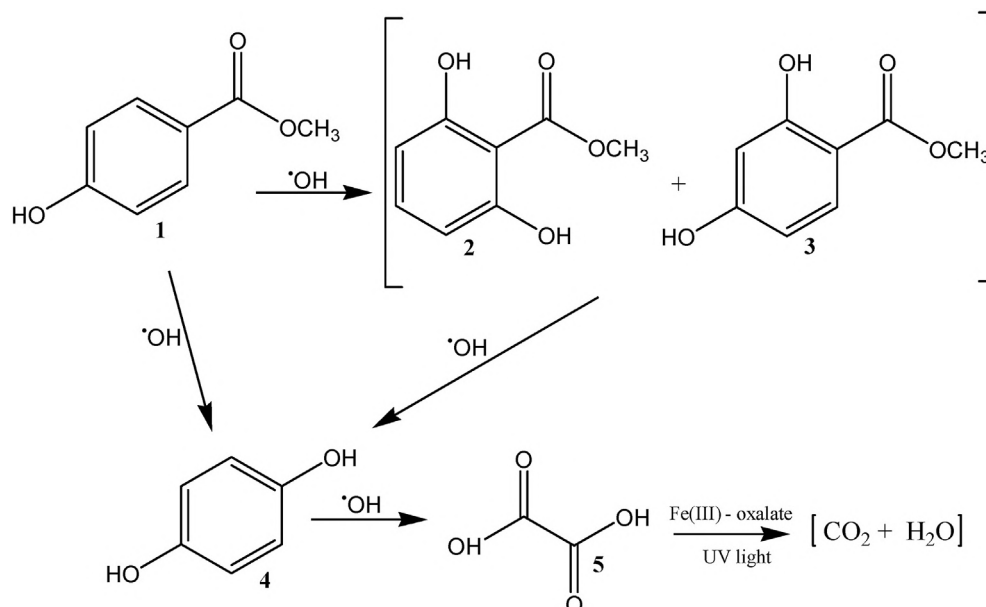


Fig. 6. Reaction sequence for MetP mineralization by the PEF process using a Pd_{1%}/PCL6/PW03 gas diffusion cathode and a BDD anode.

(oxalic acid) forms Fe(III)-oxalate complexes that can suffer photodecomposition under UVC, being then converted into CO₂ (Xu et al., 2019).

4. Conclusions

In summary, this work demonstrates that 1% of Pd NPs onto PCL6 is an active catalyst with an ~320 mV lower onset overpotential compared to bare PCL6. The selectivity towards H₂O₂ was close to 90% and its catalytic behavior was maintained after 5000 degradation cycles between -0.2 and 0.5 V_{Ag/AgCl}. Pd1%/PCL6 was obtained in a single one-pot synthesis approach with high reproducibility that can potentially be scaled up. Fundamental studies were performed in an RRDE setup and extended to a more practical relevant GDE setup where oxygen gas can be directly fed to the catalysts surface. Exemplarily, the performance towards the degradation of 0.50 mM MetP by AO-H₂O₂ and AO-H₂O₂/UVC was tested revealing lower removal efficiencies compared to EF and PEF. The $\cdot\text{OH}$ radical produced in the bulk from Fenton's reaction demonstrated to be more reactive. For the Fenton-based processes, it was verified that the concentration of Fe²⁺ greatly affects the performance of the processes. The technology that led to the highest mineralization was PEF the 90.1% operating with 21.5% of MCE. The mineralization route of MetP demonstrated the formation of three aromatic compounds and one short-chain carboxylic acid as final by-products.

Associated content

Supporting information

The supporting information contains experimental details, figures, equations, and tables concerning supplementary results, and references. This material is available free of charge via the Internet at:

CRedit authorship contribution statement

Guilherme V. Fortunato: Investigation, Methodology,

Supervision, Writing - original draft, Writing - review & editing. **Matheus S. Kronka:** Investigation, Methodology, Writing - original draft. **Alexsandro J. dos Santos:** Investigation, Methodology, Supervision, Writing - original draft, Writing - review & editing. **Marc Ledendecker:** Conceptualization, Supervision, Writing - review & editing. **Marcos R.V. Lanza:** Conceptualization, Supervision, Funding acquisition, Writing - review & editing.

Declaration of competing interest

The authors declare that they have no known competing financial interests or personal relationships that could have appeared to influence the work reported in this paper.

Acknowledgments

The authors acknowledge the financial support provided by the following Brazilian funding agencies: Brazilian National Council for Scientific and Technological Development - CNPq (grant #465571/2014-0, #302874/2017-8 and #427452/2018-0), São Paulo Research Foundation (FAPESP - grants #2014/50945-4, #2017/23464-3 #2017/10118-0, #2019/04421-7 and #2019/20634-0), and the Coordenação de Aperfeiçoamento de Pessoal de Nível Superior (CAPES - Finance Code 001). ML acknowledges the Federal Ministry of Education and Research (BMBF) in the framework of NanoMatFutur (SynKat, FK: 03XP0265) for financial support. The authors thank the Laboratory of Structural Characterization (LCE/DEMa/UFSCar) for the general facilities.

Appendix A. Supplementary data

Supplementary data to this article can be found online at <https://doi.org/10.1016/j.chemosphere.2020.127523>.

References

- Alcaide, F., Álvarez, G., Guelfi, D.R.V., Brillas, E., Sirés, I., 2020. A stable CoSP/ MWCNTs air-diffusion cathode for the photoelectro-Fenton degradation of organic pollutants at pre-pilot scale. *Chem. Eng. J.* 379, 122417.
- Antolini, E., 2012. Graphene as a new carbon support for low-temperature fuel cell

- catalysts. *Appl. Catal. B Environ.* 123–124, 52–68.
- Antonin, V.S., Garcia-Segura, S., Santos, M.C., Brillás, E., 2015. Degradation of Evans Blue diazo dye by electrochemical processes based on Fenton's reaction chemistry. *J. Electroanal. Chem.* 747, 1–11.
- Assumpção, M.H.M.T., De Souza, R.F.B., Rascio, D.C., Silva, J.C.M., Calegaro, M.L., Gaubaur, I., Paixão, T.R.L.C., Hammer, P., Lanza, M.R.V., Santos, M.C., 2011. A comparative study of the electrogeneration of hydrogen peroxide using Vulcan and Printex carbon supports. *Carbon N. Y.* 49, 2842–2851.
- Barros, W.R.P., Wei, Q., Zhang, G., Sun, S., Lanza, M.R.V., Tavares, A.C., 2015. Oxygen reduction to hydrogen peroxide on Fe₃O₄ nanoparticles supported on Printex carbon and Graphene. *Electrochim. Acta* 162, 263–270.
- Boone, C.V., Maia, G., 2019. Lowering metal loadings onto Pt–Pd–Cu/graphene nanoribbon nanocomposites affects electrode collection efficiency and oxygen reduction reaction performance. *Electrochim. Acta* 303, 192–203.
- Boone, C.V., Maia, G., 2017. Pt–Pd and Pt–Pd–(Cu or Fe or Co)/graphene nanoribbon nanocomposites as efficient catalysts toward the oxygen reduction reaction. *Electrochim. Acta* 247, 19–29.
- Brillás, E., 2020. A review on the photoelectro-Fenton process as efficient electrochemical advanced oxidation for wastewater remediation. Treatment with UV light, sunlight, and coupling with conventional and other photo-assisted advanced technologies. *Chemosphere* 250, 126198.
- Brillás, E., Martínez-Huitile, C.A., 2015. Decantation of wastewaters containing synthetic organic dyes by electrochemical methods. An updated review. *Appl. Catal. B Environ.* 166–167, 603–643.
- Campos-Martin, J.M., Blanco-Brieva, G., Fierro, J.L.G., 2006. Hydrogen peroxide synthesis: an outlook beyond the anthraquinone process. *Angew. Chem. Int. Ed.* 45, 6962–6984.
- Carneiro, J.F., Paulo, M.J., Sijaj, M., Tavares, A.C., Lanza, M.R.V., 2017. Zirconia on reduced graphene oxide sheets: synergistic catalyst with high selectivity for H₂O₂ electrogeneration. *ChemElectroChem* 4, 508–513.
- Carneiro, J.F., Silva, F.L., Martins, A.S., Dias, R.M.P., Titato, G.M., Santos-Neto, Á.J., Bertazzoli, R., Lanza, M.R.V., 2018. Simultaneous degradation of hexazinone and diuron using ZrO₂-nanostructured gas diffusion electrode. *Chem. Eng. J.* 351, 650–659.
- Choi, C.H., Kwon, H.C., Yook, S., Shin, H., Kim, H., Choi, M., 2014. Hydrogen peroxide synthesis via enhanced two-electron oxygen reduction pathway on carbon-coated Pt surface. *J. Phys. Chem. C* 118, 30063–30070.
- Cordeiro-Junior, P.J.M., Gonçalves, R., Guardado, T.T., da Silva Paiva, R., Pereira, E.C., Lanza, M.R. de V., 2020. Oxygen reduction reaction: semi-empirical quantum mechanical and electrochemical study of Printex L6 carbon black. *Carbon N. Y.* 156, 1–9.
- Daems, N., Sheng, X., Vankelecom, I.F.J., Pescarmona, P.P., 2014. Metal-free doped carbon materials as electrocatalysts for the oxygen reduction reaction. *J. Mater. Chem. A* 2, 4085–4110.
- Damjanovic, A., Genshaw, M.A., Bockris, J.O., 1967. The Role of hydrogen peroxide in oxygen reduction at platinum in H₂SO₄ solution. *J. Electrochem. Soc.* 114, 466–472.
- Dionisio, D., Santos, L.H.E., Rodrigo, M.A., Motheo, A.J., 2020. Electro-oxidation of methyl paraben on DSA®-Cl₂: UV irradiation, mechanistic aspects and energy consumption. *Electrochim. Acta* 338, 135901.
- Dirany, A., Sirés, I., Oturan, N., Özcan, A., Oturan, M.A., 2012. Electrochemical treatment of the antibiotic sulfachloropyridazine: kinetics, reaction pathways, and toxicity evolution. *Environ. Sci. Technol.* 46, 4074–4082.
- Dominguez, C.M., Oturan, N., Romero, A., Santos, A., Oturan, M.A., 2018. Removal of lindane wastes by advanced electrochemical oxidation. *Chemosphere* 202, 400–409.
- dos Santos, A.J., de Araújo Costa, E.C.T., da Silva, D.R., Garcia-Segura, S., Martínez-Huitile, C.A., 2018a. Electrochemical advanced oxidation processes as decentralized water treatment technologies to remediate domestic washing machine effluents. *Environ. Sci. Pollut. Res.* 25, 7002–7011.
- dos Santos, A.J., Garcia-Segura, S., Dosta, S., Cano, I.G., Martínez-Huitile, C.A., Brillás, E., 2019. A ceramic electrode of ZrO₂-Y₂O₃ for the generation of oxidant species in anodic oxidation. Assessment of the treatment of Acid Blue 29 dye in sulfate and chloride media. *Separ. Purif. Technol.* 228, 115747.
- dos Santos, A.J., Martínez-Huitile, C.A., Sirés, I., Brillás, E., 2018b. Use of Pt and boron-doped diamond anodes in the electrochemical advanced oxidation of Ponceau SS diazo dye in acidic sulfate medium. *ChemElectroChem* 5, 685–693.
- dos Santos, A.J., Sirés, I., Alves, A.P.M., Martínez-Huitile, C.A., Brillás, E., 2020. Vermiculite as heterogeneous catalyst in electrochemical Fenton-based processes: application to the oxidation of Ponceau SS dye. *Chemosphere* 240, 124838.
- dos Santos, A.J., Sirés, I., Alves, A.P.M., Martínez-Huitile, C.A., Brillás, E., de Lima, M.D., da Silva, D.R., Garcia-Segura, S., Martínez-Huitile, C.A., 2016. Influence of the water hardness on the performance of electro-Fenton approach: decolorization and mineralization of Eriochrome Black T. *Electrochim. Acta* 208, 156–163.
- dos Santos, A.J., Sirés, I., Martínez-Huitile, C.A., Brillás, E., 2018c. Total mineralization of mixtures of Tartrazine, Ponceau SS and Direct Blue 71 azo dyes by solar photoelectro-Fenton in pre-pilot plant. *Chemosphere* 210, 1137–1144.
- Edwards, J.K., Freakley, S.J., Lewis, R.J., Pritchard, J.C., Hutchings, G.J., 2015. Advances in the direct synthesis of hydrogen peroxide from hydrogen and oxygen. *Catal. Today* 248, 3–9.
- Fabbri, E., Taylor, S., Rabis, A., Levecque, P., Conrad, O., Kötz, R., Schmidt, T.J., 2014. The effect of platinum nanoparticle distribution on oxygen electroreduction activity and selectivity. *ChemCatChem* 6, 1410–1418. <https://doi.org/10.1002/cctc.201300987>.
- Fajardo, A.S., dos Santos, A.J., de Araújo Costa, E.C.T., da Silva, D.R., Martínez-Huitile, C.A., 2019. Effect of anodic materials on solar photoelectro-Fenton process using a diazo dye as a model contaminant. *Chemosphere* 225, 880–889.
- Fdez-Sanromán, A., Acevedo-García, V., Pazos, M., Sanromán, M.A., Rosales, E., 2020. Iron-doped cathodes for electro-Fenton implementation: application for pymetrozine degradation. *Electrochim. Acta* 338, 135768.
- Fellinger, T.P., Hasché, F., Strasser, P., Antonietti, M., 2012. Mesoporous nitrogen-doped carbon for the electrocatalytic synthesis of hydrogen peroxide. *J. Am. Chem. Soc.* 134, 4072–4075.
- Fortunato, G.V., de Lima, F., Maia, G., 2016. Oxygen-reduction reaction strongly electrocatalyzed by Pt electrodeposited onto graphene or graphene nanoribbons. *J. Power Sources* 302, 247–258.
- Fortunato, G.V., Pizzutillo, E., Mingers, A.M., Kasian, O., Cherevko, S., Cardoso, E.S.F., Mayrhofer, K.J.J., Maia, G., Ledendecker, M., 2018. Impact of palladium loading and interparticle distance on the selectivity for the oxygen reduction reaction toward hydrogen peroxide. *J. Phys. Chem. C* 122, 15878–15885.
- Ganiyu, S.O., Oturan, N., Raffy, S., Cretin, M., Esmilaire, R., van Hullebusch, E., Esposito, G., Oturan, M.A., 2016. Sub-stoichiometric titanium oxide (Ti₄O₇) as a suitable ceramic anode for electrooxidation of organic pollutants: a case study of kinetics, mineralization and toxicity assessment of amoxicillin. *Water Res.* 106, 171–182.
- Ganiyu, S.O., Vieira dos Santos, E., Tossi de Araújo Costa, E.C., Martínez-Huitile, C.A., 2018. Electrochemical advanced oxidation processes (EAOPs) as alternative treatment techniques for carwash wastewater reclamation. *Chemosphere* 211, 998–1006.
- García-Segura, S., Cavalcanti, E.B., Brillás, E., 2014. Mineralization of the antibiotic chloramphenicol by solar photoelectro-Fenton. *Appl. Catal. B Environ.* 144, 588–598. <https://doi.org/10.1016/j.apcatb.2013.07.071>.
- García-Segura, S., Nienhauser, A.B., Fajardo, A.S., Bansal, R., Coonrod, C.L., Fortner, J.D., Marcos-Hernández, M., Rogers, T., Villagran, D., Wong, M.S., Westerhoff, P., 2020. Disparities between experimental and environmental conditions: Research steps toward making electrochemical water treatment a reality. *Curr. Opin. Electrochem.* 22, 9–16.
- García-Segura, S., Ocon, J.D., Chong, M.N., 2018. Electrochemical oxidation remediation of real wastewater effluents — a review. *Process Saf. Environ. Protect.* 113, 48–67.
- Gmurek, M., Rossi, A.F., Martins, R.C., Quinta-Ferreira, R.M., Ledakowicz, S., 2015. Photodegradation of single and mixture of parabens — kinetic, by-products identification and cost-efficiency analysis. *Chem. Eng. J.* 276, 303–314.
- Han, L., Sun, Y., Li, S., Cheng, C., Halbig, C.E., Feicht, P., Hübner, J.L., Strasser, P., Eigler, S., 2019. In-plane carbon lattice-defect regulating electrochemical oxygen reduction to hydrogen peroxide production over nitrogen-doped graphene. *ACS Catal.* 9, 1283–1288.
- Inaba, M., Yamada, H., Tokunaga, J., Tasaka, A., 2004. Effect of agglomeration of Pt/C catalyst on hydrogen peroxide formation. *Electrochem. Solid State Lett.* 7, A474.
- Jiang, H., Gu, J., Zheng, X., Liu, M., Qiu, X., Wang, L., Li, W., Chen, Z., Ji, X., Li, J., 2019. Defect-rich and ultrathin N doped carbon nanosheets as advanced trifunctional metal-free electrocatalysts for the ORR, OER and HER. *Energy Environ. Sci.* 12, 322–333.
- Jiang, Y., Ni, P., Chen, C., Lu, Y., Yang, P., Kong, B., Fisher, A., Wang, X., 2018. Selective electrochemical H₂O₂ production through two-electron oxygen electrochemistry. *Adv. Energy Mater.* 8, 1801909.
- Jukk, K., Alexeyeva, N., Sarapuu, A., Ritslaid, P., Kozlova, J., Sammelsep, V., Tammeveski, K., 2013. Electroreduction of oxygen on sputter-deposited Pd nanolayers on multi-walled carbon nanotubes. *Int. J. Hydrogen Energy* 38, 3614–3620.
- Kabir, S., Serov, A., Zadick, A., Artyushkova, K., Atanassov, P., 2016. Palladium nanoparticles supported on three-dimensional graphene nanosheets: superior cathode electrocatalysts. *ChemElectroChem* 3, 1655–1666.
- Kim, H.W., Park, H., Roh, J.S., Shin, J.E., Lee, T.H., Zhang, L., Cho, Y.H., Yoon, H.W., Bukas, V.J., Guo, J., Park, H.B., Han, T.H., McCloskey, B.D., 2019. Carbon defect characterization of nitrogen-doped reduced graphene oxide electrocatalysts for the two-electron oxygen reduction reaction. *Chem. Mater.* 31, 3967–3973.
- Lima, V.B., Goulart, L.A., Rocha, R.S., Steter, J.R., Lanza, M.R.V., 2020. Degradation of antibiotic ciprofloxacin by different AOP systems using electrochemically generated hydrogen peroxide. *Chemosphere* 247, 125807.
- Lobyntseva, E., Kallio, T., Alexeyeva, N., Tammeveski, K., Kontturi, K., 2007. Electrochemical synthesis of hydrogen peroxide: rotating disk electrode and fuel cell studies. *Electrochim. Acta* 52, 7262–7269.
- Lu, Y., Sehrish, A., Manzoor, R., Dong, K., Jiang, Y., 2019. Recent progress on electrochemical production of hydrogen peroxide. *Chem. Rep.* 1, 81–101.
- Luo, Y., Alonso-Vante, N., 2015. The effect of support on advanced Pt-based cathodes towards the oxygen reduction reaction. *State Art. Electrochim. Acta* 179, 108–118.
- Ma, J., Habrioux, A., Morais, C., Lewera, A., Vogel, W., Verde-Gómez, Y., Ramos-Sanchez, G., Balbuena, P.B., Alonso-Vante, N., 2013. Spectroelectrochemical probing of the strong interaction between platinum nanoparticles and graphitic domains of carbon. *ACS Catal.* 3, 1940–1950.
- Marković, N.M., Gasteiger, H.A., Grgur, B.N., Ross, P.N., 1999. Oxygen reduction reaction on Pt(111): effects of bromide. *J. Electroanal. Chem.* 467, 157–163.
- Melchionna, M., Fornasiero, P., Prato, M., 2019. The rise of hydrogen peroxide as the main product by metal-free catalysis in oxygen reductions. *Adv. Mater.* 31, 1802920.
- Mittermeier, T., Weiß, A., Gasteiger, H.A., Hasché, F., 2017. Monometallic palladium for oxygen reduction in PEM fuel cells: particle-size effect, reaction mechanism,

- and voltage cycling stability. *J. Electrochem. Soc.* 164, F1081–F1089.
- Montenegro-Ayo, R., Morales-Gomero, J.C., Alarcon, H., Cotillas, S., Westerhoff, P., Garcia-Segura, S., 2019. Scaling up photoelectrocatalytic reactors: a TiO₂ nanotube-coated disc compound reactor effectively degrades acetaminophen. *Water* 11, 2522.
- Moreira, F.C., Boaventura, R.A.R., Brillas, E., Vilar, V.J.P., 2017. Electrochemical advanced oxidation processes: a review on their application to synthetic and real wastewaters. *Appl. Catal. B Environ.* 202, 217–261.
- Nakamura, K.C., Guimaraes, L.S., Magdalena, A.G., Angelo, A.C.D., De Andrade, A.R., Garcia-Segura, S., Pipi, A.R.F., 2019. Electrochemically-driven mineralization of Reactive Blue 4 cotton dye: on the role of in situ generated oxidants. *J. Electroanal. Chem.* 840, 415–422.
- Nesselberger, M., Roefzaad, M., Fayçal Hamou, R., Ulrich Biedermann, P., Schweinberger, F.F., Kunz, S., Schloegl, K., Wiberg, G.K.H.H., Ashton, S., Heiz, U., Mayrhofer, K.J.J., Arenz, M., 2013. The effect of particle proximity on the oxygen reduction rate of size-selected platinum clusters. *Nat. Mater.* 12, 919–924.
- Paz, E.C., Aveiro, L.R., Pinheiro, V.S., Souza, F.M., Lima, V.B., Silva, F.L., Hammer, P., Lanza, M.R.V., Santos, M.C., 2018. Evaluation of H₂O₂ electrogeneration and decolorization of Orange II azo dye using tungsten oxide nanoparticle-modified carbon. *Appl. Catal. B Environ.* 232, 436–445.
- Pérez, T., Garcia-Segura, S., El-Ghenymy, A., Nava, J.L., Brillas, E., 2015. Solar photoelectro-Fenton degradation of the antibiotic metronidazole using a flow plant with a Pt/air-diffusion cell and a CPC photoreactor. *Electrochim. Acta* 165, 173–181.
- Pesterfield, L., 2009. The 100 most important chemical compounds: a reference guide (by Richard L. Myers). *J. Chem. Educ.* 86, 1182.
- Ren, G., Zhou, M., Zhang, Q., Xu, X., Li, Y., Su, P., 2020. A novel stacked flow-through electro-Fenton reactor as decentralized system for the simultaneous removal of pollutants (COD, NH₃-N and TP) and disinfection from domestic sewage containing chloride ions. *Chem. Eng. J.* 387, 124037.
- Rosa Barbosa, M.P., Lima, N.S., de Matos, D.B., Alves Felisardo, R.J., Santos, G.N., Salazar-Banda, G.R., Cavalcanti, E.B., 2018. Degradation of pesticide mixture by electro-Fenton in filter-press reactor. *J. Water Process Eng.* 25, 222–235.
- Saha, J., Dandapat, A., De, G., 2011. Transformation of Pd → PdH_{0.7} nanoparticles inside mesoporous Zr-modified SiO₂ films in ambient conditions. *J. Mater. Chem.* 21, 11482.
- Schmidt, T.J., Paulus, U.A., Gasteiger, H.A., Behm, R.J., 2001. The oxygen reduction reaction on a Pt/carbon fuel cell catalyst in the presence of chloride anions. *J. Electroanal. Chem.* 508, 41–47.
- Schneider, A., Colmenares, L., Seidel, Y.E., Jusys, Z., Wickman, B., Kasemo, B., Behm, R.J., 2008. Transport effects in the oxygen reduction reaction on nanostructured, planar glassy carbon supported Pt/GC model electrodes. *Phys. Chem. Chem. Phys.* 10, 1931.
- Scofield, J.H., 1976. Hartree-Slater subshell photoionization cross-sections at 1254 and 1487 eV. *J. Electron. Spectrosc. Relat. Phenom.* 8, 129–137.
- Siahrostami, S., Verdaguer-Casadevall, A., Karamad, M., Deiana, D., Malacrida, P., Wickman, B., Escudero-Escribano, M., Paoli, E.A., Frydendal, R., Hansen, T.W., Chorkendorff, I., Stephens, I.E.L., Rossmeisl, J., 2013. Enabling direct H₂O₂ production through rational electrocatalyst design. *Nat. Mater.* 12, 1137–1143.
- Sopaj, F., Oturan, N., Pinson, J., Podvorica, F., Oturan, M.A., 2016. Effect of the anode materials on the efficiency of the electro-Fenton process for the mineralization of the antibiotic sulfamethazine. *Appl. Catal. B Environ.* 199, 331–341.
- Steter, J.R., Brillas, E., Sirés, I., 2016. On the selection of the anode material for the electrochemical removal of methylparaben from different aqueous media. *Electrochim. Acta* 222, 1464–1474.
- Su, J., Ge, R., Dong, Y., Hao, F., Chen, L., 2018. Recent progress in single-atom electrocatalysts: concept, synthesis, and applications in clean energy conversion. *J. Mater. Chem. A* 6, 14025–14042.
- Taylor, S., Fabbri, E., Levecque, P., Schmidt, T.J., Conrad, O., 2016. The effect of platinum loading and surface morphology on oxygen reduction activity. *Electrocatalysis* 7, 287–296.
- Venarusso, L.B., Bettini, J., Maia, G., 2016. Catalysts for oxygen reduction reaction based on nanocrystals of a Pt or Pt–Pd alloy shell supported on a Au core. *J. Solid State Electrochem.* 20, 1753–1764.
- Venarusso, L.B., Boone, C.V., Bettini, J., Maia, G., 2018. Carbon-supported metal nanodendrites as efficient, stable catalysts for the oxygen reduction reaction. *J. Mater. Chem. A* 6, 1714–1726.
- Verdaguer-casadevall, A., Deiana, D., Karamad, M., Siahrostami, S., Malacrida, P., Hansen, T.W., Rossmeisl, J., Chorkendorff, I., Stephens, I.E.L., Chorkendor, I., Stephens, I.E.L., 2014. Trends in the electrochemical synthesis of H₂O₂: enhancing activity and selectivity by electrocatalytic site engineering. *Nano Lett.* 14, 1603–1608.
- Vukmirovic, M.B., Bliznakov, S.T., Sasaki, K., Wang, J.X., Adzic, R.R., 2011. Electrodeposition of metals in catalyst synthesis: the case of platinum monolayer electrocatalysts. *Interface Mag.* 20, 33–40.
- Wu, K.-H., Wang, D.-W., Zong, X., Zhang, B., Liu, Y., Gentle, I.R., Su, D.-S., 2017. Functions in cooperation for enhanced oxygen reduction reaction: the independent roles of oxygen and nitrogen sites in metal-free nanocarbon and their functional synergy. *J. Mater. Chem. A* 5, 3239–3248.
- Xu, A., Brillas, E., Han, W., Wang, L., Sirés, I., 2019. On the positive effect of UVC light during the removal of benzothiazoles by photoelectro-Fenton with UVA light. *Appl. Catal. B Environ.* 259, 118127.
- Yan, W.M., Chu, H., Se Liu, Y.L., Chen, F., Jang, J.H., 2011. Effects of chlorides on the performance of proton exchange membrane fuel cells. *Int. J. Hydrogen Energy* 36, 5435–5441.
- Zhang, H., Lv, K., Fang, B., Forster, M.C., Dervişoğlu, R., Andreas, L.B., Zhang, K., Chen, S., 2018. Crucial role for oxygen functional groups in the oxygen reduction reaction electrocatalytic activity of nitrogen-doped carbons. *Electrochim. Acta* 292, 942–950.
- Zhang, Yinqiao, Zuo, S., Zhang, Ying, Ren, G., Pan, Y., Zhang, Q., Zhou, M., 2019. Simultaneous removal of tetracycline and disinfection by a flow-through electro-peroxone process for reclamation from municipal secondary effluent. *J. Hazard Mater.* 368, 771–777.

Support information for:

Low Pd loadings onto Printex L6: synthesis, characterization and performance towards H₂O₂ generation for electrochemical water treatment technologies

Guilherme V. Fortunato^{a, 1, *}, Matheus S. Kronka^{a, 1}, Alexandro J. dos Santos^{a, 1, *},

Marc Ledendecker^b, and Marcos R.V. Lanza^{a, *}

^a Institute of Chemistry of São Carlos, University of São Paulo, Avenida Trabalhador

São-Carlense 400, São Carlos, SP 13566-590, Brazil

^b Department of Technical Chemistry, Technical University Darmstadt, Alarich-Weiss-

Straße 8, 64287 Darmstadt, Germany

¹ These authors contributed equally to this work.

*Corresponding author's e-mails:

g.fortunato@usp.br (G.V. Fortunato)

alexsandrojhones@usp.br (A.J. dos Santos)

marcoslanza@usp.br (M.R.V. Lanza)

Rotating ring-disk electrode studies

For the rotating ring-disk electrode (RRDE) experiments, the supporting electrolyte employed was $0.1 \text{ mol L}^{-1} \text{ K}_2\text{SO}_4$, at pH of 2.5, adjusted with H_2SO_4 . All electrochemical measurements were performed in a three-electrode glass cell with a commercial rotating ring-disk electrode (RRDE) with GC disk (geometric area of 0.2475 cm^2) and Pt ring (geometric area of 0.186 cm^2 , and collection efficiency of $N = 0.37$) - acquired from Pine Research Instrumentation. A graphite rod and an Ag/AgCl electrode (3 M KCl, from Analyser Co.), separated by a Nafion membrane, were used as counter electrode and reference electrode, respectively. Prior to perform each measurement, the RRDE working electrode was polished with alumina slurries with granulometry of 0.3 and $0.05 \text{ }\mu\text{m}$. The electrode was cleaned by sonication in ultrapure water from a Millipore Milli-Q system with resistivity $>18 \text{ M}\Omega \text{ cm}$ at $25 \text{ }^\circ\text{C}$, twice in isopropanol, and in ultrapure water again for 5 min in each solvent. Using a clean and dry disk electrode surface, a uniform thin film of $200 \text{ }\mu\text{g}_{\text{Pd/C}} \text{ cm}^{-2}$ was subsequently generated by drop casting of $20 \text{ }\mu\text{L}$ of catalyst solution at 2.5 mg mL^{-1} prepared using dimethylformamide as solvent, and allowing the film to dry at room temperature.

The modified electrodes were placed in an electrochemical cell containing the supporting electrolyte, which was subsequently saturated with the following ultrapure gases: N_2 or O_2 (purity >4.0). The electrochemical techniques employed, which included cyclic voltammetry (CV) and linear sweep voltammetry (LSV), were conducted using a Metrohm Autolab model PGSTAT-128 N potentiostat. To study the oxygen-reduction reaction, the Pt ring potential was kept under potentiostatic control at $1.0 \text{ V}_{\text{Ag/AgCl}}$ in O_2 -saturated electrolyte solution, while the potentials at the modified GC disks were scanned in the same solution at 5 mV s^{-1} . For the rotating ring-disk electrode (RRDE) measurements, the experimental details are described in Support Information. The ORR curves were obtained by subtracting N_2 -background currents (in absence of O_2) to eliminate current contributions from the electrodes in contact with the electrolyte. The selectivity toward H_2O_2 production ($S_{\text{H}_2\text{O}_2}$) during the ORR was estimated from RRDE results and Eq. (S1) (Antoine and Durand, 2000; Paulus et al., 2001):

$$S_{\text{H}_2\text{O}_2} (\%) = \frac{2I_r/N}{I_d + I_r/N} \times 100 \quad (\text{S1})$$

Where I_d is the disk current, I_r is the ring currents, and N is the collection efficiency of the Pt ring electrode.

Table S1. Compositional and morphologic characteristics of Pd_{1%}/PCL6 catalyst obtained from TGA, XPS, and TEM.

Catalyst loading ($\mu\text{g cm}^{-2}$)	200
Pd loading ($\mu\text{g cm}^{-2}$)	1.8
wt. % Pd by TGA	0.9
wt. % Pd by XPS	0.87
at. % Pd by XPS	0.1
particle size by TEM (nm)	5.5 ± 1.4
<i>ipd</i>^a(nm)	170

^a interparticle distance from edge-to-edge was determined as in Ref (Fortunato et al., 2018).

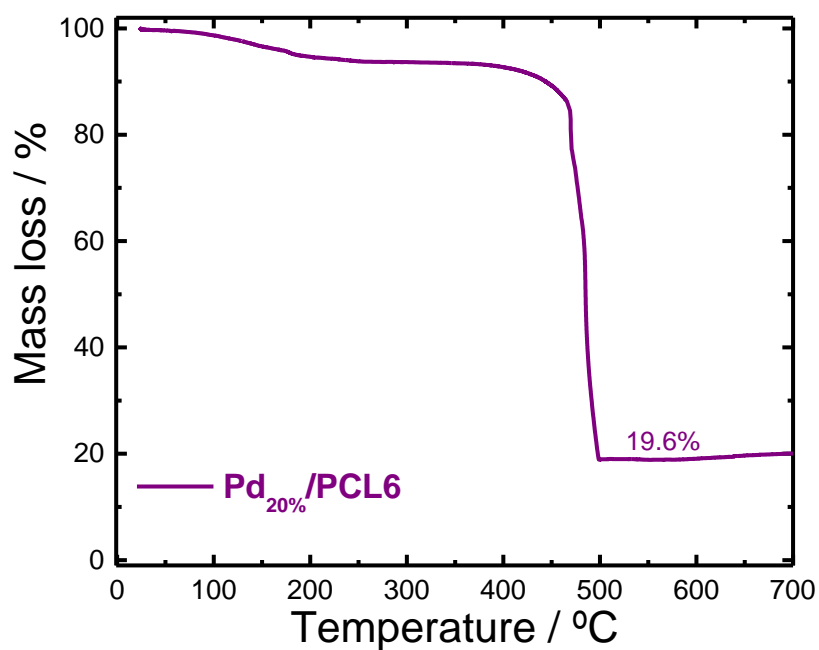
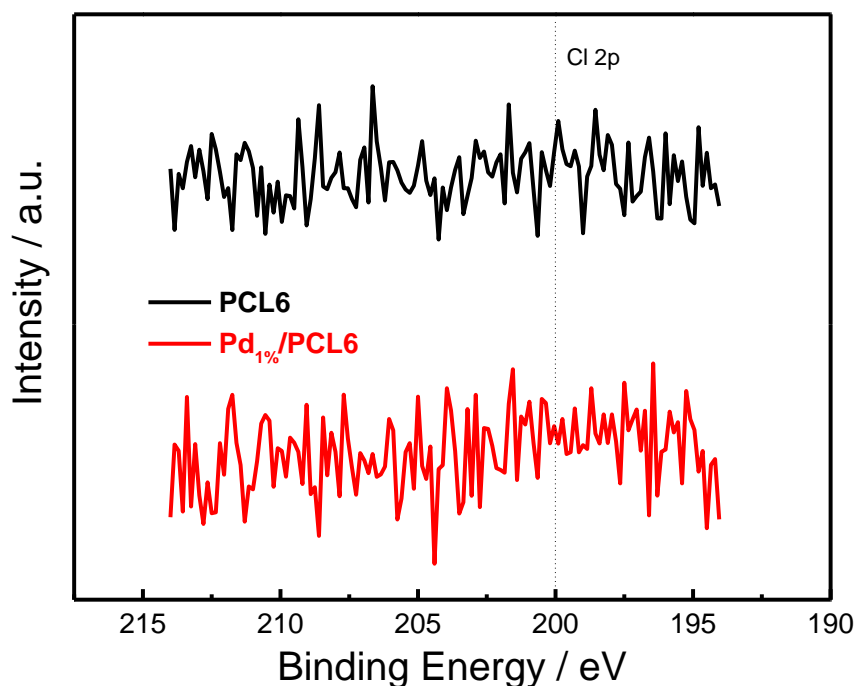
**Fig. S1.** Thermogravimetric response for Pd_{20%}/PCL6 catalyst.

Table S2. Surface composition of Pd_{1%}/PCL6 catalyst determined by XPS narrow-scans. Peaks, positions, relative sensitivity factors (R.S.F.), and atomic and weight percentages of the elements.

Peak	Position (eV)	R.S.F.	at%	wt%
C 1s	284.60	1	90.83	87.50
O 1s	532.95	2.93	9.06	11.63
Pd 3d	341.00	16	0.10	0.87
Cl 2p	198.25	2.29	-	-
N 1s	399.75	1.8	-	-

Table S3. Deconvolution results in the Pd 3d region for Pd_{1%}/PCL6 catalyst. Values obtained from the narrow-scan XPS spectrum in inset of Figures 1F.

Peak	Group	Position (eV)	Content %
Pd 3d	Pd ⁰ 3d _{5/2}	335.43	27.48
	Pd ²⁺ 3d _{5/2}	337.58	32.55
	Pd ⁰ 3d _{3/2}	341.03	18.30
	Pd ²⁺ 3d _{3/2}	343.00	21.68

**Fig. S2.** Narrow-scan XPS spectra in Cl 2p region for PCL6 and Pd_{1%}/PCL6 catalysts.

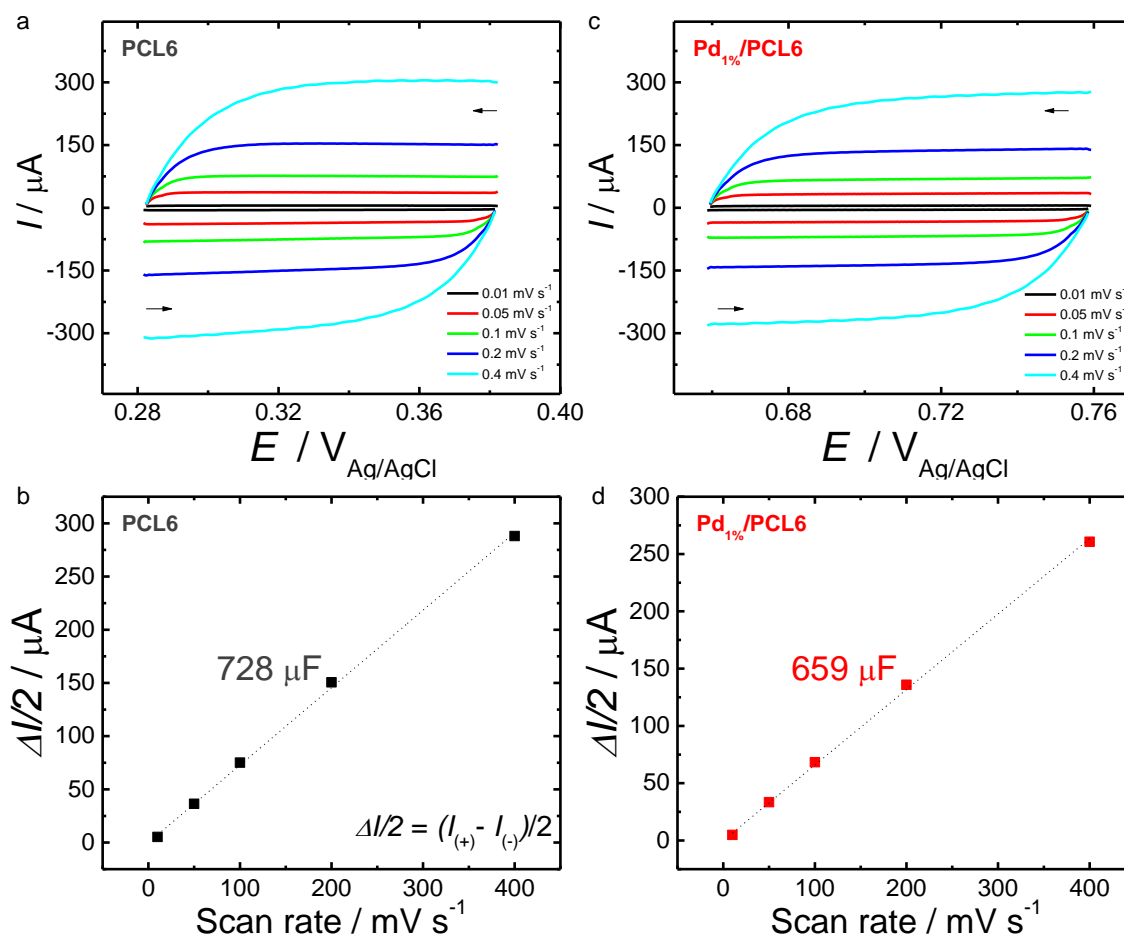


Fig. S3. Cyclic voltammograms for (a) PCL6 and (c) Pd_{1%}/PCL6 obtained in N₂-sat 0.1 mol L⁻¹ K₂SO₄ at pH 2.5 at scan rates from 10 to 400 mV s⁻¹ in a range of 0.1 V potential window centered at the OCP. (b and d) $\Delta I/2$ vs. ν plots for modified GC electrodes.

The electrochemically active surface area values for the PCL6 (A) and Pd₁%/PCL6 % (C) samples were calculated from the electrochemical double-layer capacitance (C_{dl}), in turn, obtained by the scan rate dependence of cyclic voltammograms, following the protocol reported in Ref.(McCrorry et al., 2013). Briefly, C_{dl} was obtained by collecting CVs at the scan rates of 10, 50, 100, 200, and 400 mV s⁻¹ in a range of 0.1 V potential window centered at the open circuit potential (Figure S3).

Table S4. Estimated *ECSA* values by the capacitance for catalyst samples.

Catalyst	Capacitance (μF)	Specific Capac. (μF cm ⁻²)*	<i>ECSA</i> (cm ²)	<i>ECSA</i> (m ² g ⁻¹ _{catalyst})
PCL6	728	17.0	42.8	86.5
Pd ₁ %/PCL6	659	17.0	38.8	78.4

* The values were assumed considering the capacitance of an atomically smooth planar surface of the carbon-based material under acidic conditions.(McCrorry et al., 2013)

The RDE data shown in Figures 2E and 2F were analysed by the Koutecky-Levich (K-L) Eq. (S2)(Bard and Faulkner, 2001) and the number of electrons transferred per O₂ molecule, n , could be estimated:

$$\frac{1}{j} = \frac{1}{j_k} + \frac{1}{j_d} = -\frac{1}{nFkC_{O_2}^b} - \frac{1}{0.62nFD_{O_2}^{2/3}v^{-1/6}C_{O_2}^b\omega^{1/2}} \quad (S2)$$

Where j , j_k and j_d are the measured current density, kinetic current density and diffusion-limited current density, respectively, k is the rate constant for ORR (given in cm s⁻¹), F is the Faraday constant, D_{O_2} is the diffusion coefficient of O₂ (assumed as 1.9×10⁻⁵ cm² s⁻¹) (Davis et al., 1967), ν is the kinematic viscosity of the solution (assumed as 0.01 cm² s⁻¹) (Lide, 2001), $C_{O_2}^b$ is the concentration of oxygen in the bulk solution (assumed as 1.2×10⁻⁶ mol cm⁻³) (Davis et al., 1967) and, finally, ω is the electrode rotation speed (given in rad s⁻¹).

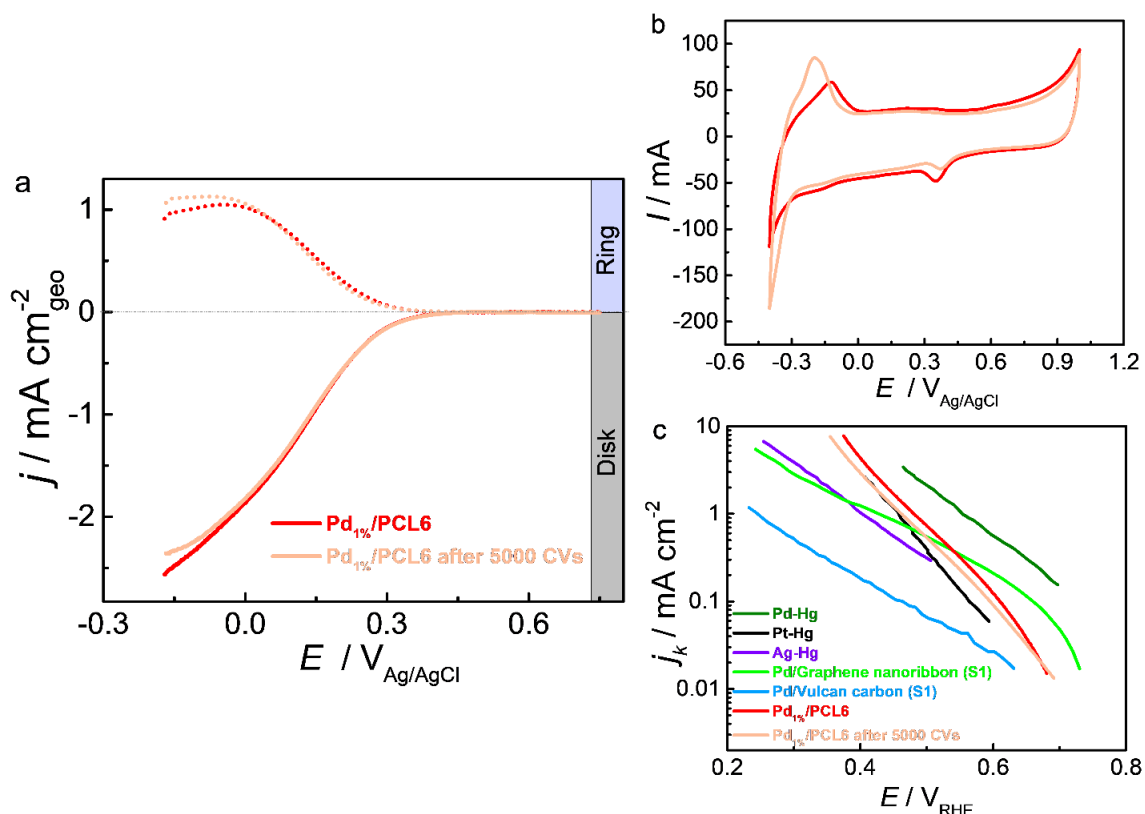
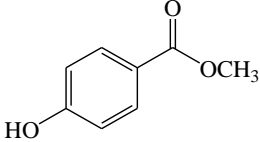
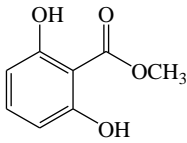
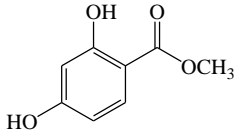
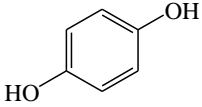


Fig. S4. (a) Linear sweep RRDE results scanning the potential at 5 mV s^{-1} and 900 rpm in O_2 -sat $0.1 \text{ mol L}^{-1} \text{ K}_2\text{SO}_4$ at $\text{pH } 2.5$ for GC electrodes modified with PCL6 and $\text{Pd}_{1\%}/\text{PCL6}$ catalysts before and after the stability test (scans started at $-0.2 \text{ V}_{\text{Ag}/\text{AgCl}}$). (b) Cyclic voltammograms before and after the stability test obtained in N_2 -sat $0.1 \text{ mol L}^{-1} \text{ K}_2\text{SO}_4$ at $\text{pH } 2.5$ for GC electrodes modified with PCL6 and $\text{Pd}_{1\%}/\text{PCL6}$ catalysts at a scan rate of 50 mV s^{-1} ; scans started at $1 \text{ V}_{\text{Ag}/\text{AgCl}}$. (c) Electrocatalytic performance comparison (in terms of kinetic current densities to H_2O_2 production as a function of the applied potential) of different metallic nanoparticles-based synthesized catalysts: Pd-Hg (Verdaguer-casadevall et al., 2014), Pt-Hg (Siahrostami et al., 2013), Ag-Hg (Siahrostami et al., 2013), hydrothermally produced Pd/Graphene nanoribbon (S1) (Fortunato et al., 2018), hydrothermally produced Pd/Vulcan carbon (S1) (Fortunato et al., 2018), $\text{Pd}_{1\%}/\text{PCL6}$ before and after the stability test [this study].

Table S5. Aromatic intermediates detected by GC-MS during the degradation of 0.50 mM MetP solution by PEF process.

Number	Chemical name	Molecular structure	t_r (min)	Fragmentation (m/z)
1	Methyl Paraben		24.5	152, 121, 93, 65
2	2,6-dihydroxy-methyl ester		26.8	168, 137, 108, 81, 69, 53
3	2, 5 -hydroxy-methylparaben		26,2	168, 136, 108, 80, 69, 55
4	Hydroquinone		20.3	110, 81, 59, 53

References

- Antoine, O., Durand, R., 2000. RRDE study of oxygen reduction on Pt nanoparticles inside Nafion®: H₂O₂ production in PEMFC cathode conditions. *J. Appl. Electrochem.* 30, 839–844.
- Bard, A.J., Faulkner, L.R., 2001. *Electrochemical methods: fundamentals and applications*, 2nd ed. John Wiley & Sons, New York.
- Davis, R.E., Horvath, G.L., Tobias, C.W., 1967. The solubility and diffusion coefficient of oxygen in potassium hydroxide solutions. *Electrochim. Acta* 12, 287–297.
- Fortunato, G. V., Pizzutilo, E., Mingers, A.M., Kasian, O., Cherevko, S., Cardoso, E.S.F., Mayrhofer, K.J.J., Maia, G., Ledendecker, M., 2018. Impact of palladium loading and interparticle distance on the selectivity for the oxygen reduction reaction toward hydrogen peroxide. *J. Phys. Chem. C* 122, 15878–15885.
- Lide, D.R., 2001. *CRC Handbook of Chemistry and Physics*, 84th Edition, 2003-2004, Handbook of Chemistry and Physics. CRC Press, Boca Raton.
- McCrorry, C.C.L., Jung, S., Peters, J.C., Jaramillo, T.F., 2013. Benchmarking heterogeneous electrocatalysts for the oxygen evolution reaction. *J. Am. Chem. Soc.* 135, 16977–16987.
- Paulus, U.A., Schmidt, T.J., Gasteiger, H.A., Behm, R.J., 2001. Oxygen reduction on a high-surface area Pt/Vulcan carbon catalyst: a thin-film rotating ring-disk electrode study. *J. Electroanal. Chem.* 495, 134–145.
- Siahrostami, S., Verdaguer-Casadevall, A., Karamad, M., Deiana, D., Malacrida, P., Wickman, B., Escudero-Escribano, M., Paoli, E.A., Frydendal, R., Hansen, T.W., Chorkendorff, I., Stephens, I.E.L., Rossmeisl, J., 2013. Enabling direct H₂O₂ production through rational electrocatalyst design. *Nat. Mater.* 12, 1137–1143.
- Verdaguer-casadevall, A., Deiana, D., Karamad, M., Siahrostami, S., Malacrida, P., Hansen, T.W., Rossmeisl, J., Chorkendorff, I., Stephens, I.E.L., Chorkendor, I., Stephens, I.E.L., 2014. Trends in the electrochemical synthesis of H₂O₂: Enhancing activity and selectivity by electrocatalytic site engineering. *Nano Lett.* 14, 1603–1608.

CHAPTER II

Sustainable microwave-assisted hydrothermal synthesis of carbon-supported ZrO₂ nanoparticles for H₂O₂ electrogeneration.

Author Contributions: Matheus S. Kronka: Investigation, Methodology, Validation, Writing – original draft, Writing – review & editing; Paulo J.M. Cordeiro-Junior: Investigation, Methodology, Validation, Writing – original draft; Letícia Mira: Investigation, Formal analysis, Writing – original draft; Alexsandro J. dos Santos: Conceptualization, Writing – review & editing, Writing – original draft; Guilherme V. Fortunato: Validation, Conceptualization, Visualization, Writing – original draft, Writing – review & editing; Marcos R.V. Lanza: Supervision, Funding acquisition, Writing – review & editing, Writing – original draft.

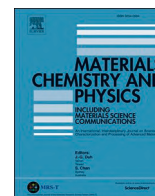
In this article, a detailed discussion on the development of microwave-assisted hydrothermal (MAH) synthesis to incorporate zirconium oxide (ZrO₂) into the PL6C matrix composition has been carried out. Each parameter of the synthesis was evaluated facing the growth of ZrO₂ in the carbonaceous structure and its influence on electrocatalytic activity and stability for ORR aiming to selectively produce H₂O₂. Therefore, it could be understood how to use MAH synthesis to produce stable and H₂O₂-selective electrochemical catalysts, although identifying some limitations. Here the authors finally reflect on the employment of a sustainable synthesis for the development of a mixed ZrO₂/PL6C catalyst that offers future possibilities in the area of cathodic catalysts for electrochemical H₂O₂ production.

This article/chapter was published in *Materials Chemistry and Physics*, v. 267, **M.S. Kronka**, P.J.M. Cordeiro-Junior, L. Mira, A.J. dos Santos, G.V. Fortunato, M.R.V. Lanza, Sustainable microwave-assisted hydrothermal synthesis of carbon-supported ZrO₂ nanoparticles for H₂O₂ electrogeneration, 124575, Copyright Elsevier (2021).



Contents lists available at ScienceDirect

Materials Chemistry and Physics

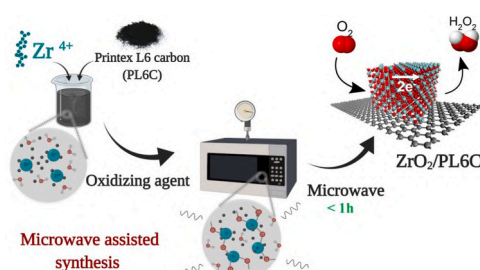
journal homepage: www.elsevier.com/locate/matchemphysSustainable microwave-assisted hydrothermal synthesis of carbon-supported ZrO₂ nanoparticles for H₂O₂ electrogenerationMatheus S. Kronka^{**}, Paulo J.M. Cordeiro-Junior, Letícia Mira, Alexsandro J. dos Santos, Guilherme V. Fortunato^{*}, Marcos R.V. Lanza^{***}

São Carlos Institute of Chemistry, University of São Paulo, Avenida Trabalhador São-Carlense 400, São Carlos, SP, 13566-590, Brazil

HIGHLIGHTS

- Carbon-based metal oxide catalyst was produced by sustainable MAH approach.
- ZrO₂-5.1 wt% on PL6C presented a gain of 140 mV in E_{1/2} and S_{H₂O₂} of 88.8%.
- Particles dispersion, ECSA, and oxide loading are key elements to consider in ORR.
- ZrO₂/PL6C presented k_{app} values for H₂O₂ production ~2x higher than bare PL6C.

GRAPHICAL ABSTRACT



ARTICLE INFO

Keywords:

Oxygen reduction reaction
 Hydrogen peroxide
 Gas diffusion electrode
 Zirconium oxide nanoparticle
 Carbon black
 Microwave-assisted hydrothermal synthesis

ABSTRACT

This work proposes the use of a novel green and fast (<math>< 1\text{h}</math>) route for the construction of electrocatalysts by microwave-assisted hydrothermal synthesis using carbon-supported metal oxide for H₂O₂ electrogeneration. Using ZrO₂ supported on carbon black Printex L6 (PL6C) as a non-toxic model catalyst, the present study evaluated different synthesis conditions and their effects on ORR activity and selectivity via the application of the rotating ring-disk electrode (RRDE) and gas diffusion electrode (GDE) techniques. RRDE results showed that the optimized ZrO₂/PL6C catalyst presented improvements in catalytic performance of 140 mV in the E_{1/2} for ORR and in selectivity for H₂O₂ production of 88.8% compared to the unmodified PL6C (78%). The improved electrocatalytic performance was attributed to the high dispersion of small ZrO₂ nanoparticles (~7 nm) in direct contact with the carbon support which helped increase the ECSA values. GDE results showed that ZrO₂/PL6C was responsible for doubling the k_{app} values of H₂O₂ production and for the reduction of energy consumption by about 150 kWh g⁻¹ compared to the unmodified matrix. Key insights related to the construction of carbon-based metal oxide catalysts and the optimization of ORR are discussed further in the work aiming at providing useful contributions for future investigations and applications.

* Corresponding author.

** Corresponding author.

*** Corresponding author.

E-mail addresses: miskonka@usp.br (M.S. Kronka), g.fortunato@usp.br (G.V. Fortunato), marcoslanza@usp.br (M.R.V. Lanza).<https://doi.org/10.1016/j.matchemphys.2021.124575>

Received 22 February 2021; Received in revised form 29 March 2021; Accepted 31 March 2021

Available online 11 April 2021

0254-0584/© 2021 Elsevier B.V. All rights reserved.

1. Introduction

Hydrogen peroxide (H_2O_2) is a versatile oxidizer which is widely employed for industrial, commercial, and domestic purposes [1,2]. Considered a green oxidizer, H_2O_2 has also been intensively applied in the environmental area [3–5]. Commercial H_2O_2 is mostly produced by the conventional method based on the oxidation of anthraquinone; this mechanism has been subject to criticism due to the environmental, logistic, and safety problems involved in this conventional process of H_2O_2 production [3,7,8]. For small scale and on-site applications, such as in the case of water treatment which typically requires low concentrations (<0.1 wt%), the use of decentralized or *in situ* methods of H_2O_2 production has been found to help effectively overcome the risks involving the transport, storage, and dilution of H_2O_2 presented by the conventional method [3]. The electrosynthesis of H_2O_2 via oxygen reduction reaction (ORR) has drawn considerable attention as a decentralized and environmentally friendly mechanism for H_2O_2 production [4]. However, due to the slow kinetics of ORR and the possibility of leading to the production of H_2O instead of H_2O_2 , the successful implementation of H_2O_2 electrosynthesis still depends on the development of economically viable materials that are able to catalyze ORR in an efficiently selective manner [4,9–11].

Platinum (Pt) and Palladium (Pd) are regarded the most active materials for ORR; however, due to their strong interaction with oxygen and oxygenated intermediates, these materials tend to break the O=O bonding mechanism, and this gives rise to the production of H_2O as the main product of reaction in a 4-electron pathway ($\text{O}_2 + 4\text{H}^+ + 4\text{e}^- \rightarrow 2\text{H}_2\text{O}$) [12,13]. In contrast, Au, Ag, Hg or C-based materials are found to be less active and tend to reduce O_2 to H_2O_2 via a 2-electron reaction pathway ($\text{O}_2 + 2\text{H}^+ + 2\text{e}^- \rightarrow \text{H}_2\text{O}_2$) as a result of their weaker interaction with oxygen [3,13–15]. Different synthesis strategies have been investigated with a view to blending the high activity of Pt and Pd with the high selectivity demonstrated by Au, Ag, Hg, and C [16–20]. However, the scarcity and high costs of these materials make real large-scale applications of noble metal-based catalysts unfeasible. As an alternative, several studies published in the literature have investigated the functionalization or modification of carbonaceous materials with a view toward improving their catalytic performance [8,21,22]. The fact that carbon materials, such as carbon black, are cheap to obtain, they are economically viable to be employed as catalysts when it comes to large-scale applications; furthermore, these materials have been shown to exhibit high selectivity toward H_2O_2 production [8–10,18,23–26]. On the other hand, unmodified carbon-based materials have been found to present low ORR activity in acidic medium; as such, they have been found to consume high amount of energy in the H_2O_2 production process [9,10,18,23–26,28,29].

Several noble metal-free modifiers for carbon matrices have been intensively investigated aiming at enhancing their ORR activity and selectivity, as well as their electrochemical stability in acidic medium [29–35]. Carbon modification through the application of low loadings of metal oxides, such as ZrO_2 (1–5 wt %) on graphene [36] or carbon black [37], Nb_2O_5 (15 wt %) on carbon black L6 [32], V_2O_5 (7 wt %) on Vulcan XC, and CeO_2 (2–25 wt %) on different carbonaceous matrices [38–41], has been found to promote synergistic effects which help improve ORR activity and selectivity of the carbon-modified materials used in H_2O_2 production. In the absence of a general consensus on the issue, studies published in the literature regarding the use of carbon-modified materials have attributed the improvement in ORR activity and selectivity to several factors including increased active area, wettability of the electronic surface, and the oxophilic character of the chemical species.

Although the thermal method is the most common route for the production of metal oxides [37,41,42], the typical application of high temperature (over than 500 °C) required in this method limits its use for the synthesis of carbon-supported metal oxides due to the carbon oxidation process involved. As an alternative, hydrothermal routes have

gained considerable popularity among researchers in the field; this technique is conducted with low toxicity solvent and requires relatively lower temperature conditions (<200 °C). The water at high pressure and temperature presents low viscosity, and this contributes to an increase in the solubility of ionic species, leading to the rapid formation of oxide nuclei [32,36,43,44]. Advances in the hydrothermal technique have given rise to the microwave-assisted approach where microwave is used as a source of energy. The microwave-assisted hydrothermal synthesis method (MAH) can be considered an energy-saving and environmentally green method due to three factors: 1) fast production of oxides (10–60 min); 2) homogeneous heating without loss by dissipation; and 3) the use of water as solvent [45–48].

In this work, we propose the use of a novel, green and fast (<1h) microwave-assisted hydrothermal synthesis route for the production of functionalized carbon-supported metal oxide catalysts employed in the electrosynthesis of H_2O_2 . Based on the use of zirconium oxide supported on carbon black Printex L6 as a non-toxic (in comparison with other transition metals) [49] model catalyst for ORR, the study sought to optimize the synthesis conditions by varying the synthesis parameters (including metal precursor concentration, synthesis time, temperature, and pressure) and investigating the effects of these parameters on the ORR activity and selectivity via the use of the rotating ring-disk electrode technique. The use of the optimized catalysts resulted in greater H_2O_2 electrogeneration, which was validated by the gas-diffusion electrode technique. Key insights related to the construction of the carbon-supported metal oxide catalysts are presented as well as novel contributions for future investigations and applications.

2. Experimental

2.1. Chemicals

All reagents used for conducting the experiments were of analytical grade and were used as received. The reagents employed included the following: metallic precursor salt (ZrO_2) $_2\text{CO}_2 \cdot \text{H}_2\text{O}$ (Alfa Aesar), Printex L6 pigment carbon (PL6C, Evonik do Brasil Ltda), sulfuric acid (Vetec, 97.8%), isopropyl alcohol (Vetec, 99.5%), potassium sulfate (Sigma-Aldrich, 99%), potassium hydroxide (J. T. Baker, 99%) and 60% w/w poly(tetrafluoroethylene) (PTFE) dispersion (Uniflon). All solutions were prepared using ultrapure water from a Milli-Q system with resistivity >18 M Ω cm and temperature of 25 °C.

2.2. Microwave-assisted hydrothermal synthesis (MAH)

The MAH method proposed by Moreira et al. [46] was adapted in order to incorporate ZrO_2 on carbon black electrode support (PL6C). Initially, an amount of 0.180 g of the metal precursor (ZrO_2) $_2\text{CO}_2 \cdot \text{H}_2\text{O}$ was dissolved in a minimum amount of HNO_3 (10 mL) under sonic stirring. Afterwards, 1.0 g of Printex L6 carbon and 11.0 g of KOH, which yielded an oxidizing medium of 2 mol L^{-1} in a total volume solution of 100 mL, were added to the solution; the solution was then kept under mechanical stirring for 20 min. The mixture was subsequently placed in a 140 mL Teflon reactor, making sure that 80% of its volumetric capacity was used before it was placed in the microwave for the hydrothermal reaction to occur.

The MAH procedure was optimized by varying the synthesis parameters: the percentages of the metal precursor Zr employed were 5, 10 and 15 wt% in relation to the quantity of PL6C; the periods of synthesis applied were 10, 20, 40, 60, and 120 min; and the temperature levels of 120, 140 and 160 °C, with 2, 4 and 7 atm of pressure, respectively, were used. The microwave oven used for the synthesis of ZrO_2 was adapted from the Panasonic® commercial device, model NN-ST354WRU, of 25 L and operated at maximum power of 800 W. The microwave reactor was made of Teflon and was hermetically sealed; this meant that temperatures above the boiling point of solvents could be applied on the equipment, modifying the pressure of the system. The synthesized

material was washed by centrifugation with ultrapure water at least 5 times and then left to dry overnight at 80 °C.

2.3. Electrochemical studies of ORR

Electrochemical assays were performed in a rotating ring-disk electrode (RRDE) via the application of the porous microlayer technique on the disk electrode. The RRDE tip was composed of a glassy carbon (GC) disk and Pt ring (efficiency collection (N) = 0.37), acquired from Pine Instrumentation. A microlayer of the catalyst with loading of 200 $\mu\text{g cm}^{-2}$ was formed on the GC disk (geometric area = 0.2475 cm^2) by drop-casting 25 μL of a solution previously prepared from 2 mg of the catalyst powder, 0.5 mL of water, and 0.5 mL of isopropanol.

The electrochemical measurements were performed using a bi-potentiostat PGSTAT 128 N from Metrohm AUTOLAB coupled to a rotation module - PINE model AFMSRCE. The cyclic voltammetry (CV) analyses were performed in the potential range of -0.8 to 1.0 $\text{V}_{\text{Ag}/\text{AgCl}}$ and scan rate of 50 mVs^{-1} . The ORR was studied by linear sweep voltammetry (LSV) in the range of 0.4 to -0.8 $\text{V}_{\text{Ag}/\text{AgCl}}$, at scan rate of 5 mVs^{-1} and rotating speed of 900 rpm. The CVs and LSVs were performed in both N_2 - and O_2 -saturated 0.1 mol L^{-1} K_2SO_4 (pH 2.5) used as electrolyte.

The electrochemically active surface area (ECSA) values were determined by the double-layer capacitance (C_{dl}) method based on the work of Jaramillo [50]. To estimate these values, CVs were obtained at several scan rates (5, 20, 50, 100, and 200 mV s^{-1}) starting from the more positive to negative direction in N_2 -saturated 0.1 mol L^{-1} K_2SO_4 at pH 2.5 in 0.1 V potential range centered at the open-circuit potential (OCP). The working electrode was kept for 10 s at each vertex potential at the beginning of each scan. The capacitance values were calculated as follows:

$$C_{dl} = \left(\left(\frac{\Delta I}{2} \right) = \left(\frac{I_a - I_c}{2} \right) \right) / v \quad (1)$$

where I_a and I_c are the anodic and cathodic currents at the OCP, and v is the potential scan rate. ECSA values were obtained by dividing the C_{dl} values by the specific capacitance (C_s) of the solution (17 $\mu\text{F cm}^{-2}$) [50].

2.4. Materials characterization

The loading of ZrO_2 was determined by thermogravimetry analysis using a TGA-50 thermogravimetric analyzer (Shimadzu). The samples (~ 5 mg) were burned under a synthetic air 5.0 FID gas flow (50 mL min^{-1}) at temperatures ranging between 25 and 900 °C, at a heating rate of 10 °C min^{-1} . The X-ray fluorescence (XRF) technique was used for the conduct of qualitative analyses aimed at determining the loading of ZrO_2 . The XRF analysis was performed using an X-ray fluorescence spectrometer - PANalytical - Model: MiniPaI4.

The morphological characterization of the catalysts was performed by scanning electron microscopy (SEM) and transmission electron microscopy (TEM). The SEM analysis was conducted using the Jeol JSM 7500F model microscope. The TEM analysis was conducted using FEI TECNAI G² F20 HRTEM microscope, operating at 200 kV. The TEM samples were prepared by dripping the catalyst solution onto a 300-mesh copper TEM grid (Electron Microscopy Sciences).

The structural analysis of the catalysts was conducted by X-ray diffraction (XRD) using a Bruker X-ray diffractometer model D8 Advance, which was operated under the following conditions: 40 kV and 40 mA (1.6 kW), Cu-K α radiation ($\lambda = 1.54051$ Å/ $8,047$ keV), scanning rate of 0.02 ° s^{-1} in 2θ , with Si powder used as reference.

The surface chemistry of the catalysts was analyzed by X-ray photoelectron spectroscopy (XPS) using Scienta Omicron ESCA + spectrometer Al K α line (energy = 1486.6 eV) as excitation source at 20 kV with 25 W. The binding energies of the survey spectra were calibrated based on the C 1s signal at 284.6 eV. The inelastic background of

the high-resolution spectra was subtracted by the Shirley method. The Voigt-type function, with Gaussian and Lorentzian combinations (in the proportion of 70:30), was used for the deconvolution of Zr 3d, C 1s and O 1s regions.

2.5. Accumulation of H_2O_2 in the bench-scale electrochemical cell

The analysis of the electrogeneration and accumulation of H_2O_2 was performed using the gas-diffusion electrode (GDE) technique. The assays were carried out in a bench-scale electrochemical cell with 3 electrodes, which consisted of a GDE used as the working cathode electrode, a platinumized titanium plate used as counter electrode, and Ag/AgCl (3 mol L^{-1} , Analyzer Co) used as reference electrode. The GDE cathode was produced based on the adaptation of the work of Valim et al. [31] (see details in Supplementary Information). The electrolysis assays used for the production of H_2O_2 were performed potentiostatically with the aid of the PGSTAT 128 equipment - from Metrohm AUTOLAB, coupled to a booster current module (BSTR-10A). A cell volume of 250 mL and 0.1 mol L^{-1} K_2SO_4 (used as electrolyte) at pH = 2.5 (adjusted with sulfuric acid) were used in all the experiments.

The quantification of H_2O_2 was performed by the photometric method through the complexation of 0.5 mL H_2O_2 with 4.0 mL $(\text{NH}_4)_6\text{Mo}_7\text{O}_{24}$ solution using UV-1900 spectrophotometer (acquired from Shimadzu). Under this method, hydrogen peroxide reacts with molybdate, generating a yellowish stable complex (peroxymolybdate) which is quantified by UV-Vis spectrophotometry at wavelength = 350 nm [51,52]. The $\text{C}_{\text{H}_2\text{O}_2}$ values were used for calculating the energy consumption (EC) based on Eq. (2) below:

$$EC \text{ (kWh kg}^{-1}\text{)} = \frac{1000 E_{cell} I t}{V_s C_{\text{H}_2\text{O}_2}} \quad (2)$$

where E_{cell} is the potential of the electrochemical cell (in V), I is the current for each potential applied (in A), t is the time of electrolysis (in h), and V_s is the volume of the solution (in L).

3. Results and discussion

3.1. Effect of initial Zr precursor concentration

Fig. 1a presents a schematic illustration of the stages involving the MAH synthesis method. Further features of MAH synthesis and advances over conventional hydrothermal methodology are detailed in the supplementary material. Thus, initially, the zirconium precursor concentration was varied between 5 and 15 wt%, while the temperature, pH, and MAH reaction time were fixed at 140 °C, 12 , and 40 min, respectively. The effects of these changes in parameter conditions on the structure, morphology, and metal oxide loading are shown in Fig. 1b-f.

The SEM images (Fig. 1b-d) show the successful incorporation and the morphologies of ZrO_2 nanoparticles supported on PL6C. Small ZrO_2 nanoparticles (NPs) can be found widely dispersed on the carbon support; this implies the occurrence of a high interaction between the metal oxide and the carbon support. The TEM images (Fig. S1) clearly show that the ZrO_2 NPs, characterized by an almost spherical shape, are in direct contact with the PL6C. These images also suggest the formation of agglomerates in some regions. The SEM images obtained in back-scattered electron (BSE) imaging mode (Figs. S2) point to an increase in the loading of ZrO_2 with higher initial concentrations of the zirconium precursor. The MAH process conducted using concentrations above Zr-5 wt.% Zr led to the formation of large porous agglomerates (c.f. Fig. S1), which reached up to ~ 1 μm (at 15 wt% of Zr).

The EDX spectra (Fig. S3) for 15 wt% Zr/PL6C and control PL6C matrix (with 0 wt% of Zr) show the presence of Zr (as the main metal in the composition), in addition to carbon and oxygen which belong to the carbonaceous material. SEM images in BSE mode (Fig. S3) for control PL6C matrix (with 0 wt% of Zr) and PL6C with 15 wt. of Zr evinced the

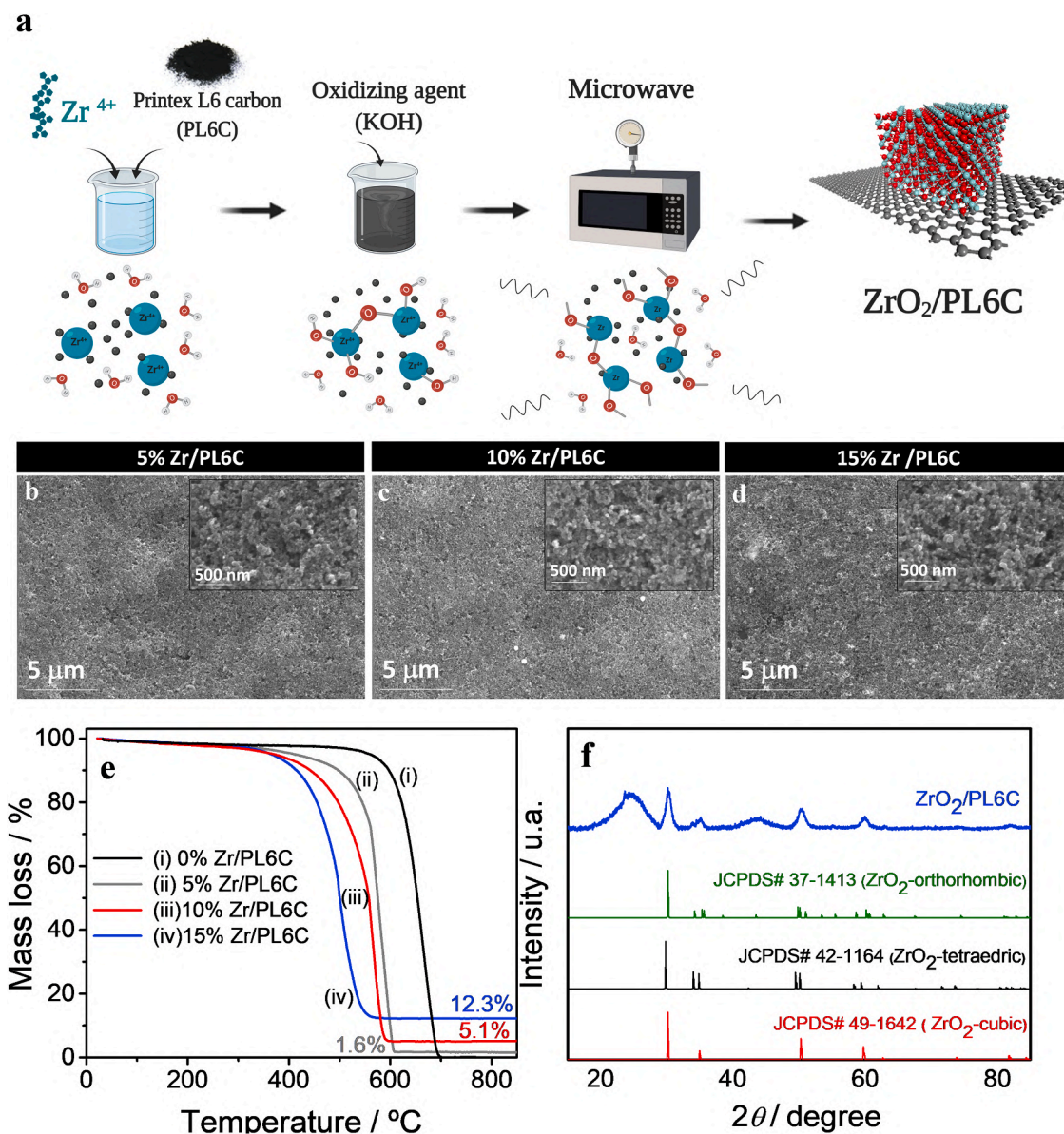


Fig. 1. (a) An illustrative scheme of the microwave-assisted hydrothermal synthesis. SEM images of (b) 5, (c) 10 and (d) 15 wt% of ZrO₂/PL6C; (e) thermogravimetric analysis of the ZrO₂/PL6C catalyst produced from the application of different initial Zr precursor concentrations; (f) XRD pattern for ZrO₂/PL6C catalyst produced from the initial Zr precursor concentration of 15 wt%.

incorporation of ZrO₂ oxides by the MAH method. The negligible presence of potassium can be attributed to the KOH residues from the synthesis procedure. The results obtained from the thermogravimetric analyses (Fig. 1e) showed that, for the synthesis conducted using 5, 10, and 15 wt% of Zr, only 1.6, 5.1, and 12.3 wt% of Zr loading, respectively, were effectively incorporated into the catalysts. The use of higher initial concentrations of Zr (10 and 15 wt%) contributed toward greater efficiency in the incorporation of the metal oxide nanoparticles; this can be attributed to the agglomeration of particles (c.f. Fig. 1, S1 and S2), which is fueled by the absence of surfactant or other structuring agent during the synthesis process. The adsorbed oxygenated anions (i.e. hydroxyl and carbonate) and the small Zr particles formed previously act as a favorable anchor point for the Zr ions available in the solution to be crystallized rather than to produce new clusters on the PL6C [53].

The results obtained from the crystallographic analysis by X-ray diffraction for the 15 wt% Zr/PL6C sample (Fig. 1f) showed the presence of four major broadened diffraction peaks at $2\theta = 30.1^\circ$, 34.9° , 50.3° , and 59.9° which corresponded to the following crystalline planes: (1 1

1), (2 0 0), (2 2 0) and (3 1 1), respectively. This XRD pattern can be associated to an overlapping of the peaks related to cubic, orthorhombic, and tetragonal crystalline features; the pattern indicated that the ZrO₂ nanoparticles were formed by a mix of these three crystal phases [37,54,55]. Also, the peak at 25.9° was found to be related to the plane (0 0 2) which corresponded to graphitic structures that are typically present in carbon materials [32,37,56]. The result obtained from the XRD analysis was found to be in line with other previously reported results obtained for ZrO₂ structures [37].

Fig. 2 shows the electrochemical characterization and the assessment of ORR activity and selectivity toward the production of H₂O₂ for the materials synthesized under the MAH method. The voltammetric profiles (Fig. 2a) showed the predominance of the capacitive characteristic typical for carbonaceous materials with high surface area for all the curves. One can notice the presence of a redox couple peaks centered at ~ 0.3 V_{Ag/AgCl} which corresponded to the quinone groups of the PL6C matrix [30,57,58]. As expected, no peaks related to the ZrO₂ species were detected in the CV profiles. Nonetheless, an increase in current was

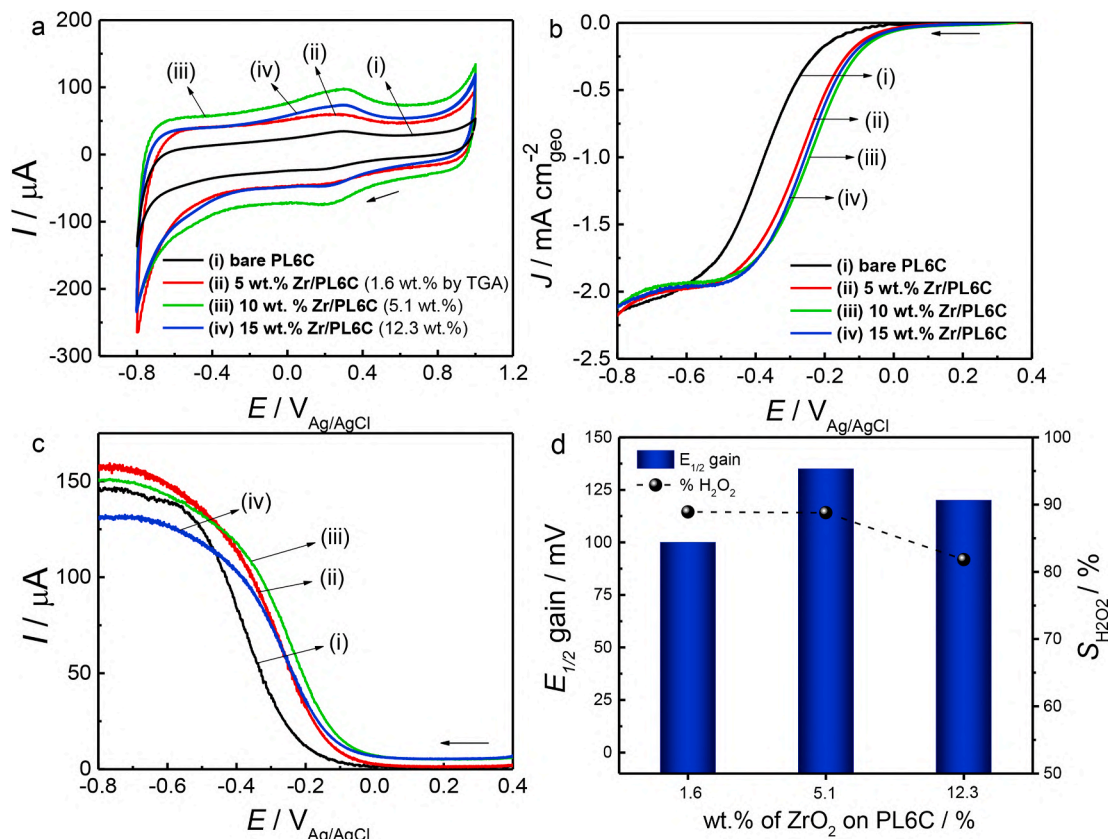


Fig. 2. (a) Cyclic voltammograms obtained from the application of N_2 -saturated $0.1 \text{ mol L}^{-1} \text{ K}_2\text{SO}_4$, with $\text{pH} = 2.5$ (H_2SO_4 adjusted), at scan rate of 50 mV s^{-1} and potential window ranging from 1 to $-0.8 \text{ V}_{\text{Ag/AgCl}}$. (b) Linear sweep voltammetry in RRDE curves for the disk electrode obtained in O_2 -saturated $0.1 \text{ mol L}^{-1} \text{ K}_2\text{SO}_4$, with $\text{pH} = 2.5$ (H_2SO_4 adjusted), at scan rate of 5 mV^{-1} and potential window ranging from 0.4 to -0.8 V at 900 rpm . (c) The values of the currents obtained for the Pt ring electrode during the potential scan on the disk electrode. The ring potential was kept at $1.0 \text{ V}_{\text{Ag/AgCl}}$. (d) Correlation between improvement in catalytic performance (in terms of $E_{1/2}$), selectivity for H_2O_2 ($S_{\text{H}_2\text{O}_2}$), and wt.% of ZrO_2 on PL6C.

observed in the presence of ZrO_2 ; this was attributed to the highly porous structure of ZrO_2 , as observed in the TEM images (Fig. S1), which led to an increase in the surface area of the catalyst. In fact, the result obtained from the determination of the electrochemically active surface area (ECSA) by the capacitance method (c.f. Fig. S4 and Table S1) showed a significant increase in the ECSA value from $85.6 \text{ m}^2 \text{ g}^{-1}$, for the unmodified PL6C, to $128.2 \text{ m}^2 \text{ g}^{-1}$, for the modified 5.1 wt% ZrO_2 -PL6C.

The LSV curves presented in Fig. 2b show the ORR electrocatalytic performance of the catalysts synthesized in this work. One can observe that all the samples modified with ZrO_2 exhibited a relatively higher ORR activity compared to the unmodified PL6C. This higher ORR activity was evidenced by the shift of the curves to more positive potentials, which was reflected in the average catalytic improvement of 115 mV in the half-wave potential ($E_{1/2}$) following the modification of the carbon matrix with ZrO_2 . To find out whether H_2O_2 was eventually formed during the ORR, the Pt ring electrode was kept fixed at 1.0 V ; this is regarded a favorable potential for the oxidation of H_2O_2 . The LSV curves obtained for the Pt ring electrode are shown in Fig. 2c. The LSV curves related to the ring confirm that, despite slight variations in the currents, all the materials exhibited high selectivity for H_2O_2 generation. Based on the data related to the disk, the ring currents and Eq. (3) below - proposed by Paulus et al. [59], we were able to estimate the selectivity of the material with respect to H_2O_2 generation ($S_{\text{H}_2\text{O}_2}$) during the ORR.

$$S_{\text{H}_2\text{O}_2} = \frac{2i_r/N}{i_d + i_r/N} 100\% \quad (3)$$

where i_d is the current of the disk, i_r is the ring current, and N is the

collection number for the ring electrode ($N = 0.37$, as provided by the manufacturer of the RRDE system).

Fig. 3d shows the relation between the loading of ZrO_2 on the carbon support and its effect on the ORR activity, in terms of half-wave potential ($E_{1/2}$), and on selectivity toward H_2O_2 production ($S_{\text{H}_2\text{O}_2}$). The results obtained showed that the incorporation of ZrO_2 on the PL6C led to an increase in ORR activity and the initial selectivity of PL6C was found to be over 85%. The material derived from the application of 10 wt% of Zr on PL6C, which effectively led to the incorporation of 5.1 wt% of ZrO_2 on the carbon matrix, exhibited the best catalytic performance with 88% of $S_{\text{H}_2\text{O}_2}$ and an improvement in catalytic performance of $\sim 140 \text{ mV}$ (in the $E_{1/2}$). The improvement observed in the electrocatalytic performance can be attributed to the following factors: 1) the presence of highly dispersed small particles on PL6C; and 2) the increase in ECSA, which helped improve the access to the catalyst surface [60] (one cannot rule out the influence of the oxophilic character of ZrO_2 [61] - its ability to dislocate the electrons from PL6C, which may influence ORR activity on the carbon surface).

However, one needs to point out that an increase in the ZrO_2 loading led to a slight decrease in both $E_{1/2}$ and $S_{\text{H}_2\text{O}_2}$; this is likely due to the increase in the surface resistivity and the formation of large agglomerates [60]. Studies published in the literature suggest that given that the metal oxide has typically low conductivity, the small particles, which are in direct contact with the highly conductive carbon support, are the only particles that can effectively participate in the ORR [60]. Thus, striking a balance between the dispersion of the particles, the ECSA, and the oxide loading is key to improving the ORR catalytic activity of carbon materials via modification with metal oxide.

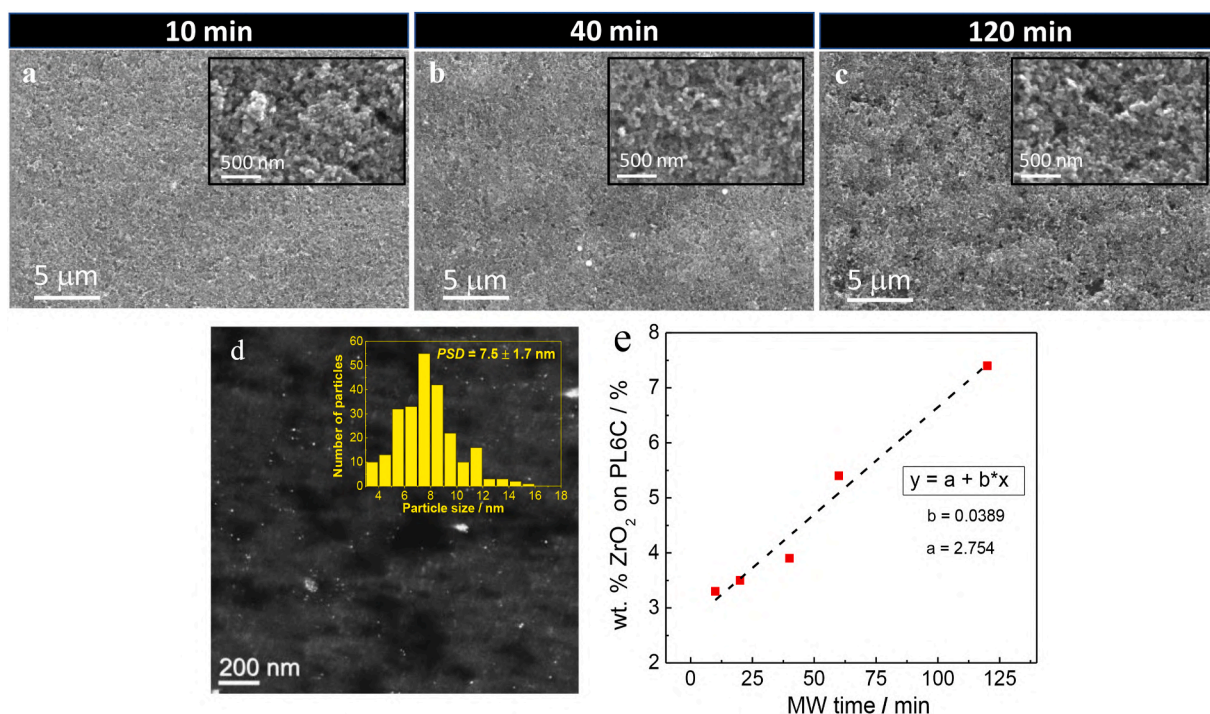


Fig. 3. SEM images in SE mode for the $\text{ZrO}_2/\text{PL6C}$ catalyst produced under different MAH synthesis in (a) 10, (b) 40 and (c) 120 min. (d) Dark-field STEM image and particle size distribution (inset) for the $\text{ZrO}_2/\text{PL6C}$ sample produced in 40 min. (e) ZrO_2 wt.% on carbon vs. MAH time plot. Data obtained by XRF quantification.

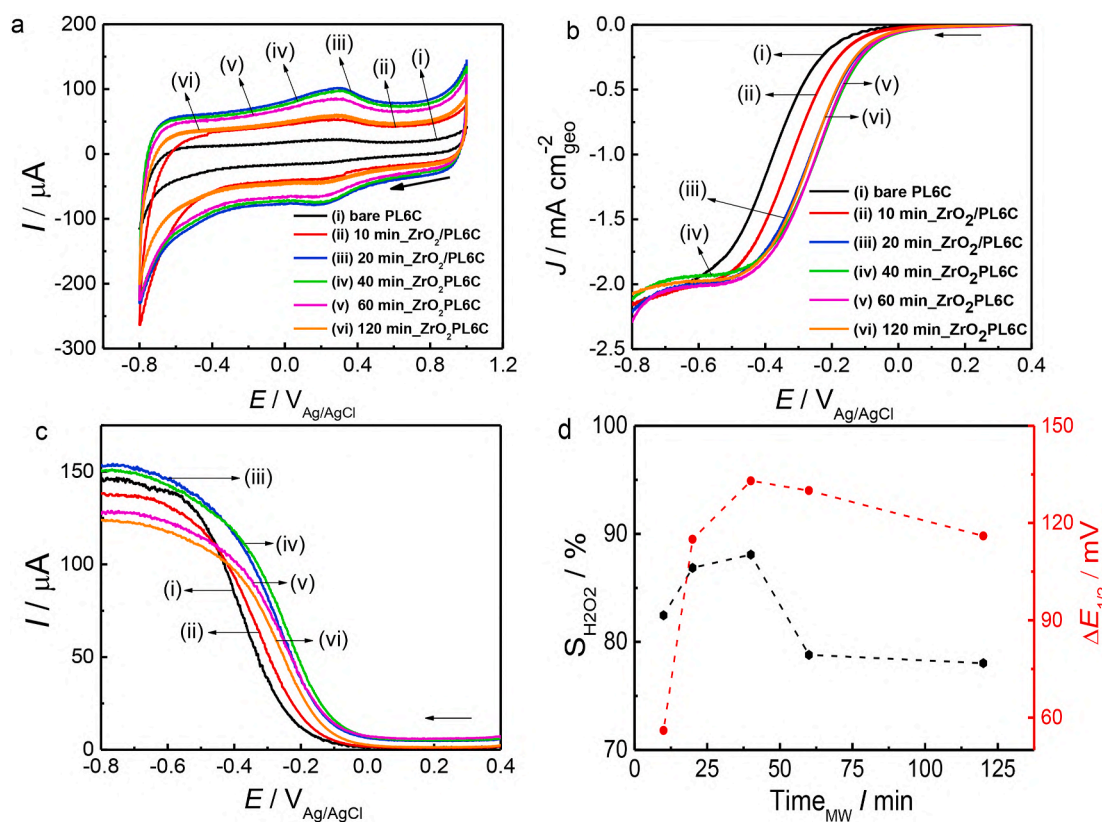


Fig. 4. (a) Cyclic voltammograms obtained in N_2 -saturated $0.1 \text{ mol L}^{-1} \text{ K}_2\text{SO}_4$, $\text{pH} = 2.5$ (H_2SO_4 adjusted), at scan rate of 50 mV s^{-1} and potential window ranging from 1 to $-0.8 \text{ V}_{\text{Ag}/\text{AgCl}}$. (b) Linear sweep voltammograms in RRDE curves for the disk electrode obtained in O_2 -saturated $0.1 \text{ mol L}^{-1} \text{ K}_2\text{SO}_4$, $\text{pH} = 2.5$ (H_2SO_4 adjusted), at scan rate of 5 mV^{-1} and potential window ranging from 0.4 to -0.8 V at 900 rpm ; (c) The values of the currents obtained for the Pt ring electrode during the potential scan on the disk electrode. The ring potential was kept at $1.0 \text{ V}_{\text{Ag}/\text{AgCl}}$. (d) Correlation between improvement in the catalytic performance (in terms of $E_{1/2}$), selectivity toward H_2O_2 ($S_{\text{H}_2\text{O}_2}$), and synthesis time.

3.2. Effect of microwave-assisted hydrothermal synthesis time

After determining the optimal concentration of the metal precursor (at 10 wt% of Zr) of the assessed percentages, the microwave-assisted hydrothermal synthesis time was the second relevant synthesis parameter that needed to be evaluated. Microwave-assisted hydrothermal synthesis was performed in 10, 20, 40, 60 and 120 min aiming at producing ZrO₂ crystallites on the carbonaceous matrix; the changes in the material structure were monitored by SEM, TEM, and XRF analyses, as shown in Fig. 3.

SEM images presented in Fig. 3a–c shows that the duration time of the MAH synthesis plays an influential role on the nucleation-growth process. Although all the samples presented very similar structures, the SEM images on BSE mode (see Fig. S5) showed an increase in the number and size of ZrO₂ particles crystallized on PL6C as the synthesis time was increased. For illustrative purposes, the dark-field STEM image (Fig. 3d) obtained for the catalyst treated for 40 min under the MAH synthesis method shows a wide distribution of small ZrO₂ nanoparticles with average size of 7.5 ± 1.7 nm (c.f. inset in Fig. 3d) on the carbon matrix and a formation of few agglomerates of particles. As expected, the XRF quantification (Fig. 3e) analysis indicates that the duration time of the MAH synthesis process directly influences the loading of the metal oxide crystallized on the carbon matrix. The analysis of the slope of ZrO₂ wt.% vs. synthesis time plot shows that the oxide crystallization process has a relatively slow kinetics (deposition rate ~ 0.04 wt%_{ZrO₂/C min⁻¹); in addition to that, the synthesis time needs to be greater than 3 h for all the Zr⁴⁺ available in the reaction media (10 wt %) to be theoretically crystallized.}

Fig. 4a shows the voltammetric profiles for the catalysts produced under different synthesis times. One will notice that, for all the synthesis times investigated, the presence of ZrO₂ led to an increase in the capacitive currents of the modified PL6C in comparison to the unmodified PL6C. However, the application of periods of time longer than 40 min led to a slight decrease in the capacitive currents, which can be attributed to the formation of large oxide particles and a consequent decrease in the surface area. These voltammetric responses are in good agreement with the SEM and TEM images shown in Fig. 3a–d and S5.

Fig. 4b shows the results obtained from the analysis of ORR activity. The LSV curves related to the disk electrode (Fig. 4b) show the enhancement of the ORR activity as the synthesis time is increased up to 40 min. In longer synthesis times above 40 min, the improvement in ORR activity is found to stabilize while a slight decrease in ring currents is observed (Fig. 4c). The correlation between the improvement in catalytic performance (in terms of E_{1/2}), selectivity toward H₂O₂ (S_{H2O2}), and MAH synthesis time (Fig. 4d) shows that the ZrO₂/PL6C catalyst produced in the synthesis time of 40 min exhibits the highest ORR activity with E_{1/2} improvement of ~ 135 mV and the highest selectivity for H₂O₂ generation (88%). These results help confirm the hypothesis that an increase in ZrO₂ loading on the carbon matrix leads to an increase in surface resistivity due to the formation of large agglomerates of oxide particles that are in poor contact with the conductive carbon support and which effectively do not take part in the reaction.

To investigate whether the synthesis procedure caused changes in the catalytic properties for ORR of bare PL6C, the control carbon matrix (with 0 wt% of Zr) was subjected to the same synthesis conditions in the absence of the metal precursor. Interestingly, even after the control material has been exposed to high pressure in a highly alkaline condition, the RRDE results (c.f. Fig. S6) showed no substantial changes in the electrocatalytic behavior for ORR.

3.3. Effect of temperature and pressure

After determining the optimal parameter conditions for the initial metallic precursor concentration (fixed at 10 wt%) and synthesis time (fixed at 40 min), another key parameter was also subjected to analysis - the temperature of synthesis. It is worth noting that variation in

synthesis temperature and pressure may lead to conformational changes in the oxide structure, and this may affect the catalytic performance. Thus, the following temperature levels were applied to the Teflon reactor in the microwave oven: 120, 140, and 160 °C; these temperature levels corresponded to the following pressure levels: 2, 4 and 7 bar. The morphological and structural changes in the ZrO₂/PL6C catalyst were monitored by SEM, TEM and XRD techniques, as shown in Fig. 5.

The SEM images (Fig. 5a–c) obtained show that the synthesis temperature plays an influential role on the deposition of the ZrO₂ nanoparticles; this implies that an increase in temperature leads to an increase in both the particle distribution on the PL6C and the size of the particles. The EDX spectra presented in Figure S7 shows that an increase in temperature resulted in higher amounts of crystallized ZrO₂. A further analysis of the surface morphology by TEM (Fig. 5d–f) showed the presence of large agglomerates of ZrO₂ when the synthesis procedure was conducted above the temperature of 140 °C. The structural analysis of the catalysts by XRD (Fig. 5g) showed the presence of a similar XRD pattern, with a mixture of cubic, orthorhombic, and tetragonal crystal-line features for all the ZrO₂/PL6C catalysts. However, a careful look at the diffractograms (c.f. Fig. 5h) showed a decrease in intensity of the secondary peaks at $2\theta = 32.4^\circ, 49.2^\circ, 55.2^\circ, 74.5^\circ, \text{ and } 81.9^\circ$, which corresponded to the orthorhombic crystal system, as the synthesis temperature was increased; this shows that the crystallization occurs preferentially in cubic and tetrahedral forms [37,54]. In line with other reports published in the literature [46,53], these findings suggest that the temperature and pressure of the MAH synthesis affect the nucleation-growth process of the metal oxide on the carbon matrix, and this leads to preferential crystallization in certain crystalline systems.

Fig. 6a presents the voltammetric profiles related to the catalysts treated at different MAH temperature levels (and pressure). The ZrO₂/PL6C catalyst produced at 120 °C exhibited a voltammetric behavior similar to the unmodified PL6C, while the catalysts produced at 140 and 160 °C presented greater capacitive currents in comparison with the unmodified PCL6; this shows that the use of MAH temperatures above 120 °C leads to higher loadings of ZrO₂ on the carbon matrix. These voltammetric responses are in agreement with the results obtained by SEM, TEM and EDX analyses (c.f. Fig. 5 and S7).

The electrocatalytic performance in ORR related to the ZrO₂/PL6C catalyst produced at different MAH temperatures are shown in Fig. 6b–d. The LSV curves related to the disk electrode (Fig. 6b) showed that the ZrO₂/PL6C catalysts produced above the temperature level of 120 °C exhibited higher ORR activity. However, the ring curves (Fig. 6c) showed that the ZrO₂/PL6C produced at 160 °C exhibited the lowest current for H₂O₂ generation (~ 75 μ A vs 160 μ A for the catalyst produced at 120 °C, and 150 μ A for the catalyst produced at 140 °C). The correlation between the improvement in catalytic performance, the selectivity toward H₂O₂, and the MAH synthesis temperature (Fig. 6d) showed that the ZrO₂/PL6C catalyst produced at 140 °C exhibited the highest ORR activity (E_{1/2} gain of ~ 140 mV) with selectivity for H₂O₂ production of about 90%. These findings clearly show that striking a balance between high dispersion of the nanoparticles, surface area, and the loading of the crystallized metal oxide is primarily important if one seeks to improve the ORR catalytic activity of carbon materials via the modification of the materials with ZrO₂.

3.4. Further investigation of the optimized catalyst

To further investigate the physicochemical properties of the optimized ZrO₂/PL6C catalyst produced by the MAH synthesis technique (under the following optimal conditions: 10 wt% of initial Zr concentration, 40 min of synthesis time, and temperature of 140 °C - which presented the best electrocatalytic performance for H₂O₂ generation), the following analyses were conducted: TEM, selected area electron diffraction (SAED), X-ray photoelectron spectroscopy (XPS), and long-term stability test. The high-resolution TEM image obtained for the optimized ZrO₂/PL6C catalyst (Fig. 7a) showed that the small ZrO₂

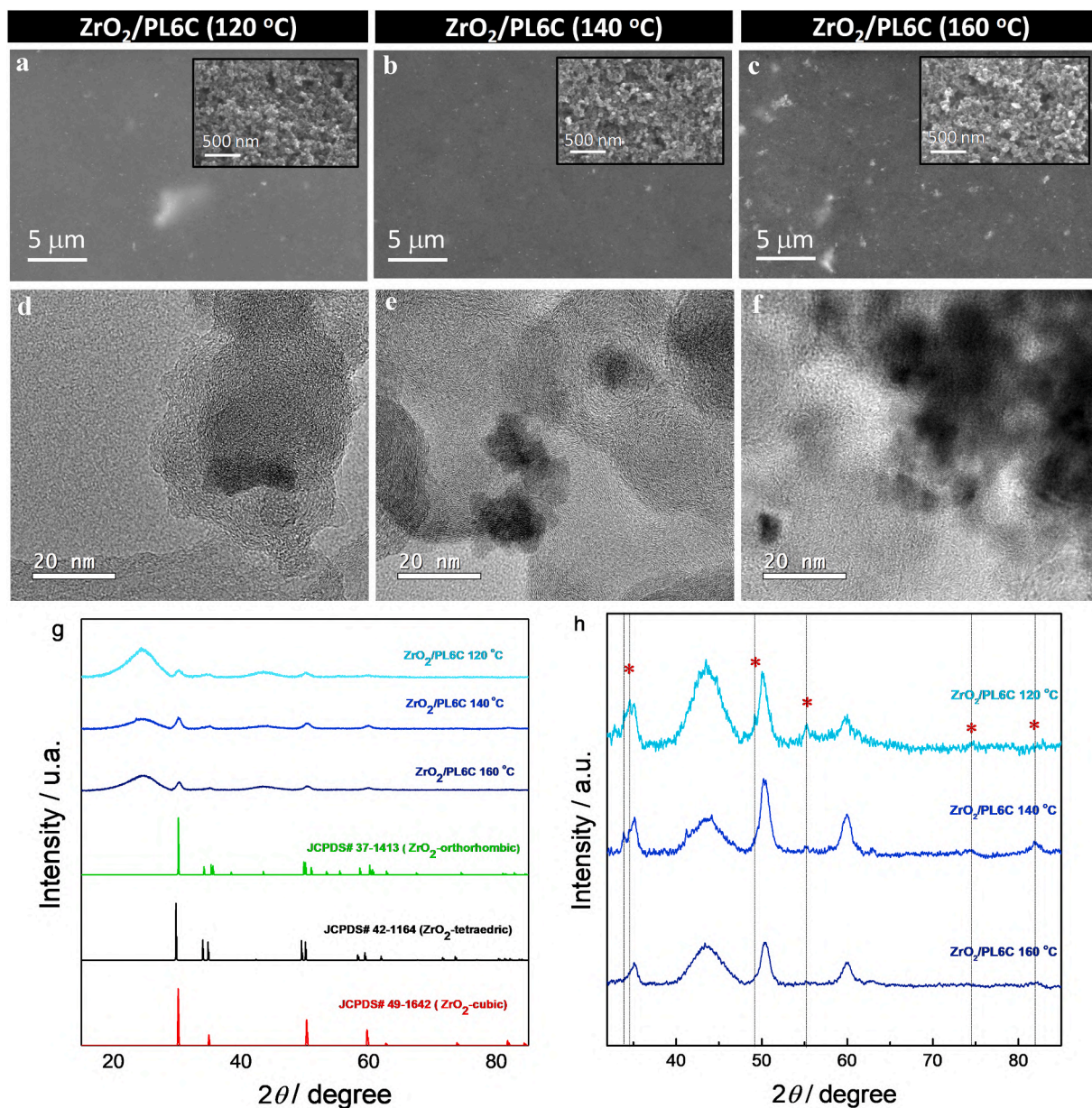


Fig. 5. SEM images in (a–c) BSE and SE (inset) mode, (d–f) TEM images, and (g–h) XRD pattern for the ZrO₂/PL6C catalyst produced at different MAH temperatures.

nanoparticles were in direct contact with the PL6C carbon support. The ZrO₂ nanoparticles exhibited lattice fringes measuring 0.29 nm on average; this is typically expected for (1 1 1) diffraction plane in the predominant face-centered cubic structures [52]. Furthermore, the selected area electron diffraction pattern shown in Fig. 7b exhibited a polymorphic and low crystallinity profile for the catalyst material due to the high amount of amorphous carbon Printex L6 in the material composition. The electron diffraction pattern presented the diffraction planes (1 1 1), (2 2 0), (2 0 0) and (3 1 1); this can be attributed to the predominance of the cubic phase of ZrO₂ [36,37].

XPS analysis was performed aiming at investigating the surface chemistry of the optimized catalyst. The XPS survey spectrum (c. f. Fig. 7d) shows the peaks related to the C1s, O1s, O KLL, and Zr 3d regions, discarding the presence of any contaminant. The XPS narrow spectra for the Zr 3d region (Fig. 7d) shows the oxidized form of Zr with the expected spin-orbit splitting (3d_{3/2} and 3d_{5/2}) and binding energy typically attributed to oxidized Zr species [37,62]. The aforementioned mentioned doublet with binding energies at 184.2 and 181.9 eV show that zirconium is predominantly in its oxidized form - Zr⁴⁺, which can be

attributed to ZrO₂. It is expected that the oxophilic character of ZrO₂ acts as a driving force for the displacement of electron charges from the PL6C; this may lead to changes in the O₂ adsorption on the carbon surface [32,37,40]. The results obtained from the XPS analysis demonstrate the efficiency of the microwave assisted hydrothermal synthesis in terms of producing the oxide of interest.

The presence of Zr in its oxidized form (Zr⁴⁺) in the catalyst composition indicates that no further oxidation of the metal is possible, and this greatly enhances the electrochemical stability of the catalyst. In order to evaluate the electrochemical long-term stability of the optimized ZrO₂/PL6C catalyst, changes in both ORR activity and H₂O₂ selectivity were monitored before and after the application of 5,000 voltammetric cycles in the potential range of -0.5 to 0.5 V_{Ag/AgCl}, at scan rate of 1 V s⁻¹. As can be seen in Fig. S8, the LSV curves before and after the long-term stability test for the ZrO₂/PL6C catalyst show that the ORR activity and selectivity toward H₂O₂ production are found to be stable even after the application of 5,000 voltammetric cycles; this evidently points to the high electrochemical stability of the catalyst in acidic condition. Table S2 summarizes the main results obtained for the

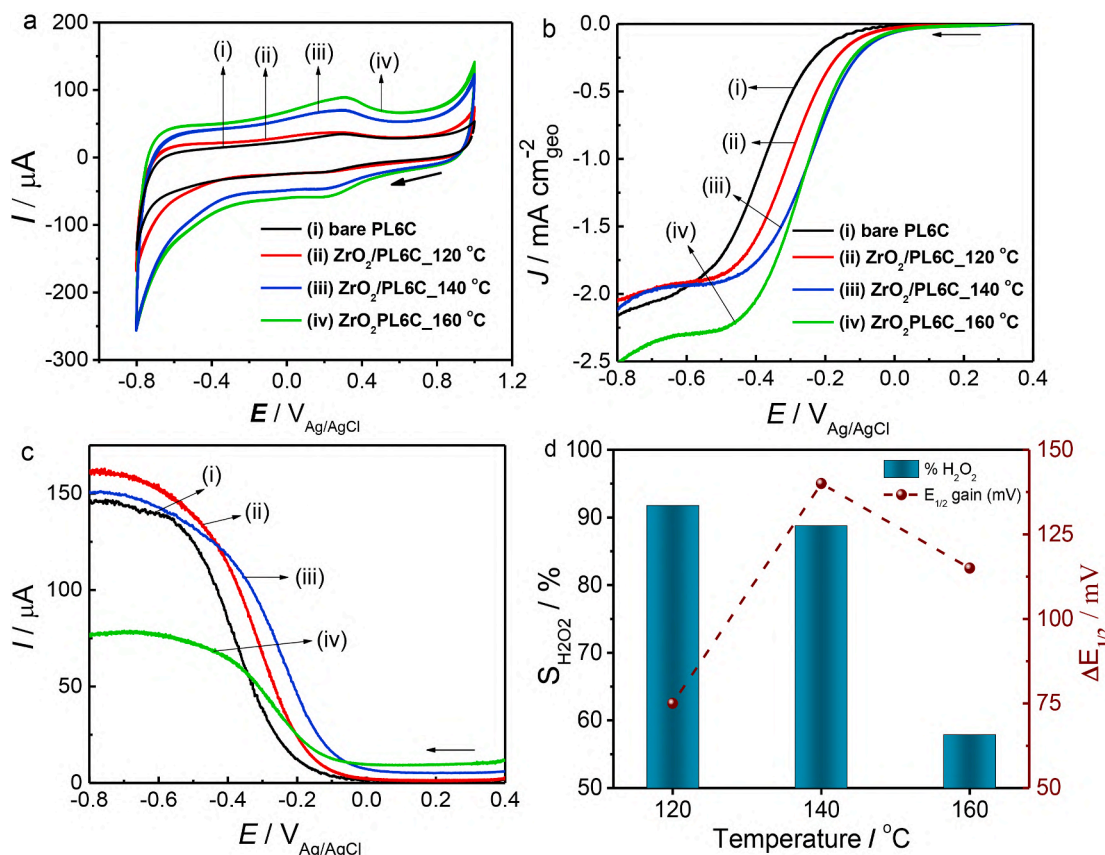


Fig. 6. (a) Cyclic voltammograms obtained using N_2 -saturated $0.1 \text{ mol L}^{-1} \text{ K}_2\text{SO}_4$, $\text{pH} = 2.5$ (H_2SO_4 adjusted), at scan rate of 50 mV s^{-1} and potential window ranging from 1 to $-0.8 \text{ V}_{\text{Ag}/\text{AgCl}}$. (b) Linear sweep voltammetry in RRDE curves for the disk electrode obtained in O_2 -saturated $0.1 \text{ mol L}^{-1} \text{ K}_2\text{SO}_4$, $\text{pH} = 2.5$ (H_2SO_4 adjusted) at scan rate of 5 mV^{-1} and potential window ranging from 0.4 to -0.8 V at 900 rpm ; (c) The values of the currents obtained for the Pt ring electrode during the potential scan on the disk electrode. The ring potential was kept at $1.0 \text{ V}_{\text{Ag}/\text{AgCl}}$. (d) Correlation between the improvement in catalytic performance (in terms of $E_{1/2}$), selectivity toward H_2O_2 ($S_{\text{H}_2\text{O}_2}$), and the temperature applied in the MAH synthesis process.

optimized catalyst $\text{ZrO}_2/\text{PL6C}$; which are compared with results previously reported for other catalysts based on metal oxides supported on carbon. It is worth to note that the optimized catalyst as well as the synthesis method proposed here presented advantages with respect to the other catalysts (and their synthesis methods), such as being greenest (uses water as solvent under a lower temperature), produced rapidly, and it demonstrated the highest activity-selectivity combination for the H_2O_2 electrogeneration.

3.5. H_2O_2 electrogeneration using the gas diffusion electrode approach

After the optimization of the synthesis parameters of the catalyst and a rigorous analysis using the RRDE mechanism, a study was conducted aiming at investigating the catalytic activity of the optimized $\text{ZrO}_2/\text{PL6C}$ catalyst in terms of H_2O_2 generation using the gas diffusion electrode (GDE) approach. Based on the GDE technique, one is able to evaluate, in a more realistic condition, the catalytic performance of different materials and the impacts of the use of these materials on energy consumption (EC). The gas diffusion electrode technique is regarded more appropriate for real application due to its ability to overcome the limitations imposed by mass transport [8,63,64]. The ability of the GDE to supply oxygen molecules directly to the electrode-solution interface rules out the need for employing O_2 -saturated solution, thus increasing the efficiency of H_2O_2 generation while minimizing the need for electrodes with large surface area [8,63–65]. The GDE cathodes were produced from the following materials: PL6C, $\text{ZrO}_2/\text{PL6C}$, and PTFE (provides physical stability to the electrode) (Fig. S9 presents information related to the construction of the GDE). Figure S10 show the profiles

related to H_2O_2 electrogeneration evaluated potentiostatically at -0.8 , -1.2 , -1.6 , and -2.0 V . The electrolytic curves for both the PL6C and the $\text{ZrO}_2/\text{PL6C}$ electrodes exhibited a sharp increase in H_2O_2 concentration in the first 30 min of electrolysis up to the point where an almost constant concentration plateau occurs - this is typically attributed to the presence of electrochemical parasitic reactions [51,66], which mainly consist of further reduction of H_2O_2 on GDE ($\text{H}_2\text{O}_2 + 2\text{H}^+ + 2\text{e}^- \rightarrow 2\text{H}_2\text{O}$) and counter electrode oxidation [3,67]. Over all, both of the GDEs (PL6C and $\text{ZrO}_2/\text{PL6C}$) presented significant production of H_2O_2 in the electrolysis at more negative potentials; however, the $\text{ZrO}_2/\text{PL6C}$ presented greater catalytic activity under all the potentials investigated. For comparison purposes, in the electrolysis performed at $-2.0 \text{ V}_{\text{Ag}/\text{AgCl}}$ for 90 min, the $\text{ZrO}_2/\text{PL6C}$ produced 570 mg L^{-1} of H_2O_2 whereas the unmodified PL6C produced only 250 mg L^{-1} .

To further investigate the kinetics and the energy consumption levels related to the electrogeneration of H_2O_2 for the PL6C and $\text{ZrO}_2/\text{PL6C}$ electrodes, the kinetic parameters [51,66] and the energy consumption (EC) were estimated and compared (see Table S3). In the electrogeneration of H_2O_2 at $-2.0 \text{ V}_{\text{Ag}/\text{AgCl}}$, the carbon-based ZrO_2 catalyst showed kinetics values ~ 2 times higher than the bare PL6C catalyst, further providing a decrease of 150 kWh g^{-1} of energy consumption. A detailed discussion on the H_2O_2 electrogeneration using the GDE approach can be found in the Supplementary Information.

4. Conclusion

The present work reported the successful synthesis of electrocatalysts derived from carbon-supported metal oxide for H_2O_2 electrogeneration

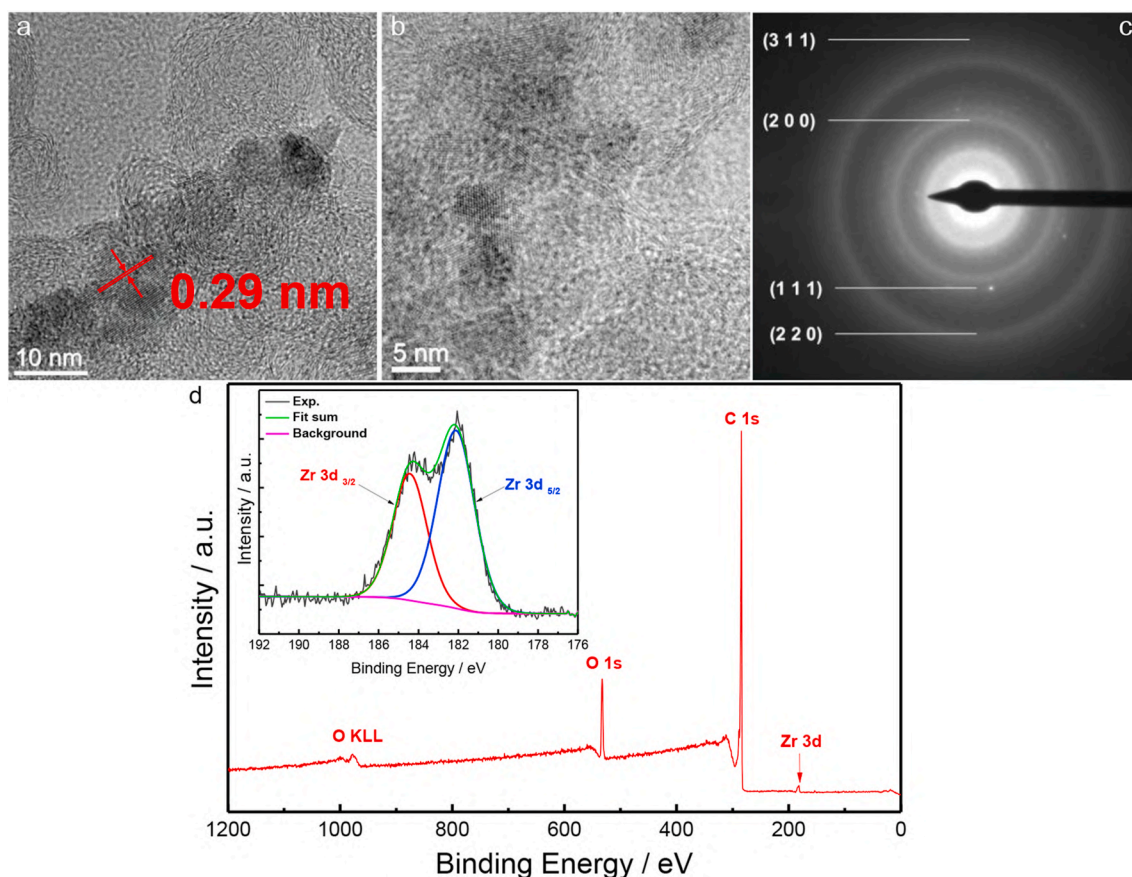


Fig. 7. (a,b) HR-TEM images, (c) selected area electron diffraction pattern, and (d) XPS survey spectrum for the optimized $\text{ZrO}_2/\text{PL6C}$ catalyst. Inset: Narrow XPS spectrum for the Zr 3d region.

through the application of a novel, green and fast mechanism based on the microwave-assisted hydrothermal synthesis approach. The loading, dispersion, size, and preferential crystallography of the carbon-modified ZrO_2 nanoparticles was optimized by adjusting the synthesis parameters, such as metal precursor concentration, synthesis time, temperature, and pressure. The results obtained from the RRDE analysis showed that the optimized catalyst produced from ZrO_2 -5.1 wt% on the PL6C electrode support presented a catalytic improvement of 140 mV (in terms of $E_{1/2}$) with respect to ORR and selectivity for H_2O_2 production of 88.8% compared to the unmodified PL6C matrix, which exhibited 78% of H_2O_2 production.

The catalytic improvement in ORR can be attributed to the following factors: 1) the presence of highly dispersed small particles (~ 7 nm) on the PL6C electrode support; and 2) the increase in ECSA, which improved the access to the surface of the catalyst. The presence of ZrO_2 in the modified $\text{ZrO}_2/\text{PL6C}$ electrode causes a displacement of the electrons from PL6C, and this may lead to changes in the adsorption of O_2 on the carbon surface. Through the application of the GDE assays, the results obtained related to H_2O_2 production helped confirm the superior catalytic performance of the modified $\text{ZrO}_2/\text{PL6C}$ over the unmodified PL6C. These findings can provide useful insights regarding the construction of carbon-supported transition metal oxides for future investigations and applications of sustainable catalyst materials for ORR and H_2O_2 electrogeneration.

CRedit authorship contribution statement

Matheus S. Kronka: Investigation, Methodology, Validation, Writing – original draft, Writing – review & editing. **Paulo J.M. Cordeiro-Junior:** Investigation, Methodology, Validation, Writing –

original draft. **Letícia Mira:** Investigation, Formal analysis, Writing – original draft. **Alexsandro J. dos Santos:** Conceptualization, Writing – review & editing, Writing – original draft. **Guilherme V. Fortunato:** Validation, Conceptualization, Visualization, Writing – original draft, Writing – review & editing. **Marcos R.V. Lanza:** Supervision, Funding acquisition, Writing – review & editing, Writing – original draft, All authors have given their approval for the submission of the final version of the manuscript.

Declaration of competing interest

The authors declare that they have no known competing financial interests or personal relationships that could have appeared to influence the work reported in this paper.

Acknowledgments

The authors gratefully acknowledge the financial support provided by the following Brazilian research funding agencies: Brazilian National Council for Scientific and Technological Development - CNPq (grant #465571/2014-0, #302874/2017-8 and #427452/2018-0), São Paulo Research Foundation (FAPESP – grants #2014/50945-4, #2017/23464-3, #2016/25831-0, # 2016/19612-4, #2017/10118-0, #2019/20634-0 and #2019/04421-7), and the Coordenação de Aperfeiçoamento de Pessoal de Nível Superior (CAPES – Finance Code 001). The authors are also grateful to the Laboratory of Structural Characterization (LCE/DEMa/UFSCar) for providing the general facilities used in the conduct of this research.

- hydrothermal method, *Cryst. Growth Des.* 9 (2008) 833–839, <https://doi.org/10.1021/cg800433h>.
- [47] J. Huang, C. Xia, L. Cao, X. Zeng, Facile microwave hydrothermal synthesis of zinc oxide one-dimensional nanostructure with three-dimensional morphology, *Mater. Sci. Eng. B Solid-State Mater. Adv. Technol.* 150 (2008) 187–193, <https://doi.org/10.1016/j.mseb.2008.05.014>.
- [48] R. Schmidt, J.P. Gonjal, E. Morán, Microwaves: microwave-assisted hydrothermal synthesis of nanoparticles, *CRC Concise Encycl. Nanotechnol.* 12 (2018) 561–570, <https://doi.org/10.1201/b19457-49>.
- [49] K.S. Egorova, V.P. Ananikov, Toxicity of metal compounds: knowledge and myths, *Organometallics* 36 (2017) 4071–4090, <https://doi.org/10.1021/acs.organomet.7b00605>.
- [50] C.C.L. McCrory, S. Jung, J.C. Peters, T.F. Jaramillo, Benchmarking heterogeneous electrocatalysts for the oxygen evolution reaction, *J. Am. Chem. Soc.* 135 (2013) 16977–16987, <https://doi.org/10.1021/ja407115p>.
- [51] F.L. Silva, R.M. Reis, W.R.P. Barros, R.S. Rocha, M.R.V. Lanza, Electrogeneration of hydrogen peroxide in gas diffusion electrodes: application of iron (II) phthalocyanine as a modifier of carbon black, *J. Electroanal. Chem.* (2014) 722–723, <https://doi.org/10.1016/j.jelechem.2014.03.007>, 32–37.
- [52] J. Moreira, V. Bocalon Lima, L. Athie Goulart, M.R.V. Lanza, Electrosynthesis of hydrogen peroxide using modified gas diffusion electrodes (MGDE) for environmental applications: quinones and azo compounds employed as redox modifiers, *Appl. Catal. B Environ.* 248 (2019) 95–107, <https://doi.org/10.1016/j.apcatb.2019.01.071>.
- [53] S.C. Padmanabhan, T.W. Collins, S.C. Pillai, D.E. McCormack, J.M. Kelly, J. D. Holmes, M.A. Morris, A conceptual change in crystallisation mechanisms of oxide materials from solutions in closed systems, *Sci. Rep.* 10 (2020) 18414, <https://doi.org/10.1038/s41598-020-75241-z>.
- [54] Z. Azdad, L. Marot, L. Moser, R. Steiner, E. Meyer, Valence band behaviour of zirconium oxide, Photoelectron and Auger spectroscopy study, *Sci. Rep.* 8 (2018) 1–6, <https://doi.org/10.1038/s41598-018-34570-w>.
- [55] L. Zhang, A.A.S. Gonçalves, M. Jaroniec, Identification of preferentially exposed crystal facets by X-ray diffraction, *RSC Adv.* 10 (2020) 5585–5589, <https://doi.org/10.1039/D0RA00769B>.
- [56] Y. Liang, Y. Li, H. Wang, J. Zhou, J. Wang, T. Regier, H. Dai, Co₃O₄ nanocrystals on graphene as a synergistic catalyst for oxygen reduction reaction, *Nat. Mater* 10 (2011) 780–786, <https://doi.org/10.1038/nmat3087>.
- [57] A. Sarapu, K. Vaik, D.J. Schiffrin, K. Tammeveski, Electrochemical reduction of oxygen on anodically pre-treated and chemically grafted glassy carbon electrodes in alkaline solutions, *J. Electroanal. Chem.* 541 (2003) 23–29, <https://doi.org/10.1016/j.jelecom.2003.10.003>.
- [58] K. Tammeveski, K. Kontturi, R.J. Nichols, R.J. Potter, D.J. Schiffrin, Surface redox catalysis for O₂ reduction on quinone-modified glassy carbon electrodes, *J. Electroanal. Chem.* 515 (2001) 101–112, [https://doi.org/10.1016/S0022-0728\(01\)00633-7](https://doi.org/10.1016/S0022-0728(01)00633-7).
- [59] U.A. Paulus, T.J. Schmidt, H.A. Gasteiger, R.J. Behm, Oxygen reduction on a high-surface area Pt/Vulcan carbon catalyst: a thin-film rotating ring-disk electrode study, *J. Electroanal. Chem.* 495 (2001) 134–145, [https://doi.org/10.1016/S0022-0728\(00\)00407-1](https://doi.org/10.1016/S0022-0728(00)00407-1).
- [60] G. Chen, M.B. Stevens, Y. Liu, L.A. King, J. Park, T.R. Kim, R. Sinclair, T. F. Jaramillo, Z. Bao, Nanosized zirconium porphyrinic metal–organic frameworks that catalyze the oxygen reduction reaction in acid, *Small Methods* 4 (2020), 2000085, <https://doi.org/10.1002/smt.202000085>.
- [61] K.P. Kepp, A quantitative scale of oxophilicity and thiophilicity, *Inorg. Chem.* 55 (2016) 9461–9470, <https://doi.org/10.1021/acs.inorgchem.6b01702>.
- [62] B. Rungtaweeworanit, J. Baek, J.R. Araujo, B.S. Archanjo, K.M. Choi, O.M. Yaghi, G.A. Somorjai, Copper nanocrystals encapsulated in Zr-based metal-organic frameworks for highly selective CO₂ hydrogenation to methanol, *Nano Lett.* 16 (2016) 7645–7649, <https://doi.org/10.1021/acs.nanolett.6b03637>.
- [63] R.M. Reis, A.A.G.F. Beati, R.S. Rocha, M.H.M.T. Assumpção, M.C. Santos, R. Bertazzoli, M.R. V Lanza, Use of gas diffusion electrode for the in situ generation of hydrogen peroxide in an electrochemical flow-by reactor, *Ind. Eng. Chem. Res.* 51 (2012) 649–654, <https://doi.org/10.1021/ie201317u>.
- [64] J.F. Carneiro, R.S. Rocha, P. Hammer, R. Bertazzoli, M.R.V. Lanza, Hydrogen peroxide electrogeneration in gas diffusion electrode nanostructured with Ta₂O₅, *Appl. Catal. Gen.* 517 (2016) 161–167, <https://doi.org/10.1016/j.apcata.2016.03.013>.
- [65] T. Muddemann, D.R. Haupt, M. Sievers, U. Kunz, Improved operating parameters for hydrogen peroxide-generating gas diffusion electrodes, *Chemie Ing. Tech.* 92 (2020) 505–512, <https://doi.org/10.1002/cite.201900137>.
- [66] W.R.P. Barros, R.M. Reis, R.S. Rocha, M.R.V. Lanza, Electrogeneration of hydrogen peroxide in acidic medium using gas diffusion electrodes modified with cobalt (II) phthalocyanine, *Electrochim. Acta* 104 (2013) 12–18, <https://doi.org/10.1016/j.electacta.2013.04.079>.
- [67] A.J. dos Santos, S. Garcia-Segura, S. Dosta, I.G. Cano, C.A. Martínez-Huitle, E. Brillas, A ceramic electrode of ZrO₂-Y₂O₃ for the generation of oxidant species in anodic oxidation. Assessment of the treatment of Acid Blue 29 dye in sulfate and chloride media, *Sep. Purif. Technol.* 228 (2019), 115747, <https://doi.org/10.1016/j.seppur.2019.115747>.

Supplementary Information for

Sustainable microwave-assisted hydrothermal synthesis of carbon-supported ZrO₂ nanoparticles for H₂O₂ electrogeneration

Matheus S. Kronka^{1*}, Paulo J. M. Cordeiro-Junior¹, Letícia Mira¹, Aleksandro J. dos Santos¹, Guilherme V. Fortunato^{1*}, Marcos R.V. Lanza^{1*}

¹*São Carlos Institute of Chemistry, University of São Paulo, Avenida Trabalhador São-Carlense 400, São Carlos, SP, 13566-590, Brazil.*

*Corresponding authors' e-mails:

mskonka@usp.br (M.S. Kronka)

g.fortunato@usp.br (G.V. Fortunato)

marcoslanza@usp.br (M. R. V. Lanza)

Experimental Details for the accumulation of H₂O₂ in the bench-scale electrochemical cell

The GDE cathode (with geometric area of 20 cm²) was produced from the following: 1) 7 g of structural mass containing carbon black PL6C homogenized with 40% of PTFE; 2) 1 g of catalytic mass containing the ZrO₂/PL6C (or unmodified PL6C) catalyst homogenized with 20% of PTFE; and 3) a commercial carbon cloth PW03 on top of the cathode which provides physical stability to the catalytic layer. The proposed methodology developed in this work was based on the adaptation of the work conducted by Valim et al. (2013) [1]. All the electrolysis assays related to the GDE were conducted in a bench-scale electrochemical cell with capacity for 250 mL solution. The electrolysis assays were conducted potentiostatically at -0.8, -1.2, -1.6, and -2.0 V vs. Ag/AgCl under constant O₂ flow of 0.2 bar.

Complementary results and discussion on effect of initial Zr precursor concentration

The microwave-assisted hydrothermal synthesis method generates an abrupt increase in water temperature, especially due to the high source of power employed in the process, and requires a few minutes for the reaction to complete. The reaction time required under the MAH method is equivalent to 24 - 48 hours of reaction under a conventionally autoclave heating method [2–6]. Microwave radiation affects the orientation of the polar molecules of the solvent, and this, in turn, leads to an increase in the molecular agitation in the system. The greatest advantage of the microwave-assisted hydrothermal method lies in the uniformity of heating it provides compared to the conventional heating method, which occurs from an induction heating source, leading to a temperature gradient in the system [2–6]. The changes in the synthesis parameters of the ZrO₂/PCL6 catalyst were made so as to boost the catalytic activity for ORR and the selectivity toward the production of H₂O₂.

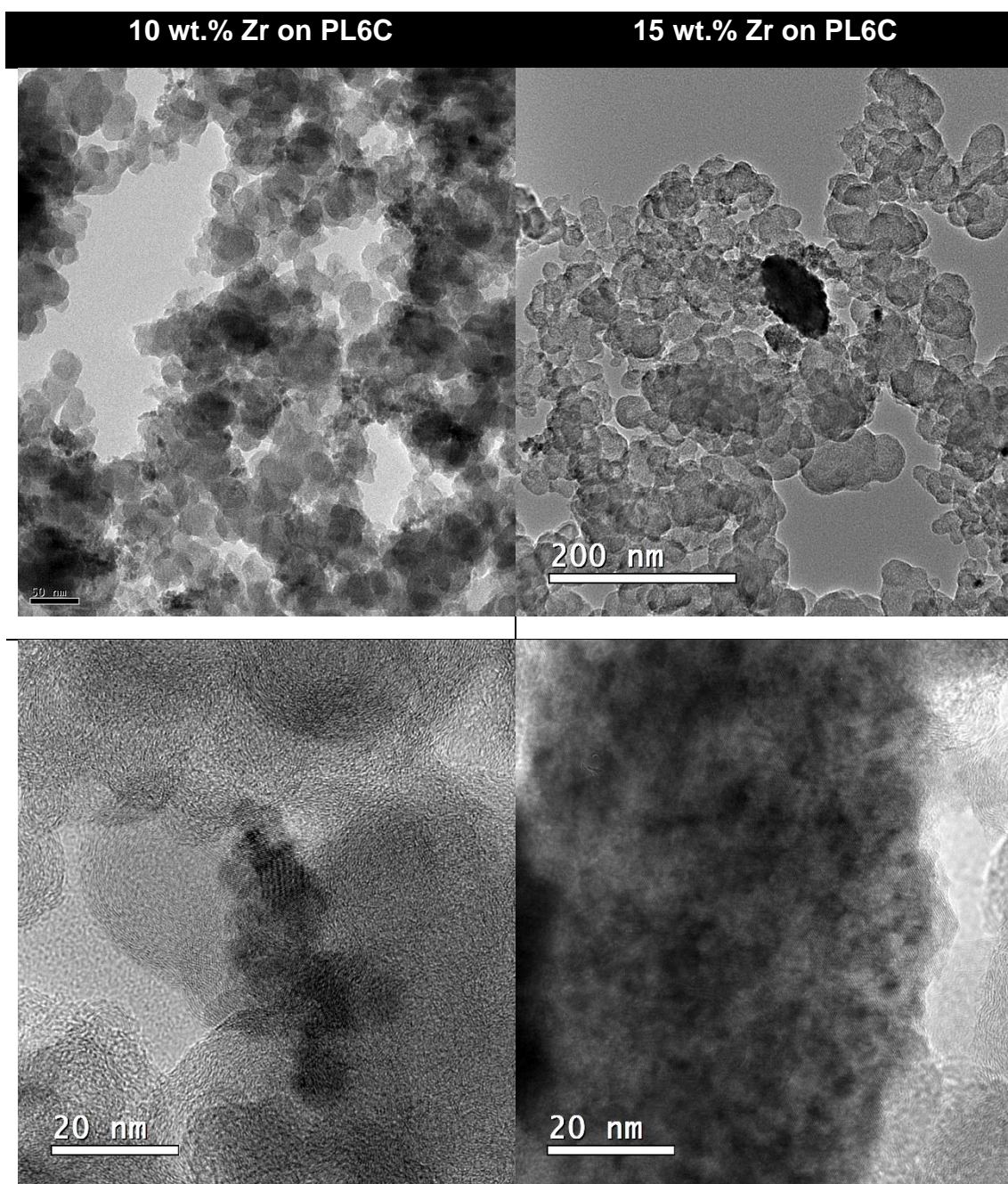


Figure S1. Bright-field STEM and TEM images for 10 wt.% Zr and 15 wt.% Zr on PL6C.

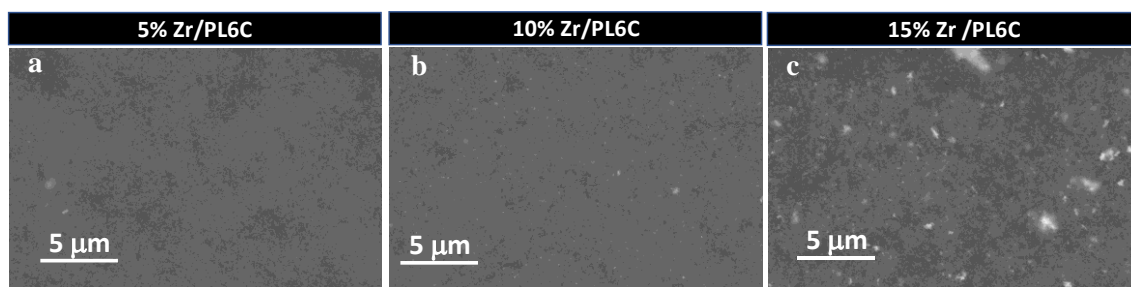


Figure S2. SEM images of (b) 5, (c) 10 and (d) 15wt.% of ZrO₂/PL6C from backscatter electrons (BSE) mode.

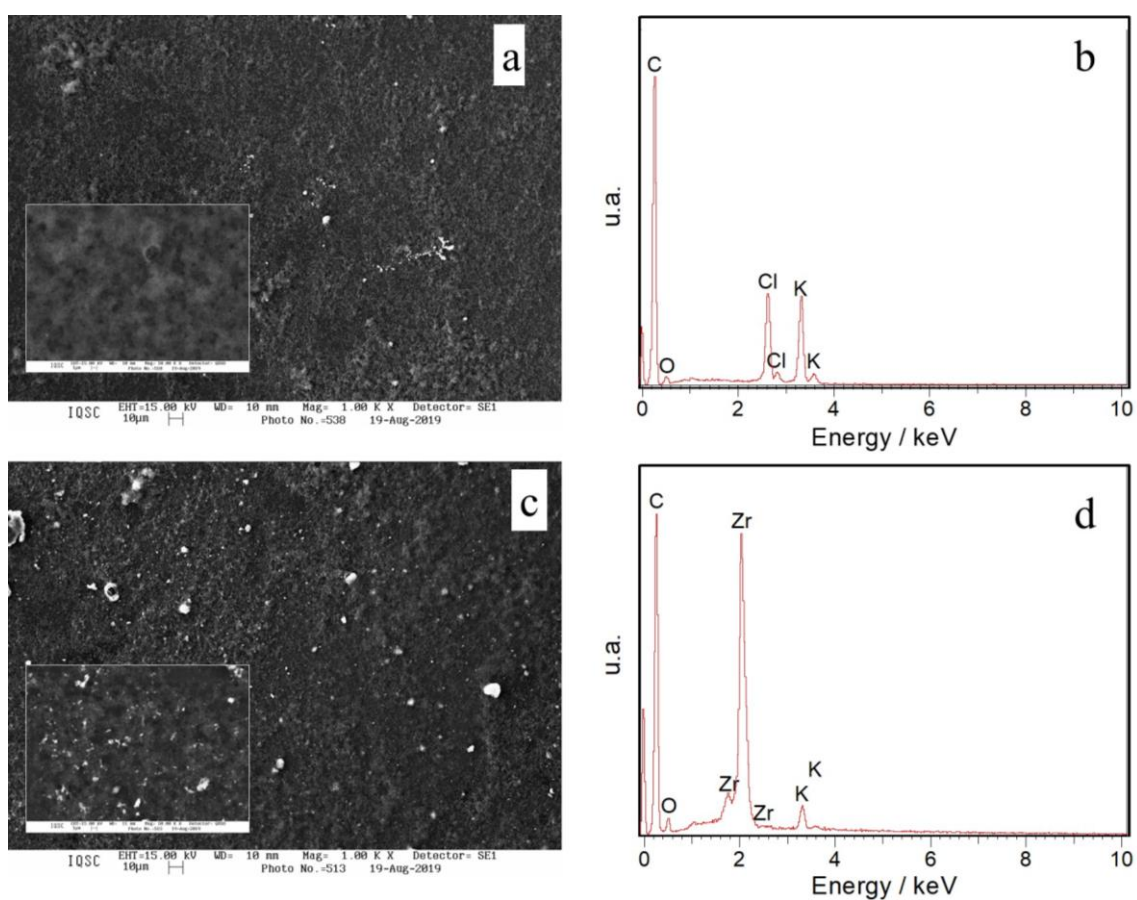


Figure S3. SEM images with magnification of 1000 x (inset: magnification of 10.000 x) in BSE mode and EDS spectra for (a,b) control PL6C (0 wt.% Zr) and (c,d) 15 wt.% Zr/PL6C.

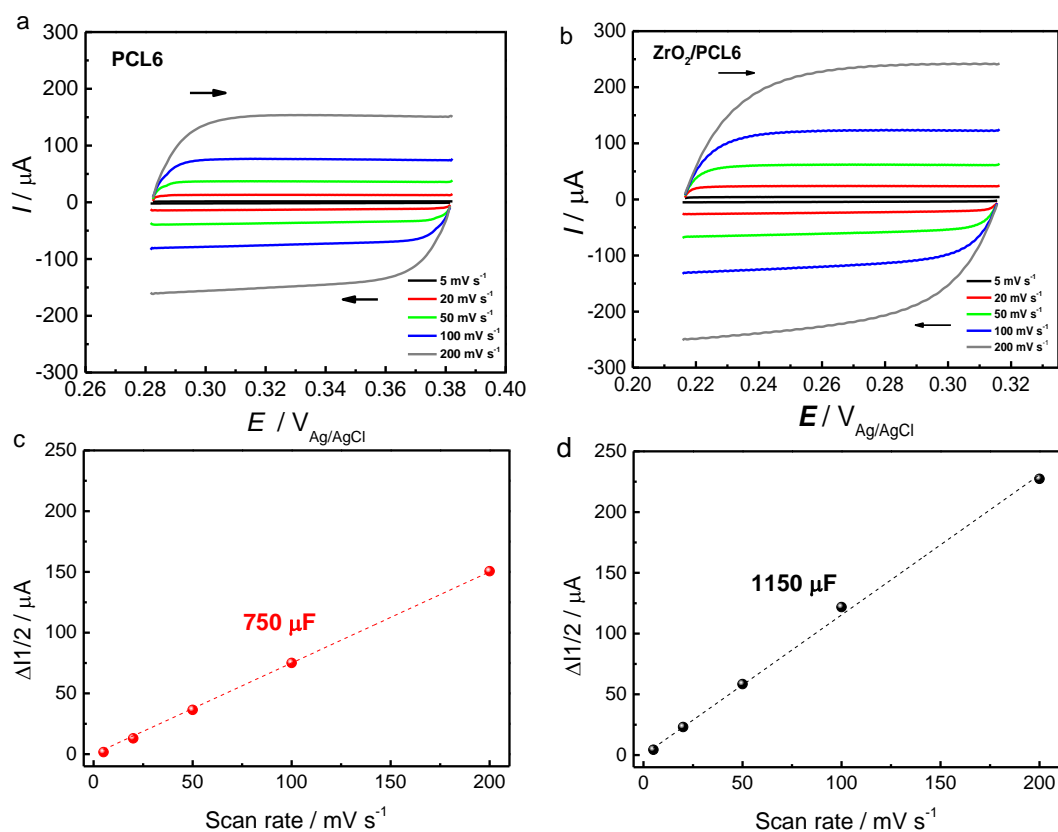


Figure S4. Cyclic voltammograms obtained from the application of N₂-saturated 0.1 mol L⁻¹ K₂SO₄ (pH = 2.5), at several scan rates for (a) bare PL6C, and (b) 10 wt.% Zr on PL6C. $\Delta I/2$ vs. scan rate plots for (c) bare PL6C and (d) 10 wt.% Zr on PL6C.

Table S1. Estimated *ECSA* values by capacitance for the catalysts investigated.

Catalyst	Capacitance (μF)	Specific Capac. (μF cm ⁻²)*	<i>ECSA</i> (cm ²)	<i>ECSA</i> (m ² g ⁻¹ _{catalyst})
PCL6	750	17.0	42.8	85.6
ZrO ₂ /PCL6	1150	17.0	67.6	128.6

*Values considering the capacitance of flat and smooth surfaces of carbonaceous materials [7].

Complementary results on effect of microwave-assisted hydrothermal synthesis time

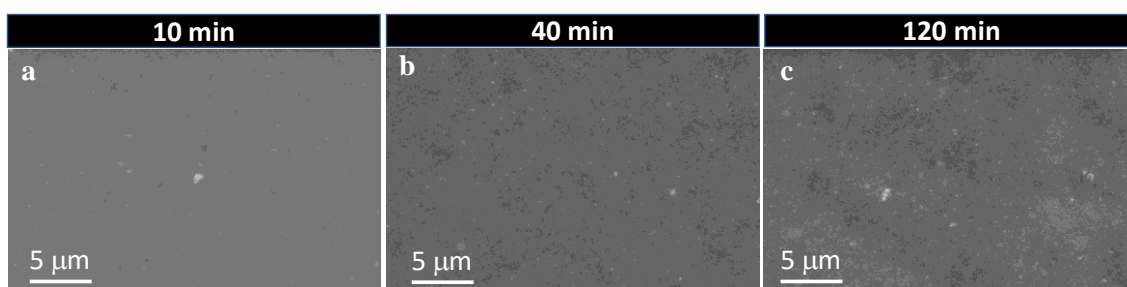


Figure S5. SEM images of (b) 5, (c) 10 and (d) 15wt.% of $\text{ZrO}_2/\text{PL6C}$ from backscatter electrons (BSE) mode.

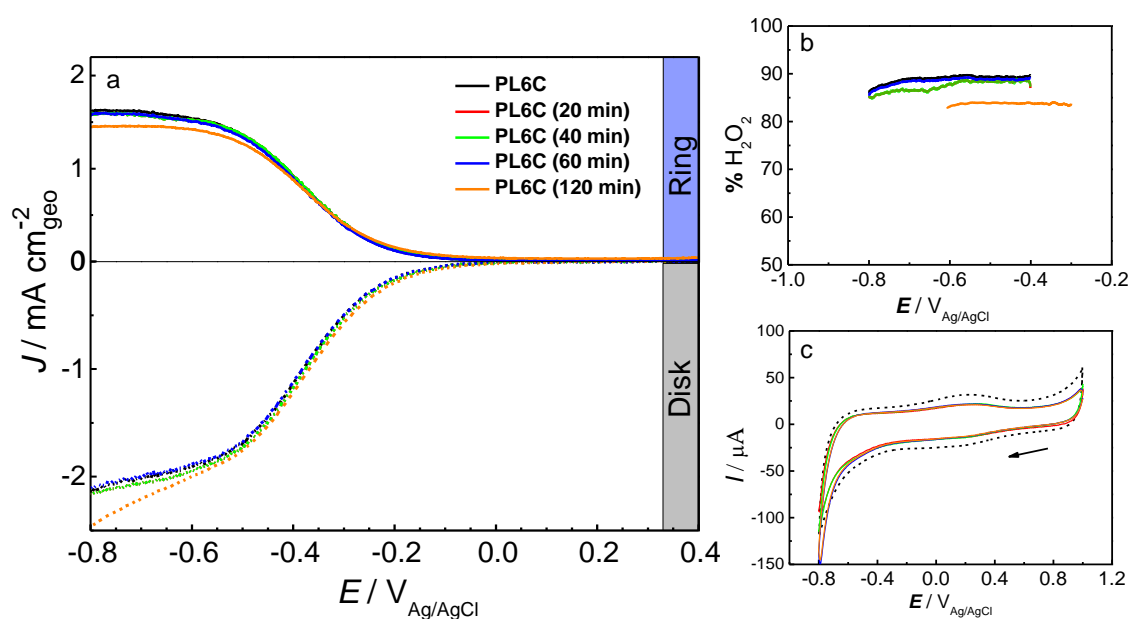


Figure S6. Results obtained from the electrochemical synthesis using microwave in the absence of the metallic precursor. **(a)** Cyclic voltammograms obtained from the application of N_2 -saturated $0.1 \text{ mol L}^{-1} \text{ K}_2\text{SO}_4$, $\text{pH}=2.5$ (H_2SO_4 adjusted), with scan rate of 50 mV s^{-1} , potential window ranging from 1 to $-0.8 \text{ V}_{\text{Ag}/\text{AgCl}}$. **(b)** Linear sweep voltammetry in RRDE curves for the disk electrode obtained from the application of O_2 -saturated $0.1 \text{ mol L}^{-1} \text{ K}_2\text{SO}_4$, $\text{pH}=2.5$ (H_2SO_4 adjusted), with scan rate of 5 mV^{-1} and potential window ranging from 0.4 to -0.8 V at 900 rpm; **(c)** The values of the currents obtained for the Pt ring electrode during the potential scan on the disk electrode. The ring potential was kept at $1.0 \text{ V}_{\text{Ag}/\text{AgCl}}$.

Complementary results on effect of temperature and pressure

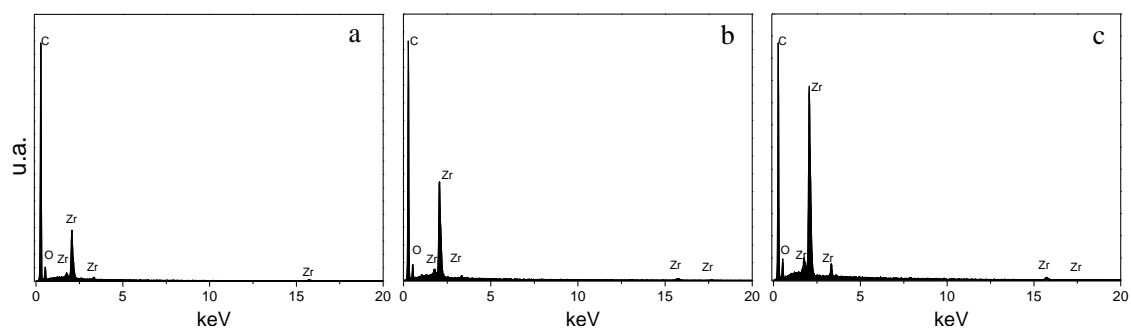


Figure S7. EDX spectra for $\text{ZrO}_2/\text{PL6C}$ catalysts produced at (a) 120, (b) 140, and (c) 160 °C of MAH synthesis temperature.

Complementary results related to the topic: Further investigation of the optimized catalyst**Table S2.** Comparing the catalyst composition, synthesis approach, and electrocatalytic performance for ORR in terms of onset potential (E_{onset} vs. RHE) and selectivity to H_2O_2 production (in %) for reported metal oxide-based electrocatalysts.

Catalyst composition		Synthesis conditions				Performance of the ORR			Ref
Oxide	Carbon-based support material	Method	Solvent	Time ^a (min)	Temperature (°C)	Electrolyte	E_{onset} (V_{RHE})	Selectivity (%)	
5.1 wt.% ZrO_2	Carbon black Printex L6 (PL6C)	Microwave-assisted hydrothermal	Water	40	140	0.1 mol L ⁻¹ K_2SO_4 (pH = 2.5)	0.33	88.8	*
5.0 wt.% ZrO_2	Carbon black Printex L6 (PL6C)	Polymeric precursors (Pechini)	Ethylene glycol + citric acid	30	500	0.1 mol L ⁻¹ K_2SO_4 (pH = 2.0)	0.32	84.2	[8]
1.0 wt.% ZrO_2	Reduced graphene oxide (rGO)	Classic hydrothermal	Anhydrous ethanol	180	150	0.1 mol L ⁻¹ K_2SO_4 (pH = 2.0)	0.31	89.5	[9]
15.0 wt.% Nb_2O_5	Reduced graphene oxide (rGO)	Classic hydrothermal	Anhydrous ethanol	180	150	0.1 mol L ⁻¹ K_2SO_4 (pH = 2.0)	0.32	85.3	[10]
7.0 wt.% V_2O_5	Carbon black Vulcan XC	Polymeric precursors (Pechini)	Ethylene glycol + citric acid	120	400	1 mol L ⁻¹ NaOH	~0.80	(-)	[11]
4.0 wt.% CeO_2	Carbon Black Vulcan XC	Polymeric precursors (Pechini)	Ethylene glycol + citric acid	120	400	1 mol L ⁻¹ NaOH	~0.79	88	[12]
5.0 wt.% Fe_3O_4	Graphene	Co-precipitation	Water + NaBH_4	20	90	1 mol L ⁻¹ NaOH	~0.81	64	[13]
5.0 wt.% Fe_3O_4	Carbon Black Printex L6 (PL6C)	Co-precipitation	Water + NaBH_4	20	90	1 mol L ⁻¹ NaOH	~0.76	68	[13]

* Results obtained in the present study. ^aThe time related to heating (ramping) and cooling were not counted.

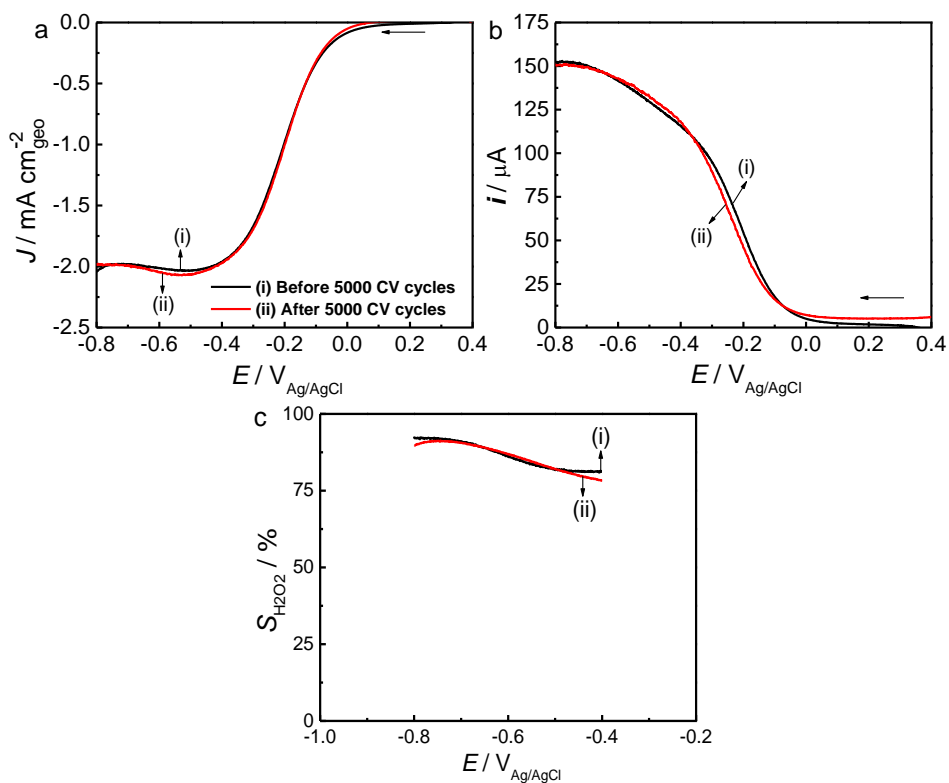


Figure S8. (a) Linear sweep voltammetry curves before and after long-term stability test obtained from the application of O_2 -saturated $0.1 \text{ mol L}^{-1} \text{ K}_2\text{SO}_4$, $\text{pH}=2.5$ (H_2SO_4 adjusted), at scan rate of 5 mV^{-1} and potential window ranging from 0.4 to -0.8 V at 900 rpm; (b) ring current (polarized at 1.0 V) for detection of H_2O_2 during the voltametric test on the RRDE disk; (c) Selectivity toward H_2O_2 ($S_{\text{H}_2\text{O}_2}$) production under several different potentials.

Complementary results and discussion on H₂O₂ electrogeneration using the gas diffusion electrode approach

Carbon cloth modified GDE

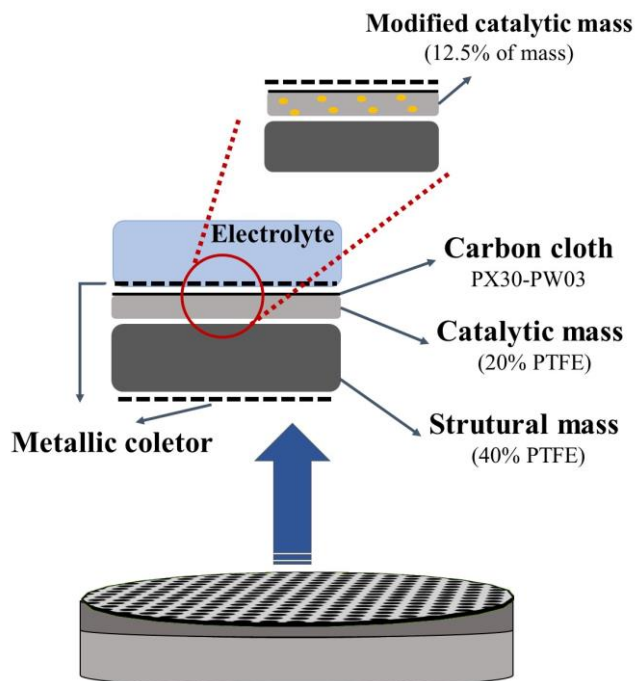


Figure S9. Structural scheme of gas diffusion electrode (GDE) used in H₂O₂ electrogeneration assays.

The bar chart in Figure S10c shows the concentration of H₂O₂ (C(H₂O₂)) as a function of the applied potentials for the PL6C and ZrO₂/PL6C electrodes. The results confirm the superior catalytic performance of the ZrO₂/PL6C electrode; the use of this catalyst led to H₂O₂ electrogeneration 2.2 times higher than the unmodified PL6C electrode under all the potentials investigated.

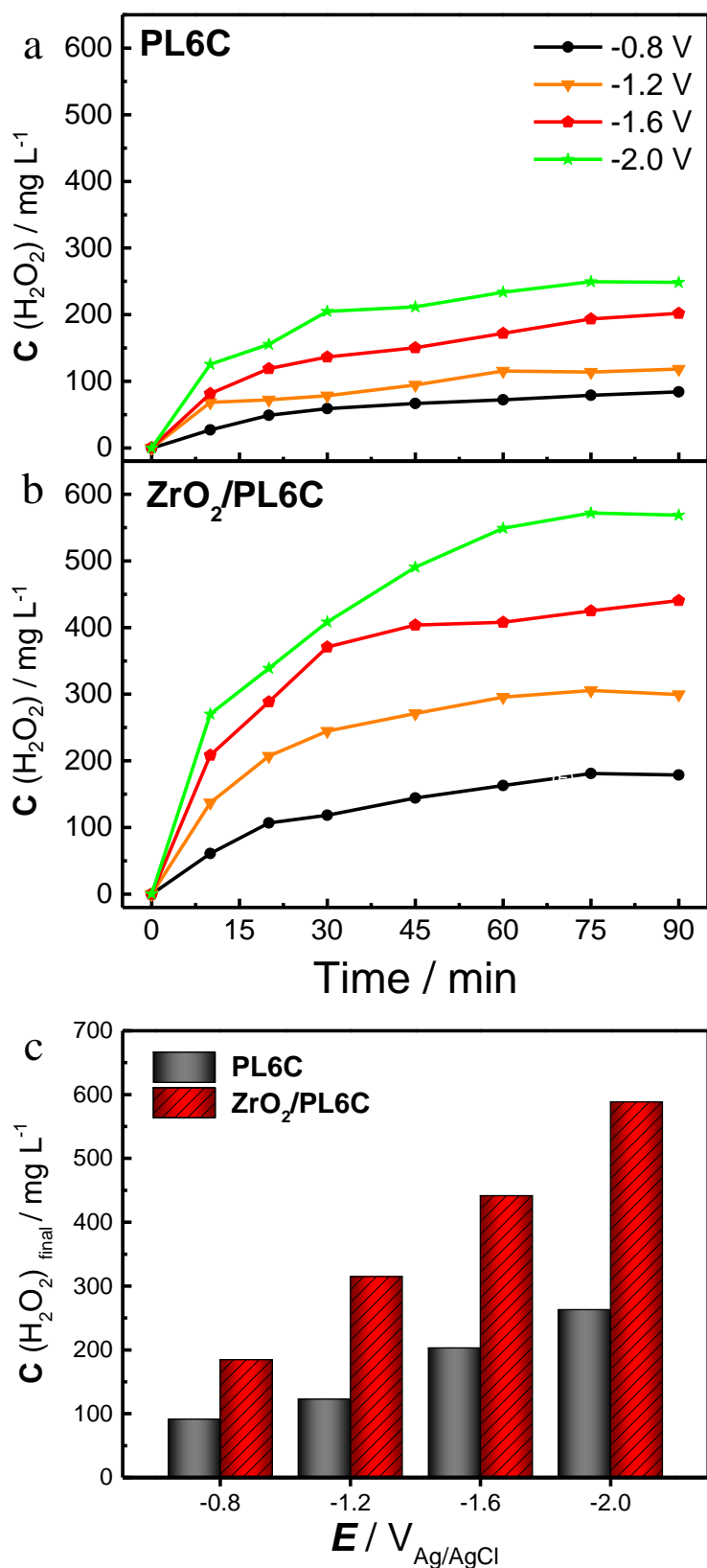


Figure S10. Analysis of H_2O_2 production for a period of 90 minutes using bench-scale electrochemical cell with $0.1 \text{ mol L}^{-1} \text{ K}_2\text{SO}_4$ (pH 2.5), platinized titanium counter electrode, Ag/AgCl reference electrode, and (a) PL6C and (b) 5 wt% $\text{ZrO}_2/\text{PL6C}$ GDEs used as working electrodes; (c) comparison of the maximum production of H_2O_2 after 90 min.

Table S3 presents the energy consumption (EC) and pseudo-zero order kinetics (k_{app}) values obtained for each of the electrolysis assays conducted. The kinetic values were obtained from the linear curve of H_2O_2 production for a period of 30 minutes due to the low influence of the parallel reactions. One will observe that an increase in the value of $E_{applied}$ led to an increase in the k_{app} value. Considering that the ORR occurs at the GDE triple interface (electrode/gas/electrolyte), there is an unlimited amount of O_2 available; as such, the ORR is fully controlled by charge transfer, and the applied potential exerts a direct influence over the electrogeneration of H_2O_2 . The k_{app} values obtained in this study were found to be higher for the $ZrO_2/PL6C$ compared to the PL6C under all the potentials investigated. The main kinetic values were recorded at $-2.0 V_{Ag/AgCl}$ for each electrode, and the kinetic value obtained for $ZrO_2/PL6C$ was $2.6 \times 10^{-1} \text{ mg L}^{-1} \text{ s}^{-1}$; this is, on average, 2 times higher than that of the unmodified PL6C, which presented a kinetic value of $1.3 \times 10^{-1} \text{ mg L}^{-1} \text{ s}^{-1}$. These findings also validate the catalytic influence of $ZrO_2/PL6C$ in H_2O_2 production via the application of the MAH method. Based on the EC values shown in Table 1, it is worth noting that, although there was an increase in the energy consumption for both electrodes, the $ZrO_2/PL6C$ catalyst exhibited relatively lower EC values compared to the unmodified PL6C under all the potentials investigated. The $ZrO_2/PL6C$ catalyst reduced more than 150 kWh g^{-1} of energy consumption in the electrolysis conducted at $-2.0 V_{Ag/AgCl}$ compared to the unmodified PL6C.

Table S3. Values obtained related to energy consumption (EC) and pseudo-zero order kinetics (k_{app}) for $ZrO_2/PL6C$ and PL6C under different electrolysis potential.

$E_{applied}$ (V)	PL6C		$ZrO_2/PL6C$	
	EC (kWh g^{-1})	k_{app} ($\text{mg L}^{-1} \text{ s}^{-1}$)	EC (kWh g^{-1})	k_{app} ($\text{mg L}^{-1} \text{ s}^{-1}$)
-0.8	85.4	3.6×10^{-2}	72.5	7.5×10^{-2}
-1.2	185.0	5.3×10^{-2}	102.8	1.5×10^{-1}
-1.6	269.1	8.7×10^{-2}	141.9	2.1×10^{-1}
-2.0	357.6	1.3×10^{-1}	204.4	2.6×10^{-1}

References

- [1] R.B. Valim, R.M. Reis, P.S. Castro, A.S. Lima, R.S. Rocha, M. Bertotti, M.R. V Lanza, Electrogeneration of hydrogen peroxide in gas diffusion electrodes modified with tert-butyl-anthraquinone on carbon black support, *Carbon N. Y.* 61 (2013) 236–244. doi:10.1016/j.carbon.2013.04.100.
- [2] B.L. Cushing, V.L. Kolesnichenko, C.J. O'Connor, Recent Advances in the Liquid-Phase Syntheses of Inorganic Nanoparticles, *Chem. Rev.* 104 (2004) 3893–3946. doi:10.1021/cr030027b.
- [3] I. Bilecka, M. Niederberger, Microwave chemistry for inorganic nanomaterials synthesis, *Nanoscale.* 2 (2010) 1358–1374. doi:10.1039/b9nr00377k.
- [4] G. Barreto, G. Morales, A. Cañizo, N. Eyler, Microwave Assisted Synthesis of ZnO Tridimensional Nanostructures, *Procedia Mater. Sci.* 8 (2015) 535–540. doi:10.1016/j.mspro.2015.04.106.
- [5] K. Wang, T. Huang, H. Liu, Y. Zhao, H. Liu, C. Sun, Size control synthesis of palladium oxide nanoparticles by microwave irradiation, *Colloids Surfaces A Physicochem. Eng. Asp.* 325 (2008) 21–25. doi:10.1016/j.colsurfa.2008.04.027.
- [6] R. Schmidt, J.P. Gonjal, E. Morán, Microwaves: Microwave-Assisted Hydrothermal Synthesis of Nanoparticles, *CRC Concise Encycl. Nanotechnol.* 12 (2018) 561–570. doi:10.1201/b19457-49.
- [7] C.C.L. McCrory, S. Jung, J.C. Peters, T.F. Jaramillo, Benchmarking Heterogeneous Electrocatalysts for the Oxygen Evolution Reaction, *J. Am. Chem. Soc.* 135 (2013) 16977–16987. doi:10.1021/ja407115p.
- [8] J.F. Carneiro, L.C. Trevelin, A.S. Lima, G.N. Meloni, M. Bertotti, P. Hammer, R. Bertazzoli, M.R.V. Lanza, Synthesis and Characterization of ZrO₂/C as Electrocatalyst for Oxygen Reduction to H₂O₂, *Electrocatalysis.* 8 (2017) 189–195. doi:10.1007/s12678-017-0355-0.
- [9] J.F. Carneiro, M.J. Paulo, M. Siaj, A.C. Tavares, M.R. V Lanza, Zirconia on Reduced Graphene Oxide Sheets: Synergistic Catalyst with High Selectivity for H₂O₂ Electrogeneration, *ChemElectroChem.* 4 (2017) 508–513. doi:10.1002/celec.201600760.
- [10] J.F. Carneiro, M.J. Paulo, M. Siaj, A.C. Tavares, M.R.V. Lanza, Nb₂O₅ nanoparticles supported on reduced graphene oxide sheets as electrocatalyst for the H₂O₂ electrogeneration, *J. Catal.* 332 (2015) 51–61. doi:10.1016/j.jcat.2015.08.027.
- [11] P.S. Simas, V.S. Antonin, L.S. Parreira, P. Hammer, F.L. Silva, M.S. Kronka, R.B. Valim, M.R.V. Lanza, M.C. Santos, Carbon Modified with Vanadium Nanoparticles for Hydrogen Peroxide Electrogeneration, *Electrocatalysis.* 8 (2017) 311–320. doi:10.1007/s12678-017-0366-x.
- [12] M.H.M.T. Assumpção, A. Moraes, R.F.B. De Souza, I. Gaubeur, R.T.S. Oliveira, V.S. Antonin, G.R.P. Malpass, R.S. Rocha, M.L. Calegari, M.R.V. Lanza, M.C. Santos, Low content cerium oxide nanoparticles on carbon for hydrogen peroxide electrosynthesis, *Appl. Catal. A Gen.* 411–412 (2012) 1–6. doi:10.1016/j.apcata.2011.09.030.
- [13] W.R.P. Barros, Q. Wei, G. Zhang, S. Sun, M.R.V. Lanza, A.C. Tavares, Oxygen reduction to hydrogen peroxide on Fe₃O₄ nanoparticles supported on Printex carbon and Graphene, *Electrochim. Acta.* 162 (2015) 263–270. doi:10.1016/j.electacta.2015.02.175.

CHAPTER III

Using Au NPs anchored on ZrO₂/carbon black toward more efficient H₂O₂ electrogeneration in flow-by reactor for carbaryl removal in real wastewater

Author Contributions: Matheus S. Kronka: Investigation, Conceptualization, Methodology, Writing – original draft, Writing – review & editing. Guilherme V. Fortunato: Investigation, Conceptualization, Writing – original draft, Writing – review & editing. Leticia Mira: Methodology, Investigation, Writing – original draft. Alexsandro J. dos Santos: Investigation, Conceptualization, Writing – original draft, Writing – review & editing. Marcos R.V. Lanza: Supervision, Funding acquisition, Writing – review & editing.

In this paper we exhibit the design of a material based on Au nanoparticles supported on the ZrO₂/PL6C hybrid material (produced in Chapter II) as an active ORR catalyst towards H₂O₂ production in acidic medium. A careful discussion was conducted concerning the role of the oxophilic support in anchoring the gold nanoparticles, as well as the contribution of the characteristics of the material on its electrochemical and catalytic properties to produce H₂O₂. From this strategy, one can see that the ZrO₂/PL6C, featuring electronegative properties, better accommodated the gold nanoparticles compared to the bare PL6C matrix. The Au NPs proved to be better stabilized under the surface of the composite containing zirconium oxides, reaching a small particle size due to the lower influence of the positive charge of the substrate. The fabrication of a GDE modified with 200 μg cm⁻² of the catalysts applied in a flow-by reactor for the treatment of a real wastewater contaminated with Carbaryl provided the opportunity to observe the enhanced catalytic effect of Au₂ZrO₂/PL6C in a more realistic system.

This article/chapter was published in Chemical Engineering Journal, v. 452, **M.S. Kronka**; G.V. Fortunato; L. Mira; A.J. dos Santos; M.R.V. Lanza. Using Au NPs anchored on ZrO₂/carbon black toward more efficient H₂O₂ electrogeneration in flow-by reactor for carbaryl removal in real wastewater, 139598, Copyright Elsevier (2023).



Contents lists available at ScienceDirect

Chemical Engineering Journal

journal homepage: www.elsevier.com/locate/cej

Using Au NPs anchored on ZrO₂/carbon black toward more efficient H₂O₂ electrogeneration in flow-by reactor for carbaryl removal in real wastewater

Matheus S. Kronka^{*}, Guilherme V. Fortunato, Leticia Mira, Alexsandro J. dos Santos, Marcos R. V. Lanza^{*}

São Carlos Institute of Chemistry, University of São Paulo, Avenida Trabalhador São-Carlense 400, São Carlos, SP 13566-590, Brazil

ARTICLE INFO

Keywords:

Hybrid carbon-based support
Gold nanoparticles
Electrochemical advanced oxidation process
Carbaryl removal
Urban wastewater

ABSTRACT

In the present study, we designed a highly efficient catalyst for H₂O₂ production using gold nanoparticles (Au NPs) anchored on hybrid substrate composed of ZrO₂ and Printex L6 carbon (Au-ZrO₂/PL6C). The higher selectivity of Au-ZrO₂/PL6C (97%) toward H₂O₂ electrogeneration and its improved activity in terms of ORR onset potential (140 mV for more positive values) compared to Au/PL6C (80%) were attributed to the synergism between Au NPs anchored on ZrO₂/PL6C hybrid support. The results obtained from the application of the catalysts for H₂O₂ generation on gas diffusion electrode (GDE) after 120 min of electrolysis reflected the following order of efficiency: PL6C (~140 mg L⁻¹) < ZrO₂/PL6C (~235 mg L⁻¹) < Au/PL6C (~374 mg L⁻¹) < Au-ZrO₂/PL6C (~600 mg L⁻¹). Given that Au-ZrO₂/PL6C exhibited the highest catalytic efficiency, this catalyst was employed for the removal of carbaryl (CBR) using different electrochemical advanced oxidation processes. The CBR degradation tests exhibited pseudo first-order kinetics, with the electro-Fenton (EF) and photoelectro-Fenton (PEF) processes recording the fastest removal kinetics (3.5 × 10⁻² s⁻¹ and 4.1 × 10⁻² s⁻¹, respectively). The PEF process exhibited the highest efficiency in terms of organic by-products mineralization; this was attributed to the additional photodecarboxylation of the Fe(III)-RCOOH complexes by UVC light. The aromatic by-products, short chain carboxylic acids, and ionic nitrogen species produced during the mineralization process contributed to the successful degradation of CBR. Apart from the analysis with synthetic water, the study also analyzed the treatment of urban wastewater spiked with CBR using a pre-pilot flow plant.

1. Introduction

The increasingly growing global demand for food caused by the dramatic rise in human population over the last 50 years has generated the need for massive production of food, and this has led to the expansion of agricultural production worldwide [1]. The expansion of agricultural activities has also given rise to widespread use of pesticides which have become indispensable for ensuring the large-scale production of food with high quality through the prevention and control of various pests and disease carriers as this contributes toward enhancing agricultural production by reducing crop losses and increasing crop yields without expanding the planted field [1,2]. According to the Food and Agriculture Organization of the United Nations (FAO), the annual global consumption of pesticides between 2010 and 2019 was >4 million tons (on average), with China, USA and Brazil accounting for

over 60% of the total amount of pesticides consumed worldwide [3]. Despite the aforementioned benefits of pesticides, their chemical compositions contain hazardous compounds, and as such, their rampant application in agricultural production has contributed significantly toward an increase in the contamination of water bodies (through leaching, erosion, and so forth) and environmental pollution worldwide. In fact, several studies reported in the literature have detected the presence of pesticides in groundwater, wastewater, surface water and tap water at concentrations ranging from 10 to 4,000 ng L⁻¹ on average [4,5]. Owing to the hazardous compounds present in pesticides, exposure to these pollutants through water bodies has been found to be extremely toxic and these compounds can potentially act as endocrine disruptors even at very low concentrations. Bearing that in mind, over the last decades, there has been a considerable interest among researchers in the development of highly effective techniques for the treatment of water and

^{*} Corresponding authors.

E-mail addresses: miskonka@usp.br (M.S. Kronka), marcoslanza@usp.br (M.R.V. Lanza).

<https://doi.org/10.1016/j.cej.2022.139598>

Received 30 May 2022; Received in revised form 30 September 2022; Accepted 2 October 2022

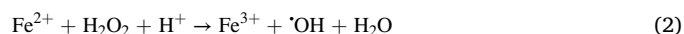
Available online 8 October 2022

1385-8947/© 2022 Elsevier B.V. All rights reserved.

wastewater containing harmful pollutants [6–8].

Electrochemical advanced oxidation processes (EAOPs) are a highly promising technology which has been proven to be suitable for application in water and wastewater treatment. Among the wide range of EAOPs reported in the literature, anodic oxidation (AO) is the most commonly applied technique. In the AO process, organic pollutants are oxidized through heterogeneous hydroxyl radicals ($\cdot\text{OH}$) formed on the surface of non-active anodes (M) after water discharge, as demonstrated in Eq. (1). As it has been extensively reported in the literature, boron-doped diamond (BDD) is the best non-active anode for water treatment due to its excellent electrocatalytic properties [7–11].

Despite the unquestionable popularity of AO, EAOPs based on electrochemical Fenton reactions have been reported to be the most efficient treatment techniques when it comes to the removal of hazardous compounds in water matrices [12,13]. This outstanding efficiency of electro-Fenton (EF) processes lies in the production of homogeneous $\cdot\text{OH}$ radicals; these radicals are generated from the activation of H_2O_2 using Fe^{2+} ions via the classical Fenton reaction (see Eq. (2)). Over the recent years, the technological advances made in the homogeneous production of $\cdot\text{OH}$ have sparked the interest of researchers in electro-Fenton processes due to the facilitated mechanism involving the electrochemical production of H_2O_2 from the selective 2-electron oxygen reduction reaction (ORR) using carbon-based catalysts configured as gas diffusion electrodes (GDE) [12–18]. Furthermore, the use of abundant, stable, and low-cost materials for the electrochemical production of H_2O_2 via inorganic metal-oxide photoanodes has also gained considerable traction among researchers in the field [19].



Studies reported in the literature show that carbonaceous catalysts have been widely employed in the composition of porous cathodes for H_2O_2 production thanks to their abundant availability, low cost, and high selectivity for ORR via 2e^- [20–24]. However, the poor electrochemical activity of carbon-based catalysts makes their application in large-scale H_2O_2 production unfeasible [25–28]. In view of that, the use of noble metal-based materials has gained enormous traction among researchers since these metals facilitate charge transfer and this helps enhance the activity of carbon catalysts. In addition to providing us with reactivity patterns, density functional theory (DFT) calculations have become an important tool in the interpretation and design of more efficient catalytic systems for H_2O_2 production [29,30]. Thermodynamic analysis based on DFT has shown that gold (Au) and silver (Ag) are among the class of noble metals that do not interact strongly with O_2 and act to facilitate the stabilization of $\cdot\text{OOH}$ on metal surfaces - the principal intermediate of ORR when it comes to high selectivity for H_2O_2 production [31–34].

While they are evidently scarce and expensive, noble metals have been proven to be capable of effectively resisting the drastic operating conditions imposed by electrochemical devices and are able to operate for a much longer period compared to non-noble metal-based catalysts. Owing to the scarcity and high costs of noble metals, new strategies have been developed with a view to minimizing the amount of these metals used in the composition of noble metal-based catalysts while preserving or even improving the electrochemical properties of the catalysts [31,32,35,36].

To boost the activity and selectivity for H_2O_2 production while decreasing the noble metal loading in the catalysts, some authors have successfully employed relatively lower amount of noble metals in combination with abundant transition metal (TM) oxides and carbon materials [30,37–39]; these studies have employed different strategies which involved the application of highly oxophilic TM oxides close to nanoparticulate Au, Pd and Au-Pd systems to synergistically enhance catalytic activity and influence the reaction pathway by which ORR will preferentially occur. Although some combination of noble metals with

TM oxides and carbonaceous materials has proven to be able to tailor the electrocatalytic activity, selectivity and stability, this class of catalysts can still be further explored for H_2O_2 electroproduction.

Thus, in the present study, we report the development of a novel cathode material based on gold nanoparticles (Au NPs) supported on hybrid substrate composed of ZrO_2 and Printex L6 carbon ($\text{ZrO}_2/\text{PL6C}$) and its application for the efficient production of H_2O_2 in wastewater treatment processes. ZrO_2 was used as supporting material for Au NPs due to its catalytic behavior has been widely studied toward the electrochemical production of H_2O_2 and also for its promising electrocatalytic properties found for electrochemical oxidation [40–43]. An advantage of choosing ZrO_2 is that its eco-friendly production via microwave-assisted hydrothermal synthesis on PL6C ($\text{ZrO}_2/\text{PL6C}$) carbon matrix has been optimized before [42]. Furthermore, ZrO_2 is a non-toxic and electrochemically stable oxide which presents electronegative and oxophilic characteristics when employed as supporting material for noble metal nanoparticles [44]. The electrochemical characterization of the materials and the analysis of their electrocatalytic properties with respect to oxygen reduction reaction (ORR) were evaluated using a rotating ring-disk electrode (RRDE) system, while the kinetics of H_2O_2 production was investigated using gas diffusion electrode (GDE). The Au- $\text{ZrO}_2/\text{PL6C}$ catalyst was used as cathode for H_2O_2 production in an electrochemical system coupled with boron-doped diamond (BDD) anode with a view to evaluating the removal of carbaryl pesticide using different EAOPs. Carbaryl has been classified as an endocrine disruptor present in water sources. The experimental tests targeted at the removal of carbaryl were carried out in a pre-pilot reactor using both synthetic and real wastewater effluents and the Au- $\text{ZrO}_2/\text{PL6C}$ cathode material [45–47].

2. Experimental

2.1. Reagents

The Printex L6 (PL6C) carbon black pigment was purchased from Evonik do Brasil Ltd. The metallic precursor (ZrO_2) $_2\text{CO}_2\cdot\text{H}_2\text{O}$ and $\text{HAuCl}_4\cdot 3\text{H}_2\text{O}$ (99%) were acquired from Alfa Aesar and Sigma Aldrich, respectively. Other reagents employed in the experiments included the following: sulfuric acid (Vetec, 97.8%), isopropyl alcohol (Vetec, 99.5%), potassium sulfate (Sigma-Aldrich, 99%), potassium hydroxide (J. T. Baker, 99%), and 60% v/v dispersion of poly(tetrafluoroethylene) (PTFE - Uniflon). Carbaryl (99%) analytical standard was acquired from Sigma-Aldrich and ion chromatography standards of NH_4^+ , N-NO_2^- and N-NO_3^- in 1000 mg L^{-1} solution were obtained from Specsol. The solutions were prepared using ultrapure water from a Milli-Q system with resistivity $> 18 \text{ M}\Omega \text{ cm}$ at 25 °C.

2.2. Synthesis of $\text{ZrO}_2/\text{PL6C}$, Au- $\text{ZrO}_2/\text{PL6C}$, and Au/PL6C catalysts

To obtain the hybrid Au- $\text{ZrO}_2/\text{PL6C}$, a 2-step hydrothermal synthesis was employed. First, the $\text{ZrO}_2/\text{PL6C}$ hybrid substrate was synthesized by the microwave-assisted hydrothermal method, as described in reference [42].

In the next step, the hydrothermal syntheses (without microwave assistance) of the Au particles supported on $\text{ZrO}_2/\text{PL6C}$ (Au- $\text{ZrO}_2/\text{PL6C}$) and on pure PL6C (Au/PL6C) were carried out based on the method proposed by Fortunato *et al.* [48] with some adaptations. Briefly, an amount of 32 mg of $\text{ZrO}_2/\text{PL6C}$ or bare PL6C was dispersed in 20 mL of Milli-Q water; this was followed by the addition of 240 μL of 0.1 mol L^{-1} HAuCl_4 aqueous solution and 8.4 mg of Pluronic F-127 (structure directing agent of metallic NPs) into the mixture. The mixture was left in an ultrasonic bath (Soni-top 404A) for 40 min. Afterwards, the solubilized mixture was heated to 100 °C using a hot plate, and an amount of 36.7 mg of ascorbic acid, which had been previously dissolved in 1 mL of ultrapure water, was quickly poured into the mixture. The heating was stopped after 5 min in boiling condition, and the solution was kept under

magnetic stirring for further 2 h until the Au particles were stabilized on the supporting material, leading to the formation of the Au/PL6C and Au-ZrO₂/PL6C composites. After reaching room temperature, the precipitates containing the composites formed were washed by centrifugation 10 times with Milli-Q water to remove the surfactant and were then dried in an oven at 80 °C overnight.

2.3. Physical-chemical characterization methods

The physical-structural characterization of the catalysts was initially performed using scanning electron microscopy (SEM) and transmission electron microscopy (TEM). The SEM analyses were performed using a Jeol JSM Microscope model 7500F. To perform the TEM and scanning-TEM (STEM) analyses, an amount of 3 µL of a diluted dispersion of the catalyst powder was dripped onto a 300-mesh copper TEM grid covered with carbon film (Electron Microscopy Sciences). The TEM and STEM images were recorded using a JEOL JEM2100 LaB₆ HRTEM or a FEI TECNAI G² F20 HRTEM microscope operating at 200 kV. For the determination of the loading of metals present in the samples, 2–5 mg amounts of the materials were placed inside a thermogravimetric analyzer TGA-50 (Shimadzu) in FID 5.0 synthetic air at a flow rate of 50 mL min⁻¹ and the analysis was performed under the heating rate of 10 °C min⁻¹ with the temperature ranging from 25 and 900 °C. Energy dispersive X-ray spectroscopy (EDS) analyses were performed in order to define the proportions of Au and Zr in the catalyst samples. The materials were placed on fluorine tin oxide plates (FTO, FlexiTec Organic Electronics) with 1.0 cm × 1.0 cm × 0.1 cm dimension and subjected to EDX analyses using ThermoNoran System Six apparatus.

The analysis of the surface of the catalysts was performed by X-ray photoelectron spectroscopy (XPS) using ESCA Scienta Omicron spectrometer operating under the following conditions: Al/Ka radiation: 1,486.6 eV; potential: 15 kV; current density: 15 mA; and power: 225 W. The survey spectra were recorded using pass energy of 50 eV with interval of 1 eV while the high-resolution spectra were recorded using pass energy of 10 eV with interval of 0.1 eV. The Shirley method was used to subtract the inelastic noise from the high-resolution spectra of Au 4f, Zr 3d, C 1 s and O 1 s. The narrow spectra were deconvoluted according to a Voigt-type function with Gaussian (70%) and Lorentzian (30%) combinations using the Casa XPS® software.

2.4. Thin film layer analysis in RRDE system

Initially, the catalyst dispersion was prepared in a ratio of 2 mg of catalyst to 1 mL of water/isopropanol dispersant (50/50 v/v) using an ultrasonic bath. The microlayer was prepared on glassy carbon disk electrode (geometric area = 0.2475 cm²) by drop casting 25 µL of the dispersion. After the evaporation of the solvent with the aid of N₂ flow, a thin film layer containing catalyst loading of 200 µg cm⁻² was obtained.

The electrochemical assays were performed in a three-compartment benchtop cell using 150 mL of 0.1 mol L⁻¹ K₂SO₄ electrolyte at pH = 2.5 (adjusted with H₂SO₄). The working electrode employed was a Pine E7R9 rotating ring-disk electrode (RRDE) composed of a glassy carbon disk and platinum ring (geometric area = 0.1866 cm²); Ag/AgCl (KCl 3 mol L⁻¹) was used as reference electrode and a 240 mm² platinum plate was employed as counter electrode. The assays were performed using Metrohm Autolab PGSTAT-302 N bi-potentiostat.

The analysis of the catalysts was conducted by cyclic voltammetry (CV) using O₂-saturated electrolyte and N₂ deaerated solution in the potential range of 1.4 to -0.6 V vs. Ag/AgCl and at scan rate of 50 mV s⁻¹. The ORR activity was investigated in a hydrodynamic system using linear sweep voltammetry (LSV) in the potential range of 0.6 to -0.8 V vs. Ag/AgCl (in the disk) and at scan rate of 5 mV s⁻¹. The working electrode was kept at 900 rpm. To monitor the presence of H₂O₂ during the assay, a constant potential of 1.0 V was applied to the ring. The analysis of the catalyst selectivity toward H₂O₂ production was performed based on Eq. (3) below [49]:

$$S_{H_2O_2} = \frac{2i_{d,r}}{i_{d,r} + i_{d,d}} \times 100 \quad (3)$$

where i_d represents the current from the ring electrode (in amperes (A)), $i_{d,r}$ refers to the current observed in the disk electrode (A), and N is the collection number provided by the manufacturer of the RRDE (PINE - $N = 0.37$). The equation is multiplied by 100 to obtain $S_{H_2O_2}$ in % terms.

The accelerated stress test (AST) was used to evaluate the long-term electrochemical stability of the gold-based catalysts. The technique consisted of evaluating both the cyclic profile of the materials and their catalytic activity in ORR using LSV tests before and after applying 5000 CVs in the potential range of 0.4–1.0 V vs RHE in 0.1 mol L⁻¹ K₂SO₄ solution (at pH 2.5) saturated with O₂ and scan rate of 500 mV s⁻¹.

2.5. H₂O₂ accumulation assays in gas diffusion electrodes

To produce the GDE, a catalytic mass was prepared in the ratio of 40% (w/w) of PTFE / Printex L6 carbon, as reported in the literature [50]. Initially, an amount of 1.2 g of catalyst mass was scattered over 120 cm² PX30-PW03 carbon cloth (purchased from Plain Weave Fabric) and transferred to a metal support. The unmodified GDE (of 10 mg cm⁻²) was produced in a thermostat hydraulic press under the following conditions: temperature: 270 °C; weight: 0.5 ton; and time: 15 min. The modified GDE was prepared by drop casting 40 mg catalysts solution - produced using 40% PTFE (w/w), on the unmodified GDE, and this yielded a catalyst loading of 200 mg cm⁻². The production of H₂O₂ was tested in a laboratory scale and in a pre-pilot plant with electrochemical flow reactor in recirculation mode under the following conditions:

Laboratory scale: The performance of PL6C, ZrO₂/PL6C, Au/PL6C and Au-ZrO₂/PL6C in terms of H₂O₂ electrogeneration was evaluated by applying a current density (j) of 50 mA cm⁻² in 150 mL synthetic medium under controlled O₂ flow rate (100 mL min⁻¹). The electrochemical cell employed consisted of GDE – employed as cathode, and BDD – employed as anode, both with a geometric area of 5.0 cm².

Pre-pilot plant: The stability of H₂O₂ production was tested in a flow-by electrochemical reactor using Au-ZrO₂/PL6C cathode material with j of 50 mA cm⁻² in 1.8 L synthetic and real media under recirculating solution at a flow rate of 50 L h⁻¹ and controlled O₂ flow rate (100 mL min⁻¹). Here, the area of the GDE and BDD electrodes was scaled to 20 cm².

In both systems, the experiments were conducted using Minipa MPS-3005B DC power supply system.

2.6. Treatment of CBR using EAOPs

A comparative degradation/mineralization analysis of 10 mg L⁻¹ CBR was performed in a benchtop cell (with 150 mL of 0.1 mol L⁻¹ supporting electrolyte) (at pH = 2.5) at fix current density (j) of 50 mA cm⁻² using the following EAOPs: AO, AO-H₂O₂, AO-H₂O₂/UVC, EF and PEF. The EF and PEF treatment processes were performed using 0.25 mmol L⁻¹ concentrations of Fe²⁺. Different parameters were analyzed under the PEF process; the parameters evaluated included current density (j ranging from 25 to 100 mA cm⁻²) and initial CBR concentration (5.0 to 20.0 mg L⁻¹). A 5 W UVC lamp (Pen-Ray 11SC-2.12 model) was used to illuminate the solution in the PEF process and to perform the CBR photolysis test [35]. Optimized laboratory-scale operating conditions were applied to a pre-pilot plant coupled to a 16 W UVC lamp for the analysis of CBR removal under the PEF process. The tests were carried out for 60 min at 50 mA cm⁻² using 1.8 L of the following effluents:

- Synthetic effluent: 50 mmol L⁻¹ K₂SO₄ in Milli-Q water at pH 2.5 (adjusted with H₂SO₄), with conductivity of 10.5 mS;
- Effluent from sewage treatment plant collected from São Paulo State, Brazil. The physical-chemical composition of the effluent can be

summarized as follows: pH = 7.1; conductivity = 1.5 mS cm⁻¹; total organic carbon (TOC) = 9.2 mg L⁻¹; dissolved solids = 391.0 mg L⁻¹; and turbidity = 29.4 NTU. The ionic species identified were ammonia (NH₄⁺) = 5.8 mg L⁻¹, calcium (Ca⁺) = 29.7 mg L⁻¹, magnesium (Mg⁺) = 5.9 mg L⁻¹, potassium (K⁺) = 15.2 mg L⁻¹, sodium (Na⁺) = 90.7, chloride (Cl⁻) = 31.2 mg L⁻¹, nitrate (NO₃⁻) = 9.4 mg L⁻¹, nitrite (NO₂⁻) = 1.1 mg L⁻¹, and sulfate (SO₄²⁻) = 22.4 mg L⁻¹. (Additional K₂SO₄ was added and the pH lowered to 2.5 so that both solutions would have similar conductivity of 10.5 mS).

2.7. Analytical techniques

The quantification of H₂O₂ was performed by UV–vis spectroscopy using 350 nm of H₂O₂ and (NH₄)₆Mo₇O₂₄ complex [50,51]. The analysis was carried out using Shimadzu UV-1900 spectrophotometer. Using the amount of H₂O₂ produced, the energy consumption was evaluated based on Eq. (4), while the percentage of current efficiency (CE) was estimated based on the Faraday's law in Eq. (5). See Equations (4) and (5) below:

$$EC(kWh\ kg_{H_2O_2}^{-1}) = \frac{i E_{cell} t}{m 1000} \quad (4)$$

$$CE_{H_2O_2}(\%) = \frac{2F C_{H_2O_2} V_s}{i t} \times 100 \quad (5)$$

where i represents the current applied (given in amperes (A)), t is the electrolysis time (in hours (h) in Eq. (4) and in seconds (s) in Eq. (5)), E_{cell} stands for electrochemical cell potential (in volts, V), m is the mass of H₂O₂ produced (in kg), 2 refers to the number of electrons involved in the reduction of an oxygen molecule to produce H₂O₂, F stands for the Faraday constant (96,487C mol⁻¹), $C_{H_2O_2}$ is the concentration of H₂O₂ (in mol L⁻¹), and v_s represents the volume of the solution (in L).

The concentration of CBR was monitored by high performance liquid chromatography (HPLC) with the aid of a Shimadzu HPLC device using the stationary phase constituted by a Supelcosil C18 pre-column (4 mm × 3.0 mm i.d.) attached to Phenomenex Luna C18 column (250 × 4.6 mm, 5 μm). A UV detector SPD-20A selected at λ = 220 nm attached to the HPLC system was used to monitor the concentration of CBR [52]. The following conditions were applied for the chromatographic analysis: retention time of carbaryl: 5.45 min in the mobile phase; mobile phase: acetonitrile/water in the ratio 60/40 (v/v); flow rate: 1.0 mL min⁻¹.

The NO₂⁻, NO₃⁻ and NH₄⁺ inorganic species were determined by ion exchange chromatography, as described in the literature [53]. The short-chain carboxylic acids were also analyzed by ion exchange chromatography. The separation was performed using Metrosep C4 column (150 mm/4.0 mm) and Metrosep C4 Guardian/4.0 pre-column at 30 °C. The elution of the small chain acids was performed using 1.7 mmol L⁻¹ nitric acid/0.7 mmol L⁻¹ dipicolinic acid at flow rate of 0.9 mL min⁻¹. The analytical curves of the carboxylic acids were constructed in the concentration range of 0 to 100 mg L⁻¹ (R² > 0.99) using the following standards: acetic acid (t_r = 3.90 min), formic acid (t_r = 4.40 min), succinic acid (t_r = 14.8 min), oxalic acid (t_r : 17.2 min), and fumaric acid (t_r = 22.9 min).

The mineralization of total organic carbon (TOC) was monitored by Shimadzu TOC-VCPN equipment; the mineralization was calculated using Eq. (6) below:

$$TOC\ mineralization(\%) = \frac{TOC_0 - TOC_f}{TOC_0} \times 100 \quad (6)$$

All samples were pre-filtered using chromafilXtra PET-45/25 0.45 μm filters. The amount of energy consumed (EC) in CBR mineralization recorded under each EAOPs was calculated based on Eq. (7) below using the TOC values:

$$EC(kWh\ kg^{-1}) = \frac{E_{cel} I t}{\Delta TOC 1000} \times 100 \quad (7)$$

where I stands for current (A), E_{cel} is the cell potential (V), and ΔTOC is

the mass of TOC removed (kg) over time.

3. Results and discussion

3.1. Physical-chemical characterization of the catalysts

Au particles were grown on bare PL6C and on the ZrO₂-PL6C synthesized hybrid material (its surface and physical properties have been described in a previous study [42]) by the hydrothermal reduction approach. The Au particles on the substrate were produced from the reduction of Au³⁺ ions by citric acid, which is typically used in synthesis processes as a reducing agent [54]. The difficulty involved in the production of Au nanoparticles lies in being able to produce small and widely distributed particles on the substrate so as to maximize the use of the metal in the catalyst and avoid the formation of large-sized particles or large metal agglomerates. In this sense, the physicochemical characteristics of the support material, such as active surface area, presence of functional groups, heteroatoms and defects, can have a direct influence on the interaction between the metal and the support material; in addition, these characteristics of the support material are also found to play a crucial role in some properties of the nanoparticle such as the distribution of the metal in the support material, the particle size, as well as the chemical attachment and stability [48,55–59]. In this context, the present study sought to evaluate the application of PL6C and ZrO₂/PL6C as supporting materials for Au nanoparticles (Au NPs) and the effects of these materials on the electrochemical catalysis of ORR targeted at the production of H₂O₂ in acid media.

Initially, the Au/PL6C and Au-ZrO₂/PL6C catalysts were characterized by field emission scanning electronic microscopy (FE-SEM), transmission electronic microscopy (TEM), scanning TEM (STEM), high-resolution TEM (HR-TEM), and selected area electron diffraction (SAED) pattern, as shown in Fig. 1a-g and S1. FE-SEM (Fig. 1a) and TEM (Fig. S1a) images recorded for Au/PL6C showed the catalyst characterized by the presence of Au particles with size of 186.7 nm (on average) which were poorly dispersed on the PL6C matrix. The HR-TEM image (Fig. 1b) obtained for the Au/PL6C catalyst showed the Au particles with nanometer dimensions, as reported in the literature [21]. In addition, the lattice fringes with distances of ca. 0.21 and 0.23 nm can be seen, which are typically related to the planes (200) and (111) for face-centered cubic structures (fcc) of Au [39]. The selected area diffraction (SAED) pattern image (Fig. 1c) obtained for the Au/PL6C catalyst revealed the presence of polycrystal structures with (111), (200), (222) and (311) orientations. According to the literature, these diffraction patterns correspond to the polycrystalline structure of Au in the catalyst [60,61].

Clearly different from what was observed in the Au/PL6C catalyst, the FE-SEM, STEM, and HR-TEM images of the Au-ZrO₂/PL6C (Fig. 1d-f and Fig. S1c-f) showed the presence of nanometric structures with predominantly icosahedral and dodecahedral shapes widely distributed on the substrate. The Au nanoparticles in the Au-ZrO₂/PL6C catalyst were ca. 77 nm on average (see Fig. S1c); this is roughly 2.5 times smaller than the size of the Au particles in the Au/PL6C catalyst. Interestingly, after a careful inspection of the STEM, dark-field STEM and HR-TEM images obtained for the Au-ZrO₂/PL6C sample (Fig. 1e,f and S1), we found that the Au NPs were anchored on top of the ZrO₂ NPs; this was clearly evident because the ZrO₂ NPs can be easily identified in the HR-TEM image (Fig. 1f) by the presence of lattice fringes measuring 0.29 nm, which are known to be typically characteristic of the d -spacing of cubic crystalline structure of zirconia [42]. The energy dispersive X-ray spectroscopy (EDX) elemental mappings of C, O, Au, and Zr obtained for the Au-ZrO₂/PL6C catalyst (Fig. S2 and S3) also indicated that Au and Zr were very close to each other, and both were found to be well dispersed on the carbon-based matrix. However, the SAED image of the Au-ZrO₂/PL6C catalyst (Fig. 1g) showed a diffraction pattern with mostly crystalline characteristics that corresponded to polycrystalline Au; this was similar to the SAED pattern observed for the Au/PL6C catalyst. The

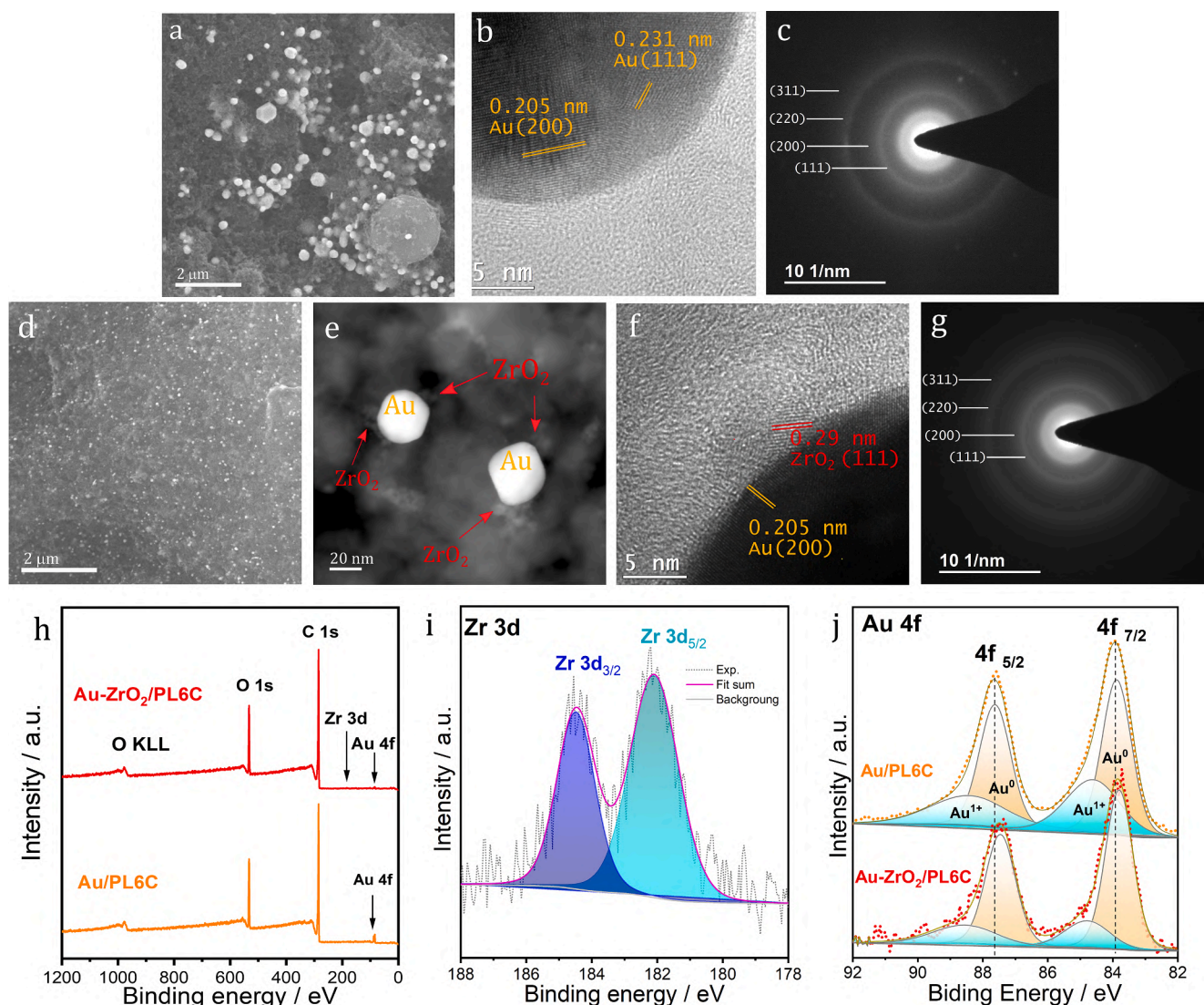


Fig. 1. FE-SEM, HR-TEM, and SAED images for the (a,b,c) Au/PL6C and FE-SEM, dark-field STEM, HR-TEM, and SAED images for (d,e,f,g) Au-ZrO₂/PL6C catalysts, respectively. (h) Survey XPS spectra for Au/PL6C and Au-ZrO₂/PL6C catalysts. (i) High resolution XPS spectrum in Zr 3d region for Au-ZrO₂/PL6C. (j) High resolution XPS spectra recorded in the Au 4f region for Au/PL6C and Au-ZrO₂/PL6C catalysts.

overlap of the larger Au NPs in the small-size ZrO₂ NPs may be a reason for the absence of the Zr diffraction pattern in the Au-ZrO₂/PL6C catalyst. Furthermore, it is relevant to mention that reducing the Au-ZrO₂/PL6C catalyst synthesis procedure from 2 steps (using microwave-assisted hydrothermal method combined with a hydrothermal reduction step) to only one step (single microwave-assisted hydrothermal approach) leads to less dispersion and the formation of Au particles with larger sizes in comparison to Au-ZrO₂/PL6C catalyst produced by 2-step synthesis procedure (c.f. Figs. 1, S1, S2, S3 and S4).

XPS analyses were performed in order to evaluate the surface chemical state of the synthesized Au-modified catalysts. The XPS survey spectrum of the Au/PL6C sample (Fig. 1h) showed the presence of peaks which corresponded to C 1s (284.5 eV), O 1s (532.6 eV), and Au 4f (85.5 eV), while the spectrum of Au-ZrO₂/PL6C exhibited in addition a small peak at 184.5 eV, which is typically attributed to the Zr 3d core level. These survey spectra rule out the presence of any other metallic impurities in both samples. The Zr 3d core-level high-resolution spectrum obtained for Au-ZrO₂/PL6C (Fig. 1i) displayed the presence of the doublet 3d_{3/2} and 3d_{5/2} due to the spin-orbit splitting at the binding energies of 184.3 and 181.9 eV, respectively, which is a binding energy range commonly associated with the Zr⁴⁺ oxidation state of zirconium

oxide [42]. The spin-orbit components 4f_{7/2} and 4f_{5/2} can be observed at ca. 84 and 88 eV in the Au 4f core-level spectra of the Au/PL6C and Au-ZrO₂/PL6C samples (Fig. 1j); both peaks can be found to be deconvoluted into two smaller peaks each at 83.8, 84.8, 87.5, and 88.6 eV corresponding to the Au⁰ 4f_{7/2}, Au¹⁺ 4f_{7/2}, Au⁰ 4f_{5/2}, and Au¹⁺ 4f_{5/2} oxidation states. In fact, the Au⁺ species found in both XPS spectra for Au/PL6C and Au-ZrO₂/PL6C samples can be explained by the partial charge transfer from the Printex L6 carbon basic groups (i.e., ketones and quinones) to the supported gold particles, as described in the literature [21,62]. In addition, as pointed out in the literature, small metal particle sizes are expected to have a higher surface energy, which is yet another factor that contributes to the existence of superficially oxidized gold particles [63]. It is worth noting however that although there appeared to be a close similarity between the spectra of the Au/PL6C and Au-ZrO₂/PL6C samples, a careful inspection of the catalysts spectra showed that the ratio of Au¹⁺/Au⁰ intensities was 2-fold higher in Au/PL6C compared to Au-ZrO₂/PL6C (even though this catalyst exhibited a smaller particle size); this shows that the presence of ZrO₂ nanoparticles in the hybrid support (a less electronegative species than Au) helped supply electrons and favor the metallic state of Au. Furthermore, a comparative analysis of the Au 4f core-level spectra of

the Au/PL6C and Au-ZrO₂/PL6C catalysts pointed to a slight shift of 0.1 eV to lower binding energy values when ZrO₂/PL6C was used as supporting material instead of pure PL6C; this result shows that the presence of oxophilic Zr exerts an influence over the electronic band structures of Au particles. It should be noted that the changes that occur in the electronic state of Au may lead to changes in the catalytic behavior of the material [30,64–67].

The metal loading in the ZrO₂/PL6C, Au/PL6C and Au-ZrO₂/PL6C carbon-based materials was evaluated using the TGA mass loss analysis shown in Fig S5. The Au/PL6C and Au-ZrO₂/PL6C catalysts recorded similar metal loadings: ~12.7 wt% and ~12.8 wt%, respectively. The results obtained from the EDS analysis helped distinguish the Zr species from the Au species in the Au-ZrO₂/PL6C catalyst; the EDS analysis

revealed the following: ~9 wt% Au loading and ~4 wt% Zr loading - see Table S1. Thus, based on the results obtained, one will observe that the bimetallic catalyst material also exhibited lower gold loading compared to the zirconium-free material. In general, the use of the ZrO₂/PL6C hybrid support contributed to the production of carbon-based catalyst of gold NPs with small particle size which were uniformly distributed on the substrate. A thorough analysis was conducted in order to evaluate the electrochemical behavior of the synthesized catalysts and H₂O₂ electrogeneration using rotating ring-disk electrode (RRDE) and GDE.

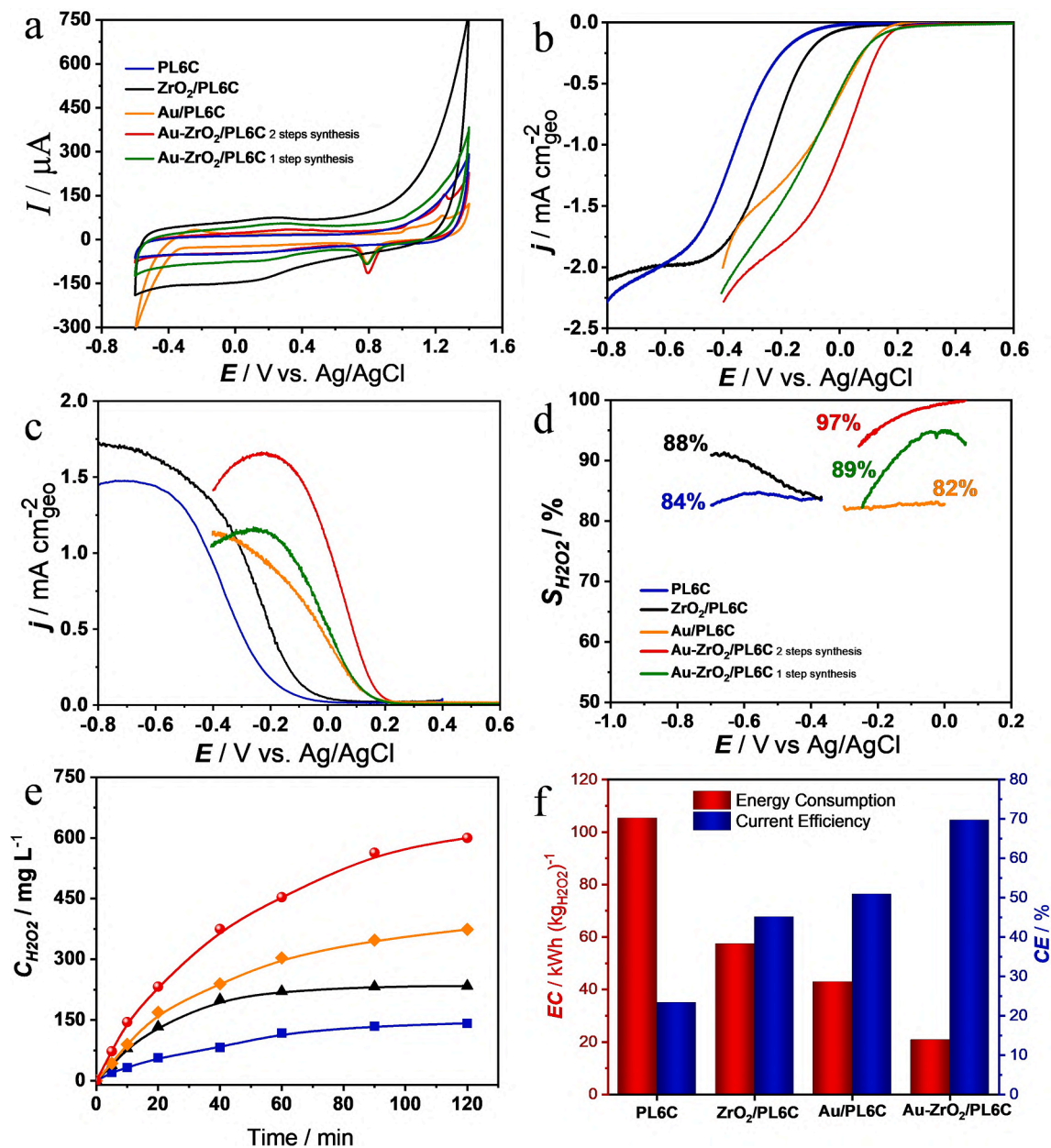


Fig. 2. Electrochemical analysis of the GC disk (RRDE system) modified with PL6C, ZrO₂/PL6C, Au/PL6C and Au-ZrO₂/PL6C catalysts. (a) Cyclic voltammograms obtained at 50 mV s⁻¹, with the application of 150 mL using N₂ bubbling to deaerate 0.1 mol L⁻¹ K₂SO₄ solution (at pH 2.5). Linear sweep voltammetry curves of the (b) disk and (c) Pt ring electrodes obtained in a RRDE configuration at scan rate of 5 mV s⁻¹ and rotation of 900 rpm, using O₂-saturated solution of 0.1 mol L⁻¹ K₂SO₄ at pH 2.5 (the abscissa of Fig. 2C refers to the applied potential at the disk electrode). (d) Selectivity toward H₂O₂ production as a function of applied potential. (e) Capacity of H₂O₂ accumulation during electrolysis at 50 mA cm⁻² for 120 min in 0.1 mol L⁻¹ K₂SO₄ (pH = 2.5) based on the application of GDE modified with PL6C, ZrO₂/PL6C, Au/PL6C and Au-ZrO₂/PL6C and using BDD as anode. (f) Current efficiency (CE) and energy consumption (EC) values obtained from H₂O₂ electrogeneration tests performed for the PL6C, ZrO₂/PL6C, Au/PL6C and Au-ZrO₂/PL6C catalysts.

3.2. Electrocatalytic performance of the materials applied for ORR aimed at H₂O₂ production

The cyclic voltammetric (CV) profiles obtained for the glassy carbon (GC) electrodes modified with PL6C, ZrO₂/PL6C, Au/PL6C or Au-ZrO₂/PL6C catalysts recorded at 50 mV s⁻¹ using N₂ bubbling to deaerate 0.1 mol L⁻¹ K₂SO₄ solution at pH 2.5 are shown in Fig. 2a. The CV profile of the PL6C-modified GC electrode exhibited mainly capacitive currents and quinone/hydroquinone redox couple centered at ca. 0.3 V vs Ag/AgCl, which are features typically observed for carbon materials in acidic solutions [21,68]. After the incorporation of zirconium oxide into the carbon matrix (ZrO₂/PL6C-modified GC electrode), the non-faradaic currents were drastically increased due to the formation of porous ZrO₂ nanostructures which were widely dispersed on the PL6C. In a previous work, we showed that the presence of ZrO₂ nanostructures in PL6C matrix led to an increase in the electrochemically active surface area (ECSA) from 85.6 to 128.2 m² g⁻¹, and this led to an increase in the capacitive current of the ZrO₂/PL6C material [42]. In general, the CV profiles of the catalysts containing Au particles (Au/PL6C and Au-ZrO₂/PL6C) exhibited a decrease in capacitive currents due to the incorporation of the metal in the surface of the supporting material, which led to a decrease in the surface area of the carbon catalyst [69]. In addition, one can observe the presence of faradaic peaks related to the formation and reduction of gold oxide species (AuO_x) on the catalyst surface at the potentials of ca. 1.1 and 0.8 V vs Ag/AgCl, respectively [31,70]. It is worth noting that the presence of ZrO₂ in Au-/PL6C (Au-ZrO₂/PL6C) caused a significant shift in the onset potential of the H₂ evolution (at ca. -0.35 V vs Ag/AgCl) to potential values that were more negative than -0.6 V vs Ag/AgCl, which typically competes with ORR when noble metals are employed at high overpotential [71].

The electrochemical analyses of ORR activity and selectivity of the catalysts were carried out by linear sweep voltammetry (LSV) using a rotating ring-disk electrode (RRDE) in O₂-saturated solution of 0.1 mol L⁻¹ K₂SO₄ at pH 2.5. The LSV curves obtained for the disk and ring electrodes are shown in Fig. 2b and 2c, respectively. As expected, the LSV curves for the disk electrode showed that the gold-based catalysts (Au/PL6C and Au-ZrO₂/PL6C synthesized in one and two steps) were more active in O₂ reduction compared to the PL6C and ZrO₂/PL6C substrates. However, a careful comparison of the Au/PL6C and Au-ZrO₂/PL6C catalysts showed that the ORR onset potential of Au-ZrO₂/PL6C produced via two-step synthesis procedure was 140 mV more positive than that of Au/PL6C and Au-ZrO₂/PL6C produced by one-step synthesis procedure. This anticipation of ORR points to the synergistic effect of the presence of ZrO₂ in the supporting material on the catalytic activity toward oxygen reduction. The Au-ZrO₂/PL6C catalyst exhibited a higher ORR activity even when the Au loading was about 25% lower in comparison to Au/PL6C (c.f. Table S1). The LSV curves of the ring electrodes (Fig. 2c) displayed the fraction of H₂O₂ produced during the oxygen reduction occurring on the disk as a function of the applied potential. In general, the LSV curves of the ring electrodes showed that the PL6C, ZrO₂/PL6C, Au/PL6C and Au-ZrO₂/PL6C materials were all highly selective for H₂O₂ production, and that the onset potentials for H₂O₂ generation coincided exactly with the ORR onset potentials of the disk electrodes. Based on the LSV curves of the disk and ring electrodes, we calculated the values related to the selectivity of the catalysts toward H₂O₂ generation (*S*_{H₂O₂}) as a function of the applied potential – see Fig. 2d and Table S1. The results obtained showed that, in general, all the catalysts exhibited high selectivity, with *S*_{H₂O₂} > 82%; unsurprisingly, the Au-ZrO₂/PL6C catalyst exhibited the highest selectivity (~97%). Based on Fig S6, we obtained the results for the accelerated stress test (AST) conducted for Au-ZrO₂/PL6C. We noted a similar cycling profile of the material before and after AST, including preserving the same charge of the gold oxidation peak at ~0.8 V vs Ag/AgCl potential – which implies that no metal loss was recorded during the test. Furthermore, a similar behavior was observed for the disk and ring LSV curves before and after AST; this pointed to a high electrocatalytic

stability of the Au-ZrO₂/PL6C when applied toward H₂O₂ production.

Thus, based on the physicochemical characterizations and electrochemical studies, we infer that the higher *S*_{H₂O₂} recorded for Au-ZrO₂/PL6C compared to Au/PL6C must be related to the reduced positive partial charge on gold NPs (caused by the donation of ZrO₂ electrons to the noble metal), which influences the interaction energy between Au and the adsorbed oxygen species. The optimal adsorption energy between Au and especially the *OOH intermediate results in the enhancement of the activity and selectivity toward H₂O₂. Apart from that, the favoring of *OOH destabilizes the formation of other intermediates, such as *O or *OH, which would lead to the production of H₂O.

The preliminary tests conducted using RRDE showed promising results related to the selectivity of the Au-ZrO₂/PL6C toward H₂O₂ production. The electrochemical behavior of the gold-based catalysts was also investigated based on the analysis of the kinetics of H₂O₂ accumulation in GDE. Fig. 2e shows the H₂O₂ production capacity profiles obtained for the different GDE modified materials investigated in this study. As can be observed, there was a gradual increase in H₂O₂ concentration over time, with the PL6C, ZrO₂/PL6C, Au/PL6C and Au-ZrO₂/PL6C GDEs recording approximately 140, 235, 374, and 600 mg L⁻¹ H₂O₂ concentration, respectively, after 120 min of electrolysis. The pseudo zero-order kinetics for H₂O₂ production also indicated the superior catalytic performance of Au-ZrO₂/PL6C (0.19 s⁻¹), with 1.7 and 5-fold increase in kinetic efficiency compared to the Au/PL6C (0.11 s⁻¹) and the unmodified PL6C catalysts (0.04 s⁻¹). The improvement observed in Au-ZrO₂/PL6C in terms of H₂O₂ electrogeneration in the GDE setup is found to be in full agreement with the results obtained from the catalytic study conducted using the RRDE.

The current efficiency (CE) values obtained also pointed to the superior performance of the Au-ZrO₂/PL6C catalyst in terms of H₂O₂ production (Fig. S7 shows the CE profile over the electrolysis time). The comparative analysis of the CE values shown in Fig. 2f was performed using optimized values up to 20 min of reaction where there was low interference of H₂O₂ consumption reactions on the BDD anode. Looking at the results, it is clear that the highest H₂O₂ production efficiency obtained for the Au-ZrO₂/PL6C catalyst resulted from the CE of 70% recorded for the catalyst compared to 52% and > 50% CE recorded for the Au/PL6C and gold-free catalysts, respectively. As expected, the higher the CE of the catalyst employed in H₂O₂ production, the lower the energy consumption (EC) – see Fig. 2f. The PL6C catalyst recorded the highest EC in H₂O₂ production (with 105 kWh kg (H₂O₂)⁻¹) after 120 min of electrolysis, while the Au-ZrO₂/PL6C catalyst exhibited the lowest EC (with only 22 kWh kg (H₂O₂)⁻¹ – >80% decrease in consumption). The results obtained from the comparative analysis of the catalysts presented in Fig. 2f pointed to the following order of efficiency: Au-ZrO₂/PL6C > Au/PL6C > ZrO₂/PL6C > and PL6C.

In fact, a combination of the following factors was found to be responsible for the high catalytic activity and selectivity toward H₂O₂ electroproduction exhibited by the Au-ZrO₂/PL6C catalyst: i) the higher availability of active Au species on the ZrO₂/PL6C hybrid substrate (evidenced by the smaller particle size and high dispersibility of the Au NPs); ii) higher metal-support interaction — propelled by the higher electronegative character of Zr which supplies electrons so that Au becomes less oxidized; and iii) greater electron donation capacity of the Au centers prompted by the presence of ZrO₂ in the hybrid matrix (evidenced by the binding energy shift in the XPS analysis) compared to the Au/PL6C catalyst. Since Au-ZrO₂/PL6C exhibited the best electrocatalytic performance in terms of cathodic production of H₂O₂ among the catalysts investigated in this study, this catalyst was employed for the conduct of further tests using electrochemical systems for the removal of CBR based on the application of EAOPs.

3.3. CBR removal using H₂O₂-based EAOPs

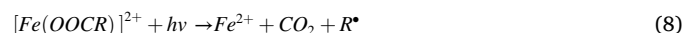
Considering the promising results obtained from the application of

the Au-ZrO₂/PL6C catalyst for H₂O₂ production, the efficiency of the catalyst in the removal of CBR was tested based on the application of BDD as anode and different EAOPs with 10 mg L⁻¹ CBR solution (at pH 2.5), at current density (*j*) of 50 mA cm⁻² and temperature of 25 °C. Fig. 3a shows the decay of the CBR over time based on the application of the following treatment processes: UVC, AO, AO/H₂O₂, H₂O₂/UVC, EF and PEF.

First, the effect of CBR photolysis in the presence of UVC radiation resulted in a removal kinetics of 2.6 × 10⁻⁴ s⁻¹ with only ~50% degradation of the compound after 60 min. Nevertheless, the photolysis process was found to exhibit very poor performance in terms of the mineralization of the organic compounds, recording only ~1% TOC removal; this may be attributed to radiation absorption of the compound in the 260–290 nm region, where it was able to degrade the CBR partially, but not mineralize it. The AO and AO-H₂O₂ processes exhibited poor electrochemical performance (see Fig. 3b), with pseudo-first order kinetics of 3.1 × 10⁻⁴ and 4.3 × 10⁻⁴ s⁻¹ for CBR removal, respectively. In both techniques, the major contribution to the pollutant degradation was obtained from the heterogeneous 'OH radicals produced on the BDD surface; this is clearly indicative of the low oxidizing power of H₂O₂ [72–74]. Under the AO-H₂O₂/UVC process, the total removal of CBR was obtained after approximately 20 min of treatment. Owing to the presence of UVC radiation in the AO-H₂O₂/UVC process (*k*₁ = 1.4 × 10⁻³ s⁻¹), the removal kinetics of this treatment technique was 2.6-fold higher compared to the AO/H₂O₂ process; this is attributed to the synergistic effect involving the contribution of UVC light in the production of homogeneous 'OH from the photolysis of H₂O₂ and the photodegradation of carbaryl. The high efficiency of homogeneous 'OH in the EF process contributed toward a rapid total removal of CBR in 10 min of treatment (*k*₁ = 3.5 × 10⁻² s⁻¹). Thus, high production of H₂O₂ on the Au-ZrO₂/PL6C cathode enhances the production of 'OH through both UVC radiation and Fenton reaction. As can be observed in Fig. 3c, the PEF process exhibited relatively faster kinetics with total CBR removal after only 4 min of treatment (*k*₁ = 4.1 × 10⁻² s⁻¹); this behavior is attributed to the synergistic action involving the heterogeneous and homogeneous 'OH processes, as well as the activation of H₂O₂ by UVC radiation and Fe²⁺ ions and the photodegradation of CBR.

Fig. 3d shows the mineralization rate for the processes investigated; the rate of mineralization was found to increase in the following order:

AO (~32%) = AO/H₂O₂(~33%) < AO/H₂O₂/UVC (~49%) < EF (~57%) < PEF (~90%). Fig. 3d also shows that the processes with the lowest mineralization rates recorded the highest energy consumption values, though a higher efficient treatment made the process cheaper. In fact, it was noted that in 60 min of electrolysis, the AO process, which exhibited poor electrochemical mineralization, recorded an energy consumption of over 100 kWh (kg TOC)⁻¹. The PEF process was found to be more efficient in CBR mineralization compared to the EF process because the former involved additional UV light photodecarboxylation process (see Eq. (8)), which is found to promote further mineralization of Fe(III) complexes.



The EF and PEF processes recorded quite similar *EC* values: 47.8 and 51.5 kWh kg⁻¹ TOC, respectively. Normally, irradiated processes exhibit a higher energy demand due to the use of UV lamp. However, these similar *EC* results were compensated by the faster mineralization rate exhibited by the PEF process.

Based on the optimal results obtained from the application of the Au-ZrO₂/PL6C catalyst in CBR removal under the PEF process, an analysis was carried out in order to evaluate under which conditions of current density and CBR concentration the system was able to sustain its high performance.

The removal of CBR normalized over time obtained from the application of different initial concentrations and current densities (*j*) are shown in Fig. 4a and b. The inset in Fig. 4 shows the pseudo-first order kinetics obtained for each parameter investigated. With regard to the different initial CBR concentrations, the application of the most diluted solution at 50 mA cm⁻² led to the fastest removal of CBR, in less than 2 min of treatment (with *k*₁ = 8.1 × 10⁻² s⁻¹). Solutions containing two or four times the initial concentration of CBR were still effectively treated, with total CBR removal obtained in 10 min of treatment (with *k*₁ values of 5.1 × 10⁻² s⁻¹ and 3.9 × 10⁻² s⁻¹, respectively). All the TOC removal rates obtained at the end of 60 min of treatment were over 90% (see Table S2). We also noticed that the efficiency of the removal process decreases when there is lower concentration of CBR in the solution under investigation. The decrease in degradation efficiency observed in the presence of low concentration of the pollutant is attributed to some competitive reactions that occur among homogeneous oxidizing species,

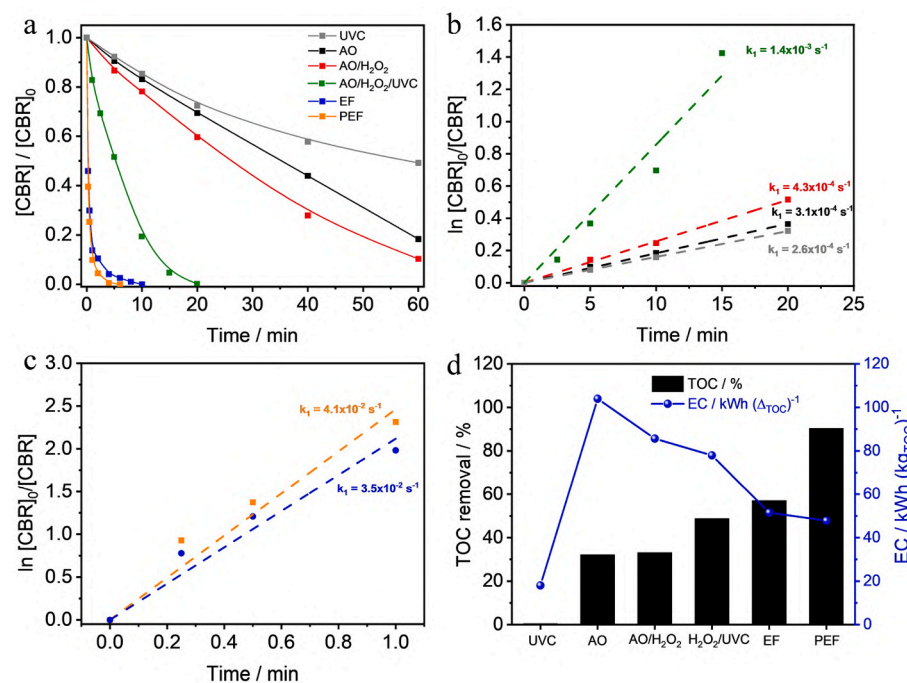


Fig. 3. (a) Analysis of the decay of 10 mg L⁻¹ CBR based on the application of different electrochemical treatment processes. Pseudo-first order kinetics evaluated in acid medium composed of 0.1 mol L⁻¹ K₂SO₄ (pH = 2.5), at current density (*j*) of 50 mA cm⁻² for the following processes: (b) UVC, AO, AO/H₂O₂ and H₂O₂/UVC and (c) EF and PEF. (d) Profile of the percentage of mineralization in relation to energy consumption in kWh kg⁻¹ TOC obtained in 60 min of treatment based on the application of EAOPs with initial TOC of ~ 6.0 mg L⁻¹.

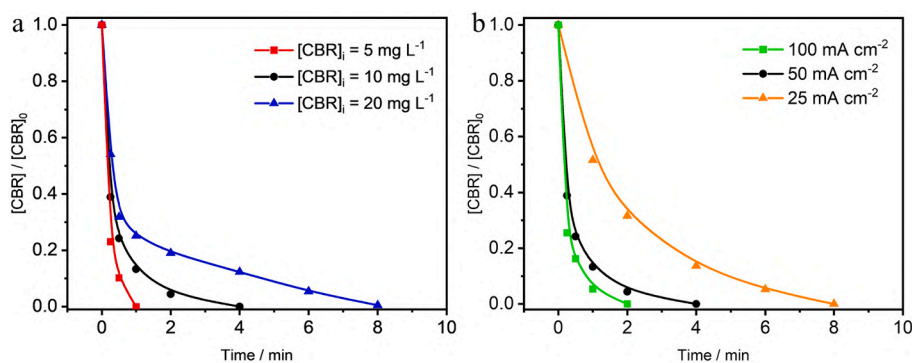
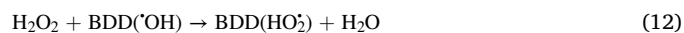


Fig. 4. (a) Analysis of the effect of initial CBR concentration using 5, 10 and 20 mg L⁻¹ CBR concentrations, and (b) influence of applied current density (j) = 25, 50 and 100 mA cm⁻² on the pollutant removal profile over time based on the application of 0.1 mol L⁻¹ K₂SO₄ (pH 2.5) as electrolyte solution at $j = 50$ mA cm⁻².

which are found in excess in the solution (see Eq. (9), (10) and (11)), along with heterogeneous species that are formed on the anodic surface (see Eq. (12)) [75–78].



Moreover, limitations of mass transport between the pollutant, which presents low concentration gradient in solution, and the anodic surface can also reduce the efficiency of the electrochemical oxidation process. Thus, we understand that the degradation of low pollutant concentration has become one of the biggest challenges that need to be overcome in future studies when it comes to the application of electrochemical technologies for wastewater treatment [76].

Fig. 4b shows the results obtained from the analysis of the effect of current density on CBR degradation based on j -dependent kinetic profile. Presumably, the dependence of the applied current density on the degradation kinetics is related to both the cathodic production of H₂O₂ and the activation of [∘]OH adsorbed on the BDD anode; both phenomena are directly associated with the production of higher amount of [∘]OH (homogeneous or heterogeneous) which oxidizes both the CBR and its by-products. Thus, increasing the j from 25 ($k_1 = 1.0 \times 10^{-2} \text{ s}^{-1}$) to 50 mA cm⁻² ($k_1 = 5.1 \times 10^{-2} \text{ s}^{-1}$) leads to a more efficient system, which is 5.1 times faster, when applied toward the removal of CBR. However, when the applied j is increased from 50 to 100 mA cm⁻² ($k_1 = 6.6 \times 10^{-2} \text{ s}^{-1}$), the kinetics of CBR removal is found to increase by only 1.3 times; this increase is mostly derived from relatively faster thermodynamics which involves the production of H₂O by reducing the adsorbed H₂O₂ via a 2-electron plus pathway at very high current densities [22,79]. A comparative analysis of the TOC removal and energy consumption after 60 min of electrolysis (Table S2) enabled us to find the optimal current density to be applied in the electrochemical process. Thus, it was assumed that, up to the current density of 50 mA cm⁻², the system behaved in a very efficient manner in terms of CBR removal.

3.4. Identification of CBR by-products

During the oxidation process, the TOC removal data obtained under the PEF process pointed to a relative resistance to complete mineralization of the organic matter possibly due to the generation of stable by-products. The GC–MS analyses of the samples enabled us to identify the by-products generated along the mineralization pathway. The characteristics of the identified by-products, such as retention time and fragmentation (m/z), are presented in Table S3. The mineralization process proposed in Fig. 5 starts from the hydroxylation of carbaryl (1); this phenomenon yields the following compounds: 1-naphthyl (2) and 2-

naphthyl (3), which, in turn, release methylcarbamic acid (the subsequent oxidation of methylcarbamic acid allows the production of further nitrogen species, apart from CO₂ and H₂O). Products 2 and 3 can be further hydroxylated to 1,4-naphthalene dione (4) or 1,2-naphthalene dione (5). The opening of the naphthalene ring leads to the production of phthalic acid (6), which can allow the loss of H₂O molecule to produce 2-carboxybenzaldehyde (7) or undergo multiple hydroxylations in order to produce catechol (8) and hydroquinone (9). Compounds 6, 7, 8, and 9 exhibit high oxidation state, and this leads to the generation of aliphatic organic compounds after the aromatic rings are fully opened – 1,2,3,4 butanetetracarboxylic acid (10), 3-(*tert*-butoxy)-3-oxopropanoic acid (11), and vinyl 2-ethylhexanoate (12).

Finally, the aliphatic organic compounds are hydroxylated to short-chain carboxylic acids. Generally, these carboxylic acids are highly efficient in producing Fe(III)-complexes ([Fe(OOCR)]²⁺) in aqueous solution during electrochemical-Fenton based processes. Thus, the short-chain carboxylic acids were monitored by ion exchange high-performance liquid chromatography (HPLC). The short-chain acids identified were as follows: succinic acid (13), fumaric acid (14), malic acid (15), formic acid (16), acetic acid (17), and oxalic acid (18). The oxidation of CBR aromatic by-products led to an increase in the concentration of the acid in the first 40 min of treatment- see Fig. 6a. The short-chain acids were expected to be converted to oxalic acid - the most oxidized product, just before CO₂ production. The second plateau in the concentration of oxalic acid indicated the continued production of the acid after the mineralization process. The short-chain acids were completely transformed into CO₂ and H₂O after 120 min of treatment; this is in line with the 99% TOC removal rate obtained, except for the remnants of tiny amounts of formic and acetic acids.

As suggested, the oxidation of methylcarbamic acid yields nitrogen species as end-products of CBR mineralization. Thus, ion exchange HPLC was also employed for the monitoring of ammonium, nitrate, and nitrite species produced throughout the PEF process.

Fig. 6b shows that the main nitrogen ion species formed as the end-product of CBR mineralization was NO₃⁻, with its maximum concentration of 0.46 mg L⁻¹ obtained in 20 min of treatment. Despite the similarity in the profile of NO₃⁻ and NO₂⁻ production, the low NO₂⁻ concentration pointed to the highly oxidative power of the processes employed in the system. Interestingly, after reaching the maximum concentration in the first 20 min of electrolysis, we noted that the oxidized nitrogen species for NH₄⁺ production were consumed; this phenomenon can be attributed to additional cathodic reaction of nitrite and nitrate reduction. Overall, the nitrogen content of all the ionic nitrogen species (N-NH₄⁺, N-NO₂⁻ and N-NO₃⁻) amounted to 0.62 mg L⁻¹ after 120 min of treatment; i.e., 89% of the expected total nitrogen (0.7 mg L⁻¹) was identified through the mineralization of 10 mg L⁻¹ of CBR. The incomplete mass balance can be explained by the production of nitrogen-based unidentified volatile species [80]. In brief, apart from it being highly efficient for H₂O₂ production targeted at the removal of

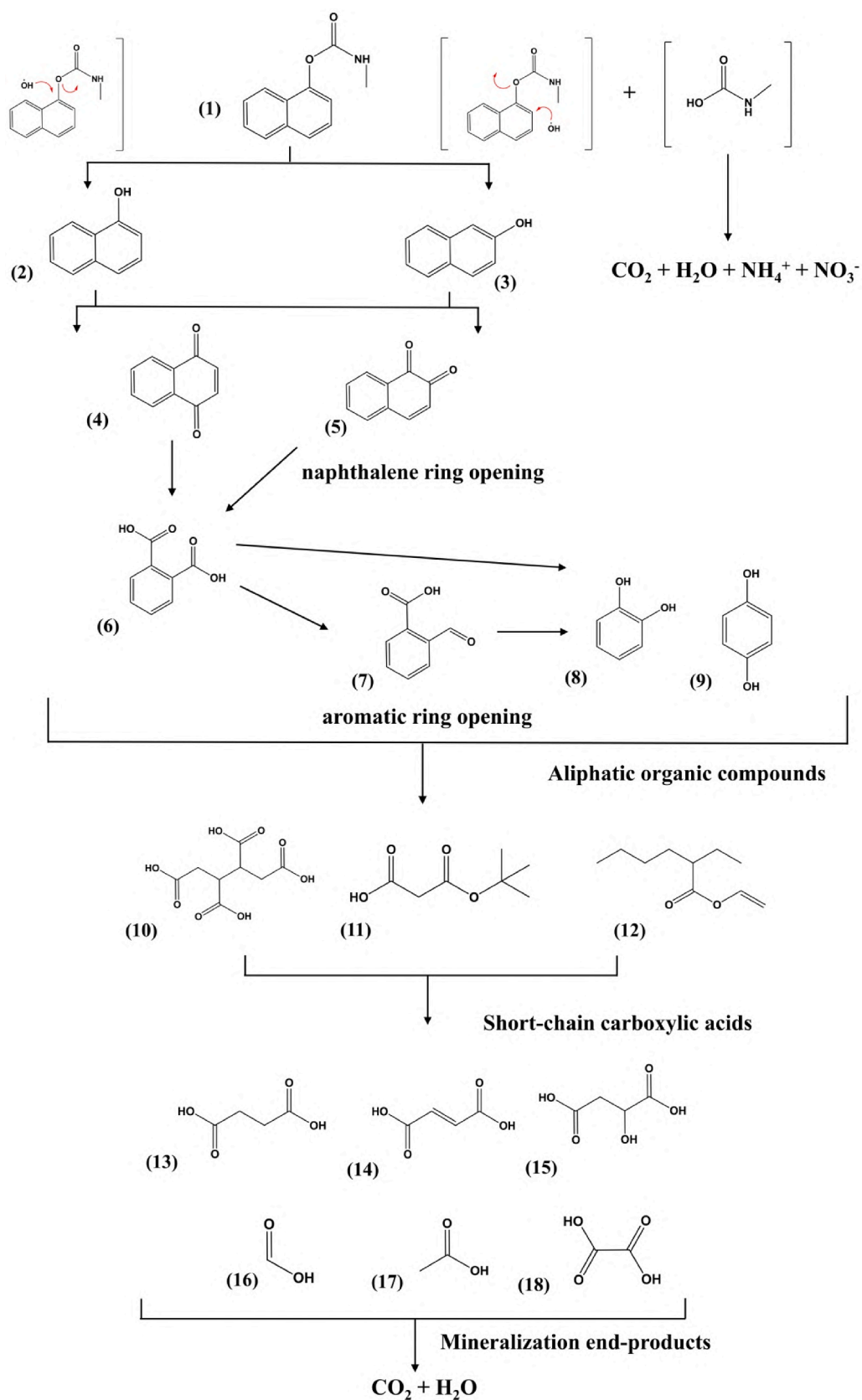


Fig. 5. Proposed route of carbaryl mineralization via hydroxyl radicals based on the application of PEF process in acid medium.

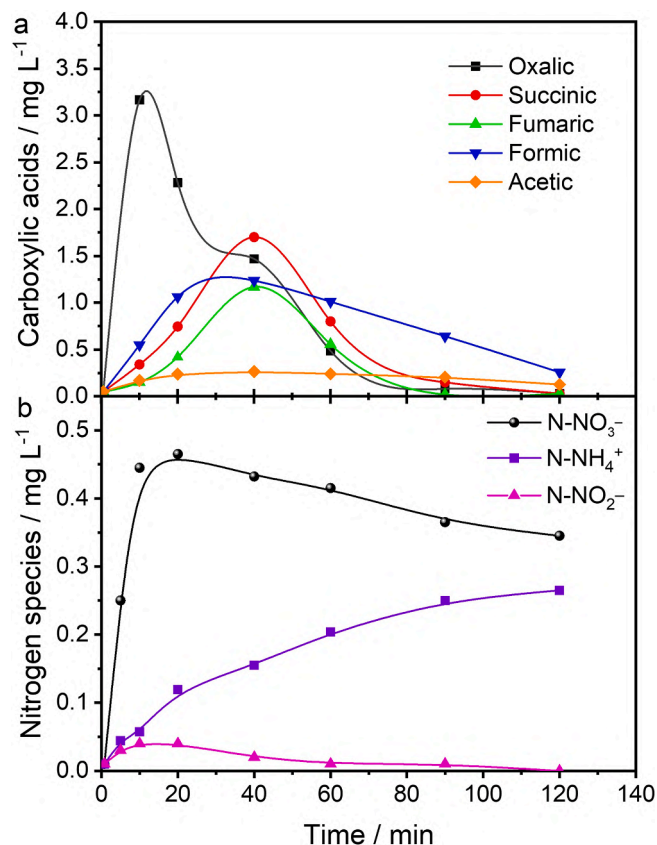


Fig. 6. Concentration of (a) small-chain carboxylic acids and (b) nitrogen species of NH_4^+ , NO_3^- and NO_2^- identified during 120 min of 10 mg L^{-1} CBR degradation under the PEF process, based on the application of 150 mL of 0.1 mol L^{-1} K_2SO_4 (pH 2.5) as electrolyte and temperature of 25°C .

CBR from water under the application of EAOPs, the Au NPs catalyst supported on $\text{ZrO}_2/\text{PL6C}$ was also found to be a promising cathodic material for further environmental applications involving nitrate reduction.

3.5. Using pre-pilot plant for CBR removal in real urban wastewater

Although the study of electrochemical materials applied for the treatment of synthetic water matrices in lab scale is essentially important for developing mechanistic concepts, this approach does not contribute meaningfully toward improving and consolidating our scientific knowledge and understanding when it comes to real water treatment; this is because the extrapolations are often unrealistic when the analytical experiments are conducted in lab scale. This observation is supported by recent works related to applied electrochemical processes for the treatment of carbaryl outlined in Table S4; one will note that all the studies were performed in synthetic media and on a lab scale. Bearing that in mind, recent research in electrochemical technologies has been directed toward the use of real water matrices and scale-up processes [12,81,82]. Taking that into account, the present study conducted a series of experiments using urban wastewater spiked with CBR in an electrochemical flow reactor pre-pilot plant equipped with Au- $\text{ZrO}_2/\text{PL6C}$ (cathode) and BDD (anode) - geometric area of both materials: 20 cm^2 . Additional details about the setup of the pre-pilot plant can be found in a paper recently published in the literature [83]. Fig. 7a shows that the amount of H_2O_2 generated in the wastewater treatment process was $\sim 185 \text{ mg L}^{-1}$ on average after performing five consecutive experiments at current density of 50 mA cm^{-2} . Further SEM images of the modified GDE (see Fig S8 of the supporting information) also showed a stable structure of the gold nanoparticles well distributed on the surface of the carbon oxide-based support after the H_2O_2 electrogeneration process. Although the amount of H_2O_2 obtained was satisfactory for environmental water treatment, it was $\sim 60\%$ lower compared to the amount of H_2O_2 obtained in the synthetic medium under the same conditions; this can be attributed to the use of a flow reactor with a more realistic scale, as well as the presence of some compounds in the real medium, such as active chlorine species (Cl_2 , HClO and ClO^-) derived

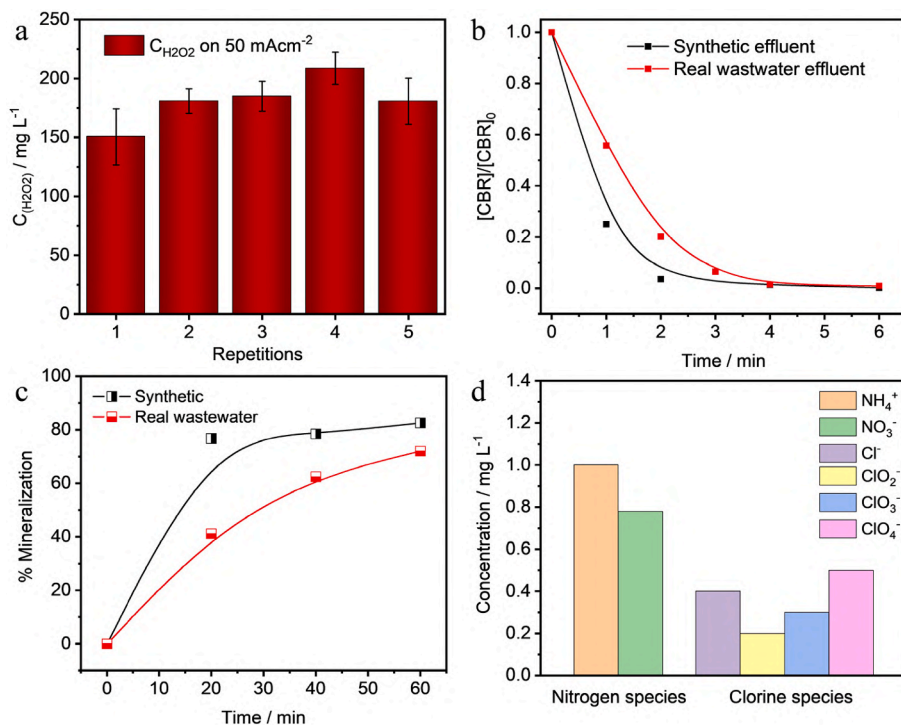
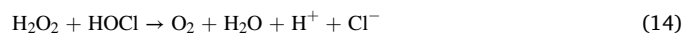


Fig. 7. (a) Stability tests related to H_2O_2 production in real wastewater effluent conducted with the aid of a flow reactor at applied current density (j) of 50 mA cm^{-2} using Au- $\text{ZrO}_2/\text{PL6C}$ cathode and BDD anode. (b) Analysis of CBR removal and (c) TOC mineralization in flow electrochemical reactor based on the application of the PEF process at $j = 50 \text{ mA cm}^{-2}$ and O_2 flow at 100 mL min^{-1} in both synthetic and real effluents. (d) Final values of nitrogenous and chlorinated species detected in real wastewater effluent after 60 min of PEF treatment.

from Cl^- oxidation, which may act as H_2O_2 scavengers, as can be observed in Eqs. 13–15 [53,84].



For the analysis with real water, we tested the degradation of 10 mg L^{-1} CBR spiked in real urban wastewater. As can be observed in Fig. 7b, 78% of the pollutant was removed in 2 min of treatment. The degradation test conducted using synthetic water matrix and the same amount of time resulted in almost 96% of CBR removal. The compound was fully degraded in 4 min in both real and synthetic aqueous media. The values obtained for pseudo-first order kinetic constants showed that the degradation in the synthetic medium ($k_1 = 2.5 \times 10^{-2} \text{ s}^{-1}$, $R^2 = 0.995$) occurred 1.6-fold faster than in the real medium ($k_1 = 1.6 \times 10^{-2} \text{ s}^{-1}$, $R^2 = 0.986$). In addition, as can be observed in Fig. 7c, the mineralization process followed the same tendency; TOC removal of 82% was obtained under the synthetic medium as opposed to 71% obtained under the urban wastewater after 60 min of electrolysis. These results demonstrate that although the concentration of H_2O_2 electrogenerated in the real wastewater was lower than that generated in the synthetic medium, this did not inhibit the occurrence of Fenton reactions. It should be noted however that the presence of natural organic matter (NOM) affects the electrochemical system because these species compete with CBR for oxidants (OH and active chlorine species); this explains why lower CBR degradation was obtained under the real medium. From a mineralization point of view, the results obtained seem reasonable. This is because the initial TOC of the real medium ($15.0 \text{ mg C L}^{-1} = \sim 9.0 \text{ mg C L}^{-1}$ from NOM + 6.0 mg C L^{-1} from CBR) was more than the double of that of the synthetic medium (containing only 6.0 mg C L^{-1} of CBR); thus, one would require a longer treatment time to obtain a complete mineralization of all the organic compounds present in the real medium. Furthermore, the residual TOC (4.4 mg C L^{-1}) in the real medium comes from NOM, which is more difficult to be mineralized than CBR. NOM is a complex mixture of organic compounds (humic acids, lipids, carbohydrates, etc.) which is derived from the breakdown of terrestrial plants and human activities [85].

Fig. 7d shows the final inorganic species left in the real medium after the electrochemical treatment. Active chloride species were converted into 0.20 mg L^{-1} of chlorite (ClO_2^-), 0.30 mg L^{-1} of chlorate (ClO_3^-) and 0.50 mg L^{-1} of perchlorate (ClO_4^-). Despite the generation of undesirable chlorine species (ClO_3^- and ClO_4^-), the concentrations of these species were found to be below the concentration limits established for the discharge of these compounds in wastewater ($=10.0 \text{ mg L}^{-1}$). $>80\%$ of nitrogen species were removed. At the end of the electrochemical treatment process, 1.0 mg L^{-1} of NH_4^+ and 0.78 mg L^{-1} of NO_3^- were detected; this result points to the ability of the Au-ZrO₂/PL6C to effectively remove this kind of ions. With regard to the results obtained here, it is essentially important to note that before applying any type of process for the treatment of wastewater, one needs to characterize the medium thoroughly in order to verify what can influence the removal of the target pollutant.

4. Conclusion

This work investigated the synergistic relation between ZrO₂/PL6C support and Au NPs. The results obtained from the RRDE analysis conducted in the study showed that the anchoring of gold NPs on ZrO₂/PL6C hybrid support (Au-ZrO₂/PL6C) led to an increase in catalytic activity and selectivity toward H_2O_2 production (ORR onset = 0.34 V vs Ag/AgCl and $S_{\text{H}_2\text{O}_2} = 97\%$) compared to the anchoring of Au particles on bare PL6C (ORR onset = 0.20 V vs Ag/AgCl and $S_{\text{H}_2\text{O}_2} = 82\%$). The ZrO₂ species present in the Au-ZrO₂/PL6C catalyst, which is less electronegative than Au, helped supply electrons and favored the metallic state of

Au NPs, which in turn boosted the catalytic activity toward H_2O_2 production.

The Au-ZrO₂/PL6C catalyst also displayed the best performance when applied in GDE, yielding an amount of 600 mg L^{-1} of H_2O_2 compared to ~ 374 , ~ 235 and $\sim 140 \text{ mg L}^{-1}$ of H_2O_2 recorded for Au/PL6C, ZrO₂/PL6C, and bare PL6C, respectively. The performance of the Au-ZrO₂/PL6C cathodic catalyst in the removal of the endocrine interferent CBR was tested in an electrochemical cell coupled with BDD anode under the application of different EAOPs. The EF and PEF processes exhibited the highest efficiency in terms of CBR removal in less than 10 min of treatment; this outstanding efficiency was attributed to the significant production of homogeneous OH in the bulk solution through Fenton reaction. In addition, the PEF process, which exhibited a high mineralization percentage ($>90\%$) in 60 min and energy consumption of 50.8 kWh kg^{-1} , was found to be the most efficient process for the treatment of CBR; the superior performance of the PEF process was attributed to the synergistic action involving OH activation via the Fenton reaction and UVC light, which occurs during the treatment process.

The tests conducted for the removal of CBR under different experimental conditions (j and [CBR]) showed that: i) the process efficiency decreases when lower concentration of CBR is applied; and ii) the application of higher current densities negatively affects the removal process due to the presence of non-negligible parallel/non-oxidizing reactions. Finally, a mineralization route was proposed based on TOC measurements coupled with the identification of aromatic degradation intermediates, short-chain acids, and ionic nitrogen species as the end-products of mineralization. The results obtained from the application of an electrochemical flow reactor at pre-pilot scale for the treatment of urban wastewater showed that the aqueous matrix influenced H_2O_2 electrogeneration and CBR degradation. Furthermore, at the end of the treatment process, the concentrations of inorganic species detected in the wastewater were found to be below the established discharge limit; this outcome pointed to the satisfactory efficiency of the process. Based on our findings, it can be concluded that the strategy proposed in this study, which involved the use of Au nanoparticles supported on ZrO₂/PL6C hybrid substrate, contributed effectively toward the cathodic production of H_2O_2 and the successful treatment of water containing complex matrices.

CRedit authorship contribution statement

Matheus S. Kronka: Investigation, Conceptualization, Methodology, Writing – original draft, Writing – review & editing. **Guilherme V. Fortunato:** Investigation, Conceptualization, Writing – original draft, Writing – review & editing. **Leticia Mira:** Methodology, Investigation, Writing – original draft. **Alessandro J. dos Santos:** Investigation, Conceptualization, Writing – original draft, Writing – review & editing. **Marcos R. V. Lanza:** Supervision, Funding acquisition, Writing – review & editing.

Declaration of Competing Interest

The authors declare that they have no known competing financial interests or personal relationships that could have appeared to influence the work reported in this paper.

Data availability

Data will be made available on request.

Acknowledgments

The authors are grateful to the LCE/DEMa/UFSCar for providing the TEM facilities. The authors acknowledge the financial support provided by the following Brazilian research funding agencies: Brazilian National

Supporting information for:

Using Au NPs anchored on ZrO₂/carbon black toward efficient H₂O₂ electrogeneration in flow-by reactor for carbaryl removal in real wastewater

Matheus S. Kronka^{*}, Guilherme V. Fortunato, Leticia Mira, Alexsandro J. dos Santos,
Marcos R.V. Lanza^{*}

¹São Carlos Institute of Chemistry, University of São Paulo, Avenida Trabalhador São-Carlense 400, São Carlos, SP, 13566-590, Brazil.

*Corresponding authors' e-mails:

marcoslanza@usp.br (M.R.V. Lanza)

mskonka@usp.br (M.S. Kronka)

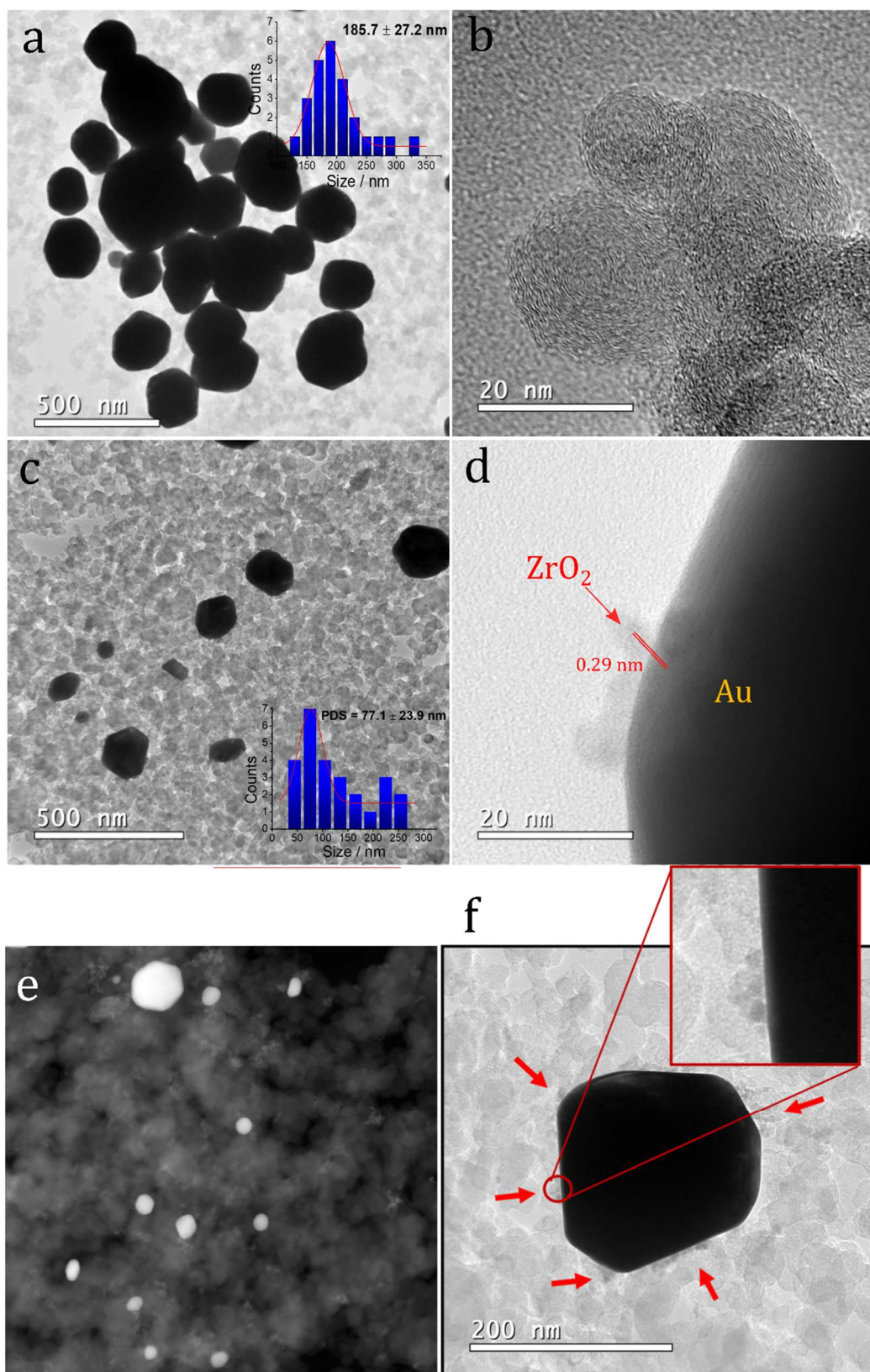


Figure S1. TEM and HR-TEM images for the (a,b) Au/PL6C and TEM, HR-TEM and dark-field STEM images for the (c-f) Au-ZrO₂/PL6C catalysts. The arrows indicate the presence of ZrO₂ NPs.

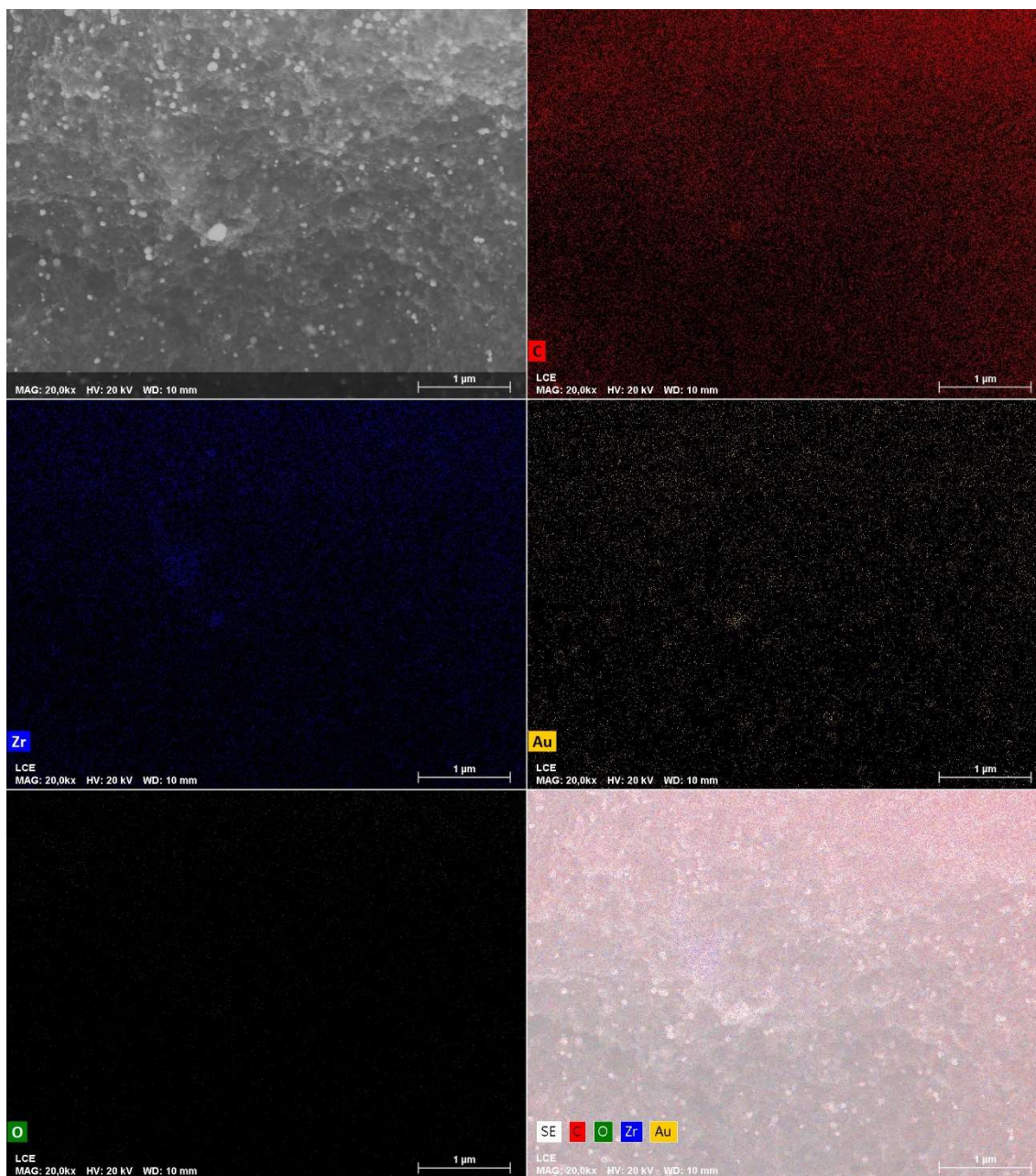


Figure S2. Scanning electron microscopic (SEM) image of the Au-ZrO₂/PL6C catalyst; energy dispersive X-ray spectroscopy (EDX) of carbon, oxygen, zirconium, and gold elements present in the catalyst sample; overlay of the elements on the PL6C support.

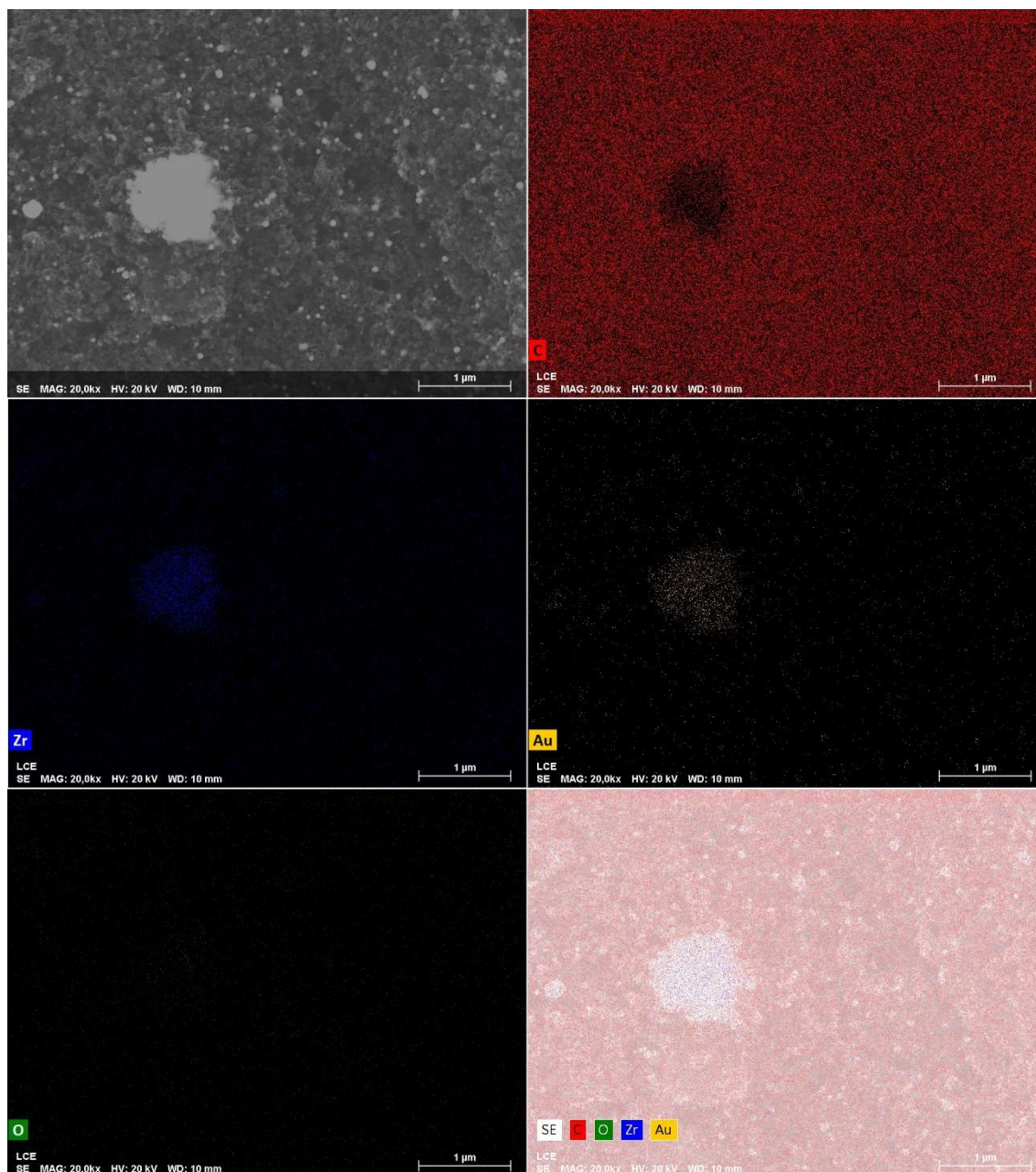


Figure S3. Scanning electron microscopic (SEM) image of the Au-ZrO₂/PL6C catalyst produced by using one-step synthesis procedure; energy dispersive X-ray spectroscopy (EDX) of carbon, oxygen, zirconium, and gold elements present in the catalyst sample; overlay of the elements on the PL6C support.

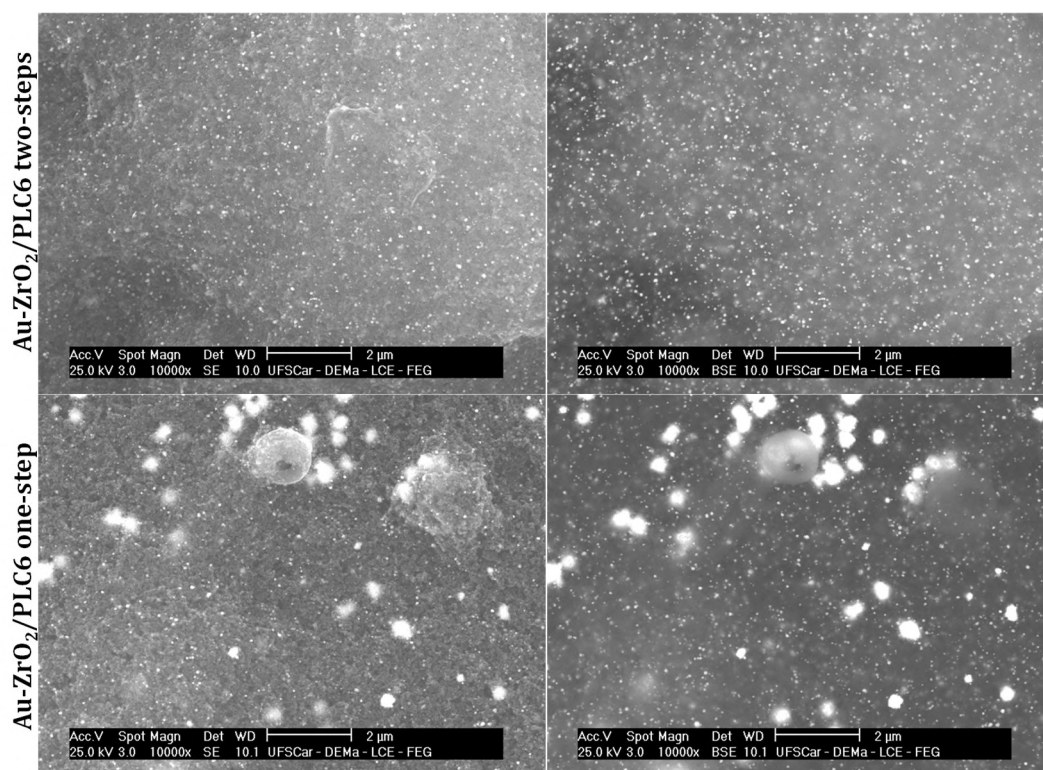


Figure S4. FEG-SEM images in (first column) SE and (second column) BSE mode obtained for Au-ZrO₂/PL6C catalyst produced by using one- and two-steps synthesis procedure.

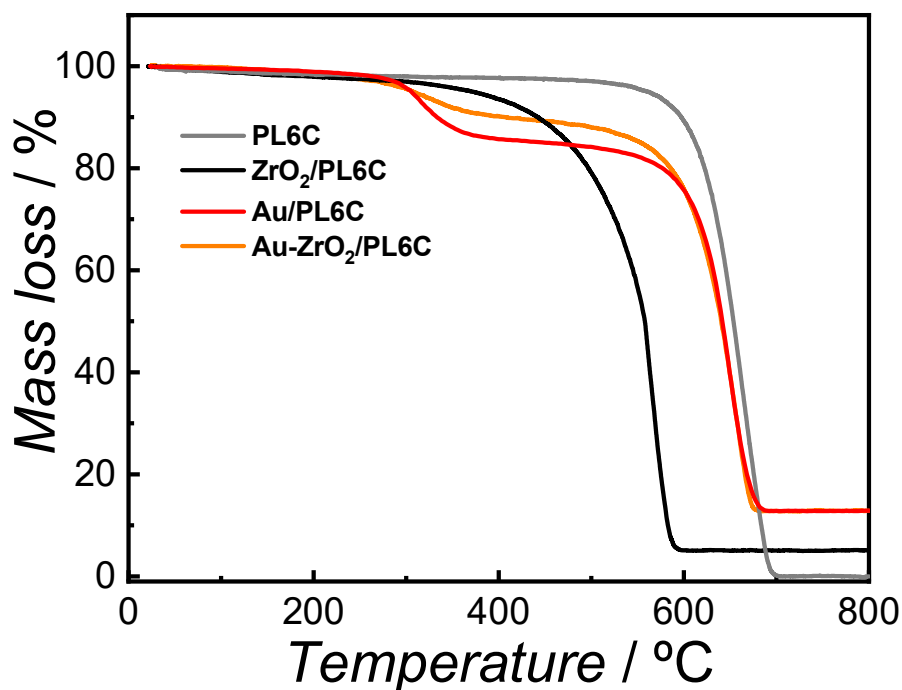


Figure S5. Thermogravimetric analysis of the PL6C, ZrO₂/PL6C, Au/PL6C and Au-ZrO₂/PL6C catalysts.

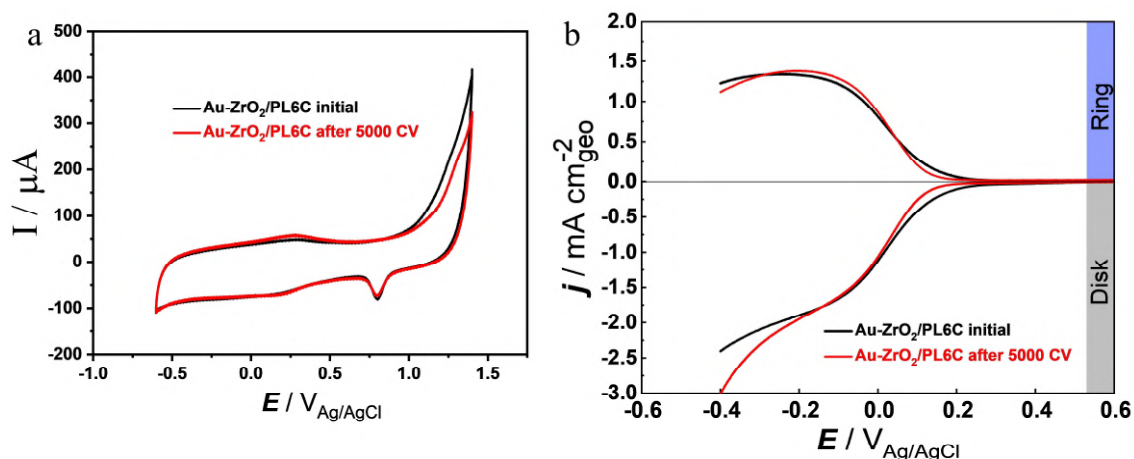


Figure S6. (a) Cyclic voltammograms before and after the accelerated stress test, obtained in O_2 -saturated $0.1 \text{ mol L}^{-1} \text{ K}_2\text{SO}_4$ at pH 2.5 for GC electrodes modified with $\text{Au-ZrO}_2/\text{PCL6}$ at a scan rate of 50 mV s^{-1} ; (b) RRDE profile of $\text{Au-ZrO}_2/\text{PL6C}$ linear sweep voltammetry using the scan rate of 5 mV s^{-1} and 900 rpm in O_2 -sat $0.1 \text{ mol L}^{-1} \text{ K}_2\text{SO}_4$ at pH 2.5 before and after the stability test.

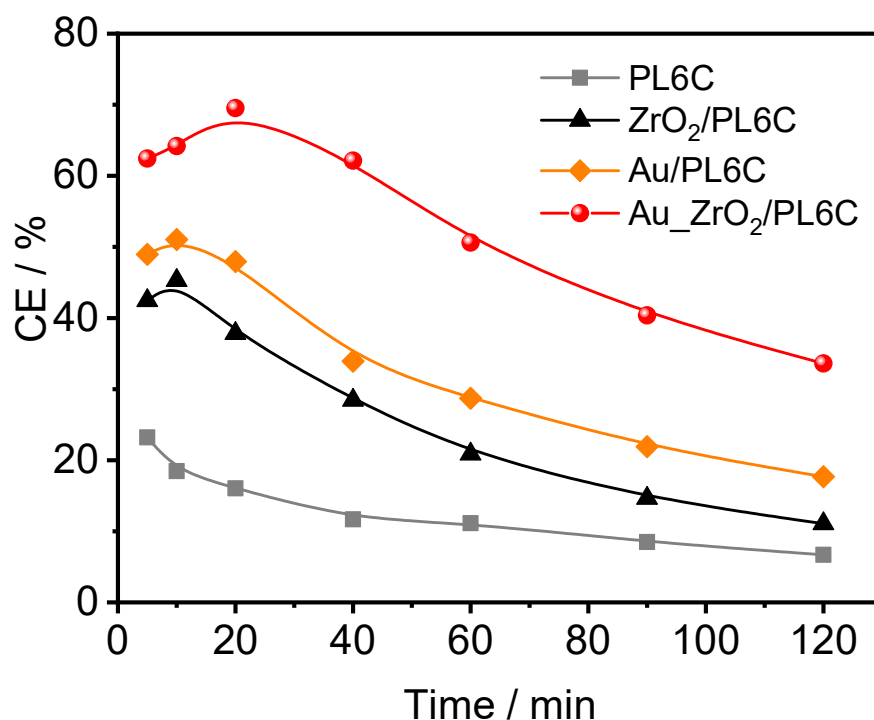


Figure S7. Current efficiency values obtained for the PL6C, $\text{ZrO}_2/\text{PL6C}$, $\text{Au}/\text{PL6C}$ and $\text{Au-ZrO}_2/\text{PL6C}$ catalysts relative to the time of electrolysis based on the application of $0.1 \text{ mol L}^{-1} \text{ K}_2\text{SO}_4$ (at pH 2.5) as electrolyte solution, current density of 50 mA cm^{-2} , and temperature of $25 \text{ }^\circ\text{C}$.

Table S1. Particle size, EDS, TG metal (unburned mass), and TG and EDS mass and atomic percentages recorded for the metal/PL6C samples.

Nanocomposite	Particle size (nm)	EDS metal mass (%)	TG metal mass (unburned - %)	TG and EDS mass (%)	Total loading in RRDE	Au loading in RRDE	Onset ($V_{Ag/AgCl}$)	$S_{H_2O_2}$ (%)
PL6C (control)^a	18 ^a	-	0.1	100 C	201 $\mu\text{g cm}^{-2}$	-	0.00	85
ZrO₂/PL6C^b	7.5 ± 1.7	-	5.1	5.1 Zr 94.9 C	201 $\mu\text{g cm}^{-2}$	-	0.13	88
Au/PL6C	185.7 ± 27.2	-	12.7	12.7 Au 88.3 C	201 $\mu\text{g cm}^{-2}$	25.7 $\mu\text{g cm}^{-2}$	0.20	80
Au-ZrO₂/PL6C	77.1 ± 23.9	74.96 Au 25.04 Zr	12.8	9.6 Au 3.2 Zr 88.2 C	201 $\mu\text{g cm}^{-2}$	19.3 $\mu\text{g cm}^{-2}$	0.34	97

^a Estimated value from literature (Jorge Marques Cordeiro-Junior et al., 2020)

^b Value obtained in preliminary studies with the material (Kronka et al., 2021)

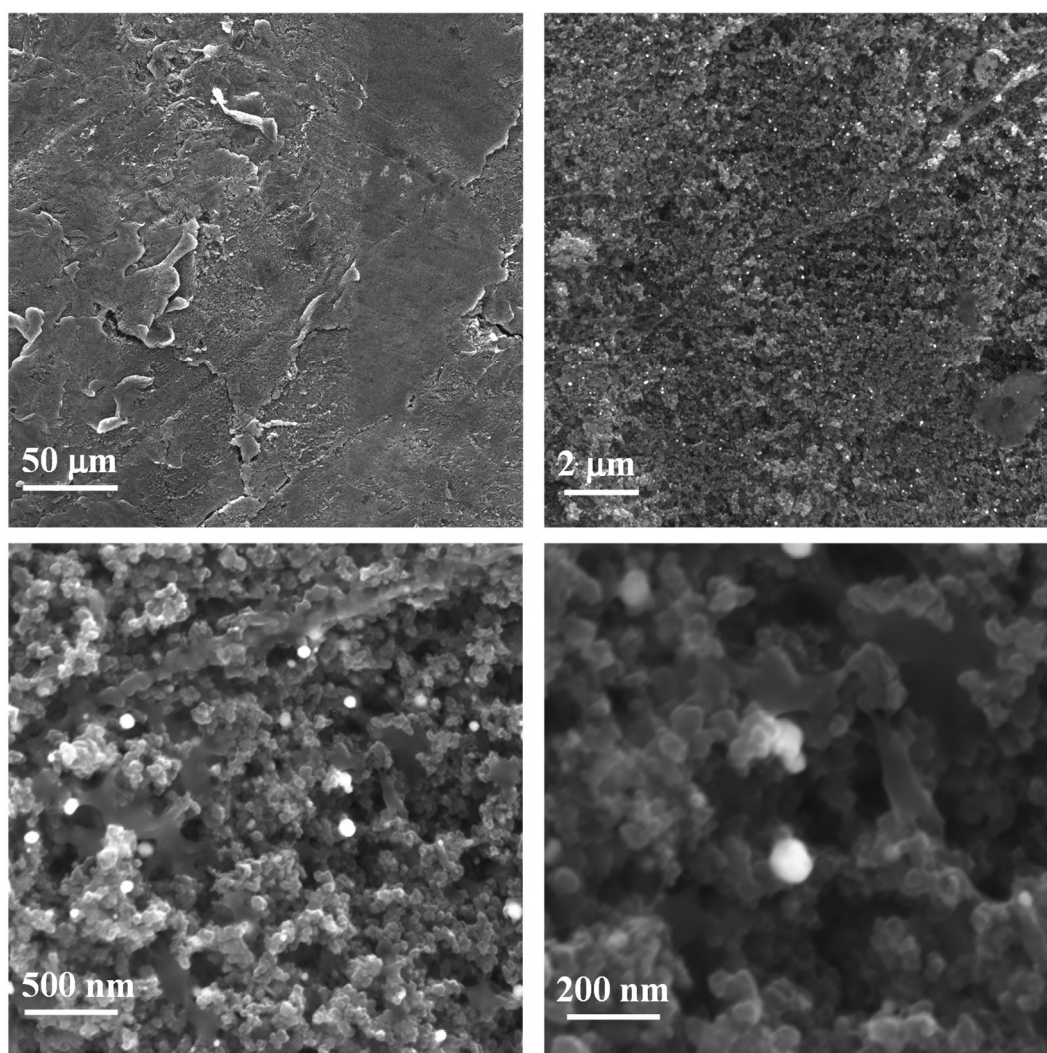
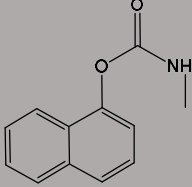
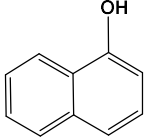
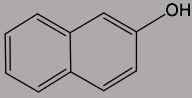
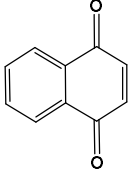
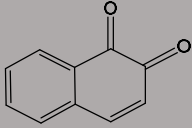
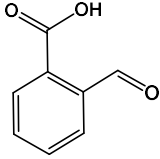
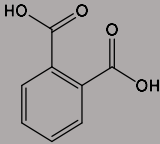
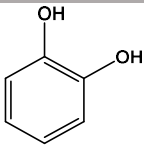
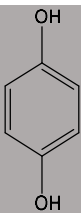


Figure S8. FEG-SEM images obtained in SE mode for GDE modified with Au-ZrO₂/PL6C catalyst produced by using one-step after consecutive tests of H₂O₂ electrogeneration in flow-by reactor.

Table S2. Total degradation time, TOC mineralization (%), energy consumption (kWh kg_{TOC}⁻¹), and apparent kinetic constant for the concentration decay (min⁻¹) with corresponding R-squared values, determined over 60 min of treatment of 150 mL CBR solution under the application of the PEF process using 0.1 mol L⁻¹ K₂SO₄ (at pH 2.5) as electrolyte solution and temperature of 25°C.

j (mA cm ⁻²)	[CBR] _i (mg L ⁻¹)	CBR removal time (min)	TOC (%)	CE kWh kg _{TOC} ⁻¹	k_{app} (min ⁻¹)	R^2
50	5	1	92.5	74.3	4.8	0.983
50	10	6	90.4	50.8	3.1	0.977
50	20	8	90.0	34.4	2.3	0.998
25	10	10	89.3	38.1	0.6	0.995
100	10	2	94.3	60.6	4.0	0.951

Table S3. Intermediates compounds detected by GC-MS during the degradation of 10 mg L⁻¹ CBR solution under the PEF treatment process.

Number	Chemical name	Molecular structure	<i>t_r</i> (min)	Fragmentation (<i>m/z</i>)
1	Carbaryl		16.89	201, 144, 127, 115, 89, 51
2	1-Naphthol		12.24	144, 115, 89, 72, 63, 50
3	2-Naphthol		12.28	144, 115, 72, 63, 51
4	1,2-Naphthalenedione		10.89	158, 130, 104, 76, 50
5	1,4-Naphthalenedione		10.89	159, 130, 102, 76, 63, 50
6	3-Carboxybenzaldehyde		27.51	149, 121, 105, 77, 65, 51, 39
7	Phthalic acid		12.38	149, 105, 76, 50, 39
8	Catechol		7.60	110, 92, 81, 64, 55, 44, 28
9	Hydroquinone		7.60	110, 81, 63, 55, 42, 28

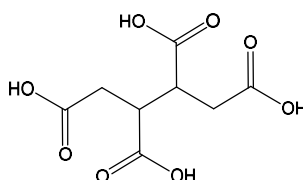
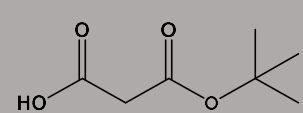
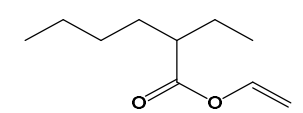
10	Butane tetracarboxylic acid		28.75	199, 154, 126, 108, 98, 54, 27
11	3-tert-Butoxy-3-oxopropanoic acid		15.30	161, 145, 101, 87, 50, 43
12	Vinyl 2-ethylhexanoate		15.55	127, 109, 99, 70, 57, 41, 29

Table S4. Summary of recent work that applied electrochemical processes for degradation of carbaryl present in aqueous solutions.

EAOP method	Experimental conditions	j (mA cm ⁻²)	Time to CBR degradation	TOC/COD removal	Ref
Anodic oxidation + Electro-Fenton	Laboratory scale BDD anode Carbon felt cathode 0.1 mM Fe ⁺² 20 mg L ⁻¹ CBR 230 mL of solution 50 mM Na ₂ SO ₄ pH 3	50	~15 min	unavailable	(Çelebi et al., 2015)
		300	~ 6 min	~90% after 120 min	
Anodic oxidation + Electro-Fenton	Laboratory scale Pt anode Carbon felt cathode 0.1 mM Fe ⁺² 20 mg L ⁻¹ CBR 230 mL of 50 mM Na ₂ SO ₄ pH 3	50	~15 min	unavailable	(Çelebi et al., 2015)
		300	~6 min	~70% after 120 min	

	Laboratory scale				
Anodic oxidation	Ti/RuO ₂ anode Pt plate cathode 10 mg L ⁻¹ CBR 30 mL of 100 mM Na ₂ SO ₄	30	> 120 min	unavailable	(T. É. S. Santos et al., 2014)
	Filter press reactor				
Photo-assisted electrochemical oxidation	Ti/Ru _{0.3} Ti _{0.7} O ₂ DSA [®] anode Ti-mesh cathode 20 mg L ⁻¹ CBR 250 mL of 33 mM Na ₂ SO ₄ 250W mercury lamp	40	~60 min	~32% after 120 min	(Malpass et al., 2009)
	Laboratory scale				
Anodic oxidation	Ti/Ru _{0.3} Ti _{0.7} O ₂ DSA [®] anode Two platinum foils cathodes 10 mg L ⁻¹ CBR 75 mL of 100 mM NaCl pH 5.3	60	~60 min	96% after 120 min	(Miwa et al., 2006)
	Laboratory scale				
Anodic oxidation	Ti/Ir _{0.3} Ti _{0.7} O ₂ DSA [®] anode Two platinum foils cathodes 10 mg L ⁻¹ CBR 75 mL of 100 mM NaCl pH 5.3	20	~60 min	> 99% after 120 min	(Miwa et al., 2006)

Laboratory scale					
Anodic oxidation	Ti/Ru _{0.3} Sn _{0.7} O ₂ DSA [®] anode	20	~60 min	96% after 120 min	(Miwa et al., 2006)
	Two platinum foils cathodes				
	10 mg L ⁻¹ CBR				
	75 mL of 100 mM NaCl				
	pH 5.3				
Laboratory scale					
Anodic oxidation + Photoelectro- Fenton	BDD anode Au-ZrO ₂ /PL6C cathode	50	4 min	90% after 60 min	*
	0.25 mM Fe ⁺²				
	10 mg L ⁻¹ CBR				
	250 mL of solution				
	100 mM K ₂ SO ₄				
	UVC 5W mercury lamp pH 2.5				
Pre-pilot scale					
Anodic oxidation + Photoelectro- Fenton	BDD anode Au-ZrO ₂ /PL6C cathode	50	4 min	71% after 60 min	*
	0.25 mM Fe ⁺²				
	10 mg L ⁻¹ CBR				
	2000 mL urban wastewater				
	50 mM K ₂ SO ₄				
	UVC 16W mercury lamp pH 2.5				

* Results from the present study

References

- [1] P. Jorge Marques Cordeiro-Junior, M. Schiavon Kronka, L. Athie Goulart, N. Carolina Veríssimo, L. Helena Mascaro, M. Coelho dos Santos, R. Bertazzoli, M. Roberto de Vasconcelos Lanza, Catalysis of oxygen reduction reaction for H₂O₂ electrogeneration: The impact of different conductive carbon matrices and their physicochemical properties, *Journal of Catalysis*. 392 (2020) 56–68. <https://doi.org/10.1016/j.jcat.2020.09.020>.
- [2] M.S. Kronka, P.J.M. Cordeiro-Junior, L. Mira, A.J. dos Santos, G. v. Fortunato, M.R.V. Lanza, Sustainable microwave-assisted hydrothermal synthesis of carbon-supported ZrO₂ nanoparticles for H₂O₂ electrogeneration, *Materials Chemistry and Physics*. 267 (2021) 124575. <https://doi.org/10.1016/j.matchemphys.2021.124575>.
- [3] M.S. Çelebi, N. Oturan, H. Zazou, M. Hamdani, M.A. Oturan, Electrochemical oxidation of carbaryl on platinum and boron-doped diamond anodes using electro-Fenton technology, *Separation and Purification Technology*. 156 (2015) 996–1002. <https://doi.org/10.1016/j.seppur.2015.07.025>.
- [4] T.É.S. Santos, R.S. Silva, C. Carlesi Jara, K.I.B. Eguiluz, G.R. Salazar-Banda, The influence of the synthesis method of Ti/RuO₂ electrodes on their stability and catalytic activity for electrochemical oxidation of the pesticide carbaryl, *Materials Chemistry and Physics*. 148 (2014) 39–47. <https://doi.org/10.1016/j.matchemphys.2014.07.007>.
- [5] G.R.P. Malpass, D.W. Miwa, A.C.P. Miwa, S.A.S. Machado, A.J. Motheo, Study of photo-assisted electrochemical degradation of carbaryl at dimensionally stable anodes (DSA®), *Journal of Hazardous Materials*. 167 (2009) 224–229. <https://doi.org/10.1016/j.jhazmat.2008.12.109>.
- [6] D.W. Miwa, G.R.P. Malpass, S.A.S. Machado, A.J. Motheo, Electrochemical degradation of carbaryl on oxide electrodes, *Water Research*. 40 (2006) 3281–3289. <https://doi.org/10.1016/j.watres.2006.06.033>.

CONCLUSION

In this thesis, technological updates were discussed concerning the development of selective catalysts based on carbon materials modified with metallic nanoparticles for the electrochemical production of H_2O_2 in acidic media.

In Chapter I, the surface modification of the Printex L6 carbon using a low Pd loading (<1% w/w) result in a ~320 mV gain in the overpotential of the onset reaction. The selectivity towards H_2O_2 in the $\text{Pd}_{1\%}/\text{PL6C}$ material was close to 90% while for high doping values of Pd, such as in the $\text{Pd}_{20\%}/\text{PL6C}$ material, only 10% selectivity was found. This result was a consequence of the larger interparticle distance in the material containing low loading of Pd, which minimized the readsorption effect of H_2O_2 and favored the release of H_2O_2 from the surface. The optimal performance of $\text{Pd}_{1\%}/\text{PL6C}$ for H_2O_2 production was further employed for homogeneous $\bullet\text{OH}$ production via EF and PEF processes to efficient methylparaben removal in acidic media. On the other hand, analysis of the catalyst surface revealed partially positively charges on the Pd NPs, suggesting a strong interaction between the functional groups of the carbon matrix and the metallic structure. Hence, Chapter II was focused to the development of a hybrid support incorporating metal oxides to shield the metal nanoparticles from the positive charge of the carbon matrix, thereby optimizing its catalytic performance for H_2O_2 production.

A $\text{ZrO}_2/\text{PL6C}$ hybrid matrix was produced in Chapter II using an innovative approach by developing microwave-assisted hydrothermal synthesis (MAH). Different parameters were evaluated to find a well-dispersed material with small particle size (7 nm) after 40 minutes of synthesis at 140 °C. The optimized $\text{ZrO}_2/\text{PL6C}$ material showed selectivity for the production of H_2O_2 ($S_{\text{H}_2\text{O}_2}$) of 89%, similar to the unmodified carbon matrix. However, the high electrochemical stability in acidic media and the 140 mV overpotential gain at the ORR onset corroborated on the use of $\text{ZrO}_2/\text{PL6C}$ as a hybrid support for anchoring metal nanoparticles.

The Chapter III studied the support of gold nanoparticles in higher amount onto the hybrid support, considering that the use of a low palladium content could make it difficult to visualize the effects of the hybrid support on metal anchoring. The hybrid support proved to be highly effective in anchoring Au NPs, resulting in well-dispersed nanoparticles with a nanometer-scale particle size of 77 nm. The oxophilic nature of ZrO_2 provided stability for the gold nanoparticles and favored the metallic state of the noble metal. Thus, we found an optimal $\text{Au_ZrO}_2/\text{PL6C}$ material exhibiting ~350 mV early

onset overpotential of reaction compared to bare PL6C, apart from achieving 97% selectivity towards H₂O₂ production. This material also proved to be highly efficient for H₂O₂ production on a laboratory scale, providing a 70% of current efficiency by producing 600 mg L⁻¹ after 120 min under $j = 50 \text{ mA cm}^{-2}$. When applied in a pre-pilot system containing a flow-by reactor coupled to a BDD anode, the Au_ZrO₂/PL6C proved to be stable for H₂O₂ production in a real sewage effluent. Even in a complex matrix containing H₂O₂ scavengers and inorganic contaminants that can passivate the catalytic surface, the Au_ZrO₂/PL6C-based catalyst showed suitable results for the pesticide removal in less than 10 minutes of PEF process.

Therefore, we strongly believe that interactions across different strategies towards modifying the carbonaceous matrices can be established to potentially find the synergy in order to increase the catalysis for H₂O₂ production. Additionally, the scalability of these materials towards H₂O₂ production during treatment of real effluents contaminated by persistent organics pollutants on a pre-pilot scale has been successfully demonstrated in the present thesis.

SCIENTIFIC PRODUCTION

The scientific articles that have been published in indexed journals as a result of this PhD thesis are as follows:

- G. V. Forrtunato, **M. S. Kronka**, A. J. dos Santos; M. Ledendecker; M. R. V. Lanza, Low Pd loadings onto Printex L6: Synthesis, characterization and performance towards H₂O₂ generation for electrochemical water treatment technologies. *Chemosphere* v. 259, 127523, (2020)
- **M.S. Kronka**, P.J.M. Cordeiro-Junior, L. Mira, A.J. dos Santos, G.V. Fortunato, M.R.V. Lanza, Sustainable microwave-assisted hydrothermal synthesis of carbon supported ZrO₂ nanoparticles for H₂O₂ electrogeneration. *Material Chemistry and Physic* v. 267 (2021).
- **M.S. Kronka**; G.V. Fortunato; L. Mira; A.J. dos Santos; M.R.V. Lanza. Using Au NPs anchored on ZrO₂/carbon black toward more efficient H₂O₂ electrogeneration in flow-by reactor for carbaryl removal in real wastewater. *Chemical Engineering Journal*. V. 452, 15 (2023), 139598

The scientific articles that have been published in indexed journals as a result of collaboration during the PhD thesis are as follows:

- A. J. dos Santos, **M. S. Kronka**, G. V. Fortunato, M. R. V. Lanza, Recent advances in electrochemical water technologies for the treatment of antibiotics: A short review. *Current Opinion in Electrochemistry* 26, 100674.
- A. J dos Santos, G. V. Fortunato, **M. S. Kronka**, L. G. Vernasqui, N. G. Ferreira, M. R. V. Lanza, Electrochemical oxidation of ciprofloxacin in different aqueous matrices using synthesized boron-doped micro and nano-diamond anodes. *Environmental Research* 204, 112027.
- A. J. dos Santos, A. S. Fajardo, **M. S. Kronka**, S. Garcia-Segura, M. R. V. Lanza. Effect of electrochemically-driven technologies on the treatment of endocrine disruptors in synthetic and real urban wastewater. *Electrochimica Acta* 376, 138034.
- A. J. M. da Costa, **M. S Kronka**, P. J. M. Cordeiro-Junior, G. V. Fortunato, A. J. dos Santos, M. R. V. Lanza. Treatment of Tebuthiuron in synthetic and real wastewater using electrochemical flow-by reactor. *Electrochimica Acta*, 376, 138034.

- P. J. M. Cordeiro-Junior, **M. S. Kronka**, L. A. Goulart, N. C. Veríssimo, L. H. Mascaro, M. C. dos Santos, R. Bertazzoli, M. R. de V. Lanza. Catalysis of oxygen reduction reaction for H₂O₂ electrogeneration: The impact of different conductive carbon matrices and their physicochemical properties. *Journal of Catalysis* 392, 56-68.
- G. V. Fortunato, L. S. Bezerra, E. S. F. Cardoso, **M. S. Kronka**, A. J. Santos, A. S. Greco, J. L. R. Júnior, M. R. V. Lanza, G. Maia. Using palladium and gold palladium nanoparticles decorated with molybdenum oxide for versatile hydrogen peroxide electroproduction on graphene nanoribbons. *ACS Applied Materials & Interfaces* 14 (5), 6777-6793
- G. O. S. Santos, P. J. M. Cordeiro-Junior, I. Sánchez-Montes, R. S. Souto, **M. S. Kronka**, M. R. V. Lanza. Recent advances in H₂O₂ electrosynthesis based on the application of gas diffusion electrodes: challenges and opportunities. *Current Opinion in Electrochemistry*, 101124.
- G. V. Fortunato, **M. S. Kronka**, E. S. F. Cardoso, A. J. dos Santos, A. C. Roveda Jr, F. H. B. Lima, M. Ledendecker, G. Maia, M. R. V. Lanza. A comprehensive comparison of oxygen and nitrogen functionalities in carbon and their implications for the oxygen reduction reaction. *Journal of Catalysis* 413, 1034-1047.
- L. G. Vernasqui, A. J. dos Santos, G. V. Fortunato, **M. S. Kronka**, H. L. Barazorda-Ccahuana, A. S. Fajardo, N. G. Ferreira, M. R. V. Lanza. Highly porous seeding-free boron-doped ultrananocrystalline diamond used as high-performance anode for electrochemical removal of carbaryl from water. *Chemosphere* 305, 135497

REFERENCES

- 1 ROHR, J. R.; BARRETT, C. B.; CIVITELLO, D. J.; CRAFT, M. E.; DELIUS, B.; DELEO, G. A.; HUDSON, P. J.; JOUANARD, N.; NGUYEN, K. H.; OSTFELD, R. S.; REMAIS, J. V.; RIVEAU, G.; SOKOLOW, S. H.; TILMAN, D. Emerging human infectious diseases and the links to global food production. **Nature Sustainability**, Berlin, v. 2, n. 6, p. 445–456, jun. 2019.
- 2 SOUZA, M. C. O.; ROCHA, B. A.; ADEYEMI, J. A.; NADAL, M.; DOMINGO, J. L.; BARBOSA, F. Legacy and emerging pollutants in latin america: a critical review of occurrence and levels in environmental and food samples. **Science of the Total Environment**, Amsterdam, v. 848, 157774, nov. 2022.
- 3 SCHWARZENBACH, R. P.; EGLI, T.; HOFSTETTER, T. B.; VON GUNTEN, U.; WEHRLI, B. Global water pollution and human health. **Annual Review of Environment and Resources**, Palo Alto, v. 35, p. 109–136, nov. 2010.
- 4 DANNER, M. C.; ROBERTSON, A.; BEHREND, V.; REISS, J. Antibiotic pollution in surface fresh waters: occurrence and effects. **Science of the Total Environment**, Amsterdam, v. 664, p. 793–804, may. 2019.
- 5 GEISSEN, V.; MOL, H.; KLUMPP, E.; UMLAUF, G.; NADAL, M.; PLOEG, M. Van Der; ZEE, S. E. A. T. M. Van De; RITSEMA, C. J. Emerging pollutants in the environment: a challenge for water resource management. **International Soil and Water Conservation Research**, Beijing, v. 3, n. 1, p. 57–65, mar. 2015.
- 6 BETHI, B.; RADHIKA, G. B.; SONAWANE, S. H. Fundamentals of advanced oxidation processes (AOPs) for wastewater treatment: Challenges and opportunities. *In*: MUNGRAY, A.; MUNGRAY, A.; SONAWANE, S.; SONAWANE, S. Novel (eds). **Approaches towards Wastewater Treatment and Resource Recovery Technologies**. Greater Noida: Elsevier, 2002. v. 1, p. 209–220.
- 7 MARTÍNEZ-HUITLE, C. A.; BRILLAS, E. Decontamination of wastewaters containing synthetic organic dyes by electrochemical methods: a general review. **Applied Catalysis B: Environmental**, Amsterdam, v. 87, p. 105–145, apr. 2009.
- 8 DONG, C.; FANG, W.; YI, Q.; ZHANG, J. A comprehensive review on reactive oxygen species (ROS) in advanced oxidation processes (AOPs). **Chemosphere**, Kidlington, v. 308, 136205, dec. 2022.
- 9 BRILLAS, E.; SIRÉS, I.; OTURAN, M. A. Electro-fenton process and related electrochemical technologies based on fenton's reaction chemistry. **Chemical Reviews**, Washington, v. 109, p. 6570–6631, oct. 2009.
- 10 BRILLAS, E. A review on the photoelectro-fenton process as efficient electrochemical advanced oxidation for wastewater remediation. treatment with uv light, sunlight, and coupling with conventional and other photo-assisted advanced technologies. **Chemosphere**, Kidlington, v. 250, n. 126198, jul. 2020.
- 11 GOZZI, F.; SIRÉS, I.; DE OLIVEIRA, S. C.; MACHULEK, A.; BRILLAS, E. Influence of chelation on the Fenton-based electrochemical degradation of herbicide tebuthiuron. **Chemosphere**, Kidlington, v. 199, p. 709–717, may. 2018.
- 12 XU, A.; BRILLAS, E.; HAN, W.; WANG, L.; SIRÉS, I. On the positive effect of UVC light during the removal of benzothiazoles by photoelectro-Fenton with UVA light. **Applied Catalysis B: Environmental**, Amsterdam, v. 259, p. 118127, apr. 2019.

- 13 BRILLAS, E.; MARTÍNEZ-HUITLE, C. A. Decontamination of wastewaters containing synthetic organic dyes by electrochemical methods. An updated review. **Applied Catalysis B: environmental**, Amsterdam, v. 166–167, p. 603–643, may. 2015.
- 14 MOREIRA, F. C.; BOAVENTURA, R. A. R.; BRILLAS, E.; VILAR, V. J. P. Electrochemical advanced oxidation processes: a review on their application to synthetic and real wastewaters. **Applied Catalysis B: Environmental**, Amsterdam, v. 202, p. 217–261, mar. 2017.
- 15 SIAHROSTAMI, S.; VERDAGUER-CASADEVALL, A.; KARAMAD, M.; DEIANA, D.; MALACRIDA, P.; WICKMAN, B.; ESCUDERO-ESCRIBANO, M.; PAOLI, E. A.; FRYDENDAL, R.; HANSEN, T. W.; CHORKENDORFF, I.; STEPHENS, I. E. L.; ROSSMEISL, J. Enabling direct H₂O₂ production through rational electrocatalyst design. **Nature Materials**, Berlin, v. 12, p. 1137–1143, nov. 2013.
- 16 YANG, S.; VERDAGUER-CASADEVALL, A.; ARNARSON, L.; SILVIOLI, L.; ČOLIĆ, V.; FRYDENDAL, R.; ROSSMEISL, J.; CHORKENDORFF, I.; STEPHENS, I. E. L. Toward the decentralized electrochemical production of H₂O₂: a focus on the catalysis. **ACS Catalysis**, Washington, v. 8, p. 4064–4081, may. 2018.
- 17 SANTOS, G. O. S.; CORDEIRO-JUNIOR, P. J. M.; SÁNCHEZ-MONTES, I.; SOUTO, R. S.; KRONKA, M. S.; LANZA, M. R. V. Recent advances in H₂O₂ electrosynthesis based on the application of gas diffusion electrodes: challenges and opportunities. **Current Opinion in Electrochemistry**, Amsterdam, v. 36, 101124, dec. 2022.
- 18 WANG, J.; LI, C.; RAUF, M.; LUO, H.; SUN, X.; JIANG, Y. Gas diffusion electrodes for H₂O₂ production and their applications for electrochemical degradation of organic pollutants in water: A review. **Science of the Total Environment**, Amsterdam, v.759, 143459, mar. 2021.
- 19 YEAGER, E. Electrocatalysts for O₂ reduction. **Electrochimica Acta**, Kidlington, v. 29, p. 1527–1537, nov. 1984.
- 20 YEAGER, E. Dioxygen electrocatalysis: mechanisms in relation to catalyst structure. **Journal of Molecular Catalysis A - chemical**, Amsterdam, v. 38, p. 5–25, nov. 1986.
- 21 KATSOUNAROS, I.; SCHENEIDER, W. B.; MEIER, J. C.; BENEDIKT, U.; BIEDERMANN, P. U.; AUER, A. A.; MAYRHOFER, K. J. J. Hydrogen peroxide electrochemistry on platinum: towards understanding the oxygen reduction mechanism. **Physical Chemistry Chemical Physics**, Cambridge, v. 14, p. 7384–7391, apr. 2012.
- 22 FORTUNATO, G. V.; PIZZUTILO, E.; CARDOSO, E. S. F.; LANZA, M. R. V.; KATSOUNAROS, I.; FREAKLEY, S. J.; MAYRHOFER, K. J. J.; MAIA, G.; LEDENDECKER, M. The oxygen reduction reaction on palladium with low metal loadings: The effects of chlorides on the stability and activity towards hydrogen peroxide. **Journal of Catalysis**, San Diego, v. 389, p. 400–408, sep. 2020.
- 23 FORTUNATO, G. V.; PIZZUTILO, E.; MINGERS, A. M.; KASIAN, O.; CHEREVKO, S.; CARDOSO, E. S. F.; MAYRHOFER, K. J. J.; MAIA, G.; LEDENDECKER, M. Impact of palladium loading and interparticle distance on the selectivity for the oxygen reduction Reaction toward hydrogen peroxide. **Journal of Physical Chemistry C**, Washington, v. 122, n. 28, p. 15878–15885, jun. 2018.
- 24 COLLMAN P.J.; DENISEVICH P.; KONAI Y.; MARROCCO M.; KOVAL C.; AND ANSO C.F. Electrode catalysis of the four-electron reduction of oxygen to water by dicobalt

- face-to-face porphyrins. **Journal of the American Chemical Society**, Washington, v. 102, p. 6027–6036, sep. 1980.
- 25 PAULING, L. Nature of the iron–oxygen bond in oxyhaemoglobin. **Nature**, Berlin, v. 203, p. 182–183, jul. 1964.
- 26 GARTES, V. A.; WEISS, D. E. A new interpretations of the acidic and basic structures in carbons. **Pure and Applied Chemistry**, Berlin, v. 7, p. 309–328, apr. 1957.
- 27 GRIFFITH, J. S. On the magnetic properties of some haemoglobin complexes. **Proceedings of the Royal Society of London. Series A. Mathematical and Physical Sciences**, London, v. 235, n. 1200, p. 23–36, oct. 1955.
- 28 VERDAGUER-CASADEVALL, A.; DEIANA, D.; KARAMAD, M.; SIAHROSTAMI, S.; MALACRIDA, P.; HANSEN, T. W.; ROSSMEISL, J.; CHORKENDORFF, I.; STEPHENS, I. E. L. Trends in the electrochemical synthesis of H₂O₂: enhancing activity and selectivity by electrocatalytic site engineering. **Nano Letters**, Washington, v. 14, n. 3, p. 1603–1608, feb. 2014.
- 29 JIRKOVSKÝ, J. S.; PANAS, I.; AHLBERG, E.; HALASA, M.; ROMANI, S.; SCHIFFRIN, D. J. Single atom hot-spots at au–pd nanoalloys for electrocatalytic h₂o₂ production. **Journal of the American Chemical Society**, Washington, v. 133, n. 48, p. 19432–19441, dec. 2011.
- 30 WU, K.-H.; WANG, D.; LU, X.; ZHANG, X.; XIE, Z.; LIU, Y.; SU, B.-J.; CHEN, J.-M.; SU, D.-S.; QI, W.; GUO, S. Highly selective hydrogen peroxide electrosynthesis on carbon: in situ interface engineering with surfactants. **Chem**, Cambridge, v. 6, n. 6, p. 1443–1458, jun. 2020.
- 31 ASSUMPCÃO, M. H. M. T.; DE SOUZA, R. F. B.; RASCIO, D. C.; SILVA, J. C. M.; CALEGARO, M. L.; GAUBEUR, I.; PAIXÃO, T. R. L. C.; HAMMER, P.; LANZA, M. R. V.; SANTOS, M. C. A comparative study of the electrogeneration of hydrogen peroxide using Vulcan and Printex carbon supports. **Carbon**, Kidlington, v. 49, n. 8, p. 2842–2851, jul. 2011.
- 32 CORDEIRO-JUNIOR, P. J. M.; GONÇALVES, R.; GUARALDO, T. T.; DA SILVA PAIVA, R.; PEREIRA, E. C.; LANZA, M. R. de V. Oxygen reduction reaction: Semi-empirical quantum mechanical and electrochemical study of Printex L6 carbon black. **Carbon**, Kidlington, v. 156, p. 1–9, jan. 2020.
- 33 CORDEIRO-JUNIOR, P. J. M.; KRONKA, M. S.; GOULART, L. A.; VERÍSSIMO, N. C.; MASCARO, L. H.; SANTOS, M. C.; BERTAZZOLI, R.; LANZA, M. R. V. Catalysis of oxygen reduction reaction for H₂O₂ electrogeneration: the impact of different conductive carbon matrices and their physicochemical properties. **Journal of Catalysis**, San Diego, v. 392, p. 56–68, dec. 2020.
- 34 DONOEVA, B.; MASOUD, N.; DE JONGH, P. E. Carbon support surface effects in the gold-catalyzed oxidation of 5-hydroxymethylfurfural. **ACS Catalysis**, Washington, v. 7, p. 4581–4591, may. 2017.
- 35 LU, Z.; CHEN, G.; SIAHROSTAMI, S.; CHEN, Z.; LIU, K.; XIE, J.; LIAO, L.; WU, T.; LIN, Di.; LIU, Y.; JARAMILLO, T. F.; NØRSKOV, J. K.; CUI, Y. High-efficiency oxygen reduction to hydrogen peroxide catalyzed by oxidized carbon materials. **Nature Catalysis**, Berlin, v. 1, n. 2, p. 156–162, jan. 2018.

- 36 HASCHÉ, F.; OEZASLAN, M.; STRASSER, P.; FELLINGER, T. P. Electrocatalytic hydrogen peroxide formation on mesoporous non-metal nitrogen-doped carbon catalyst. **Journal of Energy Chemistry**, Amsterdam, v. 25, n. 2, p. 251–257, mar. 2016.
- 37 GONG, K.; DU, F.; XIA, Z.; DURSTOCK, M.; DAI, L. Nitrogen-doped carbon nanotube arrays with high electrocatalytic activity for oxygen reduction. **Science**, Washington, v. 323, n. 5915, p. 760–764, feb. 2009.
- 38 BANDOSZ, T. J. **Surface Chemistry of Carbon Materials**. In: SERP, P.; FIGUEIREDO, J. L. *Carbon Materials for Catalysis*, Hoboken: John Wiley, 2009. v.1, p. 45–82.
- 39 KRONKA, M. S.; SILVA, F. L.; MARTINS, A. S.; ALMEIDA, M. O.; HONÓRIO, K. M.; LANZA, M. R. V. Tailoring the ORR selectivity for H₂O₂ electrogeneration by modification of Printex L6 carbon with 1,4-naphthoquinone: a theoretical, experimental and environmental application study. **Materials Advances**, Cambridge, v. 1, p. 1318–1329, jun. 2020.
- 40 MOREIRA, J.; BOCALON LIMA, V.; ATHIE GOULART, L.; LANZA, M. R. V. Electrosynthesis of hydrogen peroxide using modified gas diffusion electrodes (MGDE) for environmental applications: quinones and azo compounds employed as redox modifiers. **Applied Catalysis B: Environmental**, Amsterdam, v. 248, p. 95–107, jan. 2019.
- 41 ROCHA, R. S.; VALIM, R. B.; TREVELIN, L. C.; STETER, J. R.; CARNEIRO, J. F.; FORTI, J. C.; BERTAZZOLI, R.; LANZA, M. R. V. Electrocatalysis of hydrogen peroxide generation using oxygen-fed gas diffusion electrodes made of carbon black modified with quinone compounds. **Electrocatalysis**, New York, v. 11, n. 3, p. 338–346, mar. 2020.
- 42 REIS, R. M.; VALIM, R. B.; ROCHA, R. S.; LIMA, A. S.; CASTRO, P. S.; BERTOTTI, M.; LANZA, M. R. V. The use of copper and cobalt phthalocyanines as electrocatalysts for the oxygen reduction reaction in acid medium. **Electrochimica Acta**, Kidlington, v. 139, p. 1–6, sep. 2014.
- 43 BARROS, W. R. P.; REIS, R. M.; ROCHA, R. S.; LANZA, M. R. V. Electrogeneration of hydrogen peroxide in acidic medium using gas diffusion electrodes modified with cobalt (II) phthalocyanine. **Electrochimica Acta**, Kidlington, v. 104, p. 12–18, aug. 2013.
- 44 BARROS, W. R. P.; FRANCO, P. C.; STETER, J. R.; ROCHA, R. S.; LANZA, M. R. V. Electro-Fenton degradation of the food dye amaranth using a gas diffusion electrode modified with cobalt (II) phthalocyanine. **Journal of Electroanalytical Chemistry**, Lausanne, v. 722–723, p. 46–53, may. 2014.
- 45 SILVA, F. L.; REIS, R. M.; BARROS, W. R. P.; ROCHA, R. S.; LANZA, M. R. V. Electrogeneration of hydrogen peroxide in gas diffusion electrodes: application of iron (II) phthalocyanine as a modifier of carbon black. **Journal of Electroanalytical Chemistry**, Lausanne, v. 722–723, p. 32–37, may. 2014.
- 46 FÉLIX-NAVARRO, R. M.; BELTRÁN-GASTÉLUM, M.; SALAZAR-GASTÉLUM, M. I.; SILVA-CARRILLO, C.; REYNOSO-SOTO, E. A.; PÉREZ-SICAIROS, S.; LIN, S. W.; PARAGUAY-DELGADO, F.; ALONSO-NÚÑEZ, G. Pt-Pd bimetallic nanoparticles on MWCNTs: catalyst for hydrogen peroxide electrogeneration. **Journal of Nanoparticle Research**, Dordrecht, v. 15, n. 8, jul. 2013.
- 47 LEDENDECKER, M.; PIZZUTILO, E.; MALTA, G.; FORTUNATO, G. V.; MAYRHOFER, K. J. J.; HUTCHINGS, G. J.; FREAKLEY, S. J. Isolated Pd sites as selective catalysts for electrochemical and direct hydrogen peroxide synthesis. **ACS Catalysis**, Washington, v. 10, p. 5928–5938, apr. 2020.

- 48 XU, H.; CHENG, D.; GAO, Y. Design of high-performance pd-based alloy nanocatalysts for direct synthesis of H₂O₂. **ACS Catalysis**, Washington, v. 7, n. 3, p. 2164–2170, feb. 2017.
- 49 CARNEIRO, J. F.; TREVELIN, L. C.; LIMA, A. S.; MELONI, G. N.; BERTOTTI, M.; HAMMER, P.; BERTAZZOLI, R.; LANZA, M. R. V. Synthesis and characterization of ZrO₂/C as electrocatalyst for oxygen Reduction to H₂O₂. **Electrocatalysis**, New York, v. 8, n. 3, p. 189–195, feb. 2017.
- 50 XU, F.; SONG, T.; XU, Y.; CHEN, Y.; ZHU, S.; SHEN, S. A new cathode using CeO₂/MWNT for hydrogen peroxide synthesis through a fuel cell. **Journal of Rare Earths**, Amsterdam, v. 27, n. 1, p. 128–133, feb. 2009.
- 51 SIMAS, P. S.; ANTONIN, V. S.; PARREIRA, L. S.; HAMMER, P.; SILVA, F. L.; KRONKA, M. S.; VALIM, R. B.; LANZA, M. R. V.; SANTOS, M. C. Carbon modified with vanadium nanoparticles for hydrogen peroxide electrogeneration. **Electrocatalysis**, New York, v. 8, n. 4, p. 311–320, apr. 2017.
- 52 CARNEIRO, J. F.; ROCHA, R. S.; HAMMER, P.; BERTAZZOLI, R.; LANZA, M. R. V. Hydrogen peroxide electrogeneration in gas diffusion electrode nanostructured with Ta₂O₅. **Applied Catalysis A: General**, Amsterdam, v. 517, p. 161–167, may. 2016.
- 53 CARNEIRO, J. F.; PAULO, M. J.; SIAJ, M.; TAVARES, A. C.; LANZA, M. R. V. Nb₂O₅ nanoparticles supported on reduced graphene oxide sheets as electrocatalyst for the H₂O₂ electrogeneration. **Journal of Catalysis**, San Diego, v. 332, p. 51–61, dec. 2015.
- 54 CARNEIRO, J. F.; PAULO, M. J.; SIAJ, M.; TAVARES, A. C.; LANZA, M. R. V. Zirconia on reduced graphene oxide sheets: synergistic catalyst with high selectivity for H₂O₂ electrogeneration. **ChemElectroChem**, Weinheim, v. 4, n. 3, p. 508–513, dec. 2016.
- 55 RODRÍGUEZ-REINOSO, F.; SEPÚLVEDA-ESCRIBANO, A. Carbon as catalyst support. *In*: SERP, P.; FIGUEIREDO, J. L. **Carbon materials for catalysis**. Hoboken: John Wiley, 2009. v.1 p. 131–150.
- 56 VILLA, A.; SCHIAVONI, M.; PRATI, L. Material science for the support design: a powerful challenge for catalysis. **Catalysis Science and Technology**, Cambridge, v.2, p. 673–682, jan. 2012.
- 57 BARROS, W. R. P.; WEI, Q.; ZHANG, G.; SUN, S.; LANZA, M. R. V.; TAVARES, A. C. Oxygen reduction to hydrogen peroxide on Fe₃O₄ nanoparticles supported on Printex carbon and Graphene. **Electrochimica Acta**, Kidlington, v. 162, p. 263–270, apr. 2015.
- 58 CARNEIRO, J. F.; SILVA, F. L.; MARTINS, A. S.; DIAS, R. M. P.; TITATO, G. M.; SANTOS-NETO, Á. J.; BERTAZZOLI, R.; LANZA, M. R. V. Simultaneous degradation of hexazinone and diuron using ZrO₂-nanostructured gas diffusion electrode. **Chemical Engineering Journal**, Lausanne, v. 351, p. 650–659, nov. 2018.
- 59 DOS SANTOS, A. J.; GARCIA-SEGURA, S.; DOSTA, S.; CANO, I. G.; MARTÍNEZ-HUITLE, C. A.; BRILLAS, E. A ceramic electrode of ZrO₂-Y₂O₃ for the generation of oxidant species in anodic oxidation. assessment of the treatment of acid blue 29 dye in sulfate and chloride media. **Separation and Purification Technology**, Amsterdam, v. 228, n. 115747, dec. 2019.

- 60 GODINHO, M.; RIBEIRO, C.; LONGO, E.; LEITE, E. R. Influence of microwave heating on the growth of gadolinium-doped cerium oxide nanorods. **Crystal Growth and Design**, Washington, v. 8, n. 2, p. 384–386, jan. 2008.
- 61 CHEN, G.; STEVENS, M. B.; LIU, Y.; KING, L. A.; PARK, J.; KIM, T. R.; SINCLAIR, R.; JARAMILLO, T. F.; BAO, Z. Nanosized Zirconium Porphyrinic Metal–Organic Frameworks that Catalyze the Oxygen Reduction Reaction in Acid. **Small Methods**, Weinheim, v. 4, n. 10, 2000085, aug. 2020.
- 62 ZHAO, H.; CHEN, Y.; PENG, Q.; WANG, Q.; ZHAO, G. Catalytic activity of MOF(2Fe/Co)/carbon aerogel for improving H₂O₂ and •OH generation in solar photo–electro–Fenton process. **Applied Catalysis B: Environmental**, Amsterdam, v. 203, p. 127–137, apr. 2017.
- 63 PIZZUTILO, E.; FREAKLEY, S. J.; CHEREVKO, S.; VENKATESAN, S.; HUTCHINGS, G. J.; LIEBSCHER, C. H.; DEHM, G.; MAYRHOFER, K. J. J. Gold–palladium bimetallic catalyst stability: consequences for hydrogen peroxide selectivity. **ACS Catalysis**, Washington, v. 7, n. 9, p. 5699–5705, jul. 2017.
- 64 PIZZUTILO, E.; FREAKLEY, S. J.; GEIGER, S.; BALDIZZONE, C.; MINGERS, A.; HUTCHINGS, G. J.; MAYRHOFER, K. J. J.; CHEREVKO, S. Addressing stability challenges of using bimetallic electrocatalysts: the case of gold–palladium nanoalloys. **Catalysis Science and Technology**, Cambridge, v. 7, n. 9, p. 1848–1856, mar. 2017.
- 65 TREVELIN, L. C.; VALIM, R. B.; CARNEIRO, J. F.; DE SIERVO, A.; ROCHA, R. S.; LANZA, M. R. V. Using black carbon modified with NbMo and NbPd oxide nanoparticles for the improvement of H₂O₂ electrosynthesis. **Journal of Electroanalytical Chemistry**, Lausanne, v. 877, 114746, nov. 2020.
- 66 SUN, Y.; SILVIOLI, L.; SAHRAIE, N. R.; JU, W.; LI, J.; ZITOLO, A.; LI, S.; BAGGER, A.; ARNARSON, L.; WANG, X.; MOELLER, T.; BERNSMEIER, D.; ROSSMEISL, J.; JAOUEN, F.; STRASSER, P. Activity–selectivity trends in the electrochemical production of hydrogen peroxide over single-site metal–nitrogen–carbon catalysts. **Journal of the American Chemical Society**, Washington, v. 141, n. 31, p. 12372–12381, jul. 2019.
- 67 GAO, J.; LIU, B. Progress of electrochemical hydrogen peroxide synthesis over single atom catalysts. **ACS Materials Letters**, Washington, v. 2, n. 8, p. 1008–1024, jul. 2020.
- 68 CORDEIRO-JUNIOR, P. J. M.; MARTINS, A. S.; PEREIRA, G. B. S.; ROCHA, F. V.; RODRIGO, M. A. R.; LANZA, M. R. de V. Bisphenol-S removal via photoelectro-fenton/H₂O₂ process using Co-porphyrin/Printex L6 gas diffusion electrode. **Separation and Purification Technology**, Cambridge, v. 285, mar. 2022.
- 69 WIBERG, G. K. H.; NÖSBERGER, S.; ARENZ, M. Evolution of a GDE setup: beyond ambient conditions. **Current Opinion in Electrochemistry**, Amsterdam, v. 36, n. 101129, dec. 2022.
- 70 SOLTANI, R. D. C.; REZAEI, A.; KHATAEI, A. R.; GODINI, H. Electrochemical generation of hydrogen peroxide using carbon black-, carbon nanotube-, and carbon black/carbon nanotube-coated gas-diffusion cathodes: effect of operational parameters and decolorization study. **Research on Chemical Intermediates**, Dordrecht, v. 39, n. 9, p. 4277–4286, dec. 2012.
- 71 VALIM, R. B.; REIS, R. M.; CASTRO, P. S.; LIMA, A. S.; ROCHA, R. S.; BERTOTTI, M.; LANZA, M. R. V. Electrogenation of hydrogen peroxide in gas diffusion electrodes

modified with tert-butyl-anthraquinone on carbon black support. **Carbon**, Kidlington, v. 61, p. 236–244, sep. 2013.

72 LIMA, V. B.; GOULART, L. A.; ROCHA, R. S.; STETER, J. R.; LANZA, M. R. V. Degradation of antibiotic ciprofloxacin by different AOP systems using electrochemically generated hydrogen peroxide. **Chemosphere**, Kidlington, v. 247, p. 125807, may. 2020.

73 STETER, J. R.; BRILLAS, E.; SIRÉS, I. Solar photoelectro-Fenton treatment of a mixture of parabens spiked into secondary treated wastewater effluent at low input current. **Applied Catalysis B: environmental**. Amsterdam, v. 224, p. 410–418, may. 2018.